

ANL-7577
RETURN TO ANL (IDAHO) LIBRARY.

Argonne National Laboratory

REACTOR DEVELOPMENT PROGRAM PROGRESS REPORT

April-May 1969

The facilities of Argonne National Laboratory are owned by the United States Government. Under the terms of a contract (W-31-109-Eng-38) between the U. S. Atomic Energy Commission, Argonne Universities Association and The University of Chicago, the University employs the staff and operates the Laboratory in accordance with policies and programs formulated, approved and reviewed by the Association.

MEMBERS OF ARGONNE UNIVERSITIES ASSOCIATION

The University of Arizona
Carnegie-Mellon University
Case Western Reserve University
The University of Chicago
University of Cincinnati
Illinois Institute of Technology
University of Illinois
Indiana University
Iowa State University
The University of Iowa

Kansas State University
The University of Kansas
Loyola University
Marquette University
Michigan State University
The University of Michigan
University of Minnesota
University of Missouri
Northwestern University
University of Notre Dame

The Ohio State University
Ohio University
The Pennsylvania State University
Purdue University
Saint Louis University
Southern Illinois University
University of Texas
Washington University
Wayne State University
The University of Wisconsin

LEGAL NOTICE

This report was prepared as an account of Government sponsored work. Neither the United States, nor the Commission, nor any person acting on behalf of the Commission:

A. Makes any warranty or representation, expressed or implied, with respect to the accuracy, completeness, or usefulness of the information contained in this report, or that the use of any information, apparatus, method, or process disclosed in this report may not infringe privately owned rights; or

B. Assumes any liabilities with respect to the use of, or for damages resulting from the use of any information, apparatus, method, or process disclosed in this report.

As used in the above, "person acting on behalf of the Commission" includes any employee or contractor of the Commission, or employee of such contractor, to the extent that such employee or contractor of the Commission, or employee of such contractor prepares, disseminates, or provides access to, any information pursuant to his employment or contract with the Commission, or his employment with such contractor.

Printed in the United States of America

Available from

Clearinghouse for Federal Scientific and Technical Information
National Bureau of Standards, U. S. Department of Commerce
Springfield, Virginia 22151

Price: Printed Copy \$3.00; Microfiche \$0.65

ARGONNE NATIONAL LABORATORY
9700 South Cass Avenue
Argonne, Illinois 60439

REACTOR DEVELOPMENT PROGRAM
PROGRESS REPORT

April-May 1969

Robert B. Duffield, Laboratory Director
Stephen Lawroski, Associate Laboratory Director

<u>Division</u>	<u>Director</u>
Chemical Engineering	R. C. Vogel
EBR-II Project	M. Levenson
Metallurgy	M. V. Nevitt
Reactor Engineering	L. J. Koch
Reactor Physics	R. Avery

Report coordinated by
A. Glassner and A. D. Rossin

Issued July 7, 1969

FOREWORD

The Reactor Development Program Progress Report, issued monthly, is intended to be a means of reporting those items of significant technical progress which have occurred in both the specific reactor projects and the general engineering research and development programs. The report is organized in accordance with budget activities in a way which, it is hoped, gives the clearest, most logical overall view of progress. Since the intent is to report only items of significant progress, not all activities are reported each month. In order to issue this report as soon as possible after the end of the month editorial work must necessarily be limited. Also, since this is an informal progress report, the results and data presented should be understood to be preliminary and subject to change unless otherwise stated.

The issuance of these reports is not intended to constitute publication in any sense of the word. Final results either will be submitted for publication in regular professional journals or will be published in the form of ANL topical reports.

The last six reports issued
in this series are:

October 1968	ANL-7513
November 1968	ANL-7518
December 1968	ANL-7527
January 1969	ANL-7548
February 1969	ANL-7553
March 1969	ANL-7561

REACTOR DEVELOPMENT PROGRAM

Highlights of Project Activities for April-May 1969

EBR-II

The reactor was operated for 1820 MWd between March 21 and May 20, bringing its cumulative operational total to 25,043 MWd. Nine experimental subassemblies were loaded into the reactor between March 16 and May 15. As of May 15, the reactor contained 32 experimental subassemblies in which there are 595 experiments.

In the FCF cold line, 941 acceptable Mark-II fuel pins have been made for use in driver-fuel subassemblies planned for testing in the reactor. All production activities in the FCF hot line have been phased out.

Examination of vendor-produced Mark-IA fuel elements after they had been test irradiated in EBR-II to burnups ranging from 0.2 to 0.6 a/o revealed that most of the fuel pins in the elements had shortened during irradiation. Intensive investigations are under way to determine the cause of the shortening. Investigative efforts include extensive examinations of the irradiated elements, reviews of the vendor's manufacturing procedures, and metallurgical examinations of unirradiated as-cast and as-bonded vendor fuel. As of May 15, 22,138 elements had been received from the vendor.

Neutron radiographs showed that two encapsulated ANL-made Mark-IA elements that had been test irradiated in EBR-II to a maximum burnup of 3.5 a/o were intact. The elements are being irradiated further as part of the EBR-II extended-burnup program.

ZPR-3

Measurements with Assembly 56B (FTR-I) were completed in this time period. Experiments which were completed include the evaluation of central and peripheral worths of boron control-composition materials, axial and radial reactivity worth traverses for B-10 and Pu-239, and central fission ratios for U-238, Pu-239, Pu-240, and U-235.

Upon completion of this work, FTR-I was reassembled on ZPPR.

ZPR-6 and -9

Modifications to permit operation of these facilities with plutonium loadings are almost complete. Acceptance testing of the air-exhaust systems for the confinement shell, reactor cells, workroom, vault, and negative pressure areas was started. Mechanical back-draft dampers had been installed in the exhaust systems. These are being replaced with motorized back-draft dampers in order to meet air-flow requirements. This work delays the acceptance tests and the date when Argonne can finally accept the building.

ZPPR

As an initial step in loading the FTR-II core of the Phase B critical experiments program, the critical mass of FTR-I was determined (361.44 kg of total fissile mass) for comparison with that determined on ZPR-3. Temperature coefficient and measurements of control-rod worth have also been completed for this assembly.

TABLE OF CONTENTS

	<u>Page</u>
I. LIQUID METAL FAST BREEDER REACTORS--CIVILIAN	1
A. Fuel Development--LMFBR	1
1. Oxide	1
B. Physics Development--LMFBR	11
1. Theoretical Reactor Physics	11
2. Experimental Reactor Physics	13
3. ZPR-3 Operations and Analysis	17
4. ZPR-6 and -9 Operations and Analysis	35
5. ZPPR Operations and Analysis	38
C. Component Development--LMFBR	43
1. Sodium Technology Development	43
2. Reactor Mechanism and Instrumentation	43
3. Fuel Handling, Vessels, and Internals--Core Component Test Loop	53
D. EBR-II	55
1. Research and Development	55
a. Reactor Experimental Support--Reactor Analysis and Testing	55
b. Nuclear Analysis Methods Development	64
c. Fuel Performance Studies--Mark I Series	75
d. Mark II Driver Fuel Element Development	78
e. Equipment--Fuel Related	79
f. New Subassemblies Design and Experimental Support	81
g. Instrumented Subassembly	82
h. Process Chemistry	84
i. Experimental Irradiation and Testing	87
j. FCF Equipment Improvement	91
k. Superheater and EM Pump Study and Test	91
l. Nuclear Instrument Test Facility Study	91
m. Feasibility Study of Fuel Failure Detection-- Chemical and Mechanical Methods	96
n. Materials-Coolant Compatibility	98
o. Study of Operation with Failed Fuel	99
p. Driver Fuel Transient Performance Studies-- TREAT Experiments	101
q. Systems Engineering	103
r. Oxide Driver	108
2. Operations	109
	123

TABLE OF CONTENTS

	<u>Page</u>
II. OTHER FAST REACTORS--CIVILIAN--OTHER FAST BREEDER REACTORS	124
A. Fuel Development	124
1. Fuel Jacket Alloy Studies	124
III. GENERAL RESEARCH AND DEVELOPMENT--CIVILIAN--STUDIES AND EVALUATIONS	127
A. Fast Reactor Systems and Cost Analysis	127
1. Fuel-cycle Economic Analysis	127
PUBLICATION	127
IV. GENERAL REACTOR TECHNOLOGY	128
A. Applied and Reactor Physics Development	128
1. Theoretical Reactor Physics	128
2. Nuclear Data	135
B. Reactor Fuels and Materials Development	140
1. Fuels and Cladding	140
2. Coolants, Moderators, and Control Materials-- Fundamentals of Corrosion in Liquid Metals	153
3. Radiation Damage on Structural Materials--In-Reactor Creep Studies	155
4. Techniques of Fabrication and Testing	158
5. Engineering Properties of Reactor Materials--High Tem- perature Mechanical Properties of Ceramic Fuels	160
C. Engineering Development	163
1. Instrumentation and Control	163
2. Heat Transfer and Fluid Flow	163
3. Engineering Mechanics	165
D. Chemistry and Chemical Separations	170
1. Aqueous and Volatility Processes--Fluoride Volatility Process	170
2. Closed Cycle Processes--Compact Pyrochemical Processes	173
3. General Chemistry and Chemical Engineering	176
PUBLICATIONS	178

TABLE OF CONTENTS

	<u>Page</u>
V. NUCLEAR SAFETY	181
A. Reactor Kinetics	181
1. Accident Analysis and Safety Evaluation	181
2. Reactor Control and Stability	182
3. Coolant Dynamics	183
4. Core Structural Safety	184
5. Fuel Element Failure Propagation	187
6. Fuel Meltdown Studies with TREAT	190
7. Materials Behavior and Energy Transfer	192
8. Fast Reactor Safety Test Facility Study	196
B. TREAT Operations	197
1. Reactor Operations	197
2. Development of Automatic Power Level Control System	198
C. Chemical Reaction--Chemical and Associated Energy Problems (Thermal)	198
1. Analysis of Excursion Accidents	198
2. Pressure Generation due to Particle-Water Energy Transfer	200
D. Engineered Safety Features	201
1. Safety Features Technology--Containment	201
PUBLICATIONS	204
PUBLICATIONS--General	206

TABLE OF CONTENTS

1	Introduction
2	1. The Problem
3	2. The Method
4	3. The Results
5	4. The Discussion
6	5. The Conclusion
7	6. The Acknowledgments
8	7. The References
9	8. The Appendix
10	9. The Bibliography
11	10. The Index
12	11. The Glossary
13	12. The List of Figures
14	13. The List of Tables
15	14. The List of Equations
16	15. The List of Symbols
17	16. The List of Abbreviations
18	17. The List of Acronyms
19	18. The List of Initials
20	19. The List of Surnames
21	20. The List of First Names
22	21. The List of Middle Names
23	22. The List of Nicknames
24	23. The List of Titles
25	24. The List of Degrees
26	25. The List of Awards
27	26. The List of Honors
28	27. The List of Medals
29	28. The List of Orders
30	29. The List of Decorations
31	30. The List of Crosses
32	31. The List of Stars
33	32. The List of Ribbons
34	33. The List of Badges
35	34. The List of Pins
36	35. The List of Buttons
37	36. The List of Straps
38	37. The List of Belts
39	38. The List of Shoes
40	39. The List of Hats
41	40. The List of Coats
42	41. The List of Dresses
43	42. The List of Skirts
44	43. The List of Pants
45	44. The List of Suits
46	45. The List of Sets
47	46. The List of Outfits
48	47. The List of Ensembles
49	48. The List of Collections
50	49. The List of Lines
51	50. The List of Styles
52	51. The List of Trends
53	52. The List of Movements
54	53. The List of Schools
55	54. The List of Groups
56	55. The List of Societies
57	56. The List of Clubs
58	57. The List of Associations
59	58. The List of Organizations
60	59. The List of Institutions
61	60. The List of Agencies
62	61. The List of Companies
63	62. The List of Firms
64	63. The List of Enterprises
65	64. The List of Businesses
66	65. The List of Industries
67	66. The List of Sectors
68	67. The List of Markets
69	68. The List of Economies
70	69. The List of Systems
71	70. The List of Models
72	71. The List of Theories
73	72. The List of Hypotheses
74	73. The List of Concepts
75	74. The List of Principles
76	75. The List of Laws
77	76. The List of Rules
78	77. The List of Norms
79	78. The List of Standards
80	79. The List of Guidelines
81	80. The List of Procedures
82	81. The List of Methods
83	82. The List of Techniques
84	83. The List of Approaches
85	84. The List of Frameworks
86	85. The List of Perspectives
87	86. The List of Views
88	87. The List of Opinions
89	88. The List of Beliefs
90	89. The List of Attitudes
91	90. The List of Values
92	91. The List of Ideals
93	92. The List of Principles
94	93. The List of Ethics
95	94. The List of Morals
96	95. The List of Customs
97	96. The List of Traditions
98	97. The List of Habits
99	98. The List of Routines
100	99. The List of Patterns
101	100. The List of Behaviors
102	101. The List of Actions
103	102. The List of Reactions
104	103. The List of Responses
105	104. The List of Outcomes
106	105. The List of Results
107	106. The List of Effects
108	107. The List of Impacts
109	108. The List of Consequences
110	109. The List of Implications
111	110. The List of Significance
112	111. The List of Importance
113	112. The List of Relevance
114	113. The List of Validity
115	114. The List of Reliability
116	115. The List of Accuracy
117	116. The List of Precision
118	117. The List of Consistency
119	118. The List of Stability
120	119. The List of Durability
121	120. The List of Permanence
122	121. The List of Endurance
123	122. The List of Longevity
124	123. The List of Sustainability
125	124. The List of Viability
126	125. The List of Feasibility
127	126. The List of Possibility
128	127. The List of Probability
129	128. The List of Likelihood
130	129. The List of Chance
131	130. The List of Risk
132	131. The List of Uncertainty
133	132. The List of Ambiguity
134	133. The List of Complexity
135	134. The List of Diversity
136	135. The List of Variety
137	136. The List of Richness
138	137. The List of Depth
139	138. The List of Breadth
140	139. The List of Scope
141	140. The List of Range
142	141. The List of Extent
143	142. The List of Scale
144	143. The List of Magnitude
145	144. The List of Size
146	145. The List of Volume
147	146. The List of Mass
148	147. The List of Weight
149	148. The List of Force
150	149. The List of Energy
151	150. The List of Power
152	151. The List of Work
153	152. The List of Heat
154	153. The List of Temperature
155	154. The List of Pressure
156	155. The List of Density
157	156. The List of Viscosity
158	157. The List of Elasticity
159	158. The List of Plasticity
160	159. The List of Hardness
161	160. The List of Softness
162	161. The List of Brittleness
163	162. The List of Toughness
164	163. The List of Strength
165	164. The List of Stiffness
166	165. The List of Flexibility
167	166. The List of Elasticity
168	167. The List of Plasticity
169	168. The List of Hardness
170	169. The List of Softness
171	170. The List of Brittleness
172	171. The List of Toughness
173	172. The List of Strength
174	173. The List of Stiffness
175	174. The List of Flexibility
176	175. The List of Elasticity
177	176. The List of Plasticity
178	177. The List of Hardness
179	178. The List of Softness
180	179. The List of Brittleness
181	180. The List of Toughness
182	181. The List of Strength
183	182. The List of Stiffness
184	183. The List of Flexibility
185	184. The List of Elasticity
186	185. The List of Plasticity
187	186. The List of Hardness
188	187. The List of Softness
189	188. The List of Brittleness
190	189. The List of Toughness
191	190. The List of Strength
192	191. The List of Stiffness
193	192. The List of Flexibility
194	193. The List of Elasticity
195	194. The List of Plasticity
196	195. The List of Hardness
197	196. The List of Softness
198	197. The List of Brittleness
199	198. The List of Toughness
200	199. The List of Strength

I. LIQUID METAL FAST BREEDER REACTORS--CIVILIAN

A. Fuel Development--LMFBR

1. Oxide

a. Fuel Studies

- (i) Fuel Element Performance (L. A. Neimark, F. L. Brown, R. Natesh, E. J. Petkus, and W. F. Murphy)

Last Reported: ANL-7561, pp. 1-2 (March 1969).

(a) Identification of Phases in Irradiated Fuel. Identification of phases near the fuel-cladding interface in Element SOV-7 by means of the shielded microprobe continued (see Progress Report for February 1969, ANL-7553, p. 1). Figure I.A.1 is an optical micrograph of an unetched cross section of a sample, located near the top end of the element, where the calculated temperatures at the interface were close to 600°C. Phases that have been identified are indicated on the illustration.

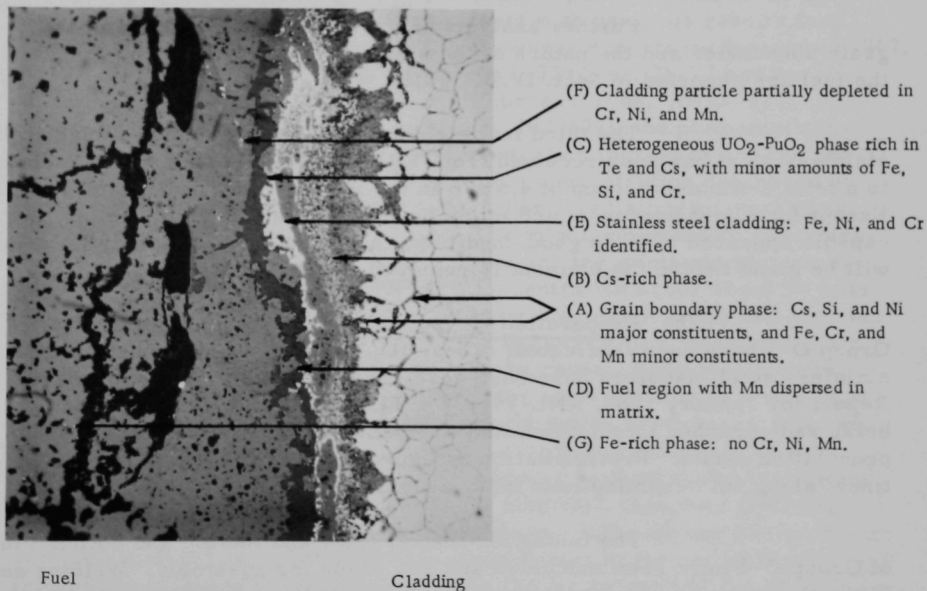


Fig. I.A.1. Fuel-Cladding Interface at the Upper End of Element SOV-7. Phase constituents that have been identified by microprobe analysis are indicated at the right (250X).

In the cladding grain boundaries (A), cesium, silicon, and nickel are major constituents, with minor amounts of iron, chromium, and manganese. A mottled cesium-rich phase (B) is located in the region of the fuel-cladding interface. The dark-gray phase (C), at the edge of the fuel, is a heterogeneous mixture of UO_2 and PuO_2 enriched in tellurium and cesium, and low in iron, silicon, and chromium. Manganese is highly dispersed in the fuel matrix near the cladding (D). The white phase (E) is essentially stainless steel cladding (iron, nickel, and chromium). The nature of these layers appears to preclude identification of the original fuel-cladding interface.

The small, light-colored particles (F) in the fuel matrix appear to be cladding alloy partially depleted in chromium, nickel, and manganese. Near the interface, microprobe analysis indicates that the nickel content of the particles (F) is about one-third that of the cladding. Similar-appearing particles were found at locations more distant from the fuel-cladding interface, and these contained still less chromium and nickel. This is consistent with the observation that nickel remains behind in the grain boundaries of the cladding. Some particles of iron (G) have been identified.

Further analysis of the nature of the cesium in the grain boundaries and the nature of the stainless steel constituents found in the fuel are reported in Sect. IV.B.1.b.(ii).

The third fuel element (SOV-1) in Group O-2 clad with stainless steel has been received from EBR-II. The element was irradiated to a total estimated burnup of 4.5 a/o in the reconstituted Subassembly XO39. Except for slight bowing, which might have been sustained in handling, the capsule appeared to be in good condition. A neutron radiograph of the capsule will be made before the element is removed for examination.

(b) Preparation of Group O-3. All 19 fuel elements of Group O-3 have been fabricated. These $(\text{U}_{0.8}\text{Pu}_{0.2})\text{O}_2$ fuel elements with stainless steel claddings have been described previously (see Progress Report for January 1969, ANL-7548, pp. 1-2). The weld closures are being radiographed to establish that the welds are sound and that adequate penetration exists. Preirradiation measurements of the fuel elements continue, along with examinations for quality assurance.

The tubing for the capsules and the top and bottom plugs of Group O-3 have been machined and are ready for assembly. Welding and inspection techniques are being developed. Techniques for filling the annulus between the fuel element and the capsule wall with sodium are being checked, and a procedure for determining the quality of the sodium bond is being developed.

(c) Diffusion of Uranium and Plutonium in Mixed-oxide Fuels (R. Natesh and D. R. O'Boyle)

Last Reported: ANL-7427, pp. 102-104 (Feb 1968).

In order to study the redistribution of uranium and plutonium in a fast-neutron flux, a bulk specimen from Element SOV-7 was analyzed with a shielded electron microprobe described recently.* The fuel element contained fully enriched UO_2 -20 w/o PuO_2 and had been irradiated in EBR-II to 3.6 a/o burnup at a maximum linear power rating of 21.3 kW/ft. The specimen examined was a cross section taken from the top end of the element where the linear power rating was 17.1 kW/ft. The maximum temperature at the center of the fuel element was estimated to be about 2800°C, and the maximum temperature at the fuel-cladding interface was estimated to be about 605°C. The fuel had an initial effective density of 85.1% of theoretical.

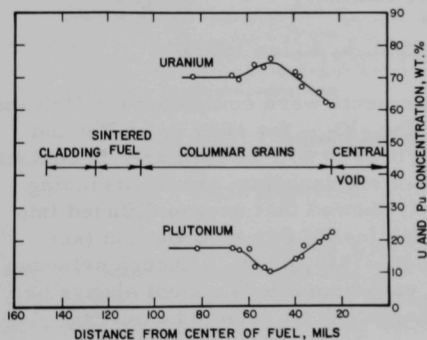


Fig. I.A.2. Distribution of Uranium and Plutonium in Element SOV-7, Irradiated to 3.6 a/o Burnup

region located from 68 to 106 mils from the center of the fuel element, uranium and plutonium form a homogeneous solid solution as a result of complete sintering of the original physically mixed particles of UO_2 and PuO_2 . In this region the nominal composition of the matrix is 70 w/o uranium and 17.7 w/o plutonium. In the cooler regions of the fuel (more than 106 mils from the center of the fuel element), complete sintering of UO_2 and PuO_2 particles has not taken place. Although the fuel-element section examined is believed to have been molten at the center during irradiation, melting is not believed to be the factor controlling redistribution of the uranium and plutonium.

Figure I.A.2 shows the distribution of uranium and plutonium along a radius in the columnar-grain region of the fuel. In agreement with previous results (see Progress Reports for September 1967, ANL-7382, pp. 76-77 and for February 1968, ANL-7427, pp. 102-104), the plutonium concentration increased and the uranium concentration decreased at higher irradiation temperatures. The maximum uranium concentration and the minimum plutonium concentration occur about 50 mils from the center of the fuel element. In the part of the columnar-grain

*Natesh, R., Koprowski, B. J., Butler, E. M., and Donahue, D. A., Proc. 16th Conf. on Remote Systems Technology, Idaho Falls, Idaho, March 11-13, 1969. Am. Nucl. Soc., 1969, pp. 243-252.

(ii) Fuel Swelling Studies (L. A. Neimark, L. C. Michels, and K. F. Smith)

Last Reported: ANL-7561, pp. 1-2 (March 1969).

A design concept for an irradiation capsule that will be used to monitor the in-pile swelling and fission gas-release behavior of UO_2 and $(\text{U,Pu})\text{O}_2$ has been developed for use in CP-5. Unless difficulties are encountered during the detailed design stage, the design will be adopted and fabrication of capsules will be started.

Swelling rates and fission-gas release will be measured under conditions of very low restraint and at hydrostatic pressures up to 10,000 psi. The anticipated fuel temperatures range from 600 to 1800°C.

(iii) Compatibility between Uranium-Plutonium Oxide and Cladding Alloys (T. W. Latimer)

Last Reported: ANL-7548, p. 2 (Jan 1969).

Microhardness measurements were completed for (1) vanadium that had been in contact with $(\text{U}_{0.8}\text{Pu}_{0.2})\text{O}_{1.97}$ for 1000 hr at 700 and 800°C; and (2) V-10 w/o Cr and V-15 w/o Cr-5 w/o Ti similarly in contact at 700°C. Previous compatibility tests of six vanadium alloys (including V-10 w/o Cr and V-15 w/o Cr-5 w/o Ti) showed that oxygen diffused into these alloys at 800°C when in contact with fuel of this composition (see Progress Report for November 1968, ANL-7518, p. 4). Although evidence of this increased oxygen content in the vanadium alloys cannot always be observed metallographically, these changes can be detected easily by microhardness measurements.

In Fig. I.A.3 hardness changes at a given contacting temperature are shown to be similar for unalloyed vanadium (containing 520 ppm oxygen originally) and V-10 w/o Cr. The as-received vanadium

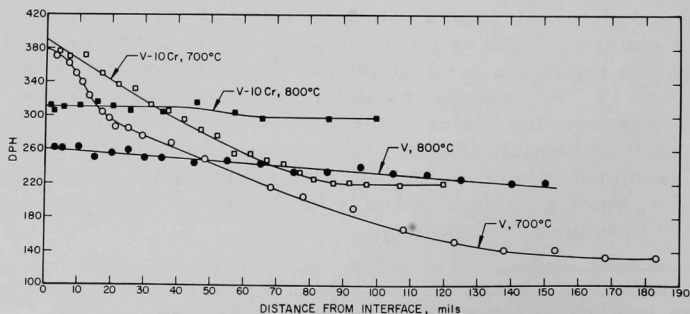


Fig. I.A.3. Hardness Profiles of Vanadium and V-10 w/o Cr after Contact with $(\text{U}_{0.8}\text{Pu}_{0.2})\text{O}_{1.97}$ for 1000 hr at 700 and 800°C

had a hardness of 136 DPH and the V-10 w/o Cr a hardness of 205 DPH. For each metal, the hardness within 30 mils of the interface was greater for the 700°C compatibility test than for the 800°C test.

In Fig. I.A.4, the effects of contact with the mixed oxide at 700 and 800°C on the hardness of V-10 w/o Cr and V-15 w/o Cr-5 w/o Ti are compared. The extent of oxygen diffusion into these alloys is much less at 700°C, and the surface layer is appreciably harder after contact at 700°C than after contact at 800°C.

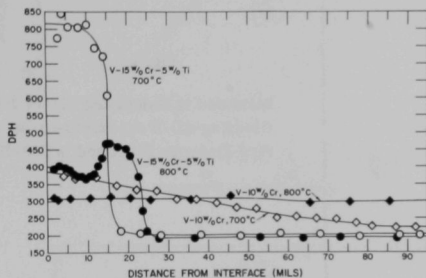


Fig. I.A.4

Hardness Profiles of V-15 w/o Cr-5 w/o Ti and V-10 w/o Cr after Contact with $(U_{0.8}Pu_{0.2})O_{1.97}$ for 1000 hr at 700 and 800°C

(iv) Fuel Element Modeling (T. R. Bump)

Last Reported: ANL-7553, pp. 2-4 (Feb 1969).

The original plan had been to perform detailed comparisons between experimental data and predictions made by the improved SWELL-3 code, which is currently being debugged. However, preliminary comparisons have now been performed using SWELL-2* and SWELL-2C.

Initial attempts to obtain agreement between SWELL-2 predictions and experimental data suggested the need for certain upgradings in SWELL-2. The current SWELL-2C version includes these changes: (1) fission gas can be considered to be released from the fuel after it travels an arbitrary minimum radial distance (A_{g3}), as well as after it reaches the columnar-grain region or the axial centerline (in non-restructured fuel), (2) in the SWELL-2 code, a pressure-reduction term p_f is subtracted from the pressure of the gas retained in the fuel, P_{r1} , to help obtain the pressure exerted by the fuel on the cladding {thus, p_f represents the ability of the fuel strength to resist fuel swelling; for SWELL-2C, the calculation of p_f includes an extra term that considers the effect of effective fuel void fraction v_0 :

$$p_f = [A_{35} + A_{36} \exp(A_{37}v_0)]P_{r1}, \quad (1)$$

and (3) the strain-to-cause-failure (ϵ_{MAX}) is now assigned a fudge factor A_{78} .

*Bump, T. R., SWELL-2: A Fuel-element-lifetime Code (to be published).

Comparisons of SWELL-2C predictions with experimental data for mixed-oxide elements are shown with respect to cladding $\Delta D/D$ in Figs. I.A.5 (EBR-II*) and I.A.6 (Dounreay**), with respect to fission-gas release in Fig. I.A.7, and with respect to cladding failure in Fig. I.A.8.

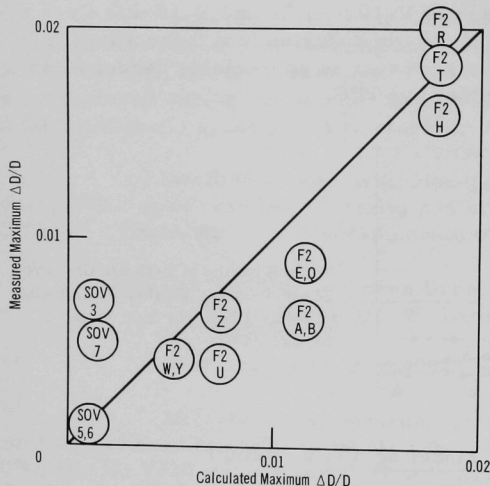
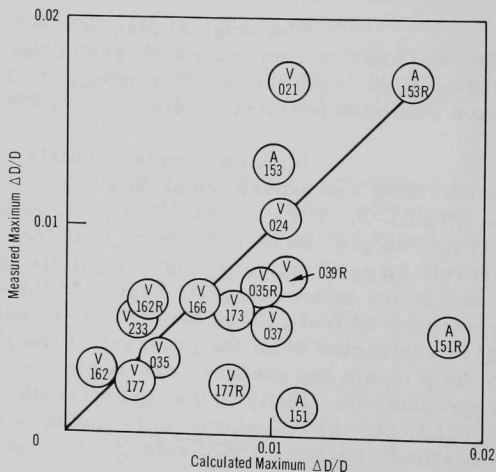


Fig. I.A.5

Measured vs Calculated Maximum Cladding $\Delta D/D$ for Mixed-oxide Fuel Elements Irradiated in EBR-II

Fig. I.A.6

Measured Maximum Cladding $\Delta D/D$ vs Calculated Maximum Cladding $\Delta D/D$ for Mixed-oxide Fuel Elements Irradiated in Dounreay Reactor



*Nelson, R. C., Rubin, B. F., Kendall, W. W., and Bailey, W. E., Performance of Mixed-oxide Fuel Pins Irradiated in a Fast Reactor to 50,000 MWt/t, Trans. Am. Nucl. Soc. **10**, 460-461 (Nov 1967); Neimark, L. A., Murphy, W. F., Brown, F. L., and Kittel, J. H., Plutonium Fuels Performance -- ANL Experience, Trans. Am. Nucl. Soc. **11**, 516-518 (Nov 1968).

**Lawton, H., et al., The Irradiation Behavior of Plutonium-bearing Ceramic Fuel Pins, Paper 4B/4. British Nuclear Soc., London Conf. on Fast Breeder Reactors, May 17-19, 1966.

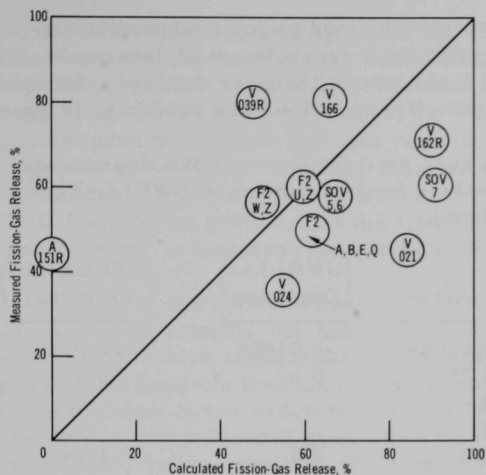


Fig. I.A.7

Measured vs Calculated Fission-gas
Release for Mixed-oxide Fuel Elements

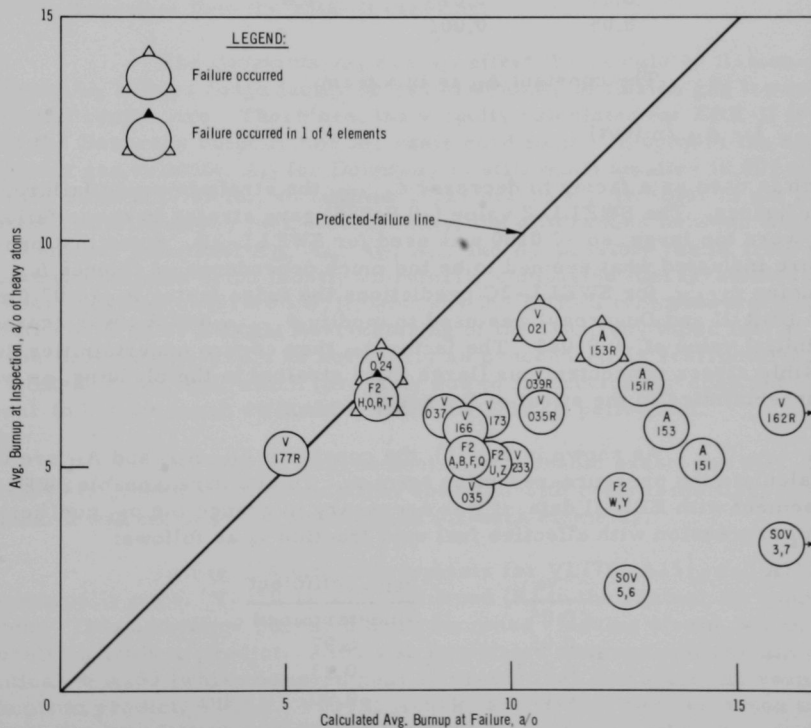


Fig. I.A.8. Average Burnup at Inspection vs Calculated Average Burnup
at Failure for Mixed-oxide Fuel Elements

The predictions were obtained by interpolation between results from parameter studies, that is, a separate set of data cards was not prepared for each individual fuel element, because detailed information concerning the conditions under which irradiations are conducted is sparse.

The agreement, such as it is, shown in the figures was obtained by using the following values for key constants (SWELL-2 and -2B values are included for comparison):

Constants	EBR-II	Dounreay	(SWELL-2) (Dounreay)	(SWELL-2B*) (Dounreay)
A ₁₅	-0.01085	-0.01085	-0.01085	-0.0180
A ₃₅	0.9	0.75	0.67	0.85
A ₃₆	0.459	0	-	-
A ₃₇	-37.6	0	-	-
A _{59A} ($\times 10^{15}$)	1.7	0.8	2.0	1.75
A ₇₃	0.05	1.0	0.4	0.4
A ₇₈	0.07	0.07	1.0	1.0
A ₈₃	0.05	0.001	-	-

The constant A₁₅ is in a term

$$1 - A_{15} \ln (\text{nvt})$$

which is used as a factor to decrease ϵ_{MAX} , the strain to cause failure, with fluence. The SWELL-2 value (-0.01085) gave strains to cause failure that were too large, so -0.0180 was used for SWELL-2B. Since that procedure indicated what seemed to be too much dependence on fluence for reducing ϵ_{MAX} , for SWELL-2C predictions the fudge factor A₇₈ (0.07 for both EBR-II and Dounreay) was used to modify ϵ_{MAX} , and A₁₅ was reassigned its initial value of -0.01085. The factor A₇₈ then covers uncertainties due to possible stress concentrations (large local strains) in the cladding, as well as uncertainties in the effect of fluence on ϵ_{MAX} .

As shown in Eq. (1), the constants A₃₅, A₃₆, and A₃₇ are used to calculate the pressure-reduction term p_f . To obtain reasonable SWELL-2C agreement with EBR-II data, it was necessary to change the p_{r1} coefficient in the p_f expression with effective fuel void fraction v_0 as follows:

v_0	p_{r1} Coefficient
<0.05	Undetermined
0.05	0.97
0.0725	0.93
>0.13	0.90

*Reactor Development Program Progress Report for February 1969, ANL-7553, pp. 2-4.

The values for A_{35} , A_{36} , and A_{37} given for EBR-II in the table produce the desired relationship between the coefficient and v_0 . When A_{36} and A_{37} are zero, the coefficient equals A_{35} . Because the pr_1 coefficient is thus always lower (0.75) for Dounreay than for EBR-II, this implies that for a given pressure of the fission gas retained in the fuel, the fuel-swelling pressure is greater for Dounreay than for EBR-II. However, as noted below, under similar conditions Dounreay fuel releases more gas than EBR-II fuel, so the pressure of the fission gas retained in the fuel is normally lower in Dounreay than in EBR-II.

It was found necessary to reduce the value of the constant A_{59A} , which is actually the effective neutron flux, in order to avoid predicting excessive irradiation-induced cladding swelling. This is a logical move, because the fluxes used earlier were intended to be the maximum fluxes in the reactors. All fuel elements considered here probably were irradiated in lower flux environments away from the centers of the reactor cores. Perhaps the need to use a much lower flux in Dounreay than in EBR-II is due to the Dounreay cladding being more swelling-resistant than the EBR-II cladding.

The constants A_{73} and A_{83} affect the calculated fission-gas release, A_{73} being a fudge factor on radial velocity of fission gas toward the fuel axial center line. Therefore, the velocity calculated for EBR-II is only 5% of the Dounreay velocity, for the same conditions. In spite of the higher Dounreay gas velocity, A_{83} for Dounreay is still much smaller (0.001 in.) than for EBR-II (0.05 in., so large it never enters in), in order to get enough release from Dounreay fuel. Incidentally, the differences between EBR-II and Dounreay constants A_{35} , A_{36} , A_{37} , A_{73} , and A_{83} possibly result from the Dounreay elements being mostly vibratorily compacted fuel irradiated at a linear heat flux under 10 kW/ft, whereas the EBR-II elements were irradiated at over 10 kW/ft. Restructuring of the Dounreay Vipac fuel at the low heat ratings would be not nearly as pronounced as restructuring of the EBR-II Vipac fuel, which (probably due to restructuring) does not appear to behave much differently from the EBR-II pellet fuel.

In Fig. I.A.5, agreement is reasonable except for SOV-3 and SOV-7. These are elements that operated with central melting; perhaps SWELL-3 will make better predictions for such elements.

In Fig. I.A.6, the agreements for V177R, A151, and A151R are unusually poor. V177R is V177 returned (R) to the reactor for additional burnup. This additional burnup did not increase cladding strain, which is a result difficult to predict. A151 was irradiated under conditions almost identical to A153 (which behaved near to prediction), and again the results are difficult to predict. V035R, V039R, A151R, and A153R were returned to the reactor for irradiation with higher cladding temperatures than during their

initial exposures. Figures I.A.6, I.A.7, and I.A.8 show predictions for these elements; it was assumed that the final conditions existed throughout the entire exposures.

In Fig. I.A.7, some of the calculated Dounreay gas releases are still too low, in spite of the exaggerated steps taken to increase calculated release.

In Fig. I.A.8 it can be seen that failures were predicted for very few of the elements (although those few which did fail are usually close to the failure line), that is, the predictions appear optimistic. This is a logical consequence of the fact that SWELL calculations halt at the predicted time of failure. To obtain the data necessary for Figs. I.A.5, I.A.6, and I.A.7, the calculated strain to cause failure (ϵ_{MAX}) was deliberately aimed in the direction of being too large rather than too small. When burnup-at-failure is the chief objective of SWELL-2C calculations, in the interests of conservatism it is probably advisable to use a smaller value for A_{78} and/or a larger negative value for A_{15} .

B. Physics Development--LMFBR

1. Theoretical Reactor Physics

a. Fast Critical Experiments--Theoretical Support (R. G. Palmer)

Last Reported: ANL-7561, pp. 2-3 (March 1969).

(i) Heterogeneity Studies. Studies are underway to ascertain the accuracy of present and proposed methods for evaluating flux-advantage heterogeneity effects in the ANL criticals. The standards against which the methods will be compared will be provided by calculations of high-order transport theory on hypothetical cores which are simple enough to be described completely and accurately by existing transport-theory codes, but complicated enough to exhibit significant heterogeneity effects. The first core, called GEDANKEN-1, consists of an infinite slab core reflected by depleted uranium, the core being eleven cells across, each cell having one Pu-U fuel plate, and two sodium and two graphite plates. The difference in k_{eff} between a completely detailed high-order transport calculation and a homogeneous transport calculation will give the heterogeneity effect. This basis for comparison of techniques is preferable to comparison with experiments due to the uncertainty of cross section in the calculation of the latter.

Tests are being made of various recipes for homogenizing the cells, both energy-wise and space-wise, such as flux and flux-adjoint bivariate weightings (see Progress Report for February 1969, ANL-7553, p. 7).

Modifications are being made to the TESS Code to include more accurate prescriptions for cell homogenization.

(ii) Adjustments of Cross Sections to Fit Integral Data. The testing of ENDF/B-based cross sections by calculations for a series of fast critical assemblies has been delayed pending implementation of necessary codes for the Idaho IBM 360/75 computer. In conjunction with the testing efforts by CSEWG, a summary of analyses submitted by various CSEWG agencies for ZPR-3 Assemblies 48 and 11 has been compiled for distribution. Some interesting points observed for Assembly 11 were a reactivity contribution from the $n,2n$ reaction of +0.7% k, and a +2.2% k difference from using a Pu-239 fission-neutron energy distribution rather than the more appropriate U-235 distribution.

(iii) Calculational Studies of Possible Physics Cores for ZPR-3. Basic parameters have been obtained for possible physics cores in the benchmark series at ZPR-3. All four cores are composed of one-drawer cells with the following configuration:

TABLE I.B.3. Central Reaction Ratios Assembly
(Diluent-Reflector)

Ratio ^a								
Numerator	Na-U	Na-Pu	Fe-U	Fe-Pu	Ni-U	Ni-Pu	U ₃ O ₈ -U	U ₃ O ₈ -Pu
Pu-239 fiss	1.08	1.08	1.06	1.06	1.02	1.02	0.984	0.985
Pu-240 fiss	0.355	0.357	0.308	0.308	0.287	0.287	0.297	0.298
Pu-241 fiss	1.30	1.30	1.30	1.30	1.31	1.31	1.30	1.29
U-238 fiss	0.0048	0.0048	0.0031	0.0031	0.0025	0.0025	0.0048	0.0048
U-238 cap	0.125	0.125	0.132	0.132	0.141	0.141	0.133	0.132

^aDenominator is U-235 fission.

2. Experimental Reactor Physics

a. Fast Critical Experiments--Experimental Support (Illinois)

(i) Detector Development (R. Gold)

Last Reported: ANL-7527, p. 9 (Dec 1968).

(a) Error Estimates for Iterative Unfolding. Some approximate formulas have been developed for errors arising from the application of iterative unfolding to experimental measurements.* For the practical case of a dominantly diagonal response matrix of large order, it has been shown that the relative error of the unfolded solution is approximately that of the original measurement. To demonstrate this behavior, actual experimental results from proton-recoil proportional counters have been used.

(ii) On-line Computer Applications (R. Gold)

Last Reported: ANL-7518, pp. 13-19 (Nov 1968).

(a) Packaging of Analog-Digital Converters. The type of analog-digital converter (ADC) used for pulse-height analysis with digital computers is commonly packaged with the ADC proper and the channel-count scaler in the same enclosure. We have found that such a configuration is suboptimal, and much is to be gained by having the ADC and the scaler in separate enclosures.**

In many situations it is necessary or desirable to have the computer and the experiment in separate locations. For example, one

*Gold, R., and Bennet, E. F., Error Estimates for Iterative Unfolding, J. Computer Physics 3, 167-175 (1968).

**Cohn, C. E., Considerations in the Packaging of Analog-Digital Converters, Rev. Sci. Instr. 40, 512 (1969).

computer may be required to serve a number of experiments located in different areas. Furthermore, a computer is a strong source of radiated electromagnetic interference and so should not be located close to low-level electronics.

With the computer located remotely from the experiment, a decision must be made regarding the allocation of the interface equipment between the two areas. For the conventional configuration of ADC and scaler in one package, there are two possibilities, neither of which are desirable. If the unit is located in the computer area, the signal to be analyzed must be transmitted over the distance between the two areas. It is then subject to degradation by extraneous pickup enroute. If the unit is located in the experiment area, only digital signals need to be transmitted and the problem of signal degradation is largely eliminated. However, an excessive amount of cabling is then required, since each data bit from the scaler must be transmitted separately.

An equipment allocation that we have found to be more nearly optimal is shown in Fig. I.B.1. Here the ADC is located at the experiment and the scaler at the computer.

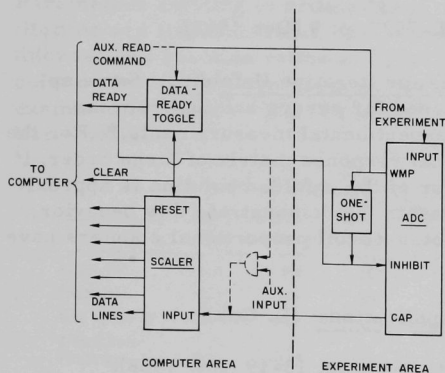


Fig. I.B.1. Suggested Interface Arrangement for Computerized Pulse-height Analysis

When the computer has read the data, it produces a clear pulse which resets the scaler and the toggle, removing the inhibit signal.

Because of transmission delays, there is a time lag between the termination of WMP and the arrival of the inhibit signal at the ADC. Another conversion can commence during this interval, perturbing the data that have already been collected. To prevent this, a one-shot at the ADC is triggered by the trailing edge of WMP to generate the inhibit signal immediately and sustain it for a few microseconds until the main signal arrives.

Overflows may be sensed and rejected by suitable logic in the scaler. Termination of conversion upon overflow would require still another cable back to the ADC. This feature may be foregone with little penalty if the upper-level discriminator in the ADC is properly set.

The separated configuration has the additional advantage of making the scaler independently useful. The scaler may be used to count pulses from a source other than the ADC, and to read the accumulated count into the computer on command. The additional arrangements needed are shown by dotted lines in Fig. I.B.1. The pulses to be counted are taken through a gate into the scaler input, replacing the pulses from the ADC. (The gate prevents counting while accumulated data are being read.) Reading is commanded by a signal triggering the data-ready toggle. (If the counts are to be read at uniform time intervals, for example, the read commands may come from a clock generator.)

b. Planning and Evaluation of FFTF Critical Assembly Experiments
(A. Travelli)

Last Reported: ANL-7561, pp. 6-8 (March 1969).

(i) Calculation of Reaction-rate Traverses in ZPR-3 Assembly 56B. The radial variations of ^{239}Pu fission, ^{238}U fission, and ^{10}B capture detector responses in ZPR-3 Assembly 56B have been calculated. The flux distribution was obtained using the 29-group cross-section set (29004, 2) (see ANL-7651) in one-dimensional cylindrical-transport theory in the S-4 approximation. The SNARG-ID* code was used in the calculations with the transport approximation for the anisotropic scattering.

The axial leakage was simulated by a DB^2 absorber. The transverse buckling ($6.202 \times 10^{-4} \text{ cm}^{-2}$) was obtained through a series of cylindrical and slab calculations converging by iteration to a pair of calculations corresponding to the same k and to transverse bucklings up to the material buckling ($1.879 \times 10^{-3} \text{ cm}^{-2}$). The dimensions and material compositions of the cylindricized reactor are given in ANL-7561, pp. 9-10 and have been corrected [(see Sect. I.B.3.a.(vii)].

Two reaction-rate traverses were computed for each of the three detector types from the neutron-flux distribution. The calculation for the first reaction-rate traverse used the 29-group cross sections obtained from a 2,100-group fundamental-mode MC^2 flux averaging** for the core composition at criticality. The flux was normalized so that the reaction rate obtained was unity at the core center. Calculation for the second reaction-rate traverse was made with the 29-group cross sections obtained from a 2,100-group fundamental-mode MC^2 flux averaging for the

*Duffy, G. J., et al., ANL-7221 (1966).

**Toppel, B. J., et al., ANL-7318 (1967).

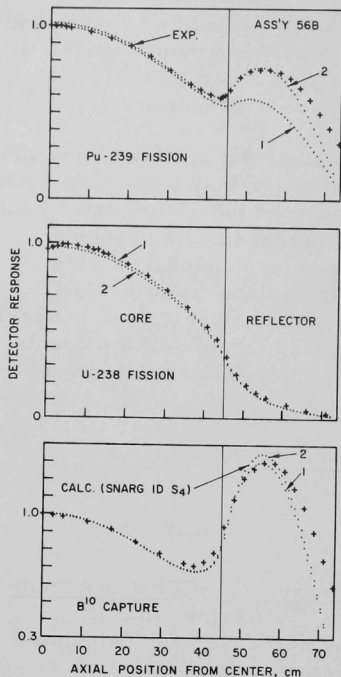


Fig. I.B.2

Radial Reaction-rate Traverses
in ZPR-3 Assembly 56B

of Assembly 56B different from a perfect cylinder, nor for heterogeneity effects. These effects are estimated to shift the calculated curves outwards by a distance between 1 and 2 cm in the region close to the core-reflector interface. The results shown in Fig. I.B.2 indicate good agreement between experiments and calculations. The fission rate of ^{239}Pu is slightly underestimated by the calculations at the edge of the core and overestimated in the reflector; the largest relative discrepancy is approximately 6%. The calculation of the fission-rate traverse in ^{238}U falls approximately within the experimental accuracy of the measurements. The calculation of the ^{10}B capture-rate traverse shows qualitatively the measured spatial behavior, but overestimates the peak value in the reflector by approximately 12%.

The spread between the calculated curves 1 and 2 shows clearly that the calculations of the fission traverses of ^{239}Pu are very sensitive to the resonance self-shielding and to the ultrafine spectrum chosen in collapsing the fission cross sections of ^{239}Pu even over the relatively fine-energy structure of set (29004, 2).

reflector composition with zero buckling. The same flux, with the same normalization, was used as in the calculation for the first reaction-rate traverse.

The computed responses for the three types of detectors are compared in Fig. I.B.2 with the experimental values reported in ANL-7651. The experimental data are indicated by crosses, the reaction rates obtained in the first calculation (core spectrum averaging) are indicated by the dotted curves labeled "1," and the reaction rates obtained in the second calculation (reflector spectrum averaging) are indicated by the dotted curves labeled "2." Type-1 curves are valid close to the core center, and type-2 curves in the regions well inside the reflector. In the region close to the core-reflector interface, and on both sides of it, the spectrum in the reactor changes rapidly and somewhat irregularly from the core spectrum to the reflector spectrum, and the results of more accurate calculations involving space-dependent cross sections would be expected to fall somewhere between curves 1 and 2.

The calculated curves shown in Fig. I.B.2 were not corrected for the irregular matrix contour that made the core of Assembly 56B different from a perfect cylinder, nor for heterogeneity effects. These effects are estimated to shift the calculated curves outwards by a distance between 1 and 2 cm in the region close to the core-reflector interface. The results shown in Fig. I.B.2 indicate good agreement between experiments and calculations. The fission rate of ^{239}Pu is slightly underestimated by the calculations at the edge of the core and overestimated in the reflector; the largest relative discrepancy is approximately 6%. The calculation of the fission-rate traverse in ^{238}U falls approximately within the experimental accuracy of the measurements. The calculation of the ^{10}B capture-rate traverse shows qualitatively the measured spatial behavior, but overestimates the peak value in the reflector by approximately 12%.

The axial variations of the same three detector responses in Assembly 56B have also been calculated in a completely similar manner except the neutron-flux distribution was obtained from a transport-theory solution of the one-dimensional slab in the S-4 approximation. The transverse buckling ($1.258 \times 10^{-3} \text{ cm}^{-2}$) and value of k (0.998) were consistent with the previous radial calculation.

The experimental axial traverse for ^{238}U shows a slight depression at the midplane of the reactor. At this position, which is the mating plane of the two halves, the columns of plates constituting the core loading are interrupted by the stainless steel drawer end plates. A corresponding gap was not introduced into the analytical model.

The calculated curves were based on a solution which assumed simply that the outer edge of the axial reflector was bare, thus causing the calculated detector responses to approach zero rapidly at that boundary. Actually, the scattering of neutrons by the stainless steel matrix structure outside the reflector is complicated by axial neutron streaming up the empty matrix tubes. The analytical model was too simple to adequately represent these features. This effect is apparent in the calculated detector responses, which are too high near the outer edge of the reflector for ^{239}Pu fission and ^{10}B capture, both of which are more sensitive to the neutron spectrum in the reflector than is the ^{238}U fission.

Otherwise, agreement between the calculated and the measured responses was within 7% for the axial variations.

3. ZPR-3 Operations and Analysis

a. Mockup Studies (W. G. Davey and R. L. McVean)

Last Reported: ANL-7561, pp. 8-15 (March 1969).

(i) FTR Critical Program. Experiments with Assembly 56B, which is Assembly I of the FTR Resumed Phase B critical experiments, were concluded. The completed experiments included the measurement of axial worth traverses, of central fission ratios, of the ratio of capture in U-238 to fission in U-235 at the core center, edge, and in the reflector, of the worth of poison control composition and axial reflector composition at the core center, and two poison control composition geometries at the core edge.

This report concludes the reporting of experimental data from Assembly I, with the exception of the foil measurements of the capture in U-238 to fission in U-235, which are still being analyzed. Corrections to the March report are included.

Upon completion of the experiment, the nickel of the reflector was moved to ZPPR to continue with the FTR Resumed Phase B Program there.

FTR-I is now critical in ZPPR.

(ii) Measurements of Small-sample Central Worth in Assembly 56B. The central worths of U-235, U-238, Pu-239, B-10, Ta, Fe, Cr, Ni, Na, and Li-6 were measured. In addition, the worths of polyethylene, C, and Type 304 stainless steel were measured as necessary auxiliary worths.

The measurements were made by monitoring the position of the autorod while alternating a sample and a dummy at a location near the center of the reactor. The sample and dummy were placed in carriers and oscillated inside a 1/2-in.-dia. radial through-tube to place them alternately within the 1-P-16 matrix location. The through-tube passed through a 3/4 x 2-in. tunnel at the front of the drawers in the P-row of Half No. 1, the stationary half. To form the tunnel, the plates in the P-row drawers were rotated 90°, and the plates in the middle 3/4-in.-wide section were pushed back from the drawer front by 2 in. This required minor additional changes in plate sizes and distribution. The resulting core configuration was the same as used for the radial reaction rate and worth traverse measurements (see Fig. I.B.8, p. 16 of ANL-7561).

The reactivity effects of the sample-dummy interchanges were determined from the average positions of the calibrated autorod as it maintained a constant power during the oscillations. The experimental configuration is a push rod, sample holder, spacer rod, dummy holder, and follower rod. The sample and dummy were separated by 40 in. so that either the sample or dummy was in the assembly at any time with a rod on both radial sides. The positions of the autorod were determined from the output of a potentiometer attached to its drive shaft. These were converted to pulse frequencies in an analog-to-digital converter. The average positions were determined by counting the pulses during 100-sec intervals. The autorod worth was $\rho = -0.12718X - (6.8255 \times 10^{-5})X^2$, where ρ is in Δk and X is the counting rate in kc corresponding to the rod position. The difference between the worth of the sample and the worth of the dummy was obtained by taking the difference between the autorod worth with a sample/dummy in the assembly and the average of the dummy/sample worth measurements preceding and following it. This procedure eliminated the effects of long-term reactivity drifts.

The samples used were cylindrical or annular in shape and are described in Tables I.B.4 and I.B.5.

TABLE I.B.4. Dimensions of Annular Samples

Material	Thickness (in.)	Circumferential ^b Length (in.)	Axial Length (in.)	Outside Diameter of Annulus (in.)
Pu ^a	0.007	1.150	1.838	0.390
Pu ^a	0.020	1.068	1.855	0.390
Pu ^c	0.006	1.150	1.838	0.390
U ^d	0.0034	1.193	1.978	0.386
U ^e	0.022	1.186	1.973	0.397
B (Set No. 2) ^f	0.010	-	1.688	0.391
B (Set No. 1) ^f	0.020	-	1.688	0.391
Ta	0.0053	1.196	1.971	0.390
Ta	0.010	1.196	1.977	0.393
Ta	0.015	1.196	1.976	0.397
Polyethylene	0.007	-	2.008	0.420
Polyethylene	0.0255	-	2.016	0.420
Polyethylene	0.0537	-	2.000	0.420

^a98.62 w/o Pu, 1.22 w/o Al, 0.16 w/o other; 95.05 w/o Pu-239, 450 w/o Pu-240, 0.45 w/o Pu-241.

^bThe annular samples of Pu, U, and Ta were made by bending a piece of foil into a cylinder. The circumferential length is the width of the foil piece.

^c98.78 w/o Pu, 1.09 w/o Al, 0.13 w/o other; 72.24 w/o Pu-239, 22.28 w/o Pu-240, 4.63 w/o Pu-241, 0.79 w/o Pu-242.

^d93.10 w/o U-235.

^e0.40 w/o U-235.

^f92.8 w/o B, 92.1 w/o of B is B-10.

TABLE I.B.5. Dimensions of Cylindrical Samples

Material	Diameter (in.) ^a	Axial Length (in.)
Pu ^a	0.201	1.918
Pu ^b	0.200	1.928
U ^c	0.200	2.002
U ^d	0.420	2.002
Be ^e	0.200	1.688
Ta	0.200	2.003
Polyethylene	0.416	2.00
SS-304, Fe, Ni, C	0.420	2.00
Cr (powder), Na	0.3906	1.688
Li-6	f	f

^a98.60 w/o Pu, 1.24 w/o Al, 0.16 w/o other; 95.06 w/o Pu-239, 4.49 w/o Pu-240, 0.45 w/o Pu-241.

^b98.78 w/o Pu, 1.09 w/o Al, 0.13 w/o other; 72.24 w/o Pu-239, 22.28 w/o Pu-240, 4.63 w/o Pu-241, 0.79 w/o Pu-242.

^c93.16 w/o U-235.

^d0.21 w/o U-235.

^e92.8 w/o B, 92.1 w/o of B is B-10.

^fThe Li-6 sample is contained in a steel capsule which is 0.364 in. in diameter and 2 in. long.

The measured worths are given in Table I.B.6. The values given are based on the measured sample worths relative to those of their dummies, after corrections where necessary for the reactivity worths of the differences in stainless steel mass between the sample and dummy, the relative worth of the empty carriers, and the worth of the hydrogen content of the samples. The uncertainties are the square root of the sums of the

TABLE I.B.6. Central Perturbation Measurements in Assembly 56

Material	Sample	Sample Mass (g)		Material Worth ^b (Ih/kg)
		Material	Stainless Steel	
Pu ^a	0.201-in.-dia Cylinder	14.965	6.655	398.5 ± 1.0
Pu ^c	0.020-in.-thick Annulus	9.315	6.498	385.1 ± 1.7
	0.007-in.-thick Annulus	2.761	6.597	358.2 ± 5.8
Pu ^d	0.200-in.-dia Cylinder	15.063	6.599	337.6 ± 1.0
	0.006-in.-thick Annulus	2.400	6.261	307.2 ± 6.7
U ^e	0.200-in.-dia Cylinder	19.63	-	276.36 ± 0.82
U ^f	0.0034-in.-thick Annulus	2.327	1.826	274.9 ± 4.9
U ^g	0.420-in.-dia Cylinder	85.76	-	-16.74 ± 0.15
U ^h	0.022-in.-thick Annulus	15.27	1.412	-15.59 ± 0.96
B ⁱ	0.200-in.-dia Cylinder	1.011	3.096	-5263 ± 15
	0.020-in.-thick Annulus	0.691	12.243	-5633 ± 17
	0.010-in.-thick Annulus	0.406	11.550	-5757 ± 33
Ta	0.200-in.-dia Cylinder	17.13	-	-95.18 ± 0.80
	0.015-in.-thick Annulus	9.670	1.774	-105.5 ± 1.6
	0.010-in.-thick Annulus	6.701	1.836	-108.8 ± 2.4
	0.005-in.-thick Annulus	3.300	1.815	-116.0 ± 4.4
Polyethylene	0.416-in.-dia Cylinder	4.072	-	1080.4 ± 3.9
	0.054-in.-thick Annulus	1.910	-	828.7 ± 8.4
	0.023-in.-thick Annulus	0.865	-	680 ± 18
	0.007-in.-thick Annulus	0.413	-	628 ± 29
SS-304	0.42-in.-dia Cylinder	35.90	-	-13.08 ± 0.34
Fe	0.42-in.-dia Cylinder	35.90	-	-12.29 ± 0.34
Cr ^j	0.42-in.-dia Cylinder	12.017	6.736	-12.7 ± 1.1
Ni	0.42-in.-dia Cylinder	40.30	-	-16.83 ± 0.39
Na	0.42-in.-dia Cylinder	3.003	6.665	-8.9 ± 4.1
C	0.42-in.-dia Cylinder	6.910	-	-24.9 ± 2.3
Li-6	0.42-in.-dia Cylinder	0.94	7.41	-4299 ± 23
Li-6 Capsule Blank		7.73	-	-12.4 ± 2.0
Empty Carriers		-	-	+0.0457 ± 0.0070 (Ih)

a98.60 w/o Pu, 1.24 w/o Al, 0.16 w/o other; 95.06 w/o Pu-239, 4.49 w/o Pu-240, 0.45 w/o Pu-241.

bCorrected for the stainless steel.

c98.62 w/o Pu, 1.22 w/o Al, 0.16 w/o other; 95.05 w/o Pu-239, 4.50 w/o Pu-240, 0.45 w/o Pu-241.

d98.78 w/o Pu, 1.09 w/o Al, 0.13 w/o other; 72.24 w/o Pu-239, 22.28 w/o Pu-240, 4.63 w/o Pu-241, 0.79 w/o Pu-242.

e93.16 w/o U-235.

f93.10 w/o U-235.

g0.21 w/o U-235.

h0.40 w/o U-235.

i92.8 w/o B, 92.1 w/o of B is ¹⁰B.

jIncludes 200 ppm H. The quoted worth has been corrected for the reactivity effect of this impurity.

squares of the uncertainties of the measured worths and these corrections. They apply to the worths of the samples relative to others in the set. An uncertainty of $\pm 1\%$ of the worth must be added (using vector addition) to get the uncertainty of the worths in terms of absolute reactivity. This increase is the uncertainty in the absolute worth of the autorod. The major contributor to the listed uncertainties was reactor noise. Its effects were calculated from the equation derived by Bennett and Long.* The measurements were made at a power of $13\frac{1}{2}$ W.

The worth of the hydrogen in the powdered chromium sample was obtained from the polyethylene worths. The linear extrapolation to infinite dilution of these worths when plotted versus the product of the atom density times the mean chord length gave a value of 578 ± 47 Ih/kg for polyethylene. The measured worth of carbon was used to correct for the carbon content of the polyethylene. The resulting hydrogen worth of $(4.16 \pm 0.32) \times 10^3$ Ih/kg gave a reactivity effect in the chromium sample of 0.832 ± 0.067 Ih/kg of chromium powder, or approximately 7% of the measured worth of the chromium sample. This correction was made to obtain the chromium worth given in Table I.B.6.

(iii) Axial Reaction-rate Traverses for Assembly 56B. Reaction-rate traverses were made in Assembly 56B to obtain the spatial variation of U-238 fission, Pu-239 fission, and B-10 capture in the axial direction. The analysis of the count rate included a small correction for dead-time losses and a normalization to the average count rate obtained at the reactor midplane.

The measurements are plotted in Figs. I.B.3, I.B.4, and I.B.5.

Count-rate data were taken while the reactor power was held constant by an autorod in matrix location O-25. The counters were the same counters which were described in ANL-7561 for the radial traverses. The counters were attached to the traversing mechanism by a stainless steel tube (of 0.376-in. OD and 0.035-in. wall thickness). The counters and traverse tube slid inside a stainless steel guide tube (of 0.504-in. OD and 0.474-in. ID) which extended through the core and axial reflector in the center of the P-16 matrix position. The guide tube was centered in a $1 \times 3/4$ -in. space formed by a rectangular stainless steel box (0.015-in. thick). This box, or sheath tube, extended the length of the core and axial reflector. Figure I.B.6 shows the arrangement of material and the position of the components inside the drawers. This drawer arrangement was also used for the reactivity traverses in which perturbation samples of B-10 and Pu-239 were traversed to obtain the spatial variation of their worths.

*Bennett, E. F., and Long, R. L., Precision Limitations in the Measurement of Small Reactivity Changes, Nucl. Sci. Eng. 17, 425-432 (1963).

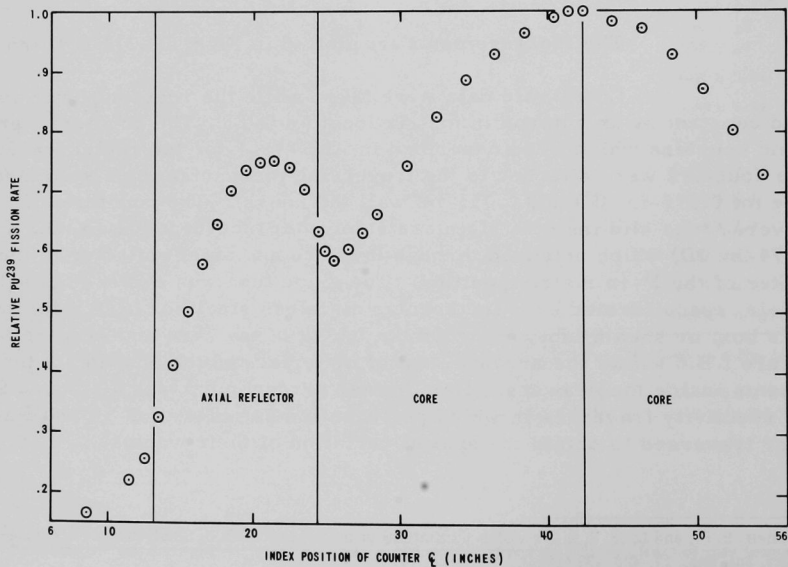
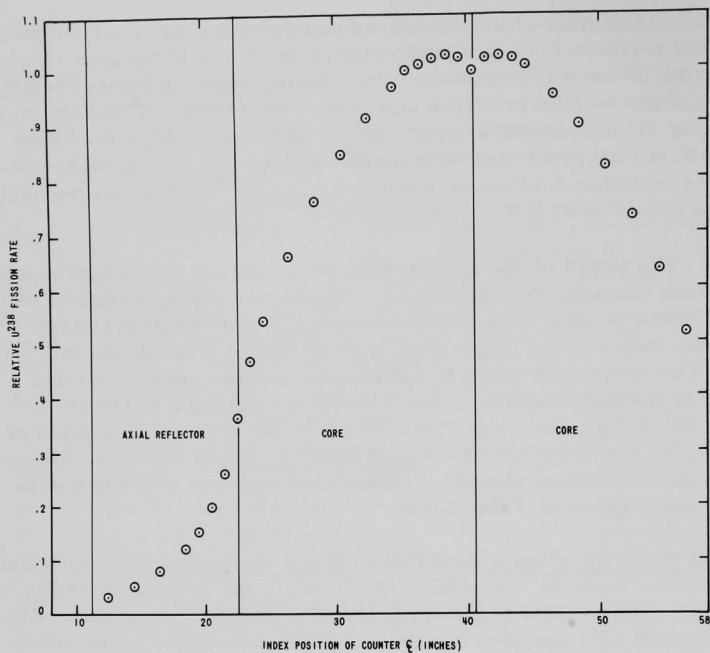


Fig. I.B.4. ^{239}Pu Axial Reaction-rate Traverse in Assembly 56B of ZPR-3

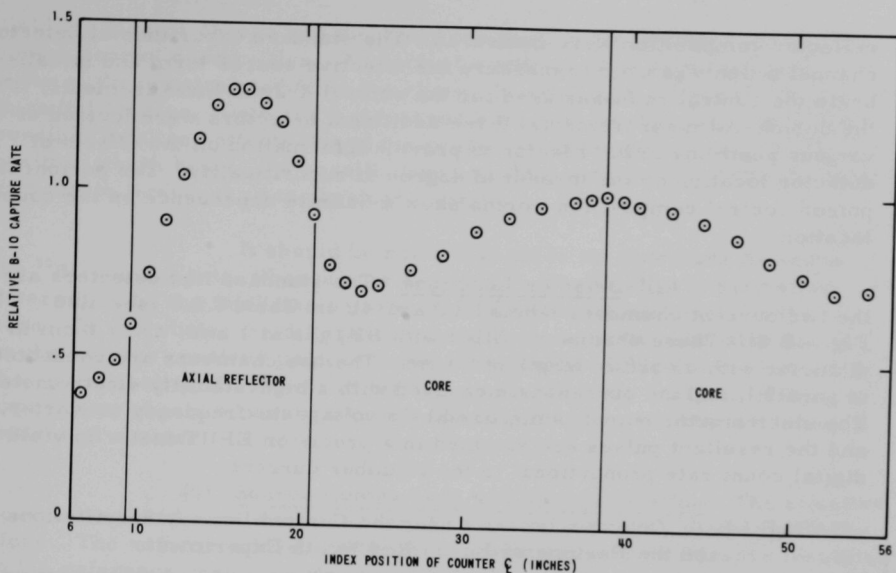


Fig. I.B.5. ^{10}B Axial Reaction-rate Traverse in Assembly 56B of ZPR-3

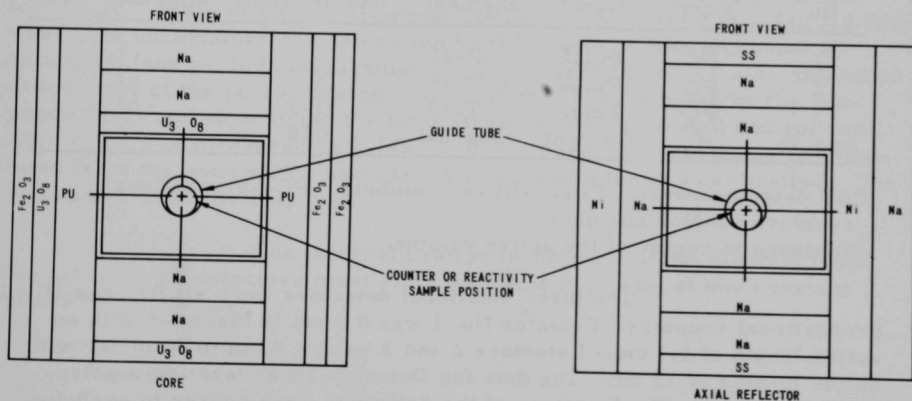


Fig. I.B.6. Platelet Arrangement in the P-16 Matrix Location during the Axial Traverse Measurements in Assembly 56B of ZPR-3

(iv) Measurements of Central and Peripheral Boron Rod Worth. The worths of replacing the central matrix position of core material by axial reflector composition and by poison control composition ($\text{B}_4\text{C} + \text{Na}$) were measured by subcritical techniques. Similarly, the worths of inserting poison control composition drawers at various locations in place of radial

reflector composition were measured. The standard experimental detector channel which was used to measure the effective source term and to calibrate the control rods was used for the central drawer measurements. For the peripheral measurements, three additional detectors were located at various positions in the reactor to provide information on the effects of detector location on the measured degree of subcriticality. The peripheral poison control composition worths show a definite dependence on the counter location.

(a) Detector Locations. The standard flux detectors are the two current chambers labeled 4a and 4b in Table I.B.7 (see also Fig. I.B.8). These chambers, filled with BF_3 gas at 1 atm, are 7.6 cm in diameter with an active length of 19 cm. The two chambers are connected in parallel, and the current is measured with a high-stability electrometer. The electrometer output is digitized by a voltage-to-frequency converter, and the resultant pulses are summed in a precision EPUT meter to yield a digital count rate proportional to the chamber current.

TABLE I.B.7. Detector Locations for the Central Drawer Substitutions and the Peripheral Boron Rod Worth Experiments

Detector No.	Type ^a	Signal	Geometric Location		
			Matrix Element	Radius ^b (cm)	Distance from Midplane ^b (cm)
1	PC	Pulse	1-P-16	0	7.6
2	PC	Pulse	2-P-16	0	63
3	PC	Pulse	1-T-12	31-3	63
4a + 4b	IC	Current	External	~110	15

^aAll detectors were BF_3 gas-filled chambers. PC--proportional counter; IC--ion chamber.

^bDistance to center of the active volume.

The three additional detectors were all BF_3 gas-filled proportional counters. Detector No. 1 was 0.9 cm in diameter with an active length of 5.1 cm. Detectors 2 and 3 were 2.5 cm in diameter with active lengths of 15 cm. The data for Detector 1 was taken on a pulse-height analyzer. The locations of the detectors were chosen to evaluate their influence upon the individual count rates as interpreted by the standard subcritical technique. Detector 1 measured the change reaction rate at the core center; hence, a simple analysis based on results from this detector would seem intuitively to yield the most nearly correct answer. Detector 2 predominantly measured the change in axial leakage; hence, it could be expected to yield too small a change and therefore too small a reactivity worth for the poison control compositions. Detectors 4a and 4b, which measured the change in radial leakage, could be expected to

yield too large a change and therefore too large a reactivity worth for the poison control composition. The actual worth could be expected to be between those calculated from the change in axial leakage and the change in radial leakage. Detector 3 measured a mixture of many effects with possible localized effects due to the proximity of the poison control composition itself; hence, the results based on this detector should be the most difficult to interpret as to physical meaning.

It should be noted that all of the detectors measure the ^{10}B reaction rate, whereas the degree of subcriticality is primarily determined by the total fission rate of all fissionable materials in the core. On the whole, the difference among the reactivity estimates based on the various counters point to some considerable difficulty in evaluating the subcriticality of systems of this type. An accurate analysis of the experiment should probably take into account the results obtained for each individual counter.

(b) Source Comparison and Intercalibration. The effective source term had been measured for the reference core by the period technique. The reference loadings for the central measurements were identical to the reference core (see Progress Report for February 1969, ANL-7553). The reference loadings for the peripheral poison control composition worth measurements were also identical to the reference core except for the additional counters. The source term measured by the period technique for the 10^{-6} scale of the electrometer (Detectors 4a + 4b) was 2.740 ± 0.026 , where the uncertainty was calculated by the standard rms technique for data from four period measurements. The source term was also measured at the start of the poison control composition* measurements by the two-power level technique using the total stroke of the calibrated control rod. This value was measured as 2.748 ± 0.028 , where the uncertainty is calculated from the nominal 1% uncertainty assigned to the rod calibration. The two values differ by only 0.3%.

The intercalibration technique follows directly from the fact that all detectors must yield the same k_{ex} (sub) at any constant power level. Hence,

$$k_{\text{ex}}(\text{sub}) = - \frac{Q_1}{n_1} = - \frac{Q_i}{n_i}$$

or

$$Q_i = Q_1 \frac{n_i}{n_1},$$

where Q_i is the effective source term for detector i and n_i the count rate of detector i . Each of the additional detectors was intercalibrated against

the standard flux monitor at a constant subcritical power level. Each pulse counter has only one effective source term, but the electrometer can be considered as having a distinct source term for each range. The range ratios have been measured to 0.1%, so that any uncertainties are not due to range changes between experiments. The source term for each detector is given in Table I.B.10.

(c) Results of the Central Matrix Position Substitution Experiments. The worths of substituting the central drawers with axial reflectors or with poison control compositions were measured as a set of successive experiments during a single day's operation. The first reference was performed, the central core drawer in both halves was replaced with axial reflector composition, the second reference was performed, and then the central core drawer was replaced with poison control composition in the region which would normally contain fuel composition. The drawer loadings for the central drawer substitutions are shown in Fig. I.B.7 and the compositions are given in Table I.B.8.

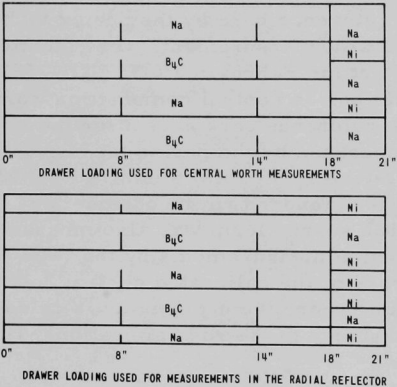


Fig. I.B.7. Drawer Loadings for Reactivity Measurements of B₄C in Assembly 56B of ZPR-3

TABLE I.B.8. Poison Control Composition for Assembly 56B of ZPR-3 (a/b-cm)

	Central Experiment	Peripheral Experiment
Na	0.009250	0.008736
B-10	0.007124	0.007145
B-11	0.02889	0.02897
C	0.009331	0.009358
Fe	0.009642	0.01054
Cr	0.002470	0.002651
Ni	0.001115	0.001177
Mn	0.0001202	0.0001192
Si	0.0001394	0.0001391

The experimental data are given in Table I.B.9, where all measurements have been corrected to the average core temperature of the first reference. The degree of subcriticality in terms of k was calculated by the standard relationship

$$k_{\text{ex}}(\text{sub}) = - Q_i / n_i,$$

and k_{ex} was converted to reactivity in inhours by the relationship

$$\rho(\text{sub}) = \frac{k_{\text{ex}}}{1 + k_{\text{ex}}} \times \text{Conv},$$

where $\text{Conv} = 1,039.08 \text{ Ih}/\% \rho$. Note that the effective source term given in the table is that which was measured for the reference core. Source neutrons were removed from their position of highest worth when the central drawer was removed for the substitutions, but the degree of subcriticality, and hence the value of total $\Delta\rho$, were calculated assuming that the source had not changed from the reference core. The experimental data must be corrected by a calculated value for the change in source. However, since the effective source was reduced by the substitutions, the values of total $\Delta\rho$ reported in Table I.B.9 can be regarded as upper limits for the reactivity worths of the substitutions.

TABLE I.B.9. Results of the Central Drawer Substitution Experiments

ρ (Ih), Core Excess Reactivity			
Reference 1: 31.4			
Reference 2: 29.3			
Average: 30.4			
Composition Substituted for Central Matrix Core Composition			
	Unit	Axial Reflector	Poison Control Composition
Effective Source (Q) ^a	ct/sec	271.0 \pm 1%	271.0 \pm 1%
Count Rate	ct/sec	63,385 \pm 0.2%	18,418 \pm 0.2%
$k_{\text{ex}}(\text{sub})^b$	% k	-0.428 \pm 0.001	-1.471 \pm 0.003
$\rho(\text{sub})^b$	Ih	-447 \pm 1	-1551 \pm 3
$\Delta\rho$ (Temp)	Ih	0.5	6.8
Total $\Delta\rho$	Ih	-477 \pm 1	-1575 \pm 3

^aFor the 10^{-8} scale on the electrometer. This value is for the reference core and must be corrected for the substitutions. See the text for additional details.

^bUncertainties are only those for the count rate. An additional 1% should be added in quadrature to account for the uncertainty in the measured source for the reference configuration.

(d) Results of the Peripheral Poison Control Composition Worth Experiments. The use of the additional detectors and the source intercalibration were performed as part of one day's experiments. The poison control composition worth measurements were performed as a set of successive experiments during the following day. The first reference was performed, and then the first set of four poison control matrix locations were loaded into the reactor, replacing radial reflector, and their worth was measured by the subcritical technique. The poison control composition replaced radial reflector composition for only the height of the core. The loading pattern of the drawers is given by the locations marked I in Fig. I.B.8. The drawer loading pattern for the poison control composition is shown in Fig. I.B.7. Next, the three additional matrix locations marked II were loaded

in each half of the reactor with the poison control drawers at each boron rod location, resulting in eight poison control drawers each with a 2×2 drawer cross section in each quadrant of the reactor. Again, their worth was measured by the subcritical technique. Finally, the poison control drawers were all replaced with the original radial blanket and the reference was repeated.

S - SAFETY ROD
C - CONTROL ROD
T - SOURCE TUBE
N - NEUTRON LEVEL DETECTOR

||||| POISON CONTROL I LOCATIONS
==== POISON CONTROL II LOCATIONS

NOTE: ALL DIMENSIONS IN CENTIMETERS

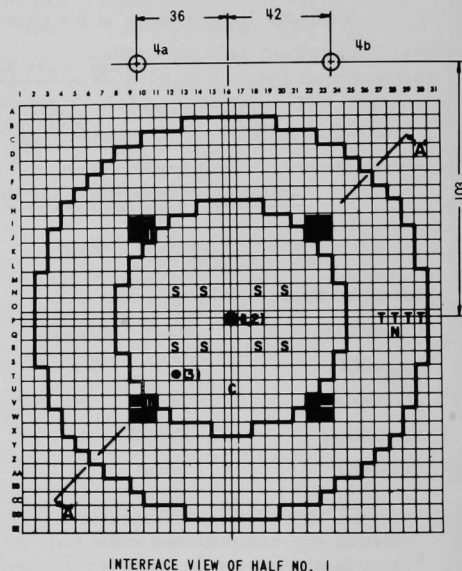
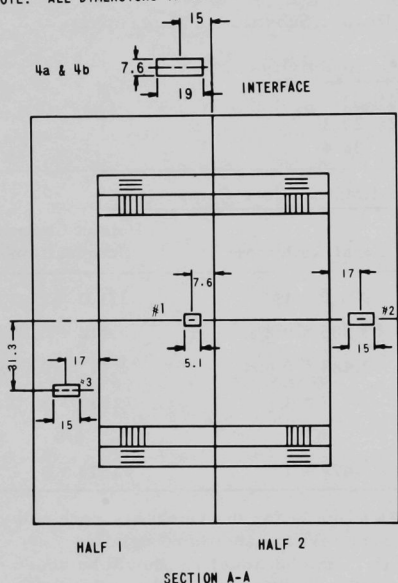


Fig. I.B.8. Detector and Matrix Locations for the Peripheral Poison Control Worth Measurements

The experimental data are given in Table I.B.10, where all of the measurements have been corrected to the average core temperature of the first reference. The values for $k_{ex(sub)}$ and $\rho(sub)$ were calculated for each detector as stated previously. As expected, the relative count rates of the detectors varied according to their location. Detector 2 showed the smallest change in count rate, and hence the smallest reactivity worth for the rods; Detector 4a + 4b showed the greatest change and largest reactivity worth; Detector 1, the central detector, showed an intermediate flux change, and hence an intermediate reactivity worth. The excellent agreement between Detectors 1 and 2 is probably fortuitous.

TABLE I.B.10. Results of the Peripheral Poison Control Composition Worth Experiments (Replacing Radial Reflector Composition)

	Experiment	ρ (lh), Core Excess Reactivity			
	Reference 1:	34.2			
	Reference 2:	32.4			
	Average:	33.3			
	Units	1	2	3	4a + 4b
Poison Control, Configuration I					
Effective Source (Q)	ct/sec	1.692 \pm 1%	38.56 \pm 1%	9.395 \pm 1%	271.0 \pm 1% ^a
Corrected Count Rate ^b	ct/sec	188.9 \pm 0.5%	4,510 \pm 0.5%	1,101 \pm 0.4%	29,310 \pm 0.2%
$k_{\text{eff}}(\text{sub})^c$	% k	-0.896 \pm 0.005	-0.855 \pm 0.005	-0.903 \pm 0.004	-0.925 \pm 0.002
ρ (sub) ^c	lh	-939 \pm 5	-896 \pm 5	-947 \pm 4	-971 \pm 2
$\Delta\rho$ (Temp)	lh	4.6	4.6	4.6	4.6
Total $\Delta\rho^c$	lh	-968 \pm 5	-925 \pm 5	-976 \pm 4	-1,000 \pm 2
Poison Control, Configurations I and II					
Corrected Count Rate ^b	ct/sec	100.4 \pm 0.6%	2,338 \pm 0.4%	560.9 \pm 0.3%	14,362 \pm 0.2%
$k_{\text{eff}}(\text{sub})^c$	% k	-1.685 \pm 0.010	-1.649 \pm 0.006	-1.675 \pm 0.005	-1.887 \pm 0.004
ρ (sub) ^c	lh	-1,781 \pm 11	-1,743 \pm 7	-1,771 \pm 5	-1,998 \pm 4
$\Delta\rho$ (Temp)	lh	9.9	9.9	9.9	9.9
Total $\Delta\rho^c$	lh	-1,804 \pm 11	-1,766 \pm 7	-1,794 \pm 5	-2,021 \pm 4

^aFor 10⁻⁸ scale on the electrometer.^bUncertainties include statistics and uncertainty in the dead time correction to the count rates.^cQuoted uncertainties are for count rate only. An additional 1% uncertainty should be added in quadrature to account for the uncertainty in the effective source term measured for the reference configuration.

(v) **Radial and Axial Worth Traverses.** Reactivity worth traverses were made with Assembly 56B for B-10, Pu-239, and stainless steel. The stainless steel traverse data were used to determine the capsule corrections for both the B-10 and the Pu-239 sample jackets. Empty carrier traverses were also made to correct for the reactivity effect due to the push rod and sample holder.

The measurement procedure for these experiments was similar to that used in the central perturbation measurements. The position of a calibrated autorod was measured when the sample was at a location in the reactor and when at a reference location out of the reactor. As the sample was moved, the autorod position changed to maintain reactor power level constant. Reactivity differences were calculated from the differences in the autorod positions. The reactivity worth of the autorod as a function of its position was a separate calibration experiment and was done using the inverse kinetics technique.

Traverses were taken to give the spatial worth distributions in both the radial and axial directions in Assembly 56B. The normalized worth distributions are illustrated in Figs. I.B.9 through I.B.14. The physical properties of the test samples are given in Table I.B.11. The drawer loadings which accommodated the traversing mechanism were identical to those used in the radial and axial reaction rate measurements for Assembly 56B.

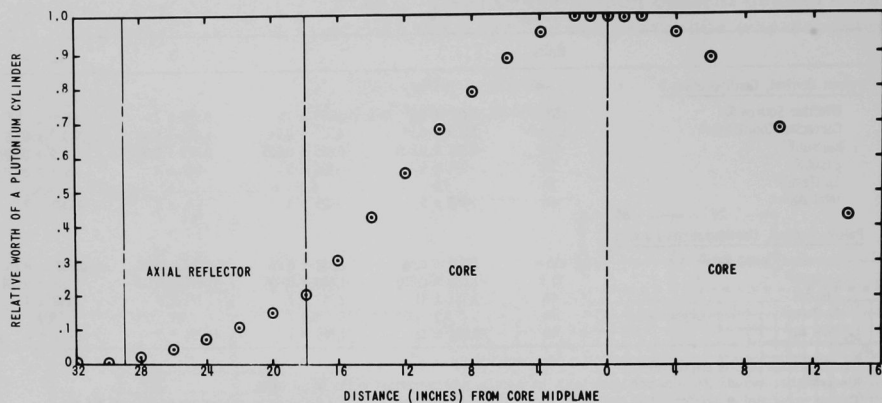


Fig. I.B.9. Axial ^{239}Pu Reactivity Traverse in Assembly 56B of ZPR-3

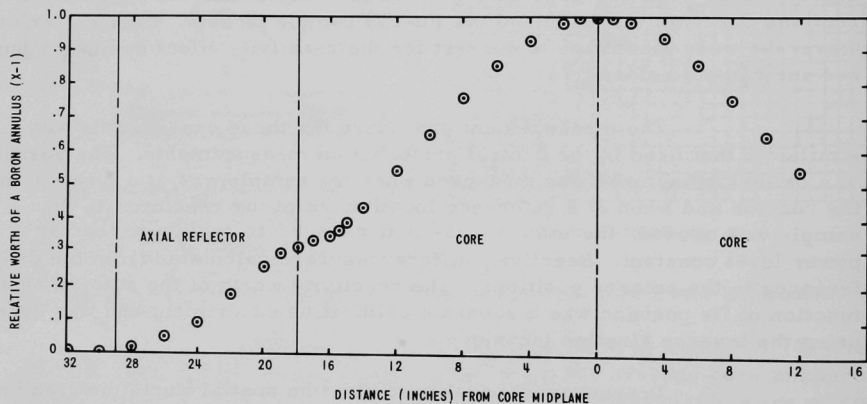


Fig. I.B.10. Axial B-10 Reactivity Traverse in Assembly 56B of ZPR-3

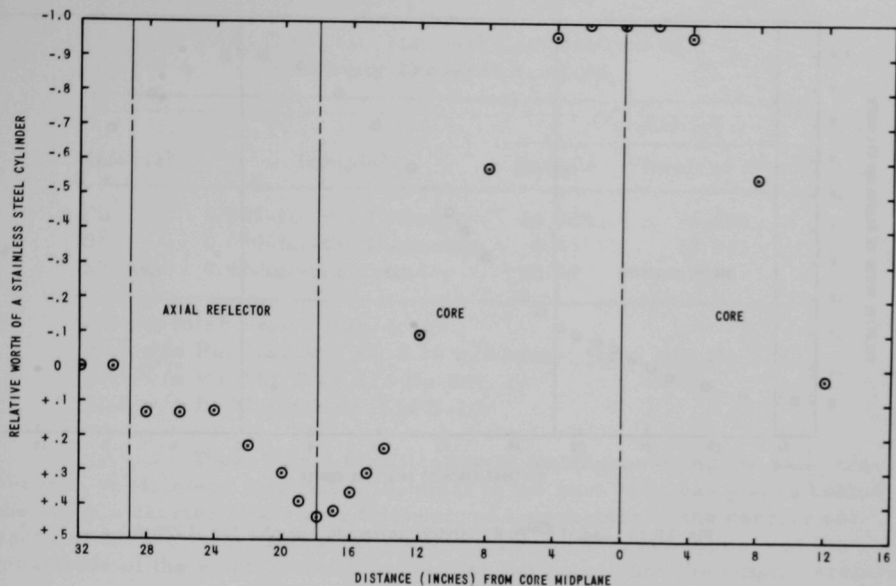


Fig. 1B.11. Axial Stainless Steel Reactivity Traverse in Assembly 56B of ZPR-3

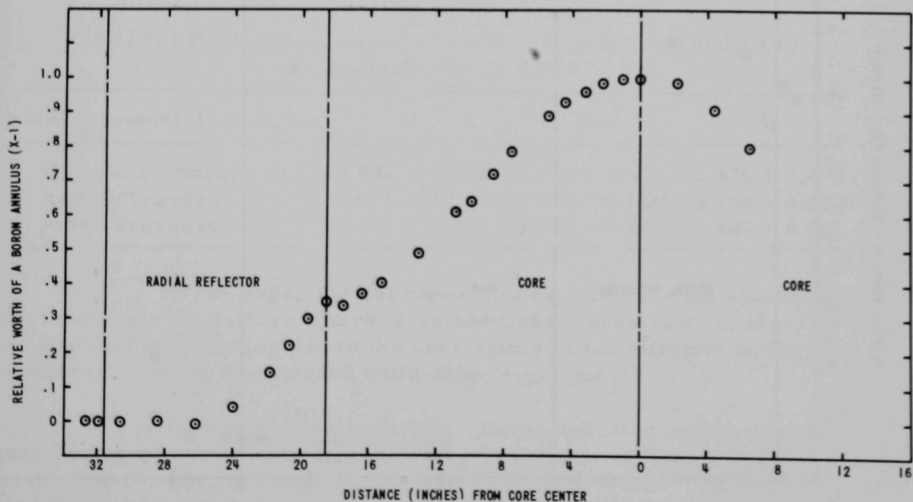


Fig. 1B.12. Radial B-10 Reactivity Traverse in Assembly 56B of ZPR-3

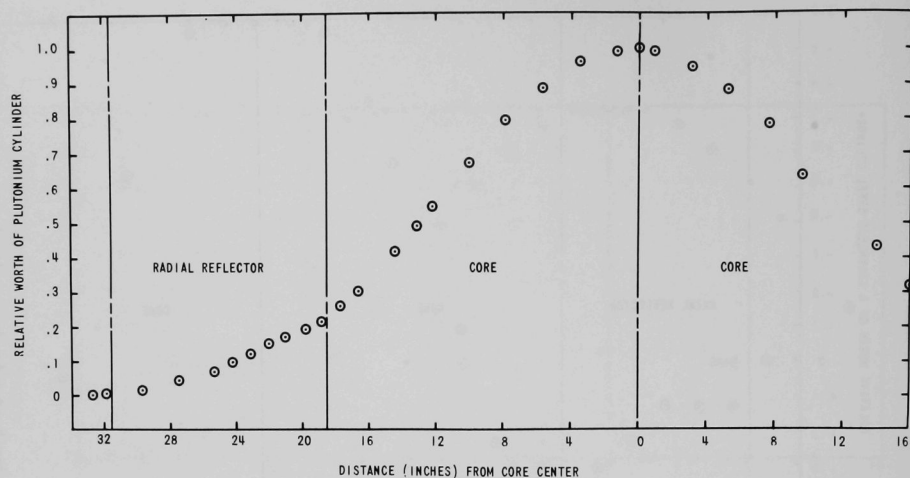


Fig. I.B.13. Radial ^{239}Pu Reactivity Traverse in Assembly 56B of ZPR-3

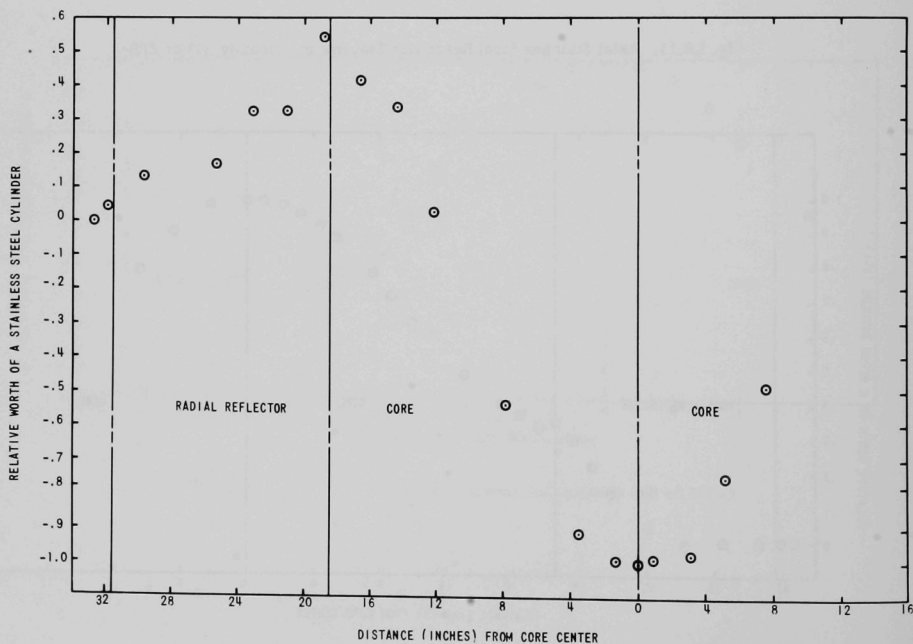


Fig. I.B.14. Radial Stainless Steel Reactivity Traverse in Assembly 56B of ZPR-3

TABLE I.B.11. Material Compositions of
Reactivity Traverse Samples

Material	Sample ^a	Weights (g)	
		Sample	Stainless Steel
Pu ^b	0.201-in.-dia Cylinder	14.965	6.655
B ^c	0.020-in.-thick Annulus	0.691	12.243
SS-304	0.42-in.-dia Cylinder	35.90	35.90

^aAll capsules were 2.0 in. long.

^b98.6 w/o Pu, 1.24 w/o Al, 0.16 w/o other; 95.06 w/o Pu-239, 4.49 w/o Pu-240, 0.45 w/o Pu-241.

^c92.8 w/o B; 92.1 w/o of B is B-10.

There was a modification in technique during the axial traverses. A stainless steel tube, identical to the push rod, was placed behind the sample carrier to act as a follower. A comparison of the carrier corrections for the radial and axial stainless steel traverses shows that the magnitude of the empty carrier correction decreased and the empty carrier worth is symmetric about the core center.

The test samples were the same samples used in the central perturbation measurements, and a comparison of the three central worth determinations is given in Table I.B.12.

TABLE I.B.12. Comparison of Central Reactivity Worths (Ih)
in Assembly 56B of ZPR-3

Measurement Technique	B	Pu	SS
Central Perturbation	3.892 ± 0.012	5.964 ± 0.015	0.470 ± 0.012
Radial Traverse	3.908 ± 0.020	5.893 ± 0.020	0.455 ± 0.020
Axial Traverse	3.952 ± 0.020	5.993 ± 0.020	0.487 ± 0.020

The experimental uncertainties given are the uncertainties due to reactor statistics. There is an additional uncertainty of about 1% in the absolute reactivities due to the uncertainty in the effective source determination during the autorod calibration experiment.

(vi) Central Fission Ratios. Central fission ratios were measured using gas-flow spherical counters.* The fission ratios desired were for U-238, Pu-239, and Pu-240, all with respect to U-235. The experimental data for U-234 and U-236 were needed to reduce the data for the U-235

*Davey, W. G., and Amundson, P. I., Nucl. Sci. Eng. 28, 111 (1967).

counter without resorting to theoretical calculations, and the U-233 data were obtained as a normal part of the experiment.

When the U-238 radial fission reaction rate traverse experiment was performed, variations of the order of 5% were obtained between the heavily and lightly loaded drawers near the core center (see ANL-7561). Consequently, central fission ratios were measured in both types of drawers to determine the magnitude of the effect on the threshold fissionable isotopes. The fission counters were placed in 2 x 2 x 2-in. voids loaded into the front of the core drawers. The drawer loading diagrams are shown in Fig. I.B.15. The fission counters were placed at the front of 1-P-15 and 2-P-17 for the measurements in the lightly loaded drawers, and in 1-O-16 and 2-Q-16 for the heavily loaded drawers. The counters were the same distance from the assembly counter for both types of drawers.

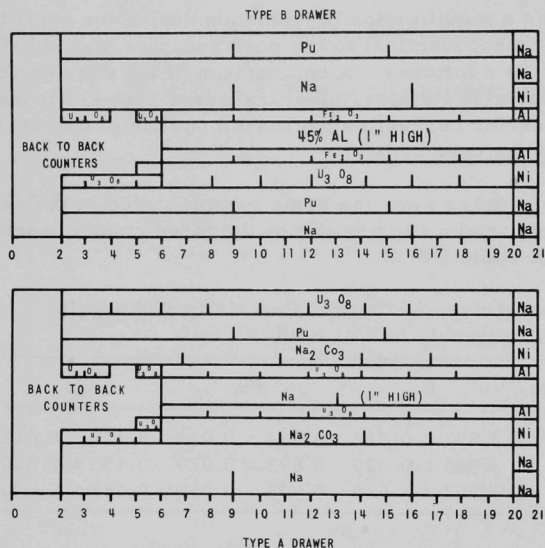


Fig. I.B.15

Drawer Loadings for Fission-rate-ratio Measurements in Assembly 56B of ZPR-3

The data for all of the detectors were taken with a pulse-height analyzer. The differential spectra were converted to fission rates by means of a computer code using an identical integration technique for all of the detectors. The detector fission rates were reduced to isotopic fission rates with a computer code containing the masses and isotopic concentrations for each of the detectors.

The reduced isotopic fission ratios are given in Table I.B.13. The large variations observed in the U-238 radial fission reaction rate data did not occur in the isotopic fission ratios as a function of drawer type.

TABLE I.B.13. Measured Central Fission Ratios in
Assembly 56B^a in ZPR-3

Nuclide	Measured in 1-O-16 and 2-Q-16 (Heavily Loaded Drawers)	Measured in 1-P-15 and 2-P-17 (Lightly Loaded Drawers)
	$\bar{\sigma}_f(i)/\bar{\sigma}_f(\text{U-235})$	$\bar{\sigma}_f(i)/\bar{\sigma}_f(\text{U-235})$
U-233	1.476	1.480
U-234	0.193	0.197
U-236	0.0638	0.0640
U-238	0.0310	0.0307
Pu-239	1.021	1.035
Pu-240	0.282	0.283

^aThe experimental uncertainty is ~1% for all ratios.

(vii) Errata to ANL-7561, March 1969. The text critical mass in Assembly 56B, Core Edge Worths and Critical Mass Adjustment should read 331.94 kg as indicated in the Assembly 56B Critical Mass Table. It should be noted that in the Table, Reactor Inventory for the Assembly 56B Reference Core the radial reflector drawer numbers are for the number of matrix positions (full radial reflector height). The radial dimensions of the Equivalent Cylindrical Loading Diagram should read 25.15 in. for the outer boundary of Zone 1, radial reflector and 31.65 in. for the outer boundary of Zone 2/3 radial reflector.

4. ZPR-6 and -9 Operations and Analysis

a Integral Studies of Large Systems (W. Y. Kato)

Last Reported: ANL-7548, pp. 18-22 (Jan 1969).

(i) Analysis of the Danger Coefficient Measurements Performed in Assembly 5 of ZPR-6. The integral transport method for treating self-shielding in the calculation of the reactivity worth of various samples (see Progress Report for December 1968, ANL-7527, pp. 22-29) was used to calculate the central worths of few samples whose worths had been measured in a large uranium carbide core, Assembly 5 of ZPR-6. Assembly 5 was a 2700-liter, cylindrical core reflected with 30 cm of depleted uranium (0.2% enrichment).

The reactivity worth of a sample was measured by either of two methods: (1) If the reactivity of a sample was one inhour or more, its worth was determined by the period method, i.e., measuring repetitively the period of a slightly above critical system (~10 lh) with and without (void

the sample at the center of the core. The accuracy of this procedure is typically 0.005 lh. (2) The reactivity of a small sample was determined by oscillating the sample relative to void and using a calibrated autorod. The accuracy inherent in this technique can be as low as 0.001 lh provided the autorod is accurately calibrated. The samples used were 2 in. square (nominally) by various thicknesses.

The calculated and measured reactivity worths of U-235 samples as a function of thickness are given in Table I.B.14. The values listed in the third column are the normalized results of first-order perturbation (FOP) calculations using a diffusion code and an equivalent homogeneous, i.e., heterogeneous, cross-section set for the core and a homogeneous (not weighted spatially) cross sections for the perturbing samples of U-235. The FOP values were normalized to the measured value of the normalization integral.* The values listed in the fourth column are the normalized FOP values corrected for flux pulsing and self-shielding. The calculated values are overpredicted by about 5%.

TABLE I.B.14. Measured and Calculated U-235 Central Worths in Assembly 5 of ZPR-6

Sample Size (cm)	Weight ^a (g)	Calculated FOP Worth ^b (lh)	Final Calculated Worth (lh)	Measured Worth ^c (lh)	Percent Difference: $\frac{\text{Cal} - \text{Meas}}{\text{Cal}}$
4.365 x 4.365 x 0.0127	4.200	0.219	0.219	0.209 ± 0.002	+4.5
4.420 x 4.420 x 0.0389	12.935	0.675	0.679	0.659 ± 0.002	+3.0
4.410 x 4.410 x 0.1140	38.582	2.016	2.053	1.938 ± 0.004	+5.6
4.401 x 4.401 x 0.1774	59.755	3.123	3.209	3.079 ± 0.012	+4.0
4.405 x 4.405 x 0.2914	98.472	5.142	5.354	4.978 ± 0.010	+7.0
5.080 x 5.080 x 0.5967	268.146	14.000	14.987	14.691 ± 0.010	+2.0

^aWeight of U-235 only.

^bFOP means first-order perturbation; the values were multiplied by 1.16, the ratio of the calculated to measured normalization integral.

^cThe values listed incorporate small corrections for the 6.9% U-238 present in the enriched foils.

The measured and calculated reactivity worths of the U-238 samples are given in Table I.B.15. The cross sections in the resonance region (groups 11-22) for each U-238 sample were generated using the formulation of Tiren** for resonance absorption in a lump surrounded by an equivalent homogeneous medium containing the same resonance absorber. Table I.B.16 shows the absorption cross sections of U-238 for groups 11-22 as a function of sample thickness. These cross sections were used with homogeneous cross sections of the first 10 groups to obtain the FOP values for the various samples.

*Reactor Physics Division Annual Report: July 1, 1966 to June 30, 1967, ANL-7310, p. 189.

**Tiren, L. I., Nucl. Sci. Eng. 33, 348 (1968).

TABLE I.B.15. Measured and Calculated U-238 Central Worths in Assembly 5 of ZPR-6

Sample Size (cm)	Weight ^a (g)	Calculated FOP ^b Worth (lh)	Final Calculated Worth (lh)	Measured Worth ^c (lh)	Percent Difference:	
					Cal - Meas	Cal
4.530 x 4.530 x 0.0139	5.345	-0.024	-0.024	-0.026 ± 0.002		+8.3
4.532 x 4.531 x 0.0418	15.917	-0.071	-0.072	-0.060 ± 0.002		-16.6
4.530 x 4.530 x 0.1670	63.958	-0.280	-0.284	-0.235 ± 0.002		-16.6
4.865 x 4.865 x 0.3175	140.361	-0.607	-0.613	-0.506 ± 0.010		-17.4
4.925 x 4.925 x 2.540	11151.29	-4.880	-4.810	-3.88 ± 0.01		-16.1

^aWeight of U-238 only.

^bFOP means first-order perturbation; the values were multiplied by 1.16, the ratio of the calculated to measured normalization integral (see Sect. IX).

^cThe values listed incorporate small corrections for the 0.2% U-235 in the depleted foils.

TABLE I.B.16. U-238 Absorption Cross Sections as a Function of Sample Thickness

Energy Group		Sample Thickness (cm)				
No.	E (keV)	0.0139	0.0418	0.1670	0.3175	2.540
11	25.0	0.433	0.432	0.436	0.427	0.419
12	15.0	0.542	0.541	0.536	0.531	0.521
13	9.12	0.642	0.639	0.630	0.620	0.602
14	4.31	0.741	0.753	0.715	0.696	0.663
15	2.61	0.796	0.781	0.744	0.717	0.682
16	2.03	0.909	0.880	0.839	0.805	0.768
17	1.23	0.769	0.740	0.708	0.682	0.648
18	0.961	0.865	0.832	0.784	0.751	0.705
19	0.583	0.829	0.784	0.726	0.687	0.633
20	0.275	0.662	0.614	0.555	0.516	0.464
21	0.101	0.800	0.771	0.698	0.663	0.611
22	0.029	0.971	0.910	0.835	0.793	0.733

It is seen from Table I.B.15 that:

(1) The calculated values are overpredicted by about 16%. The measured value for the thinnest foil appears to be in error.

(2) The broad-group self-shielding correction to the FOP values increase rather than decrease the reactivity worths of some of the samples. This is due to flux peaking in some of the groups, resulting from excessive scattering in the high-energy groups. Experimentally the reactivity worth decreases as a function of thickness. Thus it appears that the U-238 inelastic-scattering cross sections are too high.

(3) The measured value of the thinnest sample appears to be in error.

The measured and calculated reactivity worths of Fe, Cr, Ni, Na, C, Be, B-10, and Ta samples (2 x 2 x 1 in.) are given in Table I.B.17.

It is seen that the agreements between the calculated and measured values for B-10 and tantalum are very good. The agreement between calculated and measured values of scattering materials such as graphite, beryllium, and the rest is rather poor. Inaccuracies in the calculated adjoint function could be the source of error.

TABLE I.B.17. Measured and Calculated Central Worths of Various Samples in Assembly 5 of ZPR-6

Sample ^a	Sample Weight (g)	Calculated FOP Worth (Ih) ^b	Final Calculated Worth (Ih)	Measured Worth (Ih)	Percent Difference:
					$\frac{\text{Cal} - \text{Meas}}{\text{Cal}}$
Fe	488.0	-0.898	-0.847	-0.737 ± 0.005	-13.0
Cr	220.73	-0.518	-0.508	-0.339 ± 0.022	-33.2
Ni	546.0	-1.030	-1.002	-1.134 ± 0.015	+13.4
Na	51.38	-0.030	-0.031	-0.041 ± 0.010	+32.2
C	103.0	-0.111	-0.004	+0.183 ± 0.022	-47.0
Be	114.31	-1.021	-0.298	+1.143 ± 0.05	-48.0
B-10	29.29	-33.20	-22.97	-23.19 ± 0.033	+0.95
Ta	924.70	-17.46	-12.07	-11.909 ± 0.015	-1.30

^aAll samples were 2.0 x 2.0 x 1.0 in.

^b1% $\Delta k/k = 476$ Ih.

5. ZPPR Operations and Analysis

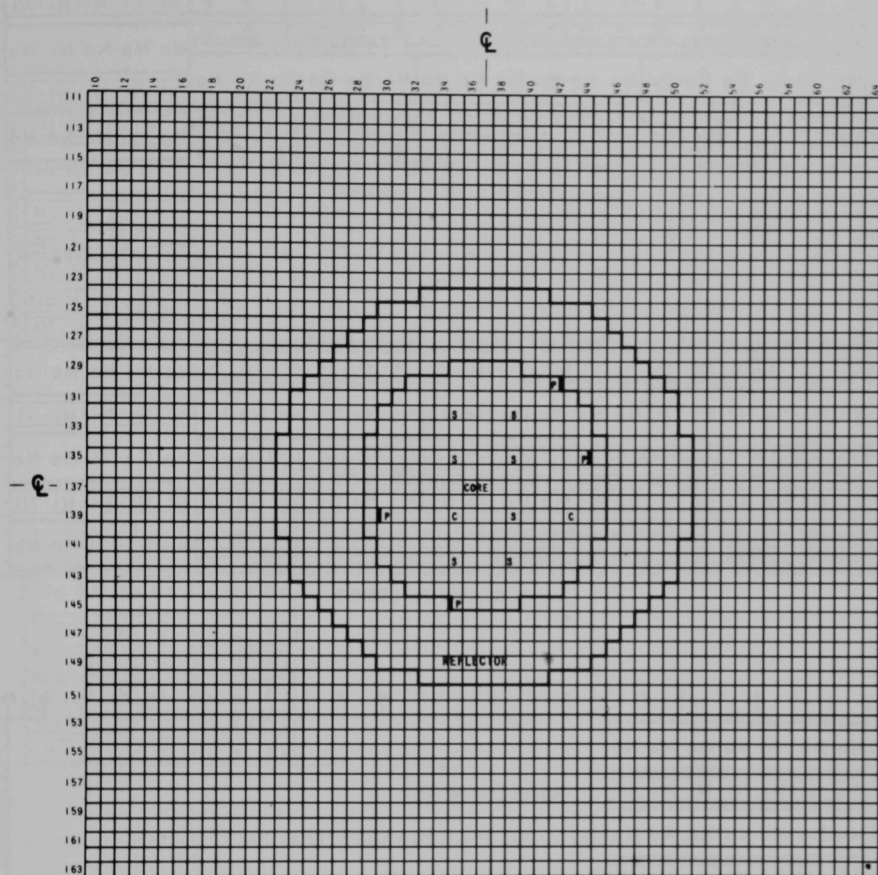
a. Mockup Studies (W. G. Davey and P. I. Amundson)

Last Reported: ANL-7553, p. 15 (Feb 1969).

(i) FTR Critical Program. With the completion of work with Assembly 56B on ZPR-3 (Assembly I of FTR Resumed Phase-B Critical Experiments), the necessary nickel material was transferred from ZPR-3 to ZPPR to permit completion of the Na-Ni radial reflector of Assembly 1 of ZPPR. Assembly 1 pertains to the FTR-II core of the Phase-B Critical Experiments Program. The initial step in achieving the FTR-II loading desired for these experiments involves the determination of the critical mass of FTR-1 for comparison with that achieved with ZPR-3. The loading to critical of FTR-I for ZPPR and the associated measurements of temperature coefficient and control and safety-rod worths have been completed. The temperature and rod-worth data are being analyzed; preliminary results indicate a total shutdown margin in excess of 3% $\Delta k/k$. The reproducibility of the reference critical between half-closures and the worth of half-separation have been measured and are being analyzed. Edge-worth measurements necessary to permit the determination of the critical mass are in progress.

The critical configuration of FTR-I as achieved in ZPPR (Loading 1-17) (see Fig. I.B.16) contains 361.44 kg total fissile mass (Pu-239, Pu-241, and U-235). The core is 91.62 cm high and enclosed by

an average 30.5-cm-thick radial and axial reflectors. Drawer loadings for the various zones are illustrated in Figs. I.B.17-I.B.19, and the corresponding as-built compositions are presented in Table I.B.18.



ZPPR HALF I

(HALF 2 IS A MIRROR IMAGE OF HALF 1)

S= SAFETY ROD

C= CONTROL ROD

P= DRAWER ADJACENT TO POISON SAFETY ROD

W= POISON SAFETY ROD (WITHDRAWN DURING OPERATION)

Fig. I.B.16. Critical Loading for ZPPR FTR-1 Reference Core

	0	1	2	3	4	5	6	7	8	9	10	11	12	13	14	15	16	17	18	19	20	21	22	23	
A	U ₃ O ₈	U ₃ O ₈	U ₃ O ₈	U ₃ O ₈	U ₃ O ₈	U ₃ O ₈	U ₃ O ₈	U ₃ O ₈	U ₃ O ₈	U ₃ O ₈	U ₃ O ₈	U ₃ O ₈	U ₃ O ₈	U ₃ O ₈	U ₃ O ₈	U ₃ O ₈	U ₃ O ₈	U ₃ O ₈	U ₃ O ₈	Na	Na	Na	Na	Na	0
B	CO ₂	CO ₂	CO ₂	CO ₂	CO ₂	CO ₂	CO ₂	CO ₂	CO ₂	CO ₂	CO ₂	CO ₂	CO ₂	CO ₂	CO ₂	CO ₂	CO ₂	CO ₂	CO ₂	Na	Na	Na	Na	Na	1/2
C	Na ₂	Na ₂	Na ₂	Na ₂	Na ₂	Na ₂	Na ₂	Na ₂	Na ₂	Na ₂	Na ₂	Na ₂	Na ₂	Na ₂	Na ₂	Na ₂	Na ₂	Na ₂	Na ₂	Ni	Ni	Ni	Ni	Ni	1
D																									
E																									
F																									
G	Pu	Pu	Pu	Pu	Pu	Pu	Pu	Pu	Pu	Pu	Pu	Pu	Pu	Pu	Pu	Pu	Pu	Pu	Pu	Na	Na	Na	Na	Na	1
H	ZPPR	ZPPR	ZPPR	ZPPR	ZPPR	ZPPR	ZPPR	ZPPR	ZPPR	ZPPR	ZPPR	ZPPR	ZPPR	ZPPR	ZPPR	ZPPR	ZPPR	ZPPR	ZPPR	Na	Na	Na	Na	Na	1 1/4
I																									
J	Na	Na	Na	Na	Na	Na	Na	Na	Na	Na	Na	Na	Na	Na	Na	Na	Na	Na	Na	Ni	Ni	Ni	Ni	Ni	2
K																									
L																									
M	U ₃ O ₈	U ₃ O ₈	U ₃ O ₈	U ₃ O ₈	U ₃ O ₈	U ₃ O ₈	U ₃ O ₈	U ₃ O ₈	U ₃ O ₈	U ₃ O ₈	U ₃ O ₈	U ₃ O ₈	U ₃ O ₈	U ₃ O ₈	U ₃ O ₈	U ₃ O ₈	U ₃ O ₈	U ₃ O ₈	U ₃ O ₈	Na	Na	Na	Na	Na	1 1/4
N																									
O																									
P	Na	Na	Na	Na	Na	Na	Na	Na	Na	Na	Na	Na	Na	Na	Na	Na	Na	Na	Na	Na	Na	Na	Na	Na	2

(a) 1-COLUMN Pu DRAWER

AXIAL
REFLECTOR

	0	1	2	3	4	5	6	7	8	9	10	11	12	13	14	15	16	17	18	19	20	21	22	23	
A	(ZPPR)	(ZPPR)	(ZPPR)	(ZPPR)	(ZPPR)	(ZPPR)	(ZPPR)	(ZPPR)	(ZPPR)	(ZPPR)	(ZPPR)	(ZPPR)	(ZPPR)	(ZPPR)	(ZPPR)	(ZPPR)	(ZPPR)	(ZPPR)							0
B	Pu	Pu	Pu	Pu	Pu	Pu	Pu	Pu	Pu	Pu	Pu	Pu	Pu	Pu	Pu	Pu	Pu	Pu							
C	ZPPR	ZPPR	ZPPR	ZPPR	ZPPR	ZPPR	ZPPR	ZPPR	ZPPR	ZPPR	ZPPR	ZPPR	ZPPR	ZPPR	ZPPR	ZPPR	ZPPR	ZPPR		Na	Na	Na	Na	Na	
D																									
E	Na	Na	Na	Na	Na	Na		Na	Na	Na	Na	Na	Na		Na	Na	Na	Na	Na		Ni	Ni	Ni	Ni	Ni
F																									
G																									
H	U ₃ O ₈	U ₃ O ₈	U ₃ O ₈	U ₃ O ₈	U ₃ O ₈	U ₃ O ₈	U ₃ O ₈	U ₃ O ₈	U ₃ O ₈	U ₃ O ₈	U ₃ O ₈	U ₃ O ₈	U ₃ O ₈	U ₃ O ₈	U ₃ O ₈	U ₃ O ₈	U ₃ O ₈	U ₃ O ₈		Na	Na	Na	Na	Na	
I																									
J	Na	Na	Na	Na	Na	Na		Na	Na	Na	Na	Na	Na		Na	Na	Na	Na	Na		Ni	Ni	Ni	Ni	Ni
K																									
L																									
M	Pu	Pu	Pu	Pu	Pu	Pu	Pu	Pu	Pu	Pu	Pu	Pu	Pu	Pu	Pu	Pu	Pu	Pu							
N	ZPPR	ZPPR	ZPPR	ZPPR	ZPPR	ZPPR	ZPPR	ZPPR	ZPPR	ZPPR	ZPPR	ZPPR	ZPPR	ZPPR	ZPPR	ZPPR	ZPPR	ZPPR							
O																									
P	Na	Na	Na	Na	Na	Na		Na	Na	Na	Na	Na	Na		Na	Na	Na	Na	Na		Na	Na	Na	Na	Na

(b) 2-COLUMN Pu DRAWER

0	1	2	3	4	5	6	7	8	9	10	11	12	13	14	15	16	17	18	19	20	21	22	23	0
A	Na · Na · Na · Na · Na · Na · Na																							
B																								
C																								
D																								
E	Ni · Ni · Ni · Ni · Ni · Ni · Ni																							$\frac{1}{2}$
F																								
G																								
H																								
I	Na · Na · Na · Na · Na · Na · Na																							1
J																								
K	Ni · Ni · Ni · Ni · Ni · Ni · Ni																							$1\frac{1}{4}$
L																								
M																								
N																								
O	Na · Na · Na · Na · Na · Na · Na																							$1\frac{1}{2}$
P																								

(c) AXIAL REFLECTOR BACK DRAWER (SAME FOR BOTH OF ABOVE CORE DRAWERS)

Fig. I.B.17. Core and Axial Reflector Drawers for FTR Half of ZPPR

	1	2	3	4	5	6	7	8	9	10	11	12	13	14	15	16	17	18	19	20	21	22	23	24	
A	Pu	Pu	Pu	Pu	Pu	Pu	Pu	Pu	Pu	Pu	Pu	Pu	Pu	Pu	Pu	Pu	Pu	Pu	Pu	Pu	Pu	Pu	Pu	Pu	Na
B	ZPPR	ZPPR	ZPPR	ZPPR	ZPPR	ZPPR	ZPPR	ZPPR	ZPPR	ZPPR	ZPPR	ZPPR	ZPPR	ZPPR	ZPPR	ZPPR	ZPPR	ZPPR	ZPPR	ZPPR	ZPPR	ZPPR	ZPPR	ZPPR	Na
C	CO ₂	CO ₂	CO ₂	CO ₂	CO ₂	CO ₂	CO ₂	CO ₂	CO ₂	CO ₂	CO ₂	CO ₂	CO ₂	CO ₂	CO ₂	CO ₂	CO ₂	CO ₂	CO ₂	CO ₂	CO ₂	CO ₂	CO ₂	CO ₂	Na
D	Na ₂	Na ₂	Na ₂	Na ₂	Na ₂	Na ₂	Na ₂	Na ₂	Na ₂	Na ₂	Na ₂	Na ₂	Na ₂	Na ₂	Na ₂	Na ₂	Na ₂	Na ₂	Na ₂	Na ₂	Na ₂	Na ₂	Na ₂	Na ₂	Na
E	U ₃ O ₈	U ₃ O ₈	U ₃ O ₈	U ₃ O ₈	U ₃ O ₈	U ₃ O ₈	U ₃ O ₈	U ₃ O ₈	U ₃ O ₈	U ₃ O ₈	U ₃ O ₈	U ₃ O ₈	U ₃ O ₈	U ₃ O ₈	U ₃ O ₈	U ₃ O ₈	U ₃ O ₈	U ₃ O ₈	U ₃ O ₈	U ₃ O ₈	U ₃ O ₈	U ₃ O ₈	U ₃ O ₈	U ₃ O ₈	Na
F	Na	Na	Na	Na	Na	Na	Na	Na	Na	Na	Na	Na	Na	Na	Na	Na	Na	Na	Na	Na	Na	Na	Na	Na	Na
G	Na ₂ CO ₃	Na ₂ CO ₃	Na ₂ CO ₃	Na ₂ CO ₃	Na ₂ CO ₃	Na ₂ CO ₃	Na ₂ CO ₃	Na ₂ CO ₃	Na ₂ CO ₃	Na ₂ CO ₃	Na ₂ CO ₃	Na ₂ CO ₃	Na ₂ CO ₃	Na ₂ CO ₃	Na ₂ CO ₃	Na ₂ CO ₃	Na ₂ CO ₃	Na ₂ CO ₃	Na ₂ CO ₃	Na ₂ CO ₃	Na ₂ CO ₃	Na ₂ CO ₃	Na ₂ CO ₃	Na ₂ CO ₃	Na
H	Na	Na	Na	Na	Na	Na	Na	Na	Na	Na	Na	Na	Na	Na	Na	Na	Na	Na	Na	Na	Na	Na	Na	Na	Na
I	Na	Na	Na	Na	Na	Na	Na	Na	Na	Na	Na	Na	Na	Na	Na	Na	Na	Na	Na	Na	Na	Na	Na	Na	Na
J	Na	Na	Na	Na	Na	Na	Na	Na	Na	Na	Na	Na	Na	Na	Na	Na	Na	Na	Na	Na	Na	Na	Na	Na	Na
K	Na	Na	Na	Na	Na	Na	Na	Na	Na	Na	Na	Na	Na	Na	Na	Na	Na	Na	Na	Na	Na	Na	Na	Na	Na
L	Na	Na	Na	Na	Na	Na	Na	Na	Na	Na	Na	Na	Na	Na	Na	Na	Na	Na	Na	Na	Na	Na	Na	Na	Na
M	Na	Na	Na	Na	Na	Na	Na	Na	Na	Na	Na	Na	Na	Na	Na	Na	Na	Na	Na	Na	Na	Na	Na	Na	Na
N	Na	Na	Na	Na	Na	Na	Na	Na	Na	Na	Na	Na	Na	Na	Na	Na	Na	Na	Na	Na	Na	Na	Na	Na	Na
O	Na	Na	Na	Na	Na	Na	Na	Na	Na	Na	Na	Na	Na	Na	Na	Na	Na	Na	Na	Na	Na	Na	Na	Na	Na

MOVABLE FUEL ROD FOR FTR-1/2 ON ZPPR

	0	1	2	3	4	5	6	7	8	9	10	11	12	13	14	15	16	17	18	19	20	21	22	23	
A	U ₃ O ₈	U ₃ O ₈	U ₃ O ₈	U ₃ O ₈	U ₃ O ₈	U ₃ O ₈	U ₃ O ₈	U ₃ O ₈	U ₃ O ₈	U ₃ O ₈	U ₃ O ₈	U ₃ O ₈	U ₃ O ₈	U ₃ O ₈	U ₃ O ₈	U ₃ O ₈	U ₃ O ₈	U ₃ O ₈	U ₃ O ₈	U ₃ O ₈	U ₃ O ₈	U ₃ O ₈	U ₃ O ₈	U ₃ O ₈	Na
B	CO ₂	CO ₂	CO ₂	CO ₂	CO ₂	CO ₂	CO ₂	CO ₂	CO ₂	CO ₂	CO ₂	CO ₂	CO ₂	CO ₂	CO ₂	CO ₂	CO ₂	CO ₂	CO ₂	CO ₂	CO ₂	CO ₂	CO ₂	CO ₂	Na
C	Na ₂	Na ₂	Na ₂	Na ₂	Na ₂	Na ₂	Na ₂	Na ₂	Na ₂	Na ₂	Na ₂	Na ₂	Na ₂	Na ₂	Na ₂	Na ₂	Na ₂	Na ₂	Na ₂	Na ₂	Na ₂	Na ₂	Na ₂	Na ₂	Na
D	U ₃ O ₈	U ₃ O ₈	U ₃ O ₈	U ₃ O ₈	U ₃ O ₈	U ₃ O ₈	U ₃ O ₈	U ₃ O ₈	U ₃ O ₈	U ₃ O ₈	U ₃ O ₈	U ₃ O ₈	U ₃ O ₈	U ₃ O ₈	U ₃ O ₈	U ₃ O ₈	U ₃ O ₈	U ₃ O ₈	U ₃ O ₈	U ₃ O ₈	U ₃ O ₈	U ₃ O ₈	U ₃ O ₈	U ₃ O ₈	Na
E	Na	Na	Na	Na	Na	Na	Na	Na	Na	Na	Na	Na	Na	Na	Na	Na	Na	Na	Na	Na	Na	Na	Na	Na	Na
F	Na	Na	Na	Na	Na	Na	Na	Na	Na	Na	Na	Na	Na	Na	Na	Na	Na	Na	Na	Na	Na	Na	Na	Na	Na
G	Na	Na	Na	Na	Na	Na	Na	Na	Na	Na	Na	Na	Na	Na	Na	Na	Na	Na	Na	Na	Na	Na	Na	Na	Na
H	Na	Na	Na	Na	Na	Na	Na	Na	Na	Na	Na	Na	Na	Na	Na	Na	Na	Na	Na	Na	Na	Na	Na	Na	Na
I	Na	Na	Na	Na	Na	Na	Na	Na	Na	Na	Na	Na	Na	Na	Na	Na	Na	Na	Na	Na	Na	Na	Na	Na	Na
J	Na	Na	Na	Na	Na	Na	Na	Na	Na	Na	Na	Na	Na	Na	Na	Na	Na	Na	Na	Na	Na	Na	Na	Na	Na
K	Na	Na	Na	Na	Na	Na	Na	Na	Na	Na	Na	Na	Na	Na	Na	Na	Na	Na	Na	Na	Na	Na	Na	Na	Na
L	Na	Na	Na	Na	Na	Na	Na	Na	Na	Na	Na	Na	Na	Na	Na	Na	Na	Na	Na	Na	Na	Na	Na	Na	Na

(a) FRONT DRAWER

	0	1	2	3	4	5	6	7	8	9	10	11	12	13	14	15	16	17	18	19	20	21	22	23	
A	Na	Na	Na	Na	Na	Na	Na	Na	Na	Na	Na	Na	Na	Na	Na	Na	Na	Na	Na	Na	Na	Na	Na	Na	Na
B	Na	Na	Na	Na	Na	Na	Na	Na	Na	Na	Na	Na	Na	Na	Na	Na	Na	Na	Na	Na	Na	Na	Na	Na	Na
C	Na	Na	Na	Na	Na	Na	Na	Na	Na	Na	Na	Na	Na	Na	Na	Na	Na	Na	Na	Na	Na	Na	Na	Na	Na
D	Na	Na	Na	Na	Na	Na	Na	Na	Na	Na	Na	Na	Na	Na	Na	Na	Na	Na	Na	Na	Na	Na	Na	Na	Na
E	Na	Na	Na	Na	Na	Na	Na	Na	Na	Na	Na	Na	Na	Na	Na	Na	Na	Na	Na	Na	Na	Na	Na	Na	Na
F	Na	Na	Na	Na	Na	Na	Na	Na	Na	Na	Na	Na	Na	Na	Na	Na	Na	Na	Na	Na	Na	Na	Na	Na	Na
G	Na	Na	Na	Na	Na	Na	Na	Na	Na	Na	Na	Na	Na	Na	Na	Na	Na	Na	Na	Na	Na	Na	Na	Na	Na
H	Na	Na	Na	Na	Na	Na	Na	Na	Na	Na	Na	Na	Na	Na	Na	Na	Na	Na	Na	Na	Na	Na	Na	Na	Na
I	Na	Na	Na	Na	Na	Na	Na	Na	Na	Na	Na	Na	Na	Na	Na	Na	Na	Na	Na	Na	Na	Na	Na	Na	Na
J	Na	Na	Na	Na	Na	Na	Na	Na	Na	Na	Na	Na	Na	Na	Na	Na	Na	Na	Na	Na	Na	Na	Na	Na	Na
K	Na	Na	Na	Na	Na	Na	Na	Na	Na	Na	Na	Na	Na	Na	Na	Na	Na	Na	Na	Na	Na	Na	Na	Na	Na
L	Na	Na	Na	Na	Na	Na	Na	Na	Na	Na	Na	Na	Na	Na	Na	Na	Na	Na	Na	Na	Na	Na	Na	Na	Na

(b) BACK DRAWER

Fig. I.B.19. Drawers Adjacent to Poison Safety Rod for FTR Half of ZPPR

TABLE I.B.18. As-built Composition for FTR 1 of ZPPR (Loading 17)

Composition by Zone (atoms/b-cm)

Nuclide	Core				Drawer Adjacent to Poison Safety Rod ^d	Axial Reflector	Radial Reflector
	1-column Pu Drawer ^a	2-column Pu Drawer ^b	Cell Average	Movable Fuel Rod ^c			
Pu-239	0.0008491	0.0016983	0.0012737	0.0016983	0.0008491		
Pu-240	0.0001125	0.0002251	0.0001688	0.0002251	0.0001125		
Pu-241	0.0000168	0.0000337	0.0000252	0.0000337	0.0000168		
Pu-242	0.0000017	0.0000035	0.0000026	0.0000035	0.0000017		
U-238	0.0055684	0.0063849	0.0059766	0.0063849	0.0055684		
U-235	0.0000122	0.0000139	0.0000131	0.0000139	0.0000122		
O	0.0150075	0.0154338	0.0152206	0.0157617	0.0150075		
Na	0.0107196	0.0063408	0.0085302	0.0063610	0.0062767	0.0133588	0.0065078
C	0.0021888	0.0010944	0.0010944	0.0032025	0.0021888	0.0000284	0.0001547
Fe	0.0087888	0.0162589	0.0125238	0.0180022	0.0097185	0.0079227	0.0068787
Ni	0.0011636	0.0011636	0.0011631	0.0023373	0.0012671	0.0189744	0.0460037
Cr	0.0025337	0.0025337	0.0025348	0.0051353	0.0027964	0.0022823	0.0019747
Mn	0.0002025	0.0002027	0.0002026	0.0004248	0.0002204	0.0002295	0.0002639
Mo	0.0002322	0.0004475	0.0003398	0.0004567	0.0002355	0.0000161	0.0000154

^aOccupies even-numbered matrix columns.^bOccupies odd-numbered matrix columns (center column is odd-numbered).^cBoth fuel safety and control rods of this composition.^dPoison rod withdrawn during operation.

C. Component Development--LMFBR

1. Sodium Technology Development

a. Engineering Development (J. T. Holmes)

Last Reported: ANL-7518, pp. 30-32 (Nov 1968).

The Sodium Analytical Loop (SAL) has been moved from Building 206 (Reactor Engineering) to Building 205 (Chemical Engineering). The reassembly of SAL is nearing completion. Plans are being made to install, operate, and evaluate a United Nuclear Corporation (UNC) carbon meter and a diffusion-type hydrogen sensor for on-line monitoring of flowing sodium. UNC oxygen meters will also be used in conjunction with these studies.

The possibility of using SAL to develop improved sodium and cover-gas samplers is being assessed. Experimental work on determining impurities in sodium with the electrical-resistivity and oscillating-mode plugging meters has been discontinued. Summary reports of our experience with these meters and with the UNC oxygen cells are being prepared.

2. Reactor Mechanism and Instrumentation

a. Instrumentation Development (T. P. Mulcahey)

(i) Out-of-core Neutron Flux Detection System (G. F. Popper)

Last Reported: ANL-7548, pp. 28-30 (Jan 1969).

(a) Detectors and Cables. A reworked Westinghouse WX-31353-25 cable was tested up to 700°F in air. The cable was described previously (see Progress Report for July 1968, ANL-7478, p. 38) except that improved hermetic seal-connector assemblies have been attached by the manufacturer. Figure I.C.1 shows the temperature variation of the insulation resistance of the cable as compared with its previous performance. Evidently the insulation resistance has greatly improved at all test temperatures; the initially reported low resistance at room temperature was, in fact, caused by lack of a good hermetic seal. After about 60 hr at 700°F, the insulation resistance increased by a decade (to 1.8×10^{10} ohm/ft) and thereafter remained essentially constant. The capacitance of the cable behaved in both magnitude and change with temperature as reported previously.

After about 150 hr (~6.3 days) of operating in air at 700°F, a cable failure occurred in the form of a dielectric breakdown at all voltages above ~1 V. This was observed as large pulse-charge transfers

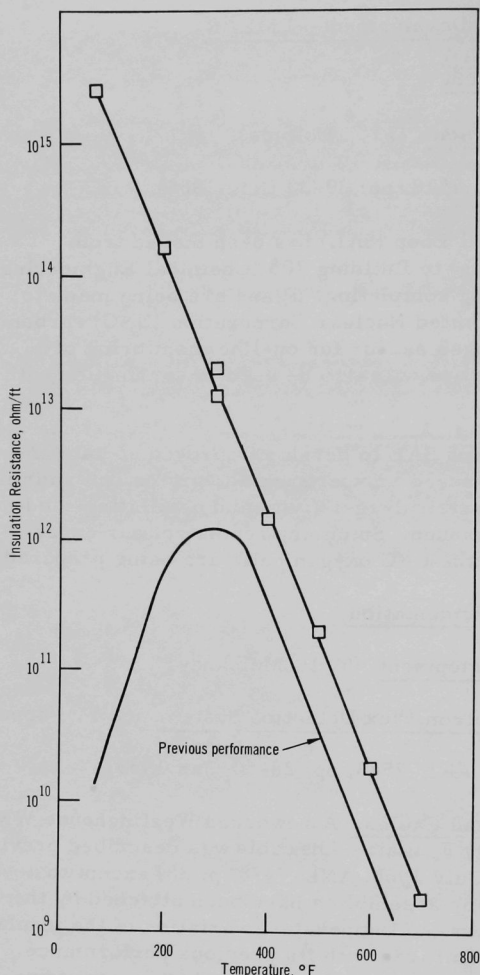


Fig. I.C.1. Changes with Temperature of Insulation Resistance in Westinghouse WX-31353-25 Cable in Air

through the attached charge-sensitive preamplifier. When the cable was cooled to room temperature, it once again held over 500 V dc, but had a much lower room-temperature insulation resistance (4.4×10^{11} ohm/ft). This was indicative of a hermetic-seal failure and appeared to repeat the initial cable results with low insulation resistance and breakdown. Subsequent heating verified the hermetic-seal failure (the insulation resistance improved at higher temperatures); 500 V dc could be kept on the cable up to $\sim 500^\circ\text{F}$. Above this temperature, even after the cable assembly had been vacuum-baked and back-filled with dry nitrogen, only ~ 5 V could be applied before large charge transfers were again noted.

To isolate the failure, the cable assembly was repositioned in the furnace so that only the connector-hermetic seal assembly was heated in dry nitrogen. Again, the breakdown phenomenon occurred at $\sim 500^\circ\text{F}$ and verified that the malfunction was associated with the connector end. Then the connector assembly was removed so that only the hermetic seal remained attached to the cable,

which was heated similarly. Again the breakdown occurred. Finally, the hermetic seal and about 8 in. of cable were removed; ~ 1 ft of cable was reinserted into the furnace and heated to 700°F in dry nitrogen. No breakdown was noted at voltages in excess of 500 V dc. The cable was kept at this temperature for slightly over 170 hr (7 days); it performed adequately. The insulation resistance was found to be very stable and of about the same value as before the initial breakdown.

The hermetic seal was helium-leaktested and found to have large leaks in the vicinity of the metallized and brazed ceramic interfaces. Although the seal was radiographed to determine the cause of the malfunction, little was learned from the radiograph. The seal was sent to the manufacturer for study and possible destructive testing.

A second sample of the Westinghouse WX-31353-25 cable will be tested along with an Electronic Specialty Company (ESC) high-temperature coaxial-cable assembly obtained from Pacific Northwest Laboratory (PNL). The 0.170-in.-dia ESC cable is rated at 1000°F with 1000 V dc applied and has a silica dielectric; the center and outer copper conductors are covered with a stainless steel sheath. The ends of the 9-ft-long cable are hermetically sealed and have HN-type connectors attached.

This recent cable failure, coupled with the previously reported one (see ANL-7548) involving the Bostrad cable used during a high-temperature detector test in the EBR-II 01 thimble, has caused greater emphasis to be placed on cable testing to ensure that a satisfactory high-temperature detector-cable combination will be available. Some temperature-life testing of the completed combinations may be necessary before in-reactor tests are started.

The detector-cable test programs at both Reuter-Stokes and Westinghouse are progressing satisfactorily. Almost all room-temperature tests are complete, including some gamma-flux measurements, and high-temperature tests have been started on some of the compensated ionization chambers.

(b) Circuits. During the recent extended EBR-II shutdown, the Gulf General Atomic (GGA) 10-decade neutron-monitoring system was modified by: (1) reinstalling the detector in the J2 thimble and in a neutron flux that allows the fission-counter chamber to be kept in saturation with 700 V applied at all reactor power levels, (2) replacing the manufacturer-specified shielded twisted pair by a coaxial cable to transmit the detector direct-current output signal from the preamplifier to the linear channel, (3) replacing the 75-ohm coaxial cable by a 93-ohm coaxial cable for transmitting the pulse and average magnitude squared (AMS) signals from the preamplifier to the log level channel, and (4) changing the linear-channel circuit-board components according to manufacturer specifications to permit the channel to accept the larger than expected direct-current signals.

Figure I.C.2 compares the outputs of the GGA system with the output of the EBR-II compensated-ionization-chamber linear channel during a typical reactor restart. Although at first glance the GGA channel appears to be following reactor power level adequately, closer examination of the GGA data reveals that: (1) the log countrate (LCR), log

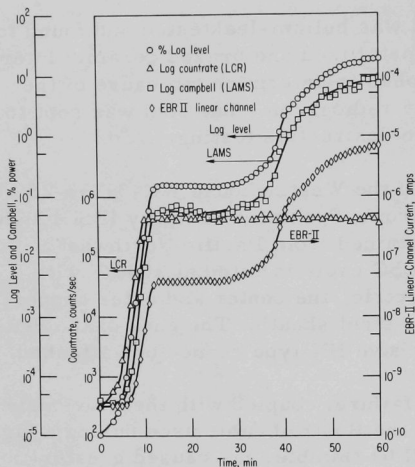


Fig. I.C.2. Comparison of Responses of Gulf General Atomic Channel (with Detector in J2 Thimble) to EBR-II Linear Channel during Typical EBR-II Restart

EBR-II linear channel, but it should be noted that an $\sim 1.7\%$ power zero offset exists in the GGA system.

Only minor alignment adjustments will be necessary to make the log level signal from the GGA system perform adequately. The problem with the recorder outputs might be caused by ground loops between the GGA system, the analog recorders, and the digital data-acquisition system (DDAS) from which all the data are being analyzed. Larger recorder output signals, along with a separation of the analog recorders from the DDAS system, might eliminate the apparently erratic performance and zero-offset problems. This, in turn, could show that adequate signal overlap actually does exist between the LCR and LAMS signals. Corrective actions to eliminate these problems are being taken.

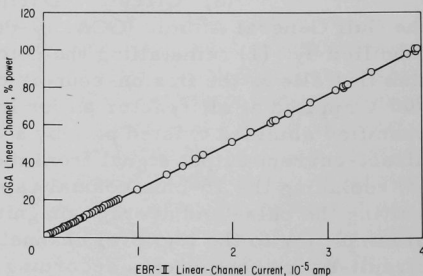


Fig. I.C.3. Comparison of DC Linear-channel Output from Gulf General Atomic System and EBR-II Linear Channel (Corrected for $\sim 1.7\%$ Power Zero Offset in GGA System)

b. FFTF Instrumentation (R. A. Jaross)

(i) In-core Flowmeter Development

Last Reported: ANL-7561, pp. 18-19 (March 1969).

(a) Flow-sensor Feasibility Studies. To simulate an annulus of sodium flowing axially over the probe, a mechanism was constructed to drive a probe-type eddy-current flow sensor in an oscillatory manner within a length of aluminum tubing. The mechanism consists of a 1-rps synchronous-motor drive with an eccentric fastened to its output shaft, a 4-ft connecting rod between eccentric and probe, and a rocker-mounted 12-in. length of 6061T6 aluminum tubing. The eccentric gives a 4- or 8-in. stroke corresponding to 1.047- or 2.094-ft/sec peak velocity, respectively. The aluminum tubing is made of two sleeves (1.5-in. OD x 1-in. ID and 2-in. OD x 1.5-in. ID) that can be used independently or telescoped together.

The flow-sensor assembly (see ANL-7561) has been completely assembled. The secondary is 2128 turns of #34 Formex copper wire located between two primaries, each of 387 turns of #26 Formex copper wire. The space between coils is $1/8$ in. Each coil is $1/2$ in. wide, of $7/16$ -in. ID and approximately $7/8$ -in. OD. Two other secondary coils were made; one is $1/4$ in. wide, of $7/16$ -in. ID and approximately $7/8$ -in. OD, with 1093 turns of #34 Formex copper wire; the other is $1/2$ in. wide, of $11/16$ -in. ID and approximately $7/8$ -in. OD, with 992 turns of the same wire. All coil forms were made from phenolic rod. Overall coil length is approximately $1\frac{3}{4}$ in. The primary and secondary leads to the instrumentation were each a twisted pair; the two pairs were bound together in a metallic braided sheath with the sheath grounded. There is some electrical coupling between the two pairs, necessitating binding the pairs together to prevent error signals due to lead motion.

The tests reported in Table I.C.1 were made with 300-mA rms primary excitation current. An oscilloscope with maximum sensitivity of 5 mV/cm was used to indicate peak-to-peak signal amplitude from the secondary coil. The oscilloscope horizontal sweep was derived from the primary excitation current. Also derived from the same source is a signal that is passed through a variable attenuator and variable phase shifter, and fed in series opposing with the secondary signal to balance out any residual signal in a zero-velocity condition. No measurements of phase angle were made because it is believed to be unimportant for the intended application. However, it was observed that at or very near maximum signal amplitude conditions there was no quadrature component.

TABLE I.C.1. Simulated Probe-type Eddy-current Flow-sensor Test with Aluminum Tubing (6061T6)^a

Frequency, Hz	Peak-to-peak Signal Amplitude, mV							
	With Coil 1/2 in. Wide and 7/16-in. ID				With Coil 1/4 in. Wide and 7/16-in. ID		With Coil 1/2 in. Wide and 11/16-in. ID	
	With 1/8-in. Coil Space		With 1/4-in. Coil Space		With 1/8-in. Coil Space		With 1/8-in. Coil Space	
	With Tube 1 x 1.5 in.	With Tube 1.5 x 2 in.	With Tube 1 x 2 in.	With Tube 1 x 2 in.	With Tube 1 x 2 in.	With Tube 1.5 x 2 in.	With Tube 1 x 2 in.	With Tube 1.5 x 2 in.
30	15	5	18	16	10			
40			22		12			
60	28	8	28	25	14			
80			32	28	16			
100	40	11	34	30	20			
140	46	12	36	30	22			
180	49	12	36	30	24			
190		12						
220	50	12	36	28	24	6	24	8
232	50							
260	50	11	35	26	24			
300	48	10	35	25	24			
350	44	10	32		22			
400	40	9	32	24	22			
500	36	8	32		22			
600	30	7	30	20	21			
800	25	5	28		20			
1000	22	4	25	15	19			
1500	18		20					

^aWith 75°F ambient temperature, 300-mA rms primary excitation current, and 2.094-ft/sec relative peak probe velocity.

Aluminum tubes of various diameters were used to show depth-of-penetration effects. In one test it was observed that with the probe and inner aluminum tubing together sliding within the 2-in.-OD x 1.5-in.-ID aluminum tubing, the signal amplitude was half that without the inner tubing. The 1/4-in.-wide secondary coil shows that even though there are half the turns, and thus the primaries are brought that much closer together, the signal is only down 33% with a 1/2-in.-thick aluminum wall because the radial flux density is greater. However, making the same comparison with 1/4-in.-thick-wall aluminum of 2-in. OD x 1.5-in. ID shows a 50% reduction in signal, probably because the increase in radial flux density is most prominent in the region nearest the coil. Because the signal is down only 33% and the coil outside dimensions are the same as a full secondary, the 1/2-in.-wide 11/16-in.-ID secondary shows that the first few innermost layers contribute considerably less to the signal than the outer layers.

All the motion tests were made with 2.094-ft/sec peak velocity. One test was made with 1.047-ft/sec peak velocity, and the output signal was exactly half that at 2.094-ft/sec peak velocity, indicating a linear relationship between the two, which was expected.

A crude crosstalk test was performed by placing the flow sensor inside the 2-in.-OD x 1-in.-ID aluminum tubing. The full secondary coil (as used in previous tests) was placed at a point of maximum

pickup (at which point its axis was 4 in. from that of the primary and pickup coils). With 300-mA rms primary excitation current, less than 0.5-mV peak-to-peak signal was observed on the oscilloscope from the pickup coil.

Fabrication is underway on a new eddy-current probe that will be drop-tested in hot sodium. The coil form is Inconel; it will be located within a Type 304 stainless steel tube of 1-in. OD and 15/16-in. ID. There will be three primary coils and two secondaries, classed as a four-section probe. The coils will all be wound with #26 ceramic-coated nickel-clad silver wire. There will be approximately 400 turns of wire on each coil, which is about the same as the primary coils of the dry-test probe but only $1/5$ of the secondary. The new probe will have twice as many primary-secondary sections, and the primaries will be excited with three or four times more current, so the sensitivity is expected to be a little more than that of the dry-test probe. Tests will be made at various temperatures above $\sim 300^{\circ}\text{F}$. Velocity is expected to reach 10 to 15 ft/sec. Velocity and signal amplitude will be recorded simultaneously from start to end of drop. The sodium apparatus is being renovated and instrumentation is being selected.

A permanent-magnet probe-type flow sensor was installed in a NaK loop and tested. Representative test data for a dc pump current of 300 A are:

Leads (see Fig. I.C.4)	NaK flow, \sim gpm	Signal, mV	Sensitivity, mV/gpm
-1, +1	1.675	0.312	0.186
-2, +2	1.675	0.625	0.373
-3, +3	1.675	0.5	0.298
-5, +5	1.675	0.275	0.164
-2, +3	1.735	0.695	0.4
-1, +5	1.25	0.745	0.595

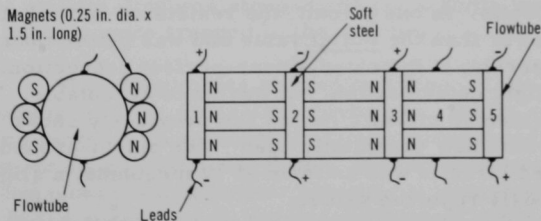


Fig. I.C.4. Configuration of Permanent-magnet Probe-type Flow Sensor Tested in NaK Loop

The ten flow-sensor leads were incorporated in the model for test purposes only; it was intended to use two leads, -1 and +5, in the final design to sense the generated signal and thus to take advantage of the series addition of the voltages produced across the tube. It is believed that the signal voltage between -1 and +5 could be increased appreciably by providing electrical insulation between the magnets and the flowtube and between the magnets and the outer tube.

Because of anticipated difficulties in achieving satisfactory calibration of this type of flow sensor (due to the uncertainty of being able to determine the portion of the coolant-channel flow that would pass through the flow-sensor tube), it was decided to discontinue work on this design in favor of a flow sensor with a solid configuration. Accordingly, two permanent-magnet (Alnico-8) solid-configuration 1-in.-OD flow sensors are being designed and fabricated. These will be drop-tested in a static sodium pot that is being modified for the tests.

(b) Materials Procurement. Bids for ceramic-insulated nickel-coated silver-magnet wire from Physical Sciences Corp. and Secon Metals Corp. have been evaluated. Although neither vendor will furnish wire completely within specifications (ANL-HTI-FFTF-503-4-G, Modified 1/67), wire will be purchased that will meet the immediate needs of the ANL-FFTF in-core flow sensor development program.

(c) Magnet Irradiation Tests. The magnet irradiation capsules are being packaged for shipment to EBR-II. Additional information for hazards evaluation is being prepared.

(ii) Signal Lead Connectors for Sodium Service (A. P. Grunwald)

Last Reported: ANL-7561, pp. 19-21 (March 1969).

The connector assembly was tested in 1000°F argon. The leakage rate through the nipple was satisfactorily small and consistent with previous results. In one circuit, the resistance in the (electrical) connections was lower than the initial value and was better than previous readings in the test series; it indicated a near-perfect connection. Another circuit showed a slight deterioration, but was quite acceptable. The third of the three instrumented circuits (which had previously shown a steep rise in resistance) was now essentially open. The pin-to-ground resistance of all instrumented circuits was uniform at 10 megohms, a slight improvement over previously reported values.

After the unit cooled, it did not unlatch freely as desired; only after rapping the breech lock (lightly) with a mallet did the lock disengage. Although no sodium was involved in this test, the MoS₂ lubricant had changed from its original dark color, and a whitish film was apparent in places.

After the unit was cleaned, the main gasket was reinstalled and lubricated with graphite powder instead of the previously used MoS_2 ; another heating cycle up to 1000°F was made, this time with sodium in the test tank. This run was completely successful in that all components performed well, no sodium leakage was observed, and the breech lock did not show excessive resistance.

A test of nipple-separation pressure was made, and the pressure at which the nipples separate was $\sim 10\%$ higher than previously reported. It is not clear what caused the change; the nipples operated freely and the springs apparently did not lose their preload. The changes in separation and closing pressure might be due to improved sealing of the nipples rather than to any deterioration of the mechanism.

(iii) Failed-fuel Location Method (E. S. Sowa)

Last Reported: ANL-7561, pp. 21-22 (March 1969).

(a) Gas Injection. The initial series of gas-injection experiments were completed in the Fuel Failure Detection Loop. The experiments consisted of six separate injections of krypton-85 gas samples into the sodium at the gas-sampling valve. The injections ranged from 12 to $36.4 \mu\text{Ci}$. Although two experiments aborted because of leakage at the capsule and at the counting chamber, the data from the remaining four experiments were satisfactory.

For the experiments, sodium flow in the loop was brought to 10 ft/sec in the riser flowtube with the loop at temperature (1000°F for Experiments 1 and 2 and 1100°F for the others). Gas circulation and activity counting were maintained continuously on the riser and surge-tank gas systems. The radioactivity was recorded continuously at sampling rates of 1.0 sec at the surge tank and 5.0 sec at the riser. The time of sample injection, the time of initial detection of activity over background, and the time to reach equilibrium were noted. After equilibrium was recorded, the sodium flow was stopped and the activity was monitored further to see if bubbles were trapped in the sodium.

The experiments showed that most of the krypton separated from the sodium into the surge-tank cover gas. While sodium flow was maintained, no increase in radioactivity (over background) was observed in the riser. Krypton found in the riser after sodium flow was stopped is attributed to backup from the orifice exit volume. It took about 90 sec for the radioactivity in the surge tank to reach equilibrium. This is consistent with the transit time, including approximately half of the time required for the krypton to separate from the sodium.

The calibration of the gas-system volume showed that quantitative recovery of 90-100% was obtained, within the limits of the experimental accuracy. Occasionally, subsequent gas releases occurred either during the experiment or on the following day. These releases, added to the quantity recovered, showed total recovery of the krypton sample. This implies that gas holdup in bubbles adhering to system surfaces is the most likely mechanism of retention.

The FFDL has been cooled to room temperature for modifications for the next series of experiments.

A glass system containing water was constructed to simulate the FFDL injection configuration. Visual observation of the gas injected showed that the injected sample fragments into bubbles of <0.1 mm diameter. High-speed photographs will be taken to determine bubble size more accurately.

c. EBR-II In-Core Instrument Test Facility (E. Hutter)

(i) Preliminary Study of Various Concepts (O. S. Seim, T. Sullivan, and J. Pardini)

Last Reported: ANL-7561, pp. 22-23 (March 1969).

(a) Test Thimbles. Evaluation of various concepts of instrument test thimbles is continuing. Preliminary calculations are being made concerning attainable instrument test temperatures. Results so far indicate that the test temperatures and the predicted temperature profile within the thimble depend significantly on the number of instruments and their arrangement within the thimble. A final selection of the cooling method will be made after all calculations have been completed and each concept has been evaluated.

(b) Supporting Facilities. A number of supporting facilities will be required to make the In-core Instrument Test Facility (INCOT) system compatible with the present reactor operating requirements and to provide the system with a reasonably wide range of instrument-testing capability. The main INCOT components which are being considered for installation above the small rotating plug are:

(1) an elevating system to raise the instrument thimble approximately 80 in. above its in-core position, thus permitting normal reactor fuel handling to take place;

(2) a movable gas seal between the instrument thimble and the control-rod penetration in the small rotating plug;

(3) special instrument-handling containers to provide for the insertion and removal of one or more test instruments from the core without removing the test thimble itself;

(4) special shielding devices to facilitate the removal and storage of gamma-active instrument sensors and their leads from the in-core thimble;

(5) provisions for special readout and/or recording equipment and related electrical and gas connections coming from the terminals of the instrument thimble;

(6) a portable or stationary calibration facility to permit the periodic checking of special test instruments removed from the core for calibration.

An important design objective is to install and operate these supporting facilities with a minimum of disassembly and/or rework of existing reactor components.

The installation and the operating and handling requirements of the INCOT system will be influenced significantly by its location in the reactor. A preliminary evaluation of the available locations for the control-rod drive on top of the rotating plug indicates that the No. 2 control-rod opening best meets the requirements. This selection is based on the assumption that the instrumented-subassembly system and the oscillator-rod drive will occupy the No. 6 and No. 8 control-rod locations, respectively. Other considerations that influenced the selection were: the requirement for maintaining a reasonably uniform control-rod spacing in the core, with control rods on both sides of the INCOT installation; space requirements for equipment to handle instruments and sensor leads; shielding devices; and accessibility to off-plug communication leads and service lines.

3. Fuel Handling, Vessels, and Internals--Core Component Test Loop (CCTL) (R. A. Jaross)

Last Reported: ANL-7561, pp. 23-24 (March 1969).

From March 20 to April 17, the CCTL operated for 670.8 hr at 1060°F and 400 gpm; the pump was off for 7.5 min during a pump coast-down and startup test. The cumulative total operating time with the loop at any temperature and the pump on is 5067 hr, of which 3686.9 hr were at 1060°F and 400 gpm.

The pump test was conducted to evaluate the vibration characteristics of the pump. An accelerometer-type sensor and a recorder were

used for acoustical observations during pump coastdown and restart. No unusual noise or vibration was noted.

The flowtest of the FFTF Mark-I subassembly, which had been scheduled to continue until May 1, was terminated April 17. At that time, a sodium leak occurred at a flow-control valve in the 2-in. pipe in the main CCTL purification loop, which includes the cold trap, plugging meter, and sodium-sample station. The leak was minor ($\sim 10 \text{ cm}^3$ of sodium), and damage was limited to the flow-control valve itself. The operators detected the leak by means of the smoke when the sodium reacted with air; the oxidation was insufficient to trip the Pyra-alarm smoke detector within the CCTL enclosure. The precise nature of the valve leakage is being investigated.

The FFTF subassembly was removed from the test vessel April 22. The subassembly internals were flushed with Dowanol-EB, then rinsed with ethyl alcohol and dried in air. Very little heat or hydrogen was generated during the sodium-removal operations. There was very little sodium residue on the outer surface of the subassembly after it was removed from the CCTL test vessel. The subassembly was shipped to Battelle Northwest Laboratory on April 25.

a. Material-property Measurements

The ultimate strength of 3/16-in.-OD austenitic stainless steel cable (individual-strand diameter was 0.011 in.) used to hold the FFTF subassembly during insertion and removal from the CCTL test vessel was measured. The cables had been exposed in sodium vapor under no load during the entire 5067 hr of CCTL operation.

In the first tensile test, the cable fractured in the center of the length tested at about 50% of its rated load capacity. In the second tensile test, failure occurred at the mechanical joint (cable clamp) at a load of 100 lb. In the third test, half of the cable used in the second test was re-tested; one end was gripped by the cable eye and the other end was gripped by the jaws of the tensile machine. The cable failed at a load of 1625 lb. The tensile strength of the unexposed as-received cable was 2750 lb (the unexposed cable was tested with both ends clamped with the V jaws of the tensile machines). Samples of sodium-exposed cable are being investigated more completely to determine the nature of the weakening.

Fortunately, although the weakening of the cable had not been anticipated, precautions were taken during subassembly removal to keep the load on the four parallel cables below 1200 lb total.

D. EBR-II

1. Research and Development

a. Reactor Experimental Support--Reactor Analysis and Testing (R. R. Smith)

(i) Operational Data Analysis

Last Reported: ANL-7500, pp. 42-44 (Sept 1968).

(a) EBR-II System Heat Balance and Thermocouple Test at 580°F (J. F. Koenig)

A test of the plant system was performed to determine the precision of the installed temperature sensors in the primary and secondary sodium systems. During the extended shutdown of this year, the secondary-sodium resistance thermometers associated with the intermediate heat exchanger were removed and calibrated at the ice point and boiling point of water. A resistance thermometer whose calibration was traceable to the National Bureau of Standards was used as the reference. Assuming that the corrections at 32 and 200°F are applicable at higher temperatures, the resistance thermometer at the inlet (R2-RT-508B) will read high by 0.3°F while the thermometer at the outlet (R2-RT-508A) will read high by 0.8°F. The inlet thermometer was chosen as the system reference because it had metal heat-transfer fins between the thermometer and the thermowell, which would minimize the in-place measurement error. Test-condition limitations, however, did not guarantee a high degree of accuracy; thermowell errors and recording errors could have been present. Nevertheless, for evaluation of heat balance and system performance, precision temperature measurements are more important than absolute accuracy. The intercomparison of temperature-sensor outputs obtained near operating conditions will give the degree of precision of the sensors and recorder.

The test was conducted with both the primary and secondary sodium systems at 580°F. The primary flow was 9000 gpm and the secondary flow 4460 gpm. The steam system was in the heatup condition with the stop valve closed, the evaporators full of water, and the superheaters containing steam and some condensate. The power to the primary-tank heater was adjusted until stable temperatures were obtained for 2 hr in the primary and secondary sodium systems and steam system. After isothermal conditions had been verified, heat-balance data and the output of the system thermocouples were recorded. All temperatures were recorded on their normal instruments. Outputs from the resistance thermometers, however, were read on a double Wheatstone bridge.

The heat balance for the primary system is given in Table I.D.1. A 10% heat loss was assumed for the primary-pump motors,

which are 90-94% efficient. The thimble cooling loss, 30 kW, was estimated from 700°F data because the outlet temperatures were not recorded. The net heat output of the primary system, 27 kW, was assumed to be transferred to the secondary system.

The heat balance for the secondary system is shown in Table I.D.2. The insulation losses were calculated from the ambient air conditions and the insulation thickness on the main piping. The total piping heat loss would be greater if all the drain lines, the storage tank, etc., were considered. The heat load of the pump-cooling water was determined in a separate test while the secondary pump was operating under similar conditions.

TABLE I.D.1. Primary-system Heat Balance
at 580°F

	kW
Heat Input	
Primary pump No. 1	105
Primary pump No. 2	105
Auxiliary pump	12
Tank heaters	6
Fuel-subassembly Decay Heat	35
Total	263
Heat Loss	
Shield cooling	135
Shutdown cooler No. 1	39
Shutdown cooler No. 2	32
Thimble cooling A	15
Thimble cooling B	15
Total	236
Net Heat to Secondary System	27

TABLE I.D.2. Secondary-system Heat
Balance at 580°F

	kW
Heat Input	
Secondary pump	161
Induction heaters	229
Resistance heaters	49
Surge-tank heaters	0
Primary system	27
Total	466
Heat Loss	
Insulation loss (main path)	188
Pump-cooling water	37
Purification	22
Total	247
Net Heat	219

The fluid temperatures were corrected to account for the heat additions and heat transfer. If 27 kW of heat were transferred by the intermediate heat exchanger while the secondary inlet resistance thermometer is at 581.9°F (corrected), the exchanger rate and heat-balance equations indicate that the primary inlet temperature would be 582.1°F, primary outlet 582.0°F, and secondary outlet 582.1°F. The last temperature may be compared to its resistance-thermometer reading of 581.0°F (corrected), which, considering that the thermometer does not have heat-transfer fins, is surprisingly close to the reference temperature. The calculated temperature rise in the reactor due to the 35 kW of decay heat was 0.1°F, whereas the temperature rise across the pumps due to 210 kW of power input was 0.6°F. Thus, the primary inlet to the pump would be at 581.4°F.

In the secondary system, the calculated heat loss in the main flow path nearly equaled the measured input of electrical power. Therefore, the induction- and resistance-heating inputs were assumed to

be offset by the insulation heat loss. The net rise in sodium temperature was 0.7°F through the pump and 0.2°F through the intermediate heat exchanger. This heat was assumed to be dissipated in the evaporators. The system temperatures as read on the automatic data logger are shown in Table I.D.3, along with reference temperatures and readout errors at operating temperatures.

TABLE I.D.3. Comparison of System Temperatures and Sensor Temperatures with Reference Temperatures

Location	Sensor Readout by ADL ^a	Sensor Temperature (°F)	Reference Temperature (°F)	Error (°F)	Readout Error at Higher Temperature (°F)	Expected Error at Operating Conditions (°F)
Primary System						
Pump inlet	A46	583.8	581.4	2.4	-0.4	2.0
Reactor outlet	A9	581.8	582.1	-0.3	2.2	1.9
HX ^b in	C-1	585.5	582.1	3.4	-	-
Secondary System						
HX ^b in	508B	582.2	581.9	0.3	(From Calibration)	
	B-5	585.4	581.9	3.5	-	3.5
HX ^b out	508A	581.7	582.1	-0.4	-	-
	B-6	583.8	582.1	1.7	2.0	3.7
Superheater, in	B-2	582.2	582.1	0.1	2.1	2.2
Superheater, 710 out	B-13	583.8	582.1	1.7	2.0	3.7
712 out	B-15	585.8	582.1	3.7	2.0	5.7
mixed out	B-3	583.4	582.1	1.3	1.0	2.3
Evaporator, 701 out	B-16	582.8	581.2	1.6	-	-
703 out	B-18	582.8	581.2	1.6	-	-
705 out	B-20	582.8	581.2	1.6	-	-
707 out	B-22	582.8	581.2	1.6	-	-
mixed out	B-4	579.8	581.2	-1.4	-	-
702 out	B-17	582.8	581.2	1.6	-	-
704 out	B-19	582.4	581.2	1.2	-	-
706 out	B-21	582.8	581.2	1.6	-	-
708 out	B-23	582.8	581.2	1.6	-	-
mixed out	B-5	579.8	581.2	-1.4	-	-

^aADL = automatic data logger.

^bHX = intermediate heat exchanger.

(b) EBR-II Heat-balance Measurements at 50 MWt
(W. R. Wallin)

Heat inputs and losses determined from heat-balance measurements made at 50 MWt on March 26, 1969, are summarized in Table I.D.4. The temperatures used in these studies were corrected in accordance with the results of calibration tests discussed in the preceding section. With the exception of secondary sodium flow, the values for flow rates were those indicated by operating instruments that had been calibrated in accordance with normal operating procedures.

During the January-February reactor maintenance shutdown, the secondary-sodium flowmeter, which uses a Foster flow tube and differential-pressure (dp) cell, was repaired and the dp cell was recalibrated. Using this flowmeter as the standard, the electromagnetic (EM) flowmeter was recalibrated.

Primary flow was measured by an outlet total flowmeter or by four inlet flowmeters. The four inlet flows were used to

obtain the reactor heat shown in Table I.D.4; use of total outlet flow gives a value for reactor heat that is about 4% higher.

TABLE I.D.4. Results of EBR-II Heat
Balance of March 26, 1969

	kW
Primary System	
Heat input	
Reactor heat	48,000
Tank heaters	6
Auxiliary pump	12
Primary pump No. 1	98
Primary pump No. 2	95
Heat loss	
Shutdown cooler No. 1	51
Shutdown cooler No. 2	50
Shield cooling	164
Thimble cooling A	21
Thimble cooling B	20
Purification	0
Net heat (to secondary sodium)	47,900
Secondary System	
Heat input	
From intermediate heat exchanger	47,300
Surge-tank heaters	0
Induction heaters	135
Resistance heaters	48
Secondary pump	185
Heat loss	
Pipe loss (main path), calculated	188
Pump-cooling water	37
Purification	15
Recirculation	36
Net heat (to steam)	47,400
Steam System	
Net heat from secondary sodium (feedwater flow less blowdown flow)	47,900
Heat loss (feedwater TC to superheat-steam TC)	140
Net heat to turbine and auxiliaries	47,800

Steam-system flow was measured by the outlet superheated-steam flowmeter or by feedwater inlet flow minus blowdown flow. Inlet flow minus blowdown flow was used to calculate the values for heat output of the steam system shown in Table I.D.4; use of steam-flow values gives a value about 10% lower.

The net heats transferred from primary to secondary sodium, from secondary sodium to steam, and from steam to the turbine-generator system agree within 1%.

(c) Studies of Instrument Probe (W. R. Wallin)

The primary purpose of the fabrication and installation of the instrument probe was to provide an installed spare for the detectors for measuring the outlet temperature and upper-plenum pressure of the reactor. The orientation of the probe with respect to the reactor and the upper coolant plenum is illustrated in Fig. I.D.1. Radially, the probe is located above grid position 14D6. The attached thermocouples are numbered such that thermocouple No. 1 is located at the bottom of the probe and No. 8 at the top.

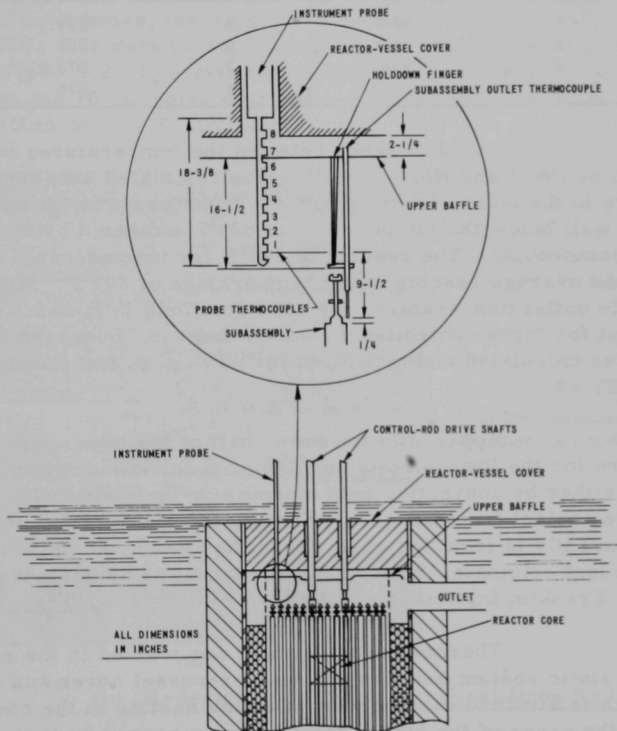


Fig. I.D.1. Schematic Diagram of a Portion of the EBR-II Inner Tank Assembly, Showing Position of Instrument Probe and Its Thermocouples

Seven of the eight thermocouples have been functioning satisfactorily since their installation at the start of Run 33 in February 1969. Thermocouple No. 4, however, malfunctioned immediately after its installation.

Typical temperatures indicated by the seven functional thermocouples during 50-MWt operation on March 10, 1969, are given in Table I.D.5. Whenever the power level is reduced to zero, the temperatures of all functional thermocouples return to approximately 700°F. The variation in indicated temperature has been shown to vary linearly with respect to power.

TABLE I.D.5. Temperatures of Upper Coolant Plenum in EBR-II

Thermocouple No.	Temperature (°F)	Thermocouple No.	Temperature (°F)
1	829	5	858.5
2	837	6	860
3	844	7	873.5
4	-	8	875

The difference between the temperatures indicated by thermocouples No. 1 and No. 8 is 46°F. The calculated subassembly outlet temperature in the outer blanket (over which the probe is located) is 700-710°F, well below the temperature of 829°F indicated by the No. 1 (lowest) thermocouple. The reading of 844°F for thermocouple No. 3 is closest to the average reactor outlet temperature of 847°F. Measured subassembly outlet temperatures for core positions 1, 2, and 3 were below 850°F except for three controlled-flow experiments. Subassembly outlet temperatures calculated and measured for Rows 4, 5, and 6 range from 850 to 899°F.

Apparently the lower half of the upper plenum provides the flow area for the low-velocity and cooler outer-blanket flow. The coolant is warmed either by convective heat transfer or by mixing with higher-temperature coolant from the core. Flow in the upper half of the upper plenum apparently is from the core where the higher-temperature and higher-velocity coolant originate. Such an interpretation is consistent with the results of the Franklin Institute flow studies.

Thermocouples 7 and 8 are located in the region of essentially static sodium between the reactor-vessel cover and the upper baffle, which is attached to the cover. Gamma heating in the cover and baffle may be the cause of the higher temperatures sensed by these thermocouples. Temperatures of coolant from Rows 4, 5, and 6 are similar to those read on thermocouples 7 and 8. To reach thermocouples 7 and 8, sodium would have to flow up through the clearance openings around the control-rod drive shafts and through a clearance gap of about 1/16 in. between the cover and the baffle. This explanation, however, is believed to be improbable because of the existing pressure gradients.

(ii) Nuclear Analysis and Safety

Last Reported: ANL-7561, pp. 25-26 (March 1969).

(a) Prototype Reactivity-monitoring Meter
(J. R. Karvinen)

Power variations resulting from rod drops at 500 kW, 27.5 MWt and 54% flow, and 50 MWt and 100% flow were monitored with the prototype reactivity-monitoring meter during Run 34. The results of these studies, under the above conditions, are illustrated in Fig. I.D.2. To illustrate the 10-Hz noise, the signal obtained at 500 kW has been amplified by a factor of 10. The data incorporating this amplification, shown as the lower trace of Fig. I.D.2, illustrate the sensitivity of the meter. As indicated in the figure, the 10-Hz noise disappeared in Run 34B and, accordingly, is missing in the Run-34B 22.5-MWt data.

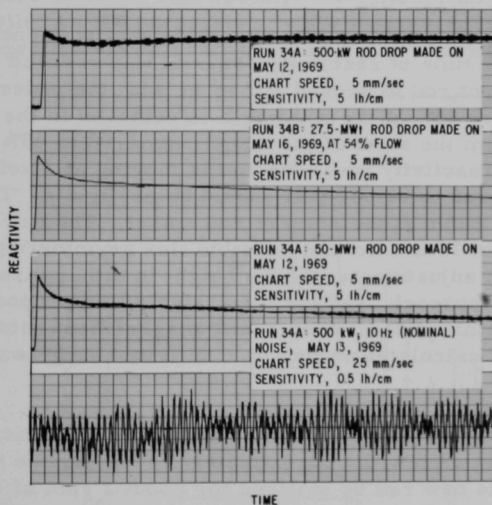


Fig. I.D.2

Data from Evaluation of Prototype
Reactivity-monitoring Meter

(b) Redesign of the Stainless Steel Drop Rod (J. K. Long)

By modifying the design of the existing stainless steel drop rod to bring about the removal of reactivity in a shorter time, the analysis of the feedback function could be extended to permit evaluation of the effects of shorter time constants. The rod accelerates rather slowly during the early portion of its travel and decelerates rather rapidly at the end of its trend.

The stainless steel portions of the rod were modified so that very little reactivity change takes place during the low-velocity

portions of the rod movement and the greater portion of reactivity change takes place while the rod is moving at high speeds. The reactor portion of the rod was modified by shortening the stainless steel rod bundle and inserting an additional block of stainless steel having the same smear density as the rod bundle. Because an unwieldy number of combinations of lengths of materials and gaps is possible in defining the geometry of the lower adapter, rod bundle, steel block, and steel follower, a computer program was written to sort out the numerous combinations and select those which seem to indicate promise for satisfying criteria for reactivity removal. The criteria require that a very small fraction of the reactivity be removed during the first 2 in. of rod travel and that a substantial tail at the end of rod travel be left with essentially no reactivity removal, the bulk of the removal taking place during the central portion of the travel. It was also required that the rod not add any significant amount of reactivity in any part of its travel. The pattern of worth of substituting stainless steel for sodium was taken from ZPR-3 critical-experiment data.*

After surveying many possible configurations, one was selected in which the effective time of reactivity removal was reduced from about 250 msec with the present rod to around 100 msec with the redesigned rod. With the proposed design, 96% of the rod worth is removed in the period between 108 and 208 msec from the start of the drop, compared to 48% with the present rod. Changes in reactivity while the rod is moving at a velocity of less than 3 ft/sec are reduced to values that should be negligible. There is a negligibly small positive pulse at the start of rod travel. The new rod is designed to be dropped from 13 in., so that possible flux asymmetries may be corrected by making small adjustments in drop height in either direction. When the same calculational approach used for the design of the proposed rod was applied to the present stainless steel drop rod, the agreement between experimentally measured and calculated values of reactivity change was within approximately 10%.

The new rod will generate 10 kW of gamma heating at 50 MWt reactor power as compared with approximately 13 kW for the present design. It is proposed that the new rod be orificed for about 2 gpm of internal sodium flow to make it subject to less overcooling than the present rod, which is cooled by a flow ranging from 10.5 to 12.5 gpm.

Scram time of the rod will not be increased by the introduction of a smaller orifice. Total pressure through the rod will be the same regardless of the orifice size. While the rod is in motion, the vertical velocity of sodium within the rod will be reduced because of the motion of the rod orifice. If the orifice were completely blocked during the interval of rod motion, a column of sodium would be moved downward with the rod. The length of this column of sodium extends from the lower plenum to the upper

*Idaho Division Summary Report: July, August, September 1960, ANL-6301.

outlet of the rod, and the column weighs less than 10 lb. The additional inertial effect of this sodium would not be significant compared to the mass of the rod itself. Therefore, the scram time will not be significantly affected by orificing.

(c) Slumped Aerojet Fuel (J. R. Trinko)

Diameter and length measurements were made in the Fuel Cycle Facility of a fuel pin fabricated by Aerojet General Corp. that had slumped during irradiation in Subassembly C2170. These data, together with a measurement of balance point of the fuel pin, were used to compare the fuel density in the lower portion of the pin with the density in upper portion. Analysis yielded

$$\rho_{\text{bottom}} = (0.992 \pm 0.010)\rho_{\text{top}},$$

where ρ is the fuel density. The uncertainty in the calculation was controlled by the uncertainty in the location of the balance point. Figure I.D.3 shows the diameter measurements as a function of axial position; it also

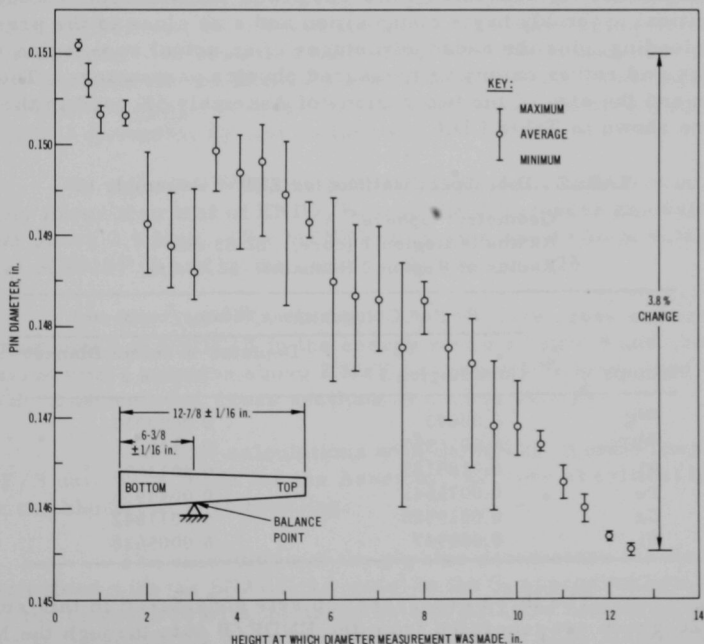


Fig. I.D.3. Diameter of Aerojet-made Fuel Pin as a Function of Position along Length of Pin

shows the location of the balance point. It can be seen that the cross-sectional area of the pin is about 7.6% greater at the bottom than at the top. The density calculation above is accurate to about 1%. Therefore, the diametric swelling is not due to foaming, but is probably due to net motion of fuel from the top of the pin to the bottom.

The reactivity insertion due to slumping was calculated to be 5.2 ± 0.5 lh. The calculation was based on the diameter and length measurements and on measured distributions of ^{235}U worth in ZPR-3.*

b. Nuclear Analysis Methods Development

Last Reported: ANL-7561, pp. 26-28 (March 1969).

(i) Intercomparison of Some Cross-section Sets for ZPR-3 Assembly 6F (B. R. Sehgal)

A detailed comparison of the results of calculations for ZPR-3 Assembly 6F with three different cross-section sets has been made. This critical assembly has a composition and size close to the present EBR-II loading, plus the added advantages of an actual two-region spherical geometry and rather extensive measured physics parameters. The composition and the size of the two regions of Assembly 6F used in the calculations are shown in Table I.D.6.

TABLE I.D.6. Specifications for ZPR-3 Assembly 6F

Geometry: Sphere		
Radius of Region 1 (core): 22.83 cm		
Radius of Region 2 (blanket): 52.83 cm		
Isotope	Region Compositions (atoms/barn-cm)	
	Core Region 1	Depleted-uranium Blanket Region 2
^{235}U	0.00673	0.0000913
^{238}U	0.0076957	0.0400656
Al	0.0189185	0.0013676
Fe	0.0075645	0.0044956
Cr	0.0019926	0.0011842
Ni	0.000947	0.0005628

The three cross-section sets considered in this study are: (1) the 26-group set generated from the ENDF/B data through the MC² code** for the Assembly-6F core and blanket materials; (2) the 26-group set

* Idaho Division Summary Report: July, August, September 1960, ANL-6301, p. 65.

** Toppel, B. J., Rago, A. L., and O'Shea, D. M., MC², A Code to Calculate Multigroup Cross Sections. ANL-7318 (1967).

generated as in (1), but incorporating Pitterle's modifications to the ENDF/B data (designated as MENDF/B);* and (3) the 22-group Set 238 generated by Madell** from the older cross-section data contributing to the Argonne Set 224, but using the MC²-generated spectra for an EBR-II core and blanket.

In the following presentation we shall designate these sets as: (1) the ENDF/B set, (2) the MENDF/B set of Pitterle, and (3) the 238 set. The last set has been used extensively in analysis calculations for the various configurations of EBR-II reactor runs.

Chronologically, Set 238 precedes and the MENDF/B set follows the ENDF/B set. It is evident from the above description of these sets that the ultrafine group spectra (in the MC² calculation) used for generating the cross-section sets are quite similar. The main differences in these sets are due to the differences in the parent-point cross-section data.

It is difficult to list the differences between the cross sections feeding into Set 238 and Set ENDF/B because documentation of the former is not available. Perhaps the major difference between the cross sections is in the substantially lower (≈ 7 to 20%) inelastic cross section for ²³⁸U in Set 238 between 40 keV and 2.2 MeV. The other cross sections are not far removed from those in the ENDF/B set. The differences between the cross sections for the ENDF/B and MENDF/B Data Files have been listed by Pitterle et al. Briefly, the more important differences pertinent to the ZPR-3 Assembly 6F are as follows:

(1) For ²³⁵U, the MENDF/B fission cross section is considerably lower than that of ENDF/B, with the differences amounting to ≈ 10 -15% above 2.5 MeV. The MENDF/B fission spectrum is notably harder than that of ENDF/B and is the same as that for Set 238.

(2) For ²³⁸U, the MENDF/B capture cross sections are lower than those of ENDF/B in the energy regions below 8 and above 50 keV. The fission cross sections above 2 MeV are about 10% lower than those in ENDF/B. The inelastic cross sections are lower by $\approx 5\%$.

The MC² calculations with the ENDF/B and Pitterle's MENDF/B data were made for the Assembly-6F core at critical buckling and for the blanket at zero buckling.

The calculation of the physics parameters for Assembly 6F was performed with the SNARG-1D code[†] in the S₈ approximation. The results of the calculation with the three sets of data are compared in Tables I.D.7 through I.D.9 and Figs. I.D.4 through I.D.6. Table I.D.7 shows

* Pitterle, T. A., Page, E. M., and Yamamoto, M., Analysis of Sodium Reactivity Measurements: Volume I: Cross Section Evaluation and Testing, APDA-216 (1968).

** Madell, J. T., A New Multigroup Cross Section Set for EBR-II Analysis, memo to P. Persiani, January 25, 1968.

† Duffy, G. J., et al., SNARG-1D, A One-dimensional Discrete Ordinate Transport Theory Program for the CDC-3600, ANL-7221 (1968).

the k_{eff} calculated with the three sets using the input geometry and composition shown in Table I.D.6. It may be seen that the 238 and MENDF/B sets are, respectively, $\approx 0.7\%$ under-reactive and $\approx 0.2\%$ over-reactive with respect to the ENDF/B set. In this context, it should be pointed out that the effect of cell heterogeneity increases k_{eff} by $\approx 0.6\%$. The adjusted values are shown in Table I.D.7. They should be compared with the experimental value of 1.0 for k_{eff} .

Table I.D.8 compares the central ^{238}U fission/ ^{235}U fission and the ^{238}U capture/ ^{235}U fission ratios calculated with the three cross-section sets with the measured values. The central fission ratio calculated with Set 238 is about the same as that calculated with ENDF/B and $\approx 3\%$ higher than the measured value. However, the central fission ratio calculated with the MENDF/B set is $\approx 4\%$ higher than that calculated with the ENDF/B set and 7% higher than the measured value. The ^{238}U capture/ ^{235}U fission ratio calculated with Sets 238 and MENDF/B agree with the experiment* but are $\approx 6\%$ lower than the value calculated with the ENDF/B set.

TABLE I.D.7. Results of Reactivity Calculations for ZPR-3 Assembly 6F

(Measured $k_{eff} = 1.0$)

Cross-section Set	k_{eff} for Homogeneous System	Adjusted k_{eff} for Heterogeneous System	% Difference from Experiment
ENDF/B	1.00262	1.00884	0.88
238	0.99532	1.00154	0.15
MENDF/B	1.005065	1.01129	1.13

TABLE I.D.8. Fission and Capture Ratios for ZPR-3 Assembly 6F

(Measured central ^{238}U fission/ ^{235}U fission ratio = 0.069 ± 0.003 ;
Measured central ^{238}U capture/ ^{235}U fission ratio = 0.103 ± 0.002)

Cross-section Set	Calculated ^{238}U Fission/ ^{235}U Fission	% Difference from Experiment	Calculated ^{238}U Capture/ ^{235}U Fission	% Difference from Experiment
ENDF/B	0.071	2.9	0.109	5.8
238	0.071	2.9	0.103	0.0
MENDF/B	0.074	7.2	0.103	0.0

TABLE I.D.9. Rossi Alpha for ZPR-3 Assembly 6F

(Measured Rossi $\alpha = (0.94 \pm 0.03) \times 10^5$;
 ^{238}U $\beta = 0.0148$; ^{235}U $\beta = 0.00641$)

Cross-section Set	Calculated Rossi α ($\times 10^{-5}$)	% Difference from Experiment	Calculated β_{eff} ($\times 10^3$)	Calculated Prompt Lifetime (10^{-8} sec)
ENDF/B	0.9965	6.01	7.006	7.03
238	1.011	7.55	6.995	6.92
MENDF/B	0.9982	6.19	7.063	7.076

* Meneghetti, D., and White, J. R., Calculations of ZPR-3 Fast Assemblies Using a 26-group Aronne Cross-section Set, ANL-7133 (January 1966).

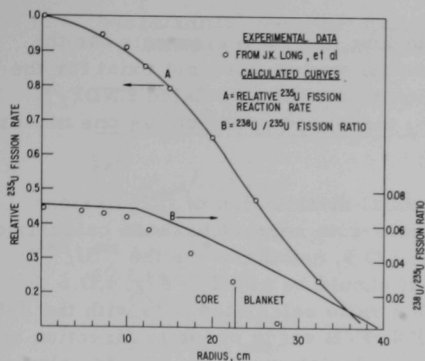


Fig. I.D.4. Comparison of Results of Calculations with Measurements for ZPR-3 Assembly 6F

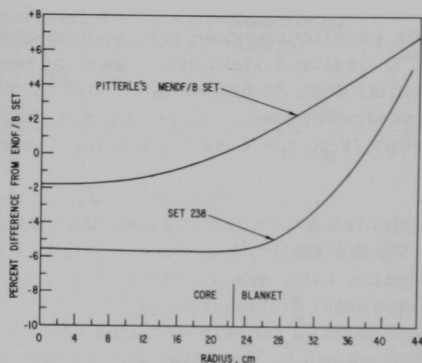


Fig. I.D.5. ^{235}U Fission Reaction Rate for ZPR-3 Assembly 6F

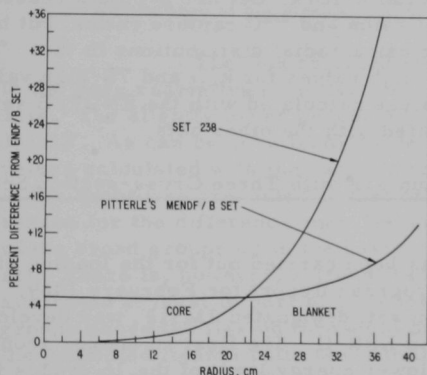


Fig. I.D.6
 $^{238}\text{U}/^{235}\text{U}$ Fission Ratio for ZPR-3 Assembly 6F

The calculated values of the Rossi $\alpha \equiv \beta_{\text{eff}}/\ell_p$ (where ℓ_p is the prompt-neutron lifetime and β_{eff} is the effective delayed-neutron fraction for an assembly) are presented in Table I.D.9. These calculations were also done with the SNARG-1D code, utilizing both the delayed-neutron fractions for ^{235}U and ^{238}U shown in the table and the spectra from Keepin.* The results show that there is little variation in the Rossi α computed with the three cross-section sets. However, these values differ from the measured value by about 6 to 7%, thus implying that the calculated spectra may be too hard.

The radial distributions of the ^{235}U fission reaction rate and the $^{238}\text{U}/^{235}\text{U}$ fission ratio calculated with the ENDF/B set are compared in Fig. I.D.4 with the measured data of Long et al.** It is surprising to see

*Keepin, G. R., Physics of Nuclear Kinetics, Addison-Wesley Publishing Co., Inc., Reading, Mass. (1956).

**Long, J. K., et al., "Fast Neutron Power Reactor Studies with ZPR-III," Proceedings of the Second Geneva Conference 12, p. 119 (1958).

the excellent agreement between calculations and measurements for the ^{235}U fission distribution. Such agreement, however, does not exist for the radial distribution of the $^{238}\text{U}/^{235}\text{U}$ fission ratio; the calculated ENDF/B spectrum appears to get harder than the measured spectrum as one moves away from the core toward the blanket.

The deviations of the radial distribution of ^{235}U fissions calculated with the 238 and MENDF/B sets with respect to those calculated with the ENDF/B set are plotted in Fig. I.D.5, and those for the $^{238}\text{U}/^{235}\text{U}$ fission ratio are plotted in Fig. I.D.6. It should be noted in Fig. I.D.6 that the radial distribution of $^{238}\text{U}/^{235}\text{U}$ fission ratio calculated both with the 238 and MENDF/B sets deviates from the ENDF/B set in opposite direction to that shown by the experiments and that the deviations in the values calculated with the 238 set are quite large.

In summary, it is clear that no set predicts all of the measurements within the quoted experimental errors. Set 238 predicts reasonably good values for k_{eff} and the ^{238}U fission and ^{238}U capture ratios, but has large discrepancies for ^{235}U and ^{238}U fission radial distributions in the blanket. The MENDF/B set gives 1%-high values for k_{eff} and 7%-high values for the $^{238}\text{U}/^{235}\text{U}$ fission ratio. The values calculated with the ENDF/B set fall in the middle of the values calculated with the other sets.

(ii) Analysis of EBR-II Run 31F with Three Cross-section Sets
(J. T. Madell)

Extensive analysis has been carried out for the loading of EBR-II Run 31F. As reported (see Progress Report for February 1969, ANL-7553, p. 36), a new cross-section set, designated JM31F, was developed to analyze the high-energy reactions in EBR-II. The first 16 energy groups have a lethargy width of $1/8$, and the lower energy limit of the 16 groups is 1.35 MeV. Not only is the energy structure of JM31F different from that of the other two sets, but the set was developed from a different library of basic neutron data. The library used for JM31F was the most recent edition of ENDF/B, whereas Set 238 used an old edition of an MC² library tape and Set 23806 is a collapsed version of 238, and thus was not produced from the MC² code directly.

Flux-convergence problems were run using the DIF-2D code in the ARC system,* and three cross-section sets JM31F, 238, and 23806. A compilation of some of the quantities of interest obtained from the three calculations is given in Table I.D.10.

*The Argonne Reactor Computation (ARC System), edited by B. J. Toppel, ANL-7332 (Nov 1967).

TABLE I.D.10. Neutronic Quantities Obtained from Two-dimensional Diffusion Calculation of EBR-II Run 31F with Cross-section Sets JM31F, 238, and 23806

Quantity	JM31F	238	23806
k_{eff}	1.002	1.000	0.998
$\phi \times 10^3, n/cm^2 \cdot sec^a$			
Center	1.63	1.59	1.59
Radial core edge	0.970	0.948	0.950
Axial core edge	1.175	1.139	1.141
$\phi(>0.83 \text{ MeV}), \%$			
Center	29	30	30
Radial core edge	24	25	26
Axial core edge	24	25	25
$^{238}\text{U}/^{235}\text{U}$ Fission Ratio			
Center	0.0607	0.0639	0.0650
Radial core edge	0.0498	0.0533	0.0545
Axial core edge	0.0469	0.0480	0.0504

^aNormalized to one fission/sec in the reactor.

The flux obtained using Set JM31F is consistently higher in the core region than the flux obtained with the other two cross-section sets. The slightly lower percentage of flux above 0.82 MeV is predicted by JM31F. As can be seen from Table I.D.10, however, the difference in the values calculated with the various sets is only 1%. The largest differences in the quantities presented is that of the fission ratio of ^{238}U to ^{235}U . The reason for the difference may lie in the difference of the energy structure of the broad groups or in the basic cross-section data used to generate the set. There is, however, a trend that suggests that the differences may be attributed at least in part to the energy structure. As the number of broad groups above the fission threshold of ^{238}U (approximately 1 MeV) decreases, the predicted fission ratio tends to increase. There are 17 broad groups above 1 MeV in Set JM31F whereas there are only 3 and 2 in Sets 238 and 23806, respectively.

(iii) Effects of Resonance Scattering on Spatial Energy Variations of Flux for Nickel- and Steel-reflected EBR-II-type Cores (D. Meneghetti and K. E. Phillips)

Spatially dependent, fine-energy-detailed neutron-flux spectra for an EBR-II-type core radially reflected by nickel-rich and by steel-rich reflectors have been calculated as part of a study of the effects of resonance scattering in the region about the interface of the core and the reflector.

The spectra, obtained by using 371 equal-lethargy energy groups in the energy range from 2.1 keV to 1.35 MeV, were calculated

by use of the composite of the ELMOE library of angular scattering data* and the Argonne discrete S_N transport code. The S_2 analysis, based on cylindrical geometry, was an inhomogeneous calculation and used the transport approximation. The analysis used 86 mesh intervals, with a mesh density that was greater near interfaces. The inhomogeneous calculation utilized an estimated spatially distributed fission source in the core to circumvent the computational time needed for source iteration. By use of fine-energy leakage absorptions, axial-leakage effects were also taken approximately into account.

In these calculations, an approximate core composition of EBR-II was radially surrounded by 25 cm of either nickel-rich or stainless steel-rich reflector followed by essentially a 10-cm-thick depleted-uranium blanket. The 25-cm-thick reflector consisted of two regions, one 10 cm and the other 15 cm thick, with the inner region containing a higher sodium content. In the case of the nickel-rich reflector, the approximate atomic densities for the two regions, respectively, in units of 10^{24} atoms/cm³, are: (1) sodium, 0.003; nickel, 0.073; and stainless steel, 0.006; and (2) sodium, 0.0016; and nickel, 0.085. For the stainless steel-reflected case, the approximate atomic densities for the two regions are: (1) sodium, 0.003; and stainless steel, 0.074; and (2) sodium, 0.0016; and stainless steel, 0.080.

The spectra at various spatial positions are shown in Figs. I.D.7 and I.D.8 for the nickel-rich reflector and the steel-rich reflector, respectively. The peaks in flux due to low-cross-section "windows" between scattering resonances are evident in core and reflector regions. In addition, the interaction of the peaks characteristic of both core and reflector compositions are present near the interface. The shape between lethargy 2.0 and lethargy 2.5 is not reliable because, at energy greater than that corresponding to the lethargy value of 2.0, the analysis utilized coarse cross sections, which cause spectral-envelope distortion.

(iv) Dependence of Core-reflector Current in Nickel- and Steel-reflected EBR-II-type Cores on Space-Energy Weighting of Multigroup Cross Sections (D. Meneghetti and K. E. Phillips)

The fine-energy-detailed neutron-flux solutions shown in Figs. I.D.7 and I.D.8, together with the corresponding fine-energy-detailed currents, have been used as weighting factors in space-energy collapse of fine cross-section detail to coarse-group cross sections. The collapsing procedure has been previously reported.**

*Meneghetti, D., Rago, A. L., and Phillips, K. E., "Use of the ELMOE-SNARG Programs to Study Details of Neutron Spectra through Regions of Resonance-scattering Media," Resumenes de los articulos Presentados en la Conferencia Internacional sobre Utilization de Reactores de Investigacion y Computo y Matematicas de Reactores, Mexico City, 1967.

**Meneghetti, D., and Phillips, K. E., Fine-Spectral Interface Effects of Resonance Scattering upon Multigroup Cross Section Averaging, Trans. Am. Nucl. Soc. 11, 205 (1968).

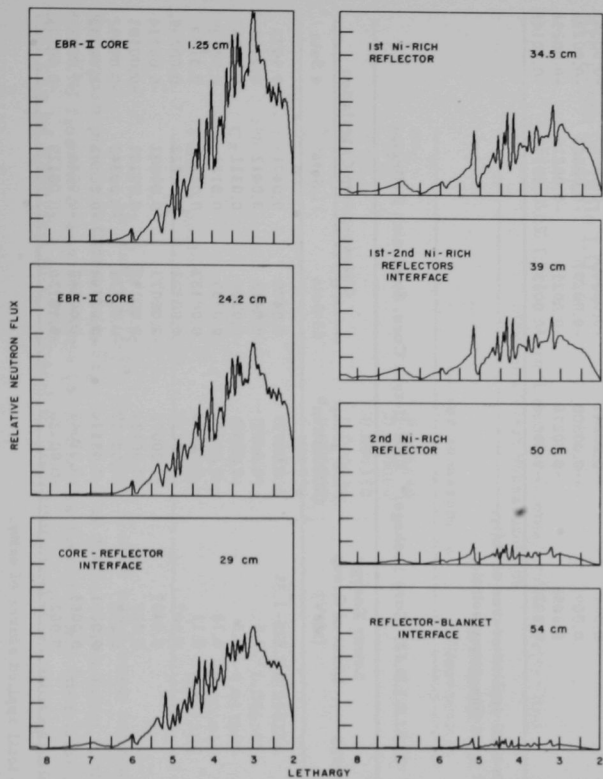


Fig. I.D.7. Neutron-flux Spectrum at Various Spatial Positions in an EBR-II Core with Nickel-rich Reflector

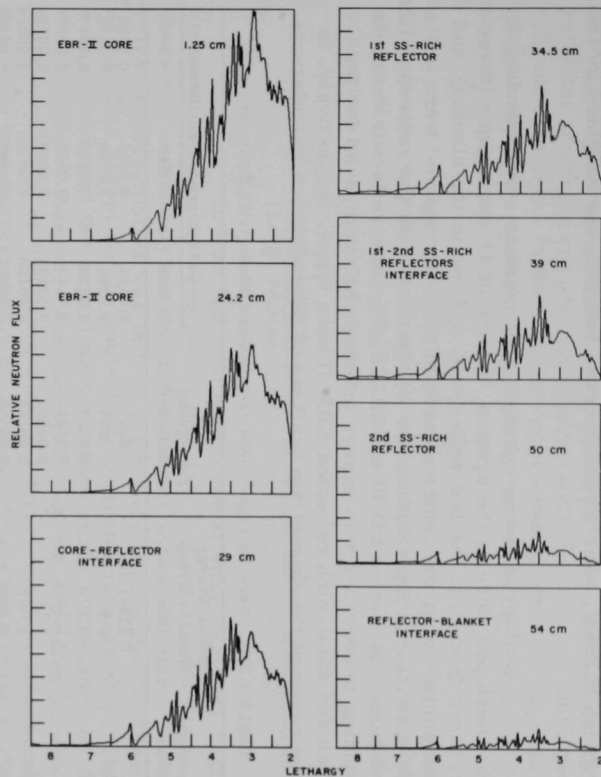


Fig. I.D.8. Neutron-flux Spectrum at Various Spatial Positions in an EBR-II Core with Steel-rich Reflector

The fine-group transport cross sections are weighted by the fine-group current, whereas other cross sections are weighted by the fine-group flux.

Collapsed coarse-group cross sections corresponding to each of 63 mesh positions in the system, to each of 11 subregions (three in the core, three in each of the two reflectors, and two in the blanket), and to four mesh positions (at the center of each of the four regions) were utilized to calculate coarse-group solutions for comparison with the reference fine-group solutions. In Tables I.D.11 and I.D.12, the core-reflector currents corresponding to coarse-group energy intervals are compared for the nickel-rich and steel-rich reflected EBR-II core types, respectively, in the energy range of the fine-group analysis of the reference calculations.

TABLE I.D.11. Core Leakage:^a EBR-II-type Core, Nickel-rich Reflector

Coarse-energy Group No.	Lower Energy Limit of Group (MeV)	Fine-group Calculation ^b	Coarse-group Calculation		
			63 Sets	11 Sets	4 Sets
4	0.825-1.35	0.0405	0.0414	0.0415	0.0428
5	0.5	0.0389	0.0396	0.0394	0.0379
6	0.3	0.0318	0.0320	0.0320	0.0317
7	0.18	0.0132	0.0133	0.0134	0.0148
8	0.11	0.00601	0.00604	0.00602	0.00584
9	0.067	0.00168	0.00168	0.00155	0.00054
10	0.0407	-0.00506	-0.00507	-0.00495	-0.00367
11	0.025	-0.00132	-0.00129	-0.00130	-0.00142
12	0.015	-0.00041	-0.00040	-0.00037	-0.00041
13	0.0091	-0.00300	-0.00297	-0.00307	-0.00221
14	0.0055	-0.00216	-0.00215	-0.00218	-0.00236
15	0.0021	-0.00134	-0.00137	-0.00139	-0.00148

^aBased on total applied source of unity.

^bSummed from fine-group solution.

TABLE I.D.12. Core Leakage:^a EBR-II-type Core, Steel-rich Reflector

Coarse-energy Group J	Lower Energy Limit of Group (MeV)	Fine-group Calculation ^b	Coarse-group Calculation		
			63 Sets	11 Sets	4 Sets
4	0.825-1.35	0.0471	0.0470	0.0471	0.0473
5	0.5	0.0407	0.0412	0.0412	0.0410
6	0.3	0.0308	0.0309	0.0311	0.0326
7	0.18	0.0183	0.0183	0.0181	0.0170
8	0.11	0.00893	0.00889	0.00901	0.0104
9	0.067	0.00223	0.00222	0.00222	0.00238
10	0.0407	-0.00073	-0.00073	-0.00081	-0.00134
11	0.025	-0.00134	-0.00133	-0.00131	-0.00101
12	0.015	-0.00337	-0.00338	-0.00343	-0.00392
13	0.0091	-0.00144	-0.00144	-0.00143	-0.00132
14	0.0055	-0.00047	-0.00047	-0.00044	-0.00051
15	0.0021	-0.00120	-0.00130	-0.00129	-0.00135

^aBased on total applied source of unity.

^bSummed from fine-group solution.

For the lower-energy groups, the differing scattering-resonance structures of the compositions on either side of the core-reflector interface are strong and are coupled with a reflector-to-core current direction. In this energy region, use of spatially dependent coarse-group collapsed sets is important if the individual coarse-group leakages are to be correctly calculated.

On the other hand, since the bulk of the core leakage in the EBR-II-type system occurs at the higher energies, calculations of the overall reactivity of such a system is not expected to require a large number of subregional cross-section sets.

(v) Flux and Fission Rate in Structural-test Subassemblies
(L. B. Miller, R. E. Jarka, and J. Sullivan)

In Run 32D, two experimental subassemblies containing structural materials were loaded into Row 2 of the reactor core. One of these was completely surrounded by driver subassemblies. One of these driver subassemblies was in turn completely surrounded by driver subassemblies except for the subject experimental subassembly. This driver subassembly and the experimental subassembly surrounded by driver subassemblies thus were symmetrically placed, providing an ideal arrangement for a study of flux depression in a structural-test subassembly. The geometry was represented in an x, y coordinate system for a DSN analysis. The atom densities in the driver and experimental structural subassemblies are given in Table I.D.13.

TABLE I.D.13. Atom Densities (atoms/cm³) in Driver and Structural-test Subassemblies

	Driver Subassembly	Structural-test Subassembly
²³⁵ U	0.006940	
²³⁹ Pu	0.000004	
²³⁸ U	0.006350	
Mo	0.000924	
Nb	0.000005	
Zr	0.000756	
Fe	0.011906	0.050256
Ni	0.00163	0.006307
Cr	0.00334	0.013869
Na	0.106290	0.003915
Fission products	0.000055	0.002300

In Table I.D.14, the group fluxes have been tabulated for the mesh points indicated in Fig. I.D.9. The fluxes have been multiplied by the ²³⁵U fission cross sections to obtain the fission rate (per atom of ²³⁵U) that can be expected in a ²³⁵U foil in the structural-test subassembly as

compared to the ^{235}U fission rate in the driver subassembly (per atom of ^{235}U). The ^{235}U fission cross sections are given in Table I.D.15, and the fission rates are shown in Table I.D.16.

TABLE I.D.14. Relative Group Fluxes in Driver and Structural-test Subassemblies

Group	E_L , eV	Mesh Point 1	Mesh Point 2	Mesh Point 3	Mesh Point 4
1	2.35×10^6	0.903	0.946	1.206	1.387
2	8.21×10^5	2.911	3.008	3.357	3.637
3	3.02×10^5	5.080	5.206	5.426	5.629
4	1.11×10^5	5.273	5.397	5.691	5.914
5	4.09×10^4	3.562	3.642	3.850	4.011
6	2.90×10^1	3.113	3.163	3.202	3.236

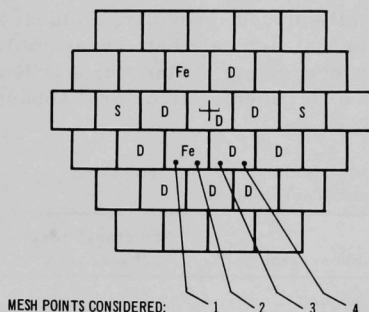


Fig. I.D.9

Position of Structural-test Subassembly and Mesh Points Used in Study of Flux Depression in the Subassembly

Fe = STRUCTURAL - EXPERIMENT SUBASSEMBLY

D = DRIVER SUBASSEMBLY

S = SAFETY SUBASSEMBLY

TABLE I.D.15. ^{235}U Fission Cross Sections

Group	Cross Sections $\sigma_f(b)$	Group	Cross Sections $\sigma_f(b)$
1	1.285	4	1.425
2	1.282	5	1.804
3	1.202	6	2.956

TABLE I.D.16. Relative Fission Rates per Atom of ^{235}U

Group	Mesh Point 1	Mesh Point 2	Mesh Point 3	Mesh Point 4
1	1.16	1.22	1.62	1.78
2	3.73	3.86	4.30	4.66
3	6.12	6.26	6.52	6.77
4	7.51	7.69	8.11	8.42
5	6.43	6.57	6.95	7.23
6	9.25	9.35	9.47	9.56
Total	34.15	34.95	36.97	38.42

The average fission rate per U-235 atom in a foil located at the center of the structural-test subassembly is 8.3% less than the fission rate per U-235 atom in a correspondingly located driver-fuel subassembly. The high-energy fission rate is depressed by 30% in the structural-test subassembly. It is significant that the flux and fission-rate depression is highly dependent on the position in the structural-test subassembly at which the foil measurements are made.

(vi) Analysis of Rod-bowing Feedback (D. Kucera)

The BOW-IV program has become operational up to an EBR-II steady-state power level of 135 MWt. The input for the hex-can temperature the program uses was derived from Run 25 with the stainless steel radial reflector.

Running time on the CDC-3600 computer has averaged less than 15 sec per power level studied, or 1.8 sec/iteration. The BOW-IV program is now far superior to any of its predecessors in terms of convergence stability and accuracy.

c. Fuel Performance Studies--Mark I Series (C. M. Walter)

(i) Driver Fuel Operation at High Temperatures and Burnups
(W. N. Beck and J. P. Bacca)

Last Reported: ANL-7561, p. 28 (March 1969).

An experimental program of irradiating encapsulated Mark-IA elements in the EBR-II reactor to burnups considerably higher than that originally set as maximum for the element (i.e., 1.2 a/o burnup) is well under way. Table I.D.17 lists the elements included in this program and the irradiation conditions for each.

TABLE I.D.17. High-burnup Mark-IA Elements

Capsule No.	Subassembly No.	Maximum Calculated Burnup (a/o)	Maximum Cladding Temp (°F)	Maximum Fuel Temp (°F)
BF02	XO66	3.5	897	1025
BF03	XO66	3.5	897	1025
BF04	XO52	2.9	918	1061
BF05	XO17	2.1 ^a	875	1003
BF08	XO52	2.9	918	1061
BF09	XO17	2.1 ^a	875	1003
BF11	XO52	2.9	918	1061

^aMeasured by chemical analysis for tellurium.

Capsules BF02 and BF03 had been successfully irradiated in Subassembly XO15 to a calculated 3.5 a/o burnup by the end of Run 34. Nondestructive examination of the capsules by neutron radiography showed the elements to be intact; and they have therefore been reinstalled in Subassembly XO66 and reinserted in the reactor. Capsules BF04, BF08, and BF11 were originally irradiated in Subassembly XO17 to a calculated 2.4 a/o burnup. The elements were then nondestructively examined and found to be intact. The irradiation period was subsequently extended to 2.9 a/o burnup without failure. Two of these elements (BF04 and BF08) are being destructively examined.

Postirradiation examination of Element BF09 has been completed. The element was irradiated to an analyzed maximum burnup of 2.13 a/o. Figure I.D.10 shows the axial burnup profile of the element, based on analysis of five sections of the fuel pin.

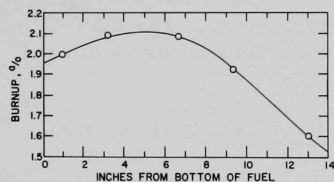


Fig. I.D.10. Axial Burnup Profile of Encapsulated Element BF09

The peak burnup occurs below the centerline of the pin and is largely attributed to the placement of the element within the capsule. The fuel was U-5 w/o Fs alloy having a silicon concentration of 150 ppm. The increase in fuel volume was determined to be 22% and the fission gas released to the plenum 3.6%. The pin was in intimate or nearly intimate contact with the ID of the cladding except at the bottom 2.5 in., where a maximum annular separation of 0.003 in. was noted. The pin had elongated 2.9%, but was still 0.05 in. from making contact with the restrainer. The fuel was initially sodium bonded to the cladding; as the fuel expanded, the sodium in the annulus was forced into the plenum region. The plenum gas was recovered and the plenum volume measured.

Transverse as well as longitudinal metallographic sections were taken from five places along the length of Element BF09. The polished sections showed no unusual fuel structures. There was no microstructural evidence of melting. Neither formation of fission-gas bubbles nor micro-tearing was discernible at a magnification of 500X. Microprobe scans were made across the interface of the fuel and cladding for U, Mo, Ru, Fe, Cr, Ni, and Cs. There was no evidence of migration of the elements of the fuel into the cladding or of cladding elements into the fuel within the one-micron resolution of the microprobe. Ruthenium was segregated on the fuel-side interface to a depth of about $3\text{ }\mu$.

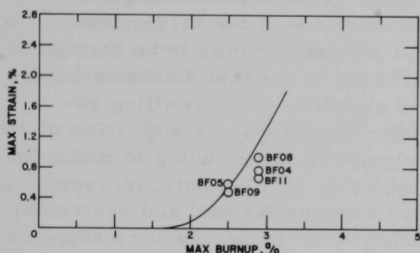


Fig. I.D.11. Comparison of Measured Changes in Strain of EBR-II Mark-IA Fuel Elements (data points) with Changes Predicted by BEMOD Code (solid line)

Further changes will be made in the code to give better agreement with both sets of data. The burnup and temperature input to BEMOD will be revised to correspond with the lower burnups experimentally found in these elements.

Postirradiation weights of Capsules BF04, BF08, and BF11 were the same as their preirradiation weights, indicating that there had been no loss or gain in the quantity of bond sodium in the capsules. Neutron radiographs at TREAT showed no abnormalities, such as fuel movement, cracking, or gross straining of the element cladding. Samples of the plenum gas in the capsule failed to show the presence of fission products. This indicates that there was no failure of the element cladding.

Precise measurements of diameter were made of both the capsules and the elements. These measurements showed peak diameter increases of the capsule OD of 0.1 to 0.2% (0.0005 to 0.0008 in.) and of the element OD of 1.0 to 1.2% (0.0016 to 0.0021 in.). The location of the greatest diameter increase for both the capsules and elements was slightly below the midlength of the fuel in the element. Little, if any, increases in element or capsule diameters occurred in the region of the gas plenum of the elements.

Diametral profiles have been obtained of five high-burnup encapsulated Mark-IA elements. The maximum cladding strains found in these elements (corrected for stainless steel swelling) are plotted versus the maximum calculated burnup in Fig. I.D.11. The solid line represents the results of BEMOD calculation. The uncertain parameters in this calculation were adjusted to give good agreement with Elements BF05 and BF09. However, the three higher-burnup pins (BF04, BF08, and BF11) now fall somewhat below the predicted curve.

d. Mark II Driver Fuel Element Development (C. M. Walter)

(i) Element Irradiation Tests (W. N. Beck)

Last Reported: ANL-7561, pp. 28-29 (March 1969).

An irradiation program is currently being conducted on encapsulated Mark-II fuel elements in a B37 subassembly (XO53, formerly XO29).

The subassembly was first removed after completion of Run 31F, the calculated maximum fuel burnup was 2.3 a/o. Neutron-radiographic examination of the capsules showed the pins to be straight, intact, and of uniform density. The increases in capsule diameter (about 0.1%) were consistent with the amount of stainless steel swelling expected at these fluences and temperatures. There was no indication of strain due to cladding creep. The fuel had elongated in the cladding to make contact with the restrainers. This was common to all elements, irrespective of type of restrainer or initial separation between the fuel and restrainer, which ranges from 0.2 to 0.7 in. The behavior of these capsules supports previously observed results which show that a restrainer will limit axial growth of a metal fuel pin and transfer it to a radial direction.

Three of the elements (201, 212, and 251) were deencapsulated and are being subjected to detailed examination.

From measurements of plenum pressure, approximately 36% of the fission gas was calculated to have been released to the plenum. Optical metallographic examinations of sections of the elements showed formation of very small fission-gas bubbles; this formation will be examined by electron microscopy. Preliminary electron-microprobe analysis indicates no detectable diffusion of the elements of the fuel into the cladding or of cladding elements into the fuel within the one-micron resolution of the microprobe.

Subassembly XO53, containing the remaining 34 Mark-II elements plus three substitution elements, is being irradiated and should attain a calculated 4-a/o burnup at the end of Run 34. An interim nondestructive examination will then be performed on all capsules in the subassembly. Some of the capsules will be selected for removal and destructive examination. The others will be reconstituted into a new subassembly for additional exposure.

e. Equipment--Fuel Related (E. Hutter)

- (i) New Control Rod Subassemblies (O. S. Seim, T. Sullivan, and J. Pardini)

Last Reported: ANL-7561, p. 29 (March 1969).

(a) Higher-worth Control Rod. Flow tests and fabrication drawings of the prototype version of the higher-worth control rod were completed. Two prototype higher-worth control rods will be constructed. One will be inserted in the reactor, replacing a rod now in use, for mechanical and performance evaluation. If the data from these tests are satisfactory, the reactor will be operated for an extensive period with the higher-worth control rod inserted to obtain life-test data.

- (ii) Oscillator Rod--Mark II (O. Seim, J. Pardini, and T. Sullivan)

Last Reported: ANL-7561, p. 29 (March 1969).

Fabrication and testing of all components for the Mark-II-B oscillator-rod system were completed. The lower bearing assembly, guide tube, guide-tube insertion tool, storage-basket adapter sleeve, and sleeve-handling tool were tested in air at room temperature and in sodium at 700°F. The tests were done in a tank containing two sleeves, one simulating a control-rod hole in the reactor grid and the other a storage-basket tube. To avoid sodium contamination of the oscillator rod, a dummy rod was used with the lower-bearing carrier assembly while performing the test in sodium. The oscillator rod had been tested previously.

The guide-tube insertion tool was locked to the guide tube and inserted in the simulated control-rod hole. A downward force of 300 lb was maintained on the guide tube while the spring-loaded bayonet lock of the guide tube was successively locked to the simulated grid pin and unlocked from the pin. This test was made to simulate the force that will be applied by the core gripper when these operations are performed in the reactor. In air at room temperature, 24 ft-lb of torque were required to lock the guide-tube bayonet, and 22 ft-lb of torque were required to unlock it. In 700°F sodium, 27 ft-lb of torque were required for locking and 23 ft-lb for unlocking.

The assembly of the dummy rod and lower bearing was then inserted in the guide tube. Again, a downward force of 300 lb was maintained on the top adapter of the dummy rod to seat the bayonet lock properly on the guide-tube pin. In air at room temperature, 11 ft-lb of torque were required to lock and unlock the bearing-carrier bayonet. In 700°F sodium, 18 ft-lb were required.

The handling tool for the storage-basket adapter sleeve was used to install and lock the sleeve in the simulated storage-basket tube. The unlocking extension was then attached to the handling tool, and the tool was used to unlock and remove the adapter sleeve from the simulated storage-basket tube.

All of the components operated satisfactorily. Cleanup of the components after testing in sodium was accomplished with no difficulty except for the sleeve-handling tool. This tool is being modified to simplify cleaning. After modification it will be tested in sodium again.

A new lower section of the oscillator-rod drive shaft is being fabricated. It incorporates labyrinth instead of bellows seals. When fabrication is complete, the modified lower section will be attached to the existing upper section.

(iii) Engineering Consultation (O. S. Seim, J. A. Pardini, T. E. Sullivan, and E. C. Filewicz)

Last Reported: ANL-7518, p. 45 (Nov 1968).

(a) Model RRR Dummy Control Rod. The continuing study to provide improved dummy control rods for reactor-kinetics experiments has resulted in a revised configuration that should reduce the effective time of reactivity removal. The Model RRR (for "rapid reactivity removal") stainless steel control rod for rod-drop tests is similar to the Model IHE dummy control rod except that it has a sodium-filled gap between the lower shield and the 19-element rod bundle, a 5-in.-long stainless steel follower below the bundle, and a 3-in. shorter tube bundle that has been raised $5\frac{3}{4}$ in. This modification provides a configuration that has an 11-in. gap between the upper shield and the tube bundle, a 9-in.-long tube bundle, a 2-in. gap between the tube bundle and the follower, and a $3\frac{1}{2}$ -in. gap between the follower and the lower shield. Because this configuration will require less cooling, the hole size in the orifice plate is being reduced to provide approximately 2 gpm of internal flow.

f. New Subassemblies Design and Experimental Support
(E. Hutter)

(i) Irradiation Subassemblies (O. Seim and W. Ware)

Last Reported: ANL-7553, pp. 43-45 (Feb 1969).

(a) Mark E61. Hydraulic flowtests of the Mark-E61 subassembly were performed to determine the characteristics of pressure drop versus flow. The tests were made in the stainless steel pressurized-water loop, and data were collected for reactor row positions 1 through 5. The data obtained from the tests, based on a reference 67-subassembly core, are presented in Table I.D.18. Table I.D.19 shows the reference values of flow versus pressure drop for a standard EBR-II core subassembly.

TABLE I.D.18. Results of Flowtest
of Mark-E61 Irradiation
Subassembly

Reactor Row	Effective Pressure Drop (psi)	Sodium Flowrate at 800°F (gpm)
1, 2	38	93
3	39	88
4	34.5	72
5	34	63

TABLE I.D.19. Reference Values of
Flow vs Pressure Drop for an EBR-II
Standard Core Subassembly

Reactor Row	Effective Pressure Drop (psi)	Sodium Flowrate at 800°F (gpm)
1, 2	38	139
3	39	123
4	34.5	93.5
5	34	78

Fabrication of new nonstandard hardware for two Mark-E61 subassemblies was started.

(b) Mark J37. A 37-element model of the Mark-J subassembly was designed. The model is identical to the Mark J19 (see Progress Report for October 1968, ANL-7513, p. 64) except that it has 0.250-in.-OD elements wrapped with 0.040-in.-OD spacer wire and a five-bar grid assembly. The five-bar grid assembly is the same as that for the Mark-H37 subassembly. All hardware used in the Mark J37 was designed previously and can be fabricated from existing drawings.

The principal feature of the Mark-J series of subassemblies is the argon-gas insulating plenum between the inner and middle hex tubes at the core-region elevation. This insulation reduces conductive heat losses radially from the experimental fuel pins and provides a more even temperature distribution in the element bundle.

Flowtests will be performed to confirm proper coolant flow at the effective pressure drops through the subassembly for various row positions of the reactor core.

(c) Mark K1. Preliminary layouts have been made for a proposed high-temperature (~1350°F) materials-surveillance subassembly.

The initial purpose of this subassembly is to obtain corrosion data for various types of stainless steels in flowing, high-temperature sodium under actual reactor conditions of sodium quality and irradiation environment. Creep and rupture tests also may be performed later.

To obtain the high sodium temperature in the section holding the test specimens, 0.1-0.5 gpm of the normal coolant flow will be orificed into a preheater section at the lower end of the subassembly. The preheater section consists of a thick-wall, $1\frac{3}{4}$ -in.-OD x $5\frac{7}{8}$ -in.-ID, Type 304 stainless steel cylinder enclosed in a 2-in.-OD x $1\frac{7}{8}$ -in.-ID evacuated or inert-gas-filled outer cylinder. The gas space will reduce conductive heat loss from the inner cylinder. The preheater section extends upward past the top of the core region to within $6\frac{1}{4}$ in. of the bottom of the top fixture. The test section is located in the top 20 in. of the heater to take maximum advantage of the rise in sodium temperature.

The test section is a $1\frac{1}{2}$ -in.-OD x $1\frac{1}{4}$ -in.-ID tube on which several rings of the various materials being tested are stacked. The temperature of the hot sodium flowing over the surface of these test samples will be monitored by approximately ten temperature sensors, each ~2 in. long, stacked inside the tube. Each sensor will indicate the temperature of the test material at that particular elevation. Thus, a temperature profile may be plotted against the corresponding corrosion rates of the test samples. In addition to the corrosion rates, data on heat generation in structural materials at various locations in the reactor may be obtained to aid in making physics calculations.

To reduce the subassembly outlet temperature to an acceptable level, the hot sodium effluent will be mixed with the cold ($\sim 735^{\circ}\text{F}$) bypass flow in a mixer section located at the top of the test section. The effects of pressure drop, flow velocity, and estimated heating rates must be calculated to give a mixed-sodium outlet temperature at the top of the subassembly that is within $\pm 100^{\circ}\text{F}$ of the outlet temperatures of adjacent subassemblies.

g. Instrumented Subassembly (E. Hutter and A. Smaardyk)

(i) Capsule-heating Test (C. Divona and R. Brubaker)

Not previously reported.

When an instrumented-subassembly capsule (or any other sodium-bonded fuel element) is heated so that bond melting begins at the bottom (or dead end), expansion of the molten sodium is likely to cause a pressure buildup within the capsule. A test has been performed to determine what effect, if any, this pressure buildup would have on the capsules.

This test was performed with two test capsules that were fabricated to the exact specifications of the prototype capsules for the instrumented subassembly. Before testing, the outside diameter of the capsules was measured at 20 places along the length of the sodium bond. After the measurements were made, the capsules were radiographed (Fig. I.D.12 is a portion of one of these radiographs). Nine Chromel-Alumel thermocouples were fixed along the length of the capsules, seven of them along the length of the sodium bond.

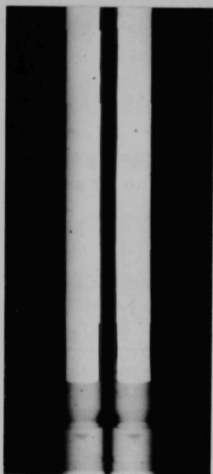


Fig. I.D.12

Instrumented-subassembly
Capsule before Heating

The capsules were placed in a furnace so that the temperature gradient decreased from the bottom to the top of the capsule. This arrangement allowed the sodium bond at the bottom to melt while that at the top remained solid. Heating rates were varied to melt the bottom of the bond rapidly (in 2 min) and slowly (in $8\frac{1}{2}$ min). Bond melting was continued until 80% of the bond was melted. When 80% melting had occurred, the capsules were removed from the furnace and cooled in room air. After cooling, the capsules were examined and their outside diameters remeasured. The diameters were the same as the "as built" diameters.

After the measurements had been taken, a second set of radiographs were made. Figure I.D.13, a portion of one of these radiographs, shows that the inner capsule tube had been forced upward approximately 0.010 in. Subsequently, the entire bond length was melted, after which the inner capsule tube had returned to its original position.

In a second test, only the lower 20% of the bond was melted. After heating, the capsules were removed from the furnace and measured while cooling. The outside diameter was measured at 290, 270, and 200°F. In all cases, the capsule diameter had increased by 0.0005 in. When the capsules had cooled to room temperature, the outside diameter had returned to its original dimension. The diameter increase, therefore, is attributed to the normal thermal expansion of the capsule material.

These tests indicate that no deformation of the instrumented-subassembly capsule or element tube occurs when the sodium bond is melted from the bottom. Initial melting at the bottom, however, does cause a temporary displacement of the element tube.



Fig. I.D.13

Instrumented-subassembly
Capsule after Heating

h. Process Chemistry (D. W. Cissel)

- (i) Sodium Coolant Quality Monitoring and Control
(W. H. Olson, C. C. Miles, E. R. Ebersole, G. O. Haroldsen,
and T. P. Ramachandra)

Last Reported: ANL-7561, pp. 31-36 (March 1969).

(a) Radionuclides in Sodium. The results of analyses for ^{137}Cs and ^{131}I in primary sodium are listed in Table I.D.20. The present level of ^{22}Na is $\sim 3.2 \times 10^{-2} \mu\text{Ci/g}$.

TABLE I.D.20 ^{137}Cs and ^{131}I in Primary Sodium

Sample Date	^{137}Cs ($\mu\text{Ci/g} \times 10^2$)	^{131}I ($\mu\text{Ci/g}$)	Sample Date	^{137}Cs ($\mu\text{Ci/g} \times 10^2$)	^{131}I ($\mu\text{Ci/g}$)
3/10/69	1.3	$< 4.2 \times 10^{-5}$	4/22/69	1.2	3.5×10^{-4}
3/14/69	1.3	$< 3.0 \times 10^{-5}$	4/28/69	1.2	2.4×10^{-4}
3/27/69	1.4	3.9×10^{-5}	5/2/69	1.2	2.2×10^{-4}
4/1/69	1.5	3.2×10^{-5}	5/7/69	1.4	2.0×10^{-4}
4/9/69	1.3	1.9×10^{-5}	5/12/69	1.3	1.6×10^{-4}
4/14/69	1.2	4.8×10^{-5}	5/16/69	-	2.7×10^{-4}
4/18/69	1.3	3.0×10^{-4}			

The results of analyses for radionuclides in secondary sodium are listed in Table I.D.21. The only radionuclide found was ^{24}Na .

Saturation activity of ^{24}Na in secondary sodium with the reactor at 50 MWt is $\sim 3 \times 10^{-2} \mu\text{Ci/g}$.

TABLE I.D.21. ^{24}Na in Secondary Sodium

Sample Date	^{24}Na ($\mu\text{Ci/g}$)
3/26/69	1×10^{-2}
4/23/69	6.5×10^{-3}

(b) Trace Metals in Sodium. The results of analyses for trace metals in sodium are listed in Table I.D.22. Metal concentrations were determined by atomic-absorption spectrophotometry.

TABLE I.D.22. Trace Metals in Sodium (ppm)

Sample Date	Al	Bi	Cd	Co	Cr	Cu	Fe	Mn	Ni	Pb	Sn	Zn
<u>Primary Sodium</u>												
3/10/69	<0.9	1.4	<0.03	<0.04		0.09		<0.01	<0.1	11.0	16.2	
3/14/69						0.08						
4/1/69	<0.6	2.1	<0.03	<0.08	<0.04	0.08	0.25	0.02	0.09	10.7	19.4	0.04
5/2/69												
<u>Secondary Sodium</u>												
2/17/69	<0.3	<0.3	<0.01	<0.04		0.04		0.04	0.1	0.3	<1.3	<0.01
3/16/69	<0.3	<0.3	<0.01	<0.04		0.05		0.02	0.1	0.4	<1.3	<0.04
4/15/69	<0.3	<0.3	<0.03	<0.1	0.2	0.1	1.0	0.03	0.3	0.65	<1.0	0.03

Investigation continued into the recovery of metallic impurities from residues of vacuum-distilled sodium. About 10 g of secondary sodium were spiked with small amounts of trace metal salts, and the distillation residue was taken up in an HCl-alcohol medium for atomic-absorption analysis. The results of the analysis are shown in Table I.D.23. Calcium and magnesium showed erratic recovery, possibly due to contamination. Zinc and cadmium were lost during distillation.

TABLE I.D.23. Recovery of Trace Metals from Vacuum-distillation Residues of Sodium (~10-g sample)

Metal	PPM Added		PPM Recovered	
	Test 1	Test 2	Test 1	Test 2
Bi	1.08	0.54	1.19	0.50
Ca	0.435	0.435	0.39	0.66
Co	0.40	0.20	0.5	0.21
Cr	0.20	0.20	0.20	0.15
Cu	0.40	0.20	0.46	0.20
Fe	0.40	-	0.46	-
Mg	0.20	0.08	0.32	0.11
Mn	0.08	0.04	0.09	0.04
Ni	0.40	0.20	0.04	-
Pb	1.25	0.65	1.25	0.60
Sn	4.15	10.45	4.15	10.7

A 43-g sample of primary sodium taken on 4/9/69 in a tantalum crucible was vacuum distilled in the laboratory. Results of atomic-absorption analysis of the residue are listed in Table I.D.24.

TABLE I.D.24. Trace Metal Impurities in Vacuum-distillation Residue of 43-g Sample of Primary Sodium

Metal	Concentration (ppm)	Metal	Concentration (ppm)
Al	<0.14	Mg	0.035 ($\pm 20\%$) ^a
Bi	2.15 ($\pm 10\%$) ^a	Mn	<0.01
Co	<0.047	Mo	<0.07
Cr	0.023 ($\pm 30\%$) ^a	Ni	<0.012
Cu	0.051 ($\pm 20\%$) ^a	Pb	12.7 ($\pm 10\%$) ^a
Fe	0.09 ($\pm 10\%$) ^a	Sn	14.0 ($\pm 10\%$) ^a

^aEstimated error for this sample only. Does not include sampling error.

(c) Oxygen in Sodium. The results of analyses for oxygen in sodium by the mercury-amalgamation method are listed in Table I.D.25. Oxygen concentrations determined with plugging indicators are also listed in the table for comparison. Solubility of oxygen in sodium is taken from AI-AEC-12685 (Atomics International).

TABLE I.D.25. Oxygen Content of Sodium

Sample Date	No. of Aliquots	Average Concentration (ppm)	Oxygen Equivalent of Plugging Run (ppm)
<u>Primary Sodium</u>			
4/1/69	3	5.5 ± 2.6	<0.5
<u>Secondary Sodium</u>			
3/25/69	6	7.5 ± 2.3	<0.5

(d) Carbon in Sodium. Results of analyses for carbon in sodium are listed in Table I.D.26. Carbon is determined by the oxyacidic flux method.

TABLE I.D.26. Carbon Content of Sodium

Sample	No. of Aliquots	Average Concentration (ppm)
<u>Primary Sodium</u>		
4/1/69	2	1.3 ± 0.1
<u>Secondary Sodium</u>		
3/25/69	6	2.4 ± 0.8

(e) Test of UNC Oxygen Meter. Two United Nuclear (UNC) oxygen meters* are being tested in static sodium at 600°F. One is located in the high γ -radiation field of the room containing the primary-sodium cold trap. The other is in a nonradioactive area. Since the last progress report (ANL-7561), the two probes have been reversed and the second probe is now in the γ field. No change of signal due to γ radiation has been noted. The γ field on this probe has exceeded 1000 R/hr for 42 days (as of 5/22/69). Estimated maximum activity with ^{24}Na saturation at 50 MWt is $\sim 10,000$ R/hr.

*These are not the probes that had been calibrated at ANL-Illinois for installation in the EBR-II secondary sodium system. They had been reported to be the same in ANL-7561, p. 35.

(f) Hydrogen and Nitrogen in Cover Gas. Concentrations of hydrogen and nitrogen in the primary and secondary argon cover-gas systems are summarized in Table I.D.27.

TABLE I.D.27. Hydrogen and Nitrogen in Primary and Secondary Argon Cover-gas Systems (ppm)

	Primary			Secondary		
	High	Low	Average	High	Low	Average
<u>April</u>						
H ₂	132	0	16	28	0	7
N ₂	7,000	4,400	5,100	14,800	4,000	8,300
<u>May</u>						
H ₂	200	0	12	4	0	4
N ₂	9,000	4,600	6,700	7,000	5,200	5,900

i. Experimental Irradiation and Testing (R. Neidner)

(i) Experimental Irradiations

Last Reported: ANL-7561, p. 37 (March 1969).

Table I.D.28 shows the status of the experimental sub-assemblies in EBR-II as of May 15, 1969. New experimental subassemblies loaded into the grid for Runs 33B and 34A were XO18A, XO42A, XO54, XO56, XO58, XO59, XO60, XO61, and XO66. Subassemblies approved for irradiation since the start of Run 34A are:

Subassembly Number	Assigned Position	Capsule or Element Content and No. of Each ()	Experimenter	Approximate Burnup Goal (fuels--a/o) (nonfuels--nvt x 10 ⁻²²)
XO62	6F2	Series F9B--UO ₂ -25 w/o PuO ₂ (37)	GE	5.3
XO64	4F2	Series F5--UO ₂ -20 w/o PuO ₂ (19)	GE	10.5
XO67	4A3	Weldment Materials (4)	PNL	0.7
		Insulator Materials (1)	ORNL	-
		Structural Materials (1)	ORNL	-
		Structural Materials (1)	GE (NSP)	-

TABLE I.D.28. Status of EBR-II Experimental Irradiations as of May 15, 1969

Subassembly No. and (Position)	Date Charged	Capsule Content and No. of Capsules ()	Experi- menter	Accumulated Exposure (MWd)	Estimated Goal Exposure (MWd)	Burnup ^a
XG03 (7D1)	7/16/65	UO ₂ -20 w/o PuO ₂ (2) Stainless Dummies (17)	GE	21,624	23,300	5.6
XG04 (7B1)	7/16/65	UO ₂ -20 w/o PuO ₂ (2) Stainless Dummies (17)	GE	21,624	45,000	5.6
XA08 (4F2)	12/13/65	UC-20 w/o PuC (8) Structural (9) Structural (2)	ANL ANL GE	17,794	20,700	10.5 7.9 7.9
X012 (4B2)	8/10/66	UO ₂ -20 w/o PuO ₂ (19)	NUMEC	14,394	21,400	8.4
X018A (4E2)	4/23/69	Thermocouple (2) Structural (2) Structural (3)	PNL ANL GE	848 11,594	2,700 22,900	0.3 5.0 5.0
X019 (6D2)	1/13/67	UO ₂ -20 w/o PuO ₂ (7) UC-20 w/o PuC (3) Structural (8) Graphite (1)	GE UNC PNL PNL	11,174	13,000	4.6 5.1 3.1 3.1
X020 (6B5)	1/13/67	UO ₂ -PuO ₂ (9) UC-20 w/o PuC (3) Structural (4) Structural (2) Graphite (1)	GE UNC PNL ANL PNL	11,587	13,000	4.8 5.2 3.2 3.2 3.2
X021B (2D1)	2/23/69	Structural (7)	PNL	10,988	23,200	4.4
X027 (4B3)	11/21/67	UO ₂ -25 w/o PuO ₂ (18) Structural (1)	GE PNL	8,910	7,700	5.1 4.1
X032 (6E5)	11/22/67	UO ₂ -25 w/o PuO ₂ (19)	PNL	9,213	11,900	3.8
X033 (5E2)	12/22/67	UC-20 w/o PuC (19)	UNC	8,057	10,900	4.0
X034 (2F1)	4/13/68	Structural (7)	ORNL	8,439	14,800	3.9
X035 (7B4)	4/13/68	Structural (7)	ORNL	8,022	44,800	2.0
X036 (7E1)	7/25/68	UO ₂ -25 w/o PuO ₂ (19)	GE	6,308	33,300	1.7
X038 (7C5)	5/7/68	Structural (7)	INC	7,513	17,700	1.7
X040 (5B2)	8/14/68	UO ₂ -20 w/o PuO ₂ (19) UO ₂ -25 w/o PuO ₂ (16)	ANL GE	5,598	7,000	2.7 2.9
X041 (7A3)	7/24/68	Structural (7)	PNL	5,974	16,700	1.3
X042A (7D5)	4/2/69	B ₄ C, Ta (7)	PNL	5,787	25,000	1.2
X043 (4D2)	2/20/69	UO ₂ -25 w/o PuO ₂ (37)	GE	2,024	5,500	1.1
X044 (7A1)	9/28/68	Oxide Insulator (1)	LASL	4,649	8,100	0.8
X050 (4C2)	2/23/69	UO ₂ -20 w/o PuO ₂ (4) UO ₂ -28 w/o PuO ₂ (4) UO ₂ -20 w/o PuO ₂ (5) UC-18 w/o PuC (2) Structural (4)	GE GE ORNL W GE	2,024	7,500	1.1 + 7.7 ^b = 8.8 1.1 1.1 1.1 0.7 + 5.3 ^b = 6.0
X051 (3A2)	12/16/68	UO ₂ -25 w/o PuO ₂ (37)	PNL	2,569	16,400	0.5
X053 (4E3)	11/27/68	Mark II (37)	ANL	3,421	3,800	1.8 + 2.3 ^b = 4.1

TABLE I.D.28 (Contd.)

Subassembly No. and (Position)	Date Charged	Capsule Content and No. of Capsules ()	Experimenter	Accumulated Exposure (MWd)	Estimated Goal Exposure (MWd)	Burnup ^a
X054 (4E1)	3/31/69	UO ₂ -25 w/o PuO ₂ (37)	PNL	1,424	10,000	0.8
X055 (6A4)	2/23/69	UC-15 w/o PuC (19)	UNC	2,024	20,000	0.6
X056 (5C2)	4/3/69	UO ₂ -25 w/o PuO ₂ (37)	GE	1,424	10,600	0.7
X057 (2B1)	2/23/69	Structural (7)	PNL	2,024	15,000	0.8
X058 (7F3)	4/24/69	UO ₂ -25 w/o PuO ₂ (37)	GE	848	16,000	0.3
X059 (4A1)	4/23/69	UO ₂ -25 w/o PuO ₂ (37)	PNL	848	17,500	0.3
X060 (7C3)	4/3/69	Structural (7)	INC	1,424	5,400	0.3
X061 (7A5)	4/23/69	Structural (7)	INC	848	18,000	0.2
X066 (4A3)	4/24/69	Mark IA (2)	ANL	848	1,200	0.2 + 3.4 ^b = 3.6

^aApproximate accumulated center burnup on peak rod (fuels--a/o; nonfuels--nvt x 10⁻²²).

^bPrevious exposure from another subassembly.

The following two experimental subassemblies were removed from the grid after Runs 33A and 33B:

Subassembly Number	From Position	Capsule or Element Content and No. of each ()	Experimenter	Approximate Burnup Goal (fuels--a/o) (nonfuels--nvt x 10 ⁻²²)
XO10	7F3	Series FO--UO ₂ -20 w/o PuO ₂ (4)	GE	5.7
		Structural Materials (11)	ANL	3.8
		Structural Materials (4)	PNL	3.8
XO15	4A2	Series B--UO ₂ -20 w/o PuO ₂ (11)	NUMEC	5.8
		Series F7--UO ₂ -20 w/o PuO ₂ (2)	GE	5.5
		UC-20 w/o PuC (4)	ANL	5.9
		Mark IA (Metal) (2)	ANL	3.4 (peak)

Postirradiation neutron radiography of the 11 NUMEC capsules from Subassembly XO15 disclosed that Capsule B11 contained a failed element. This indicated failure is the eleventh indicated and/or confirmed failure of an encapsulated element in EBR-II since the initiation of the experimental irradiation program in May 1965. Table I.D.29 summarizes these failures.

(ii) Handling and Examination (D. W. Cissel)

(a) Profilometry. Several different techniques for obtaining the profile of irradiation specimens have been investigated. The techniques that appear to be most attractive are the electro-optical system, optical-mechanical system, and electro-mechanical system.

TABLE I.D.29. Fuel-element Failures in the EBR-II Experimental Program

Subassembly No.	Date Discharged	Capsule	Sponsor	Fuel Type	Approx Max Power (kW/ft)	Average Burnup (a/o)	Cladding	Failure Type ^a
X009	11/66	UNC-78	UNC	UC-20 PuC	28	2.7	V-20 Ti	A
XG06	2/67	F2F	GE	UO ₂ -20 PuO ₂	15	4.7	INC-800	B
X011	6/67	F4D	GE	UO ₂ -20 PuO ₂	16.6	3.3	INC-800	A
		F4F	GE	UO ₂ -30 PuO ₂	16.7	3.4	INC-800	B
		HOV-4	ANL	UO ₂ -20 PuO ₂	22.4	3.3	HAST-X	B/C
		HOV-10	ANL	UO ₂ -20 PuO ₂	23.5	3.3	HAST-X	B
XG05	3/68	F20	GE	UO ₂ -20 PuO ₂	15	6.5	347 SS	B
		NMV-11	ANL	UC-PuC	19.3	6.7	Nb-1Zr	D
X028	5/68	BC02	ANL	U-15 Pu-10 Zr	9.5	0.9	316 SS	B/C
X017	8/68	UNC-89	UNC	UC-20 PuC	26.8	4.0	316 SS	D
X015	4/69	B-11	NUMEC	UO ₂ -20 PuO ₂	13	5.4	316 SS	B-1

^aFailure Type:

A Small gas leak through cladding wall.

B Gross cladding failure.

B-1 Cladding fracture assumed from neutron radiography only.

C Additional gas leak through capsule wall.

D Significant cracking of cladding wall, but not detectable with neutron radiographs.

The electro-optical system has the potential of measuring the profile of an element without the need for installing the detection equipment in the hot cell. The information is transmitted out of cell through light-transmitting elements in the biological shielding surrounding the cell.

The principle of the optical-mechanical system is the use of a small beam of light as a weightless, pushless index stop. This system has been developed in concept only, but it appears to have the capability for measuring the profile of an element both accurately and rapidly.

The electro-mechanical profilometer in the ANL Metallurgy Division has been inspected. This is one of the best electro-mechanical systems in operation, but there are some features that are not compatible with FCF use. This system is being studied in detail to determine whether inspection of wire-wrapped elements can be made without a reference measurement.

Studies of fundamental limits in accuracy have shown the following:

1. Tube ovality of 0.0002 in. can be expected.
2. The diameter increase from decay heat can be as high as 0.0004 in. at the axial center of the core.

j. FCF Equipment Improvement (M. J. Feldman)

- (i) Process Equipment (N. R. Grant, J. P. Bacca, and V. G. Eschen)

Last Reported: ANL-7561, pp. 37 and 39 (March 1969).

The stereomicroscope has been assembled in the mockup area of the Fuel Cycle Facility and is being checked out for acceptance. The position stage is being used to position capsules for checkout of the macro-scope. The control system for the stage is being completed.

k. Superheater and EM Pump Study and Test (R. A. Jaross and E. Hutter)

- (i) Superheater Vibration Study (G. S. Rosenberg and M. W. Wambsganss)

Last Reported: ANL-7561, pp. 39-40 (March 1969).

A final report on the state-of-the-art evaluation of the potential for tube vibration in the EBR-II steam superheater and evaporator is being prepared.

l. Nuclear Instrument Test Facility Study (R. E. Rice)

Last Reported: ANL-7527, p. 64 (Dec 1968).

- (i) Out-of-core Thimble Modification to Provide a Facility for Tests from 650/700 to 1200°F

- (a) Facility Design (J. D. Cerchione, P. M. Long, and L. J. Christensen)

A combined report covering the conceptual and preliminary system design descriptions on the EBR-II high-temperature, out-of-core nuclear instrument test facility (NITF) was issued. The main function of the out-of-core NITF is to provide adequate space for testing experimental neutron detectors and cable in a high-level gamma-neutron environment at temperatures up to 1200°F. Tables I.D.30 and I.D.31 list the design criteria and engineering data, respectively, for this facility.

The EBR-II J-2 thimble has been selected for location of the NITF because of its availability, large size, and the higher neutron and gamma fluxes that result from proximity to the reactor core. A plant modification has been proposed to remove operational nuclear detectors from the

J-2 thimble and make the thimble available for experimental use. When the thimble is available, measurements of temperature, neutron- and gamma-flux distribution, and neutron spectrum will be made.

TABLE I.D.30. Design Criteria for Out-of-core
Nuclear Instrument Test Facility

Location	EBR-II J-2 thimble
Thimble Length, ft	28
Thimble OD, in.	15
Oven Length, ft	19.5
Oven ID, in.	7.1
Length of Cable Test Section, ft	13
Cable Outlet Space	Three 1.5-in. conduits
Length of Detector Test Section, ft	6.5
ID of Detector Test Section, in.	6.1
Temperature Range, °F	700 to 1200 ± 20
Gamma Flux, Max, R/hr at 62.5 MWt	~1 × 10 ⁶
Gamma Flux, Max, R/hr (10 sec after shutdown from 62.5 MWt)	~8 × 10 ⁴
Neutron Flux, Max, nv at 62.5 MWt	~8 × 10 ¹⁰

TABLE I.D.31. Engineering Data for Out-of-core
Nuclear Instrument Test Facility

Heater Type	Watlow Firebar strip heaters
Heat Density	8 W/in.
Heater Design	Four vertical zones; nine heaters per zone; three 3-heater circuits per zone consisting of one heatup circuit, one steady-state circuit, and one spare circuit
Oven Insulation	Laminations of stainless steel with mineral fiber and/or air gaps
Total Power Required	10 kW
Steady-state Heat Loss	2 kW
Voltage	250 V dc
Heater Control	Variable
Instrumentation	Thermocouple throughout facility
Alarms	High- and low-temperature for each oven zone; high-temperature shutdown for each oven zone
Coolant Air	20- to 50-cfm for detector-cable cooling at oven outlet
Supplementary Source	None required
Vertical Actuation	None required
Heatup Time (700 to 1200°F)	One heater circuit per zone--10 hr; two heater circuits per zone--5 hr
Cooldown Time, Avg (1200 to 1000°F)	10°F/hr

A series of gamma-flux measurements was recently made in the EBR-II J-2 thimble. A Westinghouse WL-23152 chamber was placed in the J-2 carrier and located at approximately the core horizontal midplane in the thimble. The measured gamma flux is plotted as a function of operating time at various power levels in Fig. I.D.14. Gamma decay following two reactor scrams and a reactor shutdown is plotted along with buildup of gamma flux after reactor startup. The maximum gamma flux measured was about 1.0×10^6 R/hr with reactor power at 50 MWt. Immediately after reactor shutdown, the gamma flux dropped to 3.2×10^4 R/hr and rapidly decayed to 5×10^3 R/hr in 24 hr.

The J instrument thimbles in EBR-II enter the primary tank at an angle of about 11° , slant down through the primary sodium, and penetrate the reactor-vessel neutron shield. The bottom end of each J thimble rests in a bracket fastened to the outside of the reactor vessel. Complete removal and replacement of a J thimble would be a difficult task. Instead of replacing the J-2 thimble, the top flange and all internals of the thimble, including the temperature-limiting aluminum baffles, will be removed. Following removal of the thimble internals, the new NITF will be installed as shown in Fig. I.D.15.

The NITF will consist of: (1) a new assembly of the top flange and insert tube; (2) an oven-sleeve assembly; and (3) an assembly of the top shield plug and detector carrier. The top support flange and outer tube of the J-2 thimble will remain in place to house the NITF. The overall length of the thimble is about 28 ft. The lower portion, which is immersed in the 700°F primary sodium, is a 15-in.-OD stainless steel tube. The thimble's support flange is bolted to a flanged nozzle attached to the top cover of the EBR-II primary sodium tank. The upper 8 ft of the thimble and plug assembly consists of a heavy radiation shield made of concrete and steel balls.

One of the design criteria for the high-temperature NITF is the minimizing of the length of the temperature transition zone just above the oven. The existing thimble-cooling system will be utilized to reduce the temperature of experimental cables from 1200°F to $<300^\circ\text{F}$ in a minimum space. Cooling air will be drawn down through the cable outlet conduits in the shield plug to a small, well-insulated plenum located at the top of the 1200°F oven. Air flow will then be directed back up through three conduits to the top flange of the shield plug, where it will be piped into the existing EBR-II thimble-cooling system.

Another important criterion for the NITF is the capability for removing one or more experimental detectors from the carrier and inserting them in the carrier soon after its removal from the thimble. In the present EBR-II thimble design, an aluminum carrier is utilized to reduce greatly the radioactivity of the structure. Because of the 1200°F

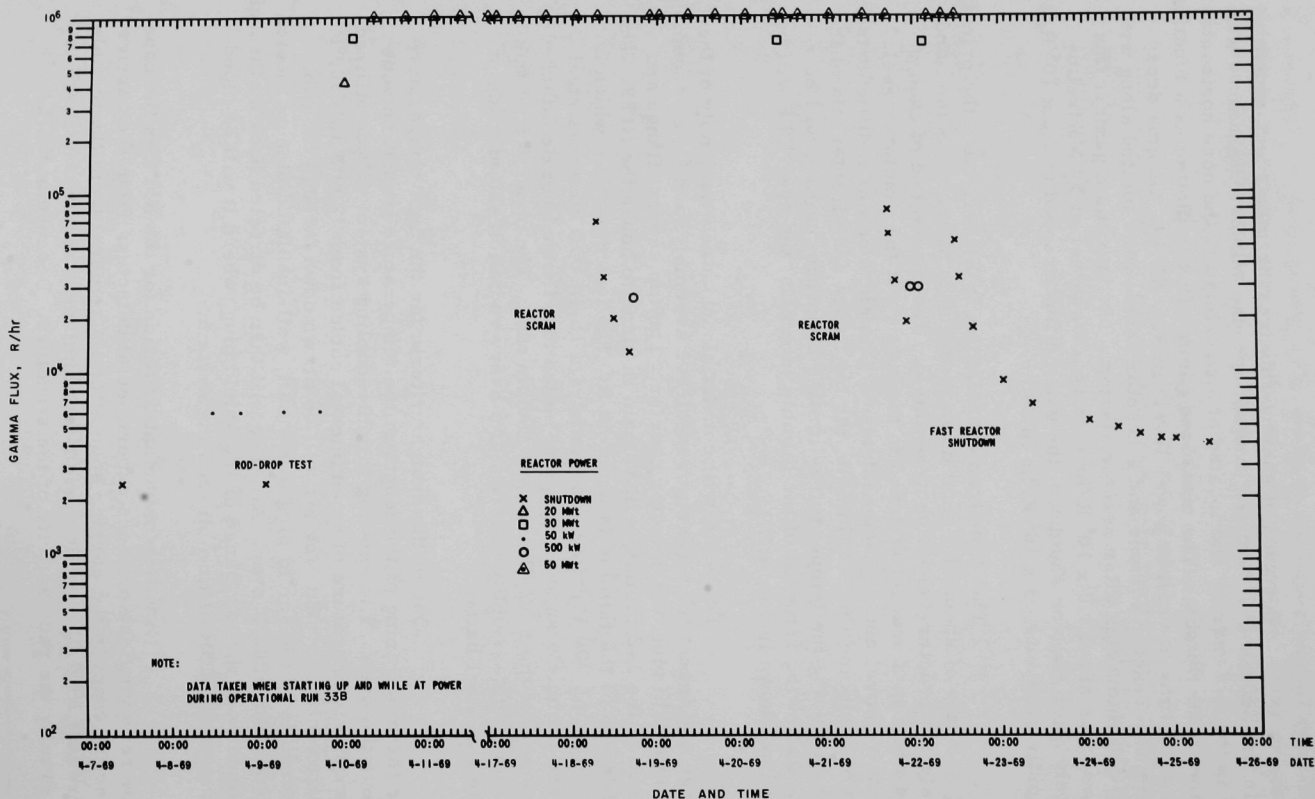


Fig. I.D.14. Gamma-ray Flux History in EBR-II J-2 Thimble

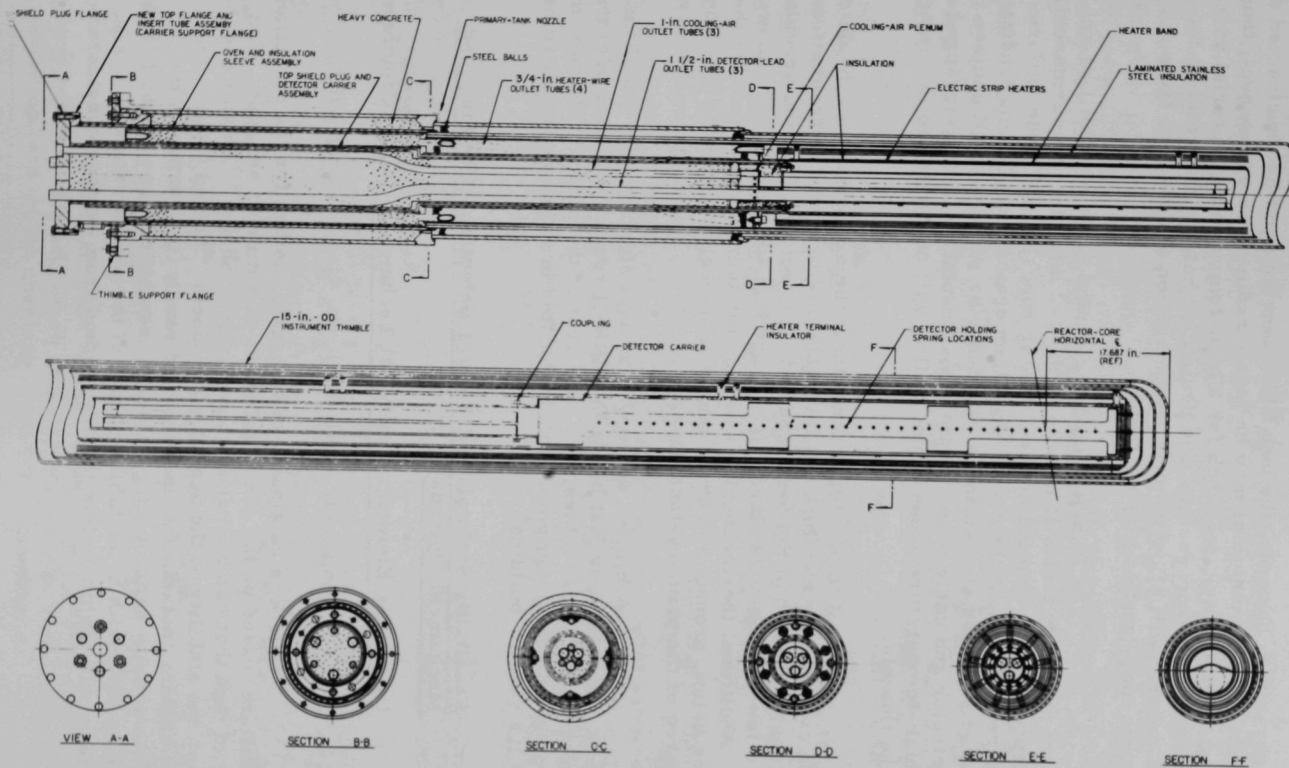


Fig. I.D.15. Assembly of Out-of-core Nuclear Instrument Test Facility

oven temperatures, however, the new NITF carrier must be constructed of stainless steel. This material may be highly radioactive on removal, thus prohibiting close access. A search for a high-temperature material with low activation was unsuccessful. The design for holding detectors in the new NITF carrier will allow removal and insertion of detectors from a distance with long-handled gripper tools.

The 19.5-ft-long detector and cable oven will be an independent assembly that will remain in the J-2 thimble semipermanently. Four independently controlled vertical heater zones will provide uniform temperatures throughout the oven. High-temperature insulation, consisting of laminated stainless steel-mineral fiber and/or air gaps, will enclose the entire detector and cable oven. Heaters and insulation will be arranged so that all high-temperature areas of the facility will be limited to the central part of the thimble.

Temperatures throughout the axial length of the detector and cable oven will be monitored at intervals of 2 to 3 ft. Representative thermocouples in each of the four zones will control heaters, and provide high- and low-temperature alarm signals and high-temperature shutdown signals. Additional thermocouples will monitor temperatures outside the insulation below, around, and above the oven, as well as near the top plug and the area of the primary-tank cover.

A limited space will be available near the top of the instrument thimble, on or just below the EBR-II reactor-building operating floor, for preamplifiers, cables, etc. The rest of the control, instrumentation, and experimental equipment will be located in the new test instrument room in the reactor building.

m. Feasibility Study of Fuel Failure Detection--Chemical and Mechanical Methods

(i) Trace Elements Analytical Techniques (C. E. Crouthamel)

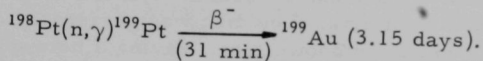
Last Reported: ANL-7561, pp. 41-42 (March 1969).

Work is continuing on a tagging method for the detection of fuel failure, based on the use of mixtures of antimony and gold. The number of tags that can be manufactured from ^{121}Sb and ^{197}Au will depend in part on the stability of the activation products ^{122}Sb and ^{198}Au in the primary sodium coolant. Instability would result in a change in the $^{122}\text{Sb}/^{198}\text{Au}$ activity ratio of a tag. If these instabilities are minor (<10%), they can be dealt with by suitable spacing of the weight ratios; gross instabilities could eliminate this tagging method from further consideration.

An experiment is being planned to obtain stability data on the antimony-gold tags in the primary sodium system of EBR-II. Present plans call for inserting milligram quantities of preactivated antimony and gold into EBR-II sodium and subsequently determining the $^{122}\text{Sb}/^{198}\text{Au}$ activity ratio in samples of the primary sodium. The degree of stability will be ascertained by comparing the ratio obtained with the sodium samples with the ratio obtained with an antimony-gold control sample. The detailed procedure for this experiment is being established.

The magnitude of the fast-capture cross sections of isotopes constituting a tag is important in the evaluation of the tag applicability. The activity level expected from irradiation of ^{197}Au in the EBR-II was reported previously (see ANL-7561). Although adequate experimental data on the fast-capture cross section of ^{121}Sb are not available, sufficient data are available to estimate the differential cross sections with the NEARREX Computer Code.* These calculations were made for ^{121}Sb , and the capture cross sections obtained were summed over a typical EBR-II flux spectrum. The results indicate that the capture cross section of ^{121}Sb in EBR-II will be about 70 mb, as compared to about 200 mb for ^{197}Au . A capture cross section of 70 mb will produce sufficient ^{122}Sb to be detectable.

A preliminary evaluation has revealed that another set of tags might be constituted from the isotopes ^{197}Au and ^{198}Pt . A method based on these tags would operate on the same general principles as the antimony-gold method. In this case, however, tag identification would be made on the basis of the $^{198}\text{Au}/^{199}\text{Au}$ ratio. The ^{199}Au is produced by the reactions



Estimations of the capture cross section of ^{198}Pt in EBR-II, made by the method described above, indicate a value of the same magnitude as that of ^{121}Sb , namely, about 70 mb.

One attractive feature of the platinum-gold tagging method is that tag identification is made on the basis of the ratio of two isotopes of gold. Since no difference would be expected in the behavior of the two isotopes, no alternation of the $^{198}\text{Au}/^{199}\text{Au}$ activity ratios would occur as a result of instability.

(ii) Sodium Loop--Tag Confirmation Study (J. T. Holmes)

Last Reported: ANL-7553, p. 49 (Feb 1969).

Installation and helium leaktesting of piping for the sodium loop have been completed. Work is proceeding on the installation of heaters and insulation, and on the checking of the instrumentation.

*Moldauer, P. A., Engelbrecht, C. A., and Duffy, G. J., NEARREX, A Computer Code for Nuclear Reaction Calculations, ANL-6978 (1964).

n. Materials-Coolant Compatibility (D. W. Cissel)

- (i) Examination of Reactor Parts (W. E. Ruther, T. D. Claar, and S. Greenberg)

Last Reported: ANL-7561, p. 43 (March 1969).

(a) Secondary-system Piping. The inner surface of the section of vent line 2-31-549 was removed to a depth of 0.003 in., and the chips were analyzed for carbon and nitrogen. Chips from the center of the pipe wall were included as controls. Carbon was analyzed as 0.13 w/o in the surface cut and 0.06 w/o in the control. The corresponding values for nitrogen were 0.022 and 0.021 w/o.

A very thin deposit, brushed off the inner surface of the pipe, was dissolved in 6N HCl, and the solution was spectrochemically analyzed. The major constituents were found to be Fe, Cr, and Ni in the ratio of 20:4:1. The accuracy of the analysis was not adequate to decide if this was a meaningful deviation from the 9:2:1 ratio for Type 304 stainless steel.

The results of this examination show that the piping appears to be in excellent condition with slight compositional changes limited to within 0.002 in. of the inner surface, which is in contact with the sodium.

(b) Inconel Rupture Disc. The first of two rupture discs in series on one of the headers of the secondary-sodium system of EBR-II leaked, allowing sodium to trip an alarm. The disc was perforated about 3/4 in. up from the circumferential holddown ring, leaving a network of thinned metal and open areas, about 1/2 in. in diameter. When initially separated from its vacuum support and backup cover, the perforated area was covered with a hard, crusted corrosion product that had restricted the flow of sodium. Qualitative analysis of the crusted corrosion product revealed no elements extraneous to Inconel. A rough check of the Curie temperature for the disc material verified that it was Inconel.

Microscopic (transverse section) examination of the corroded network section in the as-polished condition indicated extensive intergranular penetration, cracking, and loss of whole grains in most areas. In other areas, the metal was rather smoothly corroded and showed little indication of intergranular penetration. The original perforation could not be pinpointed within the network area. Most of the attack on the metal occurred from the air side of the rupture disc.

A microprobe analysis of the metal in the perforated area indicated a significant increase in the carbon content of the grain boundaries as compared with the uncorroded disc, substantiating a suggestion

made by C. R. Sutton that the Inconel was likely to have suffered embrittlement as a result of carbonaceous contamination--a drop of thread lubricant, for example--during assembly.

It appears that the small initial perforation, possibly a crack, permitted sodium to react with the atmosphere on the outside of the disc, forming Na_2O and NaOH . These compounds, in combination with the metallic sodium present, reacted with and cracked the disc metal around the original site. The fact is well-established that caustic solutions of more than 92 w/o concentration will cause stress cracking of Inconel at elevated temperatures.

o. Study of Operation with Failed Fuel (R. R. Smith)

(i) The Origin of the December 24, 1968, Fission-product Release (R. M. Fryer)

Last Reported: ANL-7548, pp. 38-39 (Jan 1969).

Following the shutdown of the primary pump at the completion of Run 32B on December 24, 1968, a fission-product release occurred. The release was indicated by a gradual buildup of ^{135}Xe activity. Because no evidence of a step increase in activity was noted, the defect was at that time concluded to involve the slow extrusion of bond sodium that contained chemically fixed iodine species. These species, after their release to the primary-coolant system, subsequently decayed to their respective xenon daughters.

Control-rod Subassembly L462, previously identified as containing a fuel element with a cladding defect, was eliminated as a suspect because it had been removed from the core seven days earlier.

The time-dependent behavior of the ^{135}Xe activity at the end of Run 32B has been illustrated graphically in Fig. I.E.2 on page 39 of ANL-7548. In that illustration, a separation of the net release of ^{135}Xe on December 24 was effected by subtracting calculated values for the normal ^{135}Xe activity (from tramp sources) from experimentally established data. An inspection of the shape of the buildup curve for the release of ^{135}Xe demonstrates conclusively the existence of a bond-release mechanism.

As an illustration of the manner in which a bond release affects the shape of the time-dependent buildup curve for ^{135}Xe , experimental values of the ^{135}Xe activity are compared in Fig. I.D.16 with expected values for an instantaneous release of bond sodium and for a complete bond release that takes place over a period of 12 hr.

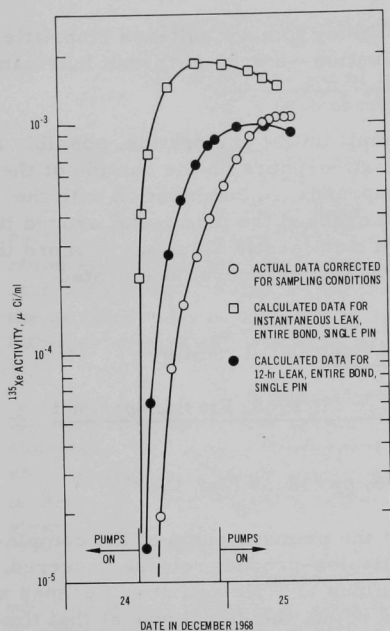


Fig. I.D.16. Comparison of Measured ^{135}Xe Activity with That Calculated for an Instantaneous and a 12-hr Bond Leak

The similarities that exist between the amplitudes and shapes of the actual and the 12-hr buildup curves suggest that the bond release was gradual rather than instantaneous. From this information and a knowledge of coolant-pump pressure, it was concluded that the defective element would refill with sodium prior to the next reactor startup when the coolant pumps were turned on.

Because no release of this magnitude after pump shutdown had been noted in runs just preceding Run 32B, the tentative conclusion was made that the driver subassemblies installed in the core for Run 32B were the most suspect sources. These subassemblies were C2008, C2181, C2182, L473, and C2136.

Subsequently, the xenon data from each reactor shutdown following Run 32B were analyzed for evidence of further releases. The conclusions from these analyses were crosschecked against routine reactor fuel-loading changes.

The important data and conclusions collected during this phase can be summarized as follows:

Run 32C. At the start of this run, C2136 was removed from the core. Purging of the reactor cover gas after run shutdown prevented any conclusion as to whether the leaker was still present.

Run 32D. A short pump shutdown at the end of this run resulted in a small release. Because C2136 was not in the core, it was eliminated as a suspect. After Run 32D, C2008 was removed from the core, whereas C2181, C2182, and L473 remained.

Run 33A. Analysis of shutdown data on March 5, March 12, March 15, and March 29 did not reveal a release. Figure I.D.17 showing the March 26 through March 29 xenon data, is presented as typical of the Run 33A shutdowns. The very close agreement between calculated normal tramp xenon and the actual data led to the conclusion that the leaker was not in the core during Run 33A. Because C2181, C2182, and L473 were in

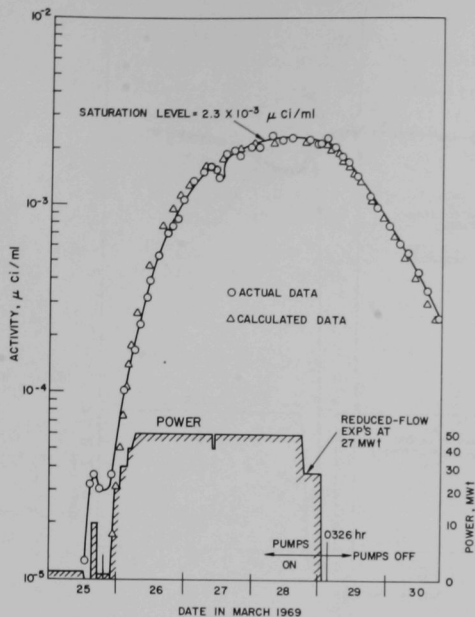


Fig. I.D.17. Comparison of Measured and Calculated ^{135}Xe Activities during Run 33A; No Leaker in Core (Run 33A, C2008 not in the core)

the core, they were absolved, and Subassembly C2008 became the principal suspect.

Run 33B. For Run 33B, C2008 was installed in core position 3E2. A scram shutdown of the reactor on April 18 and final shutdown on April 22, both followed by pump shutdown, resulted in activity releases. Figures I.D.18 and I.D.19, respectively, illustrate the xenon data taken on those dates. The net xenon activity from the leaker is clearly evident from the information given in those figures.

After Run 33B, C2008 was transferred to the Fuel Cycle Facility for dismantling and inspection. The experience with C2008 confirms calculations (see ANL-7548, p. 39) that indicated that a Mark-IA driver-fuel element having a defect at

the spade end cannot unbond during power operation when the primary coolant pumps are on. The fission-product release from C2008 is regarded as a typical example of a loss-of-bond type of cladding defect. For such a defect, iodine-rich bond sodium is extruded from the element as a result of the sharp reduction in coolant pressure that occurs when the primary pumps are turned off.

p. Driver Fuel Transient Performance Studies--TREAT Experiments

(i) Mark IA Fuel TREAT Experiments (A. B. Rothman)

Last Reported: ANL-7561, p. 44 (March 1969).

The TREAT test series with Element BF05 has been completed. Prior to TREAT study, the element, which had a nominal burnup of 2.5 a/o, had swollen to the restrainer cap.

In TREAT, the cladding of Element BF05 failed mildly on the fourth transient at about 860°C , a somewhat lower failure temperature than that for Element E34 (see Progress Report for January 1969, ANL-7548, p. 55), the fuel element with 1.2 a/o burnup. A fifth transient with BF05 caused a more severe cladding failure.

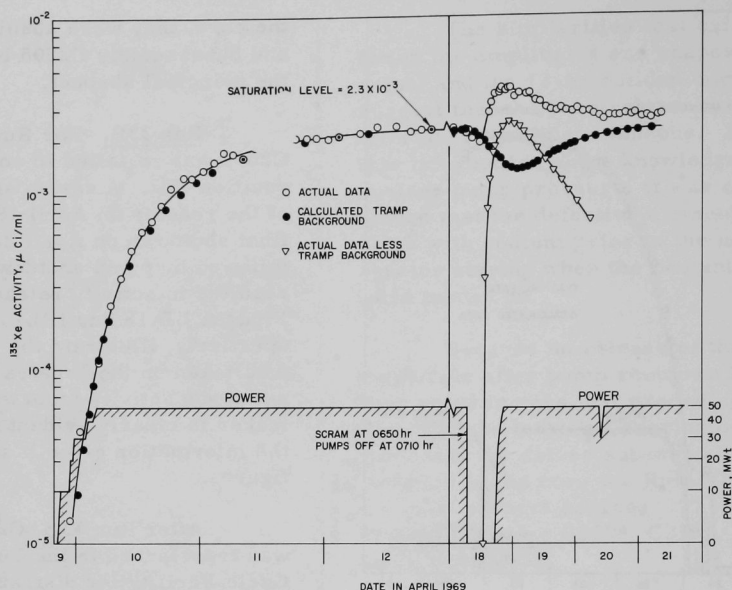


Fig. I.D.18. Separation of the ^{135}Xe Component Originating from a Sodium-bond Release on April 17, 1969, during Run 33B

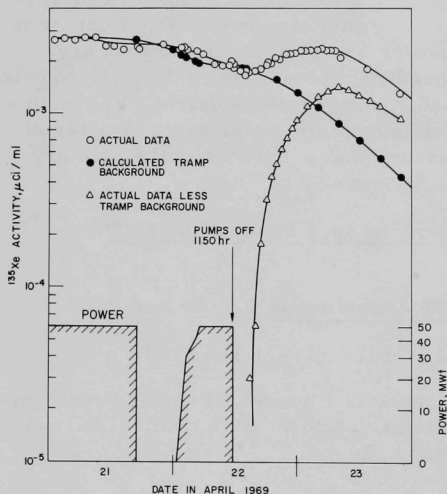


Fig. I.D.19. Separation of the ^{135}Xe Component Originating from a Sodium-bond Release on April 22, 1969, at End of Run 33B

The test capsules for Elements BF05 and E34 have been disassembled, and post-test examination of the pins and motion-detector data are in progress. The high temperatures of cladding failure and preliminary examination of the pins suggest that the mechanism of expansion of trapped sodium may not be a serious consideration. The cladding of Element E34 failed at the fuel midplane in a manner similar to that in previous tests of pre-irradiated fuel with lower swelling properties. The cladding of Element BF08 failed at the top of the element, evidently from expansion of the fuel pin against the top restrainer. This failure appeared to occur after the pin reached peak power. In both

cases, molten fuel was expelled from the fuel element. The molten fuel from Element E34 collected on the lower transducer; the molten fuel from Element BF05 collected between the element and the upper motion transducer.

q. Systems Engineering (B. C. Cerutti)

(i) Surveillance, Evaluation, and Studies of Systems

Last Reported: ANL-7553, pp. 53-54 (Feb 1969).

(a) Study of Fusible Alloy in EBR-II Rotating-plug Seals
(T. F. Kassner and C. A. Youngdahl)

A phase-diagram study of the Na-Bi-Sn system was made to provide information concerning the effect of sodium ingress on the melting point of the fusible alloy used in the EBR-II rotating-plug seals. The liquidus curve for the isopleth between the Bi-Sn eutectic alloy and sodium was determined by differential thermal analysis for a range of compositions between 0 and 60 a/o sodium.

Twenty-four alloy compositions were prepared in tantalum capsules by weighing desired amounts of the eutectic alloy and sodium in a helium-atmosphere glovebox. The capsules, each containing ~1.5 g of alloy, were heated to ~270°C and stirred to promote homogeneity. Tantalum capsules were also filled with the Bi-Sn eutectic alloy, indium, tin, bismuth, lead, and zinc to serve as standards for calibration of a modified Fisher series 200A Differential Thermalizer. Similar capsules with a Bi-Sn-In ternary eutectic alloy (mp 78.8°C) were used as a reference in the thermal-analysis apparatus.

Thermograms obtained from the standards when cooling at a rate of 5°C/min agreed within $\pm 0.5^\circ\text{C}$ of the reported melting points.

One of the standard materials was run simultaneously with the Na-Bi-Sn alloys so that appropriate corrections of $\sim 1^\circ\text{C}$ could be applied to the thermal-arrest temperatures. For sodium concentrations below 18 a/o, the Bi-Sn eutectic alloy standard was used; at higher sodium concentrations, bismuth or tin standards were included. Before a cooling run, the alloy specimens were held at 600°C for 1 hr and stirred occasionally to ensure that all the sodium was in solution and that the alloy was homogeneous. Selective oxidation of sodium in the samples was reduced by placing the furnace in a glovebox and by using purified helium as the cooling gas fed to the furnace. Several heating and cooling runs were made for each of the samples listed in Table I.D.32. The thermal-arrest temperatures obtained on cooling are reported and represent average values from two or three runs.

TABLE I.D.32. Differential-thermal-analysis Data for Na-Bi-Sn Alloys that Form an Isopleth between the 57 w/o Bi-43 w/o Sn Eutectic Alloy and Sodium

Sodium in Alloy ^a		Thermal-arrest Temperatures on Cooling (°C)	Sodium in Alloy ^a		Thermal-arrest Temperatures on Cooling (°C)
(w/o Na)	(a/o Na)		(w/o Na)	(a/o Na)	
0.0	0.0	139	4.65	25.2	333, 127
0.48	3.2	137.5	5.17	27.3	338, 161, 125
0.67	4.4	137	5.89	30.1	344, 183
1.07	6.9	135	7.06	34.3	341, 197
1.41	9.0	136	8.10	37.8	339, 328, 216
1.62	10.2	131	8.75	39.7	330, 216
1.99	12.2	130.5	10.0	43.5	330, 216
2.44	14.7	133	11.3	46.7	337, 326, 217
2.73	16.2	126.5	12.7	50.0	343, 330, 218
3.23	18.7	308, 128	14.3	53.5	337, 324, 217
3.51	20.0	310, 133, 125	15.9	56.5	327, 219
4.11	22.9	324, 125	18.0	60.3	336, 327, 218

^a The ratio of bismuth to tin in the alloy samples was maintained at a constant value set by the binary eutectic composition.

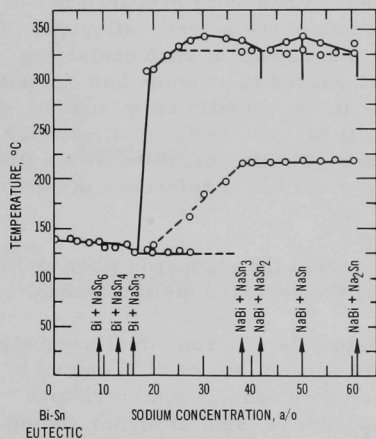


Fig. I.D.20. Portion of the Isopleth between the 57 w/o Bi-43 w/o Sn Eutectic Alloy and Sodium

The data, which are plotted in Fig. I.D.20, indicate a significant decrease in the liquidus temperature as the sodium concentration approaches ~16 a/o, followed by a sharp increase in temperature at higher sodium concentrations. These results suggest a possible ternary eutectic in the system at a composition of ~15 a/o sodium.

The vertical lines indicate the sodium compositions at which tie lines between the specified single-phase regions (in a low-temperature isothermal section) intersect the isopleth. No experimental evidence was obtained to verify that the two-phase equilibria were chosen correctly other than the correspondence between minima (e.g., at 41.5 and 61 a/o Na) and the maximum (50 a/o Na) in the liquidus curve, and the constant thermal-arrest

temperature of 218°C for sodium concentrations greater than ~38 a/o. Metallography and X-ray analysis work to develop other features of the phase diagram was not attempted because of oxidation problems with the reactive alloy samples.

(ii) Secondary and Power Systems Improvements

Last Reported: ANL-7553, pp. 54-56 (Feb 1969).

(a) Instrument-air System (H. W. Buschman)

On August 23, 1968, an exhaust valve failed in the No. 2 air compressor. The compressor was shut down and the No. 1 compressor placed in operation. Reverse flow through the No. 2 compressor then occurred, resulting in a rapid reduction of instrument-air pressure. The loss of pressure was detected immediately, and the failed compressor was isolated in time to prevent failure of the instrument-air system.

A review of operational logs revealed that similar valve failures had occurred in the past. Two piston-controlled check valves specifically designed for pulsating pressure service was procured from the manufacturer of the valves, Daniel Industries, Inc. One was installed in each of the outlet lines from the instrument-air compressors. The two valves have operated satisfactorily for a total of 1000 hr to date.

(iii) Instrumentation Improvements (R. E. Rice and H. H. Hooker)

Last Reported: ANL-7553, p. 56 (Feb 1969).

Preliminary proposals for the following instrumentation-improvement projects for FY 1969 Modifications of EBR-II and Related Facilities have been sent to the AEC for review and approval: (a) improved alarm and control system; (b) steam-generator instrumentation; (c) improved sodium-level sensor; (d) improvement of fission-product-monitoring systems; and (e) upgrading of shutdown circuit.

(a) Improved Alarm and Control System (F. H. Just)

Many alarms and control actions in the existing primary-purification, secondary-sodium, steam, and water systems are initiated by switches that are in turn actuated by servo-actuated indicator or recorder mechanisms. The work proposed in this modification consists of revising about 30 channels of this kind to separate the alarm and control functions from the indicator or recorder mechanisms. Alarm and control then will not depend on a servo-actuated indicator or recorder.

The existing servo-actuated units can fail "as is," which invalidates the alarm and control functions. The proposed electronic amplifier and switches have a failsafe feature that provides for either up-scale or downscale indication if the detecting device fails. The proposed system separates the three functions--recording (or indicating), control, and alarm--into independently operated functions and eliminates the existing arrangement where the alarm, control, and indication are incorporated in

(b) Steam-generator Instrumentation (H. H. Hooker)

To evaluate the performance of the EBR-II superheaters, more data are needed on the operating characteristics of the individual units. The existing steam-generator instrumentation is not capable of providing the type or quality of data needed for adequate analyses of performance.

This modification covers the installation of two sodium-flow sensors and two steam-flow sensors with associated transducers, piping, and valves; one pressure transducer with associated piping and valves; one calorimeter for steam quality; and up to 30 thermocouples. Data acquisition will be provided by the existing automatic data logger (ADL) and a future digital data-acquisition system.

Steam-generator (evaporator and superheater) performance is of particular interest because of its potential to limit reactor operation. Changes in performance could have serious effects on the reactor, particularly during power changes, because the secondary sodium returning to the main heat exchanger affects the reactor inlet temperature. Data on the performance of individual EBR-II system components also will provide a firmer basis for the design of steam-generating components for large LMFBR plants.

(c) Improved Sodium-level Sensor (L. J. Christensen)

A new kind of sodium-level sensor, which employs a displacer suspended from a load cell, has been developed and tested with success in the EBR-II primary tank. The displacer compensates for changes in density with temperature. The weight measured by the load cell is an inverse linear function of the amount of sodium displaced (or the height of the sodium in the tank). The output signal from the load cell is linearly proportional to the suspended weight. The load cell is designed for a range from 0 to 50 lb. The range of levels covered is 284 to 304 in.

Test and evaluation information gathered with the prototype probe indicate that use of the improved design will reduce reactor downtime for maintenance. It is proposed that a second sodium-level sensor of the new design be added to the primary tank to provide a redundant unit.

(d) Improvement of Fission-product-monitoring Systems
(L. J. Christensen)

Three instrument subsystems are now responsive to the presence of fission products in the reactor coolant and cover gas: (1) fuel-element-rupture detector (FERD), (2) fission-gas monitor (FGM), and (3) reactor cover-gas monitor (RCGM). The proposed work includes modernization and standardization of the electronic components and reduction

of the number of different kinds of components, such as low-voltage power supplies and amplifiers, in the FERD and FGM systems.

The FERD system has been a source of spurious scrams. The present equipment requires much maintenance, lacks redundancy, and has individual units that are not entirely mutually compatible. The proposed equipment will provide three completely independent channels, thus ensuring against a reactor scram from a single component failure. The new system should also decrease maintenance time and increase repeatability of measurement and system reliability. Increased system reliability will be provided with bin-type solid-state instrumentation.

The FGM, EBR-II's most sensitive system for online monitoring of fission products, has proved invaluable in detecting and diagnosing fission-product releases. The present system is an outgrowth of experimental equipment tested at EBR-I, and needs changing to provide standardization throughout the plant to reduce the number of spare parts and types of maintenance functions performed. Signal drift occurs, and frequent maintenance is required to ensure proper operation. The proposed work includes modernizing and upgrading the instrumentation, and providing an equipment cabinet for the mechanical components. The modification should increase reliability and accuracy while reducing maintenance. The new system will provide two independent channels of information for redundancy.

(e) Upgrading of Shutdown Circuit (L. J. Christensen)

The proposed work is oriented toward the replacement of the existing startup and intermediate channels with wide-range (10-decade) nuclear channels. It may be expanded to cover the existing power-level channels.

Reactor protective functions now performed by the nine channels in the startup, intermediate, and power ranges possibly will be assumed by the new wide-range channels. This modification will reduce the number of trip devices connected to the reactor shutdown circuit by reducing the number of auxiliary units, such as power supplies, that are required. In addition, the high-maintenance effort associated with the present channels should be greatly reduced.

It now appears possible to cover the 10-decade range of reactor power by using a single detector and wide-range counting-campbelling system. By use of the wide-range systems, three channels might be able to perform the necessary functions, including protective trips, that are now provided by the nine existing channels. The number of shutdown-circuit trip contacts would be reduced from 52 to 24. The total number of nuclear channels could be reduced from 11 to 5, the number of power supplies from 9 to 7, and the number of detectors from 11 to 5.

r. Oxide Driver (G. H. Golden)

Last Reported: ANL-7561, pp. 46-48 (March 1969).

(i) Temperature Distribution and Doppler Effect of Mechanically Mixed Oxide Fuels (R. K. Lo)

A transient-heat-transfer computer code (THTB) is being used to determine the temperature distribution and effective Doppler reactivity of a heterogeneous fuel of PuO_2 and UO_2 . The diameter of the fuel rod being considered is 0.25 in., the cladding is 0.015 in. thick, the size of the PuO_2 particles is $20\ \mu$, and the size of the UO_2 particles is $500\ \mu$.* The contact conductance between PuO_2 and UO_2 particles is $4000\ \text{Btu/hr-ft}^2\text{-}^\circ\text{F}$, and that between UO_2 particles and the cladding is $1500\ \text{Btu/hr-ft}^2\text{-}^\circ\text{F}$. The heat-transfer coefficient between flowing sodium and cladding is $1400\ \text{Btu/hr-ft}^2\text{-}^\circ\text{F}$. The linear heat generation is $16\ \text{kW/ft}$. The power density in the plutonium is assumed to be 97%, and that in the uranium 3%. The power trace calculated by the SASIA code,** using a reactivity insertion ramp of 50 cents per sec, is as follows:

Time, sec	0	0.4	0.8	1.2	1.6
Normalized power	1.0	1.6	3.2	5.5	10.5

Using the tabulated power-trace data and the heat-generation rate of $16\ \text{kW/ft}$ as input to the THTB, one obtains the temperature distribution in the PuO_2 and UO_2 particles. At steady-state conditions, the center temperature is about 5000°F . The calculated volume-weighted average temperatures are shown in Fig. I.D.21 (the terms q in the figure are in Btu/hr-ft^3). It can be seen that at no time does the volume-weighted average temperature of PuO_2 lag behind that of UO_2 for this case.

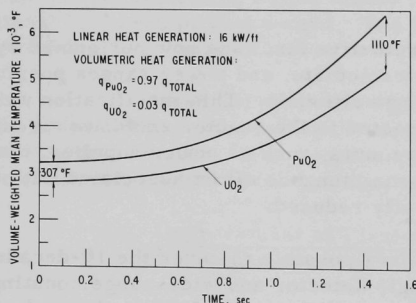


Fig. I.D.21

Transient Average Temperature
of PuO_2 and UO_2

*The particle sizes have been modified.

**Private communication from N. McNeal, May 1, 1969.

2. Operations

a. Reactor Plant (G. E. Deegan)

Last Reported: ANL-7561, pp. 48-50 (March 1969).

The reactor was operated for 1820 MWd in Runs 33A, 33B, 34A, and 34B from March 21 through May 20. This raised the cumulative total of reactor operation to 25,043 MWd.

The plant had been shut down by a rupture-disk failure in the secondary system before the start of this period. Both disks in the north rupture-disk assembly were replaced, and the assembly was reinstalled and checked. A normal plant heatup from ambient temperature to 580°F was then accomplished, after which heat-balance tests were conducted at 580°F. Reactor power was used to heat the primary tank to 700°F. While raising power above 10 MWt, the water level in the steam drum could not be maintained, so power was immediately reduced. An isolating valve in the condensate system had been closed while pressurizing the No. 2 feed-water heater; after this valve was opened, power was raised to 50 MWt.

After the end of Run 33A, on March 29, the rotating-plug seal troughs had to be cleaned. Final cleaning was in progress following fuel handling for Run 33B when a small sodium fire broke out in the room containing the cold trap of the primary purification system. A sodium sample was being taken from the primary system at the time. The sampling loop and purification system were shut down. The fire, caused by a steady dripping of sodium from the sampling-pump area, was extinguished in about 4 hr. Damage was limited to the sampling loop; there were no personnel injuries or spread of contamination.

The source of the sodium leak was traced to a failure of the tube of the electromagnetic sampling pump where one of the electrodes was brazed to it. The pump tube was replaced by a piece of tubing; samples are being taken by using the head developed by the main pump of the purification system.

Cleaning of the seal trough was completed and the reactor was started up on April 7. Analysis of previous operating history indicated that Subassembly C2008, a half-worth driver, might be the source of the intermittent, small fission-product releases observed in recent months. Loading for Run 33B included the installation of this subassembly in the reactor to check this theory.

Fifty-megawatt operation was attained on April 10 and continued until April 18, when a spurious scram occurred. The primary pumps were shut down for 6 hr while the primary-tank cover gas was closely monitored

for an increase in ^{133}Xe and ^{135}Xe . Soon after the primary pumps were re-started, a step increase in these activities confirmed a fission-product release and indicated that C2008 was probably the source of the release. Power operation was then resumed and continued until the FERD instrumentation developed erratic behavior, causing a scram, and becoming too unstable for continued reactor operation. Run 33, therefore, was terminated on April 22, after accumulating 1126 MWd of operation.

During fuel handling for Run 34A, extensive maintenance was performed on the FERD system. Separate power supplies were provided for each FERD channel, and new cables were installed and rerouted to the cable-routing room. During Run 33, each channel had consisted of two BF_3 chambers. The existing chambers were left in channel A, the chambers in channel B were replaced by four B-10 detectors, and two new BF_3 chambers were placed in channel C.

During fuel handling for Run 34A, all four surveillance sub-assemblies containing vendor-produced fuel were removed from the core when postirradiation examination of the lead subassembly revealed some shortening of the fuel. Routine physics experiments, which were conducted on April 29 at the beginning of Run 34A, were followed by uninterrupted 50-MWt operation until the midrun shutdown on May 13.

Fuel handling for Run 34B consisted of removing a 70%-enriched subassembly and installing a special subassembly with a known defect in the upper cladding weld. Physics experiments were performed at the beginning of Run 34B. The run is continuing at 50 MWt.

b. Fuel Cycle Facility (M. J. Feldman)

Last Reported: ANL-7561, pp. 50-56 (March 1969).

(i) Fuel Production

(a) Hot Line (N R. Grant)

Table I.D.33 summarizes production activities for March 16 through May 15, 1969, and for the year to date. The final production activities in the hot line have been completed. The last subassembly made from hot-line-produced fuel was C2192.

(b) Cold-line Production and Assembly (D. L. Mitchell)

Table I.D.34 summarizes the production activities for March 16 through May 15, 1969, and for the year to date. A total of 941 acceptable pins has resulted from ten Mark-II injection-casting batches.

Five of these batches (~100 pins/batch) have been loaded into jackets and leaktested. The acceptance rate for eddy-current bond and level testing of the two batches tested to date is higher (96%) than normally experienced with Mark-I fuel.

TABLE I.D.33. Production Summary for FCF Hot Line
(All hot-line production operations have been discontinued.)

	3/16/69 through 5/15/69	Total This Year
Subassemblies received		
Core, control, and safety	24	35
Other	1	5
Subassemblies dismantled for surveillance or examination	30	64
Subassemblies transferred		
To reactor	16	27
To L&O vault and interbuilding corridor for storage	0	0
Subassemblies transferred to ICPP for storage	0	1
Subassemblies returned from ICPP storage	0	2
Subassemblies fabricated	9	21
<u>Processing</u>		
Elements processed		
Accepted	0	1115
Rejected	0	291
Elements welded	100	1519
Elements rewelded	0	0
Elements leaktested		
Accepted	235	1588
Rejected	1	64
Elements bonded (including recycle)	356	2261
Elements bondtested		
Accepted	834	2226
Rejected	37	181
Elements to surveillance	795	1933
Number from subassemblies	21	50
<u>Fuel-alloy and Waste Shipments</u>		
Cans to burial ground	4	13
Oxide and glass scrap to ICPP	0	2
Recoverable fuel alloy to ICPP		
Fuel elements	4 (70.4 kg of alloy)	14 (243.4 kg of alloy)
Subassemblies	1 (5.8 kg of alloy)	2 (11.7 kg of alloy)
Nonspecification material	0	4 (71 kg of alloy)

TABLE I.D.34. Production Summary for FCF Cold Line

	3/16/69 through 5/15/69		Total This Year	
	Mark IA	Mark II	Mark IA	Mark II
Alloy-preparation runs				
New fuel	0	7	1	7
Remelts	0	3	5	3
Total	0	10	6	10
Injection-casting runs	0	10	6	10
Pins processed				
Accepted	0	941	758	941
Rejected	0	53	27	53
Elements welded	0	534	1,707	534
Elements rewelded	0	0	0	0
Elements leaktested				
Accepted	196	333	1,705	333
Rejected	0	15	40	15
Elements bondtested				
Accepted	356	182	1,730	182
Rejected	38	2	262	2
Subassemblies fabricated (cold-line Mark-IA fuel)	7	-	10	-
Elements received from vendor	7,301	-	22,138 ^a	-
Inspected and accepted	6,718	-	18,454 ^a	-
Inspected and rejected	254	-	1,200 ^a	-
Subassemblies fabricated (vendor fuel)	1	-	2	-
Total elements available for subassembly fabrication as of 5/15/69				
Cold-line fuel				
Mark IA	970			
Mark II	182			
Vendor fuel (all Mark IA)	17,779			

^aTotal includes figures for 1968.

(ii) Inspection of Vendor Fuel (D. L. Mitchell)

A summary of the data relating to receipt and acceptance of fuel produced by Aerojet-General Corporation is included in Table I.D.34. The acceptance rate for the ANL verification inspection of the fuel has continued to be greater than 95%.

(iii) Surveillance (M. J. Feldman, J. P. Bacca, and E. R. Ebersole)

(a) Chemical Analyses (E. R. Ebersole)

The number of fuel-product analyses of hot-line, cold-line, and vendor-fuel samples made during the reporting period, together with the average values and ranges, are shown in Table I.D.35.

TABLE I.D.35. Analyses of Fuel-product Samples

Analyzed for	Number of Analyses	Average Value	Range
Total U ^a	15	94.85 w/o	94.47-95.54
²³⁵ U (% of total U) ^a	15	64.10 w/o	63.95-64.20
Total U ^b	7	95.38 w/o	95.04-95.64
²³⁵ U (% of total U) ^b	7	51.92 w/o	51.71-52.10
Mo	27	2.51 w/o	2.34-2.61
Ru	27	2.01 w/o	1.84-2.10
Rh	27	0.277 w/o	0.253-0.291
Pd	27	0.192 w/o	0.169-0.206
Zr	33	0.133 w/o	0.058-0.290
Nb	20	0.010 w/o	0.007-0.011
Si	26	414 ppm	50-590
Al	12	83 ppm	45-161
C	14	240 ppm	83-394
Cr	16	38 ppm	32-50
Fe	19	112 ppm	89-150
Ni	16	87 ppm	48-188
Total Analyses	308		

^a64%-enriched fuel.^b52%-enriched fuel.

Analyses for surveillance of irradiated fuel pins from the reactor during the reporting period are shown in Table I.D.36.

TABLE I.D.36. Analyses of Irradiated Fuel Pins

Analyzed for	Number of Analyses	Average Value	Range
Total U	7	92.63 w/o	92.61-92.66
Mo	3	2.53 w/o	2.46-2.57
Ru	4	1.94 w/o	1.88-1.99
Rh	3	0.272 w/o	0.265-0.282
Pd	3	0.194 w/o	0.190-0.204
Zr	24	0.170 w/o	0.125-0.230
Nb	18	0.010 w/o	0.006-0.014
Cr	3	38 ppm	33-44
Fe	3	156 ppm	127-212
Ni	3	174 ppm	163-192
Si	4	375 ppm	251-512
Tc	17	405 ppm	257-459
Burnup	33	1.61 a/o	0.40-2.14
Total Analyses	125		

(b) Postirradiation Analysis of EBR-II Fuel (J. P. Bacca)

(1) Surveillance of Vendor-produced Fuel. Postirradiation examination of fuel elements produced by Aerojet-General Corp. (AGC) has revealed shortening of the fuel pins in these elements after they have been irradiated to between 0.2 and 0.6 a/o fuel burnup.

The shortening was first observed for fuel pins from Subassembly C2178, which had obtained 0.6 a/o burnup. This subassembly had been designated as the "lead" subassembly of five subassemblies in the program designed to qualify the vendor fuel for use in EBR-II. The remaining four subassemblies of this program then were removed from the reactor core. Of these subassemblies, three (C2181, C2183, and C2189) have been disassembled and subjected to postirradiation examination. The fourth subassembly (C2182) had received 0.5 a/o burnup and is being held in the primary-tank basket.

Table I.D.37 shows the lengths of the fuel pins from the subassemblies examined, as determined by eddy-current techniques. From these data, three salient points become apparent:

1. The shortening is a function of AGC fuel manufacturing and not a function of abnormalities introduced during the handling or irradiation of the subassemblies. This is evidenced by the normal behavior of FCF cold-line fuel irradiated along with vendor-produced fuel in C2183.
2. The degree of shortening appears to be a function of irradiation (burnup) of the fuel, because the amount of shortening is approximately proportional to atom percent of burnup over the range of the subassembly burnups (0.2-0.6 a/o).

TABLE I.D.37. Postirradiation Measurements of Length of Pins Made from Vendor-produced Fuel (nominal length of as-fabricated fuel pin: 13.500 ± 0.032 in.)

AGC Casting Batch No.	Number of Elements	Length of Fuel Pin (in.)		AGC Casting Batch No.	Number of Elements	Length of Fuel Pin (in.)	
		Average	Range			Average	Range
<u>Subassembly C2178, 0.60 a/o Burnup</u>				<u>Subassembly C2183, 0.48 a/o Burnup</u>			
100	2	12.75	12.7-12.8	100	20	13.5	All 13.5
100	8	13.5	All 13.5	100	9	13.18	12.9-13.4
107	10	12.76	12.7-12.8	107	11	13.14	12.8-13.3
112	13	12.66	12.6-12.8	112	17	12.81	12.6-13.0
114	8	12.83	12.6-13.1	114	24	12.88	12.7-13.1
115	39	12.75	12.6-13.1	119	6	12.76	12.7-12.9
119	<u>11</u>	<u>12.68</u>	<u>12.6-12.8</u>				
Total	91	12.81	12.6-13.5	Subtotal	87	13.06	12.6-13.5
<u>Subassembly C2181, 0.56 a/o Burnup</u>				FCF Cold- line Fuel	<u>4</u>	13.5	All 13.5
100	3	12.80	12.7-12.9	Total	91		
100	4	13.5	All 13.5	<u>Subassembly C2189, 0.18 a/o Burnup</u>			
107	12	12.79	12.7-12.9	100	6	13.5	All 13.5
112	11	12.67	12.6-12.8	100	6	13.25	13.2-13.3
114	10	12.81	12.6-12.9	107	8	13.24	13.2-13.3
119	11	12.76	12.7-12.9	115*	15	13.23	13.2-13.3
150	15	12.89	12.7-13.2	150	1	13.5	-
153	10	12.79	12.7-12.9	150	13	13.33	13.3-13.4
154	<u>15</u>	<u>12.77</u>	<u>12.6-13.1</u>	153	1	13.5	-
Total	91	12.82	12.6-13.5	153	29	13.30	13.2-13.4
				154	<u>12</u>	13.26	13.2-13.3
				Total	91		

3. All of the nine AGC batches of fuel from which the inspected fuel pins were made acted similarly with the exception of batch 100: approximately 65% (38 out of 58) of the fuel pins made from this batch did not shorten.

Examination of the irradiated fuel elements from Subassemblies C2178, C2181, C2183, and C2189 are continuing. In addition, reviews are being made of AGC manufacturing procedures to determine the differences that exist between their procedures and those used in the FCF cold line and what variations in AGC procedures may have existed during the fabrication of batch 100. Also being conducted are basic physical-metallurgical tests and examinations to determine differences between AGC and FCF fuel and between AGC batch 100 and the other AGC fuel batches.

The status of investigations within these three general areas is discussed below.

(A) Examination of Irradiated Elements and Fuel Pins

1. Neutron radiographs of representative elements from all four subassemblies were obtained at TREAT. These radiographs confirmed the length measurements obtained by eddy-current examination.

2. Fuel pins from 15 elements were removed from their stainless steel jackets, the adhering sodium on the pins was removed, and the diameter profiles of the pins were measured precisely. The lengths of the fuel pins also were measured to confirm previous data. Figure I.D.22 illustrates typical results of the diameter-profile measurements.

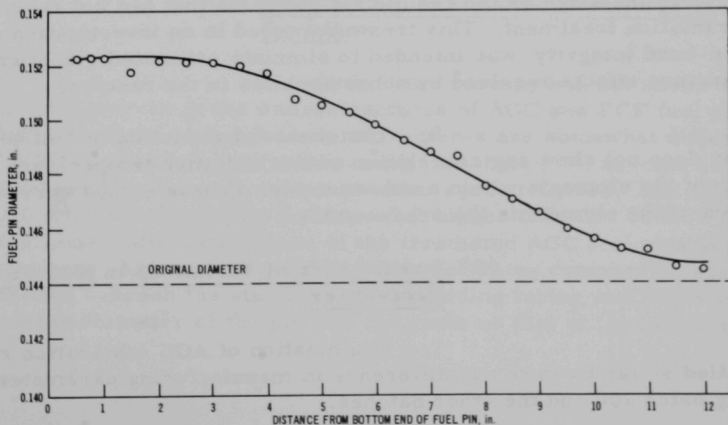


Fig. I.D.22. Diameter Profile of De jacketed Fuel Pin E25 from Subassembly C2175 (grid position, 4A1; burnup, 0.60 a/o; AGC casting batch 112; pin length, 12.7 in.)

These results show that an increase in fuel-pin diameter accompanies a decrease in pin length. In most cases, the largest increase occurred in the lower region of the fuel pin; however, in 3 of 15 pins measured to date, the largest diameter increase occurred in the upper portion of the fuel-pin length.

3. Measurements of the level of the bonding sodium by eddy-current techniques show that the volume swelling of the AGC fuel was comparable to that previously observed for FCF-produced fuel that had undergone similar burnup.

4. Precision measurements of the outside diameters of the elements (fuel pins plus cladding) did not show diameter increases (jacket straining) in any of the elements measured--even in the cases where the fuel pin was in intimate contact with the jacket.

5. The pressures of gas in the fuel-element plenums were measured and found to be at essentially ambient pressures, indicating that no fission gas had been released by the fuel pins. Analysis of the fission gas confirmed this premise in that the total quantity of fission gas (primarily xenon and krypton) found in the plenum can be accounted for by fission recoil from the surfaces of the fuel pins.

6. Axial gamma scans of the fuel elements showed a shifting of the peak activities in the direction toward the region of the pin with the larger diameter.

7. The results of postirradiation examination of AGC and FCF cold-line elements that had received a preirradiation vibration simulation (1-2 mils horizontal amplitude at 500°C for 12½, 24, or 72 hr) were the same as the results for elements that had not received this preirradiation treatment. This treatment, used in an investigation of sodium-bond integrity, was intended to simulate estimated vibration and temperature effects received by subassemblies in the reactor.

8. The observed reduction in fuel-pin lengths does not show any correlation with irradiation temperature or burnup of the elements within a subassembly. (These values vary with location of the element in the subassembly.)

(B) Investigation of Variations in Manufacturing Procedures

1. Examination of AGC fabrication records has failed so far to show any difference in manufacturing parameters for casting batch 100 and the other batches.

2. None of the chemical analyses of any AGC batches (including batch 100) show any significant differences or any variations from ANL fuel specifications.

3. Both AGC and FCF fuel pins are injection cast. Differences in furnace design may produce differences in casting or cooling parameters; however, neither the AGC nor the ANL furnace is adequately instrumented to provide data for complete analysis of these parameters.

4. The only step in which the AGC manufacturing operation differs significantly from the ANL process is the sodium-bonding step. In the AGC process, the fuel elements are bonded by a centrifugal process in which the elements are inclined at approximately 7° from the horizontal (top ends lower than the bottom ends). While being rotated, the elements are heated to 500°C in 1 hr, bonded at 500°C for 20 min, and then cooled to less than 100°C (the solidification point of sodium) in 20 min. In the FCF process, the fuel elements are vertical during all phases of bonding. They are heated to 500°C , while stationary, in 1 hr, bonded at 500°C by 1000 cycles of impact for 10 min, and then cooled, while stationary, to less than 100°C in 4-6 hr.

The most obvious differences between the two processes are: (a) centrifugal (AGC) versus impact (FCF) bonding; (b) in the AGC process, transformation of gamma to alpha phase in the fuel pin takes place while the fuel is under centrifugal force; in the FCF process, this transformation is complete before force is applied (by impact); (c) the cooling rate used in the AGC centrifugal-bonding process is much higher than the cooling rate used in the FCF impact bonders.

(C) Investigation of Physical Metallurgy of Fuel Pins

1. Optical microscopy has not shown any significant differences in the microstructures of AGC and FCF fuel pins as cast. However, their as-bonded microstructures are somewhat different in that the AGC alloy shows a structure much like that of the as-cast alloy and the FCF as-bonded alloys shows a somewhat aged structure. Microhardness of the AGC as-bonded fuel pins is somewhat higher than that of the FCF as-bonded fuel pins. Microstructures of the irradiated AGC fuel pins are very similar to those observed for FCF fuel pins following comparable burnup. No interaction between the stainless steel cladding tubing and fuel was seen, even when the diameter of the pin was the same as that of the inside of the jacket.

2. Electron microscopy using replica techniques showed a possibly higher degree of microtearing for irradiated AGC fuel than that observed for FCF fuel of comparable burnup. This information is very preliminary and is being investigated further.

3. Thermal coefficients of expansion, as determined by dilation tests, indicated differences between the coefficients for FCF fuel and AGC fuel. In addition, differences in the coefficients of samples from the tops and from the bottoms of both FCF and AGC fuel pins were observed. These studies were made on unirradiated, as-bonded fuel pins.

4. Thermal cycling of 2-in.-long sections of unirradiated, as-bonded AGC and FCF fuel pins for 675 cycles between 100 and 530°C resulted in the following length decreases:

AGC batch 107	0.0007 in.
AGC batch 100	0.0007 in.
FCF batch 0456	0.0012 in.
FCF batch 0457	no change

Another test, using a different temperature interval, is being planned.

5. Straightness measurements of unirradiated, bonded AGC fuel pins showed bowing ranging from 30 to 80 mils. Unirradiated, bonded FCF fuel pins showed less bowing, usually ranging from 6 to 30 mils.

(2) 50-MWt Surveillance Program. Postirradiation examinations of elements from Subassembly C2086 of the 50-MWt surveillance program were completed. This subassembly is the first of three comprising the Phase-II portion of this program. The calculated maximum burnup of C2086 was 0.83 a/o, all of which was accumulated at the 50-MWt power level in EBR-II. For elements in the subassembly that were fabricated from U-5 w/o Fs alloy having a silicon content of 230 ppm, the average swelling was 3.8% and the swelling range was from 2.8 to 4.6%. For elements utilizing fuel with a silicon content of 140 ppm silicon, the average swelling was 4.9% and the range was from 4.1 to 6.4%.

These values are very similar to those obtained in the past for driver fuel after it had been irradiated in EBR-II at a 45-MWt power level and also after it had been irradiated at both 45- and 50-MWt power levels.

(3) 70%-enriched Fuel Experiment. Subassembly C2175S, containing 70%-enriched fuel, was irradiated to a calculated maximum burnup of 1.23 a/o (1.03 a/o average) in reactor grid positions 4E1 and 4B1. Table I.D.38 shows the fuel swelling that took place in the elements

during irradiation. Average volume swelling of the fuel pins in all the elements of the subassembly averaged 6.6%. (Silicon content of the fuel ranged from 260 to 533 ppm.) Swelling of individual elements ranged from 4.7 to 8.1%. These data, shown with data for other subassemblies containing 70%-enriched fuel in Fig. I.D.23, indicate that irradiation swelling of the 70%-enriched fuel continues to be slightly higher than that shown in the past by similar 52%-enriched U-5 w/o Fs alloy (silicon content greater than 200 ppm) after comparable burnup. This slightly increased swelling rate is attributed to the higher irradiation temperatures experienced by the 70%-enriched fuel in the reactor.

TABLE I.D.38. Fabrication and Irradiation-performance Data for 70%-enriched-fuel Subassembly C2175S (Calculated burnup: 1.12 a/o max; 1.03 a/o avg)

Injection-casting Batch No.	Silicon Content of Fuel (ppm)	Number of Elements	Element-burnup Range (a/o)	Total Volume Swelling of Fuel ($\Delta V/V$, %)		Calculated Temperature Range at Centerline of Fuel ($^{\circ}\text{F}$)
				Average	Range	
0700	260	4	1.15-1.19	6.63	6.26-7.17	1148-1162
0701	533	4	1.15-1.20	7.60	6.86-8.11	1152-1170
0702	362	11	1.13-1.22	6.91	5.74-7.47	1127-1174
0703	407	25	1.12-1.23	6.72	5.23-7.96	1066-1174
0704	409	15	1.12-1.22	6.33	4.73-7.31	1076-1172
0705	437	32	1.12-1.23	6.43	4.88-7.50	1046-1176

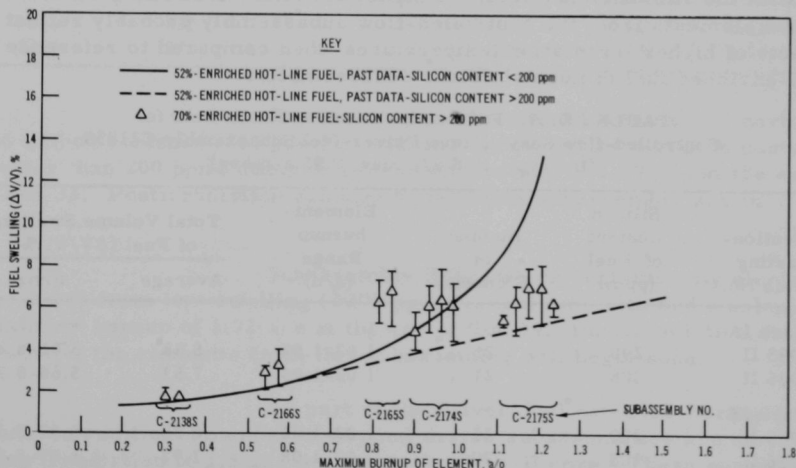


Fig. I.D.23. Swelling of 70%-enriched U-5 w/o Fs Alloy as a Function of Burnup

No interaction of fuel and cladding was observed during metallographic analyses of a high-temperature, high-burnup element from the subassembly. No jacket straining was indicated by

measurements of the outside diameters of selected elements. The latter result was expected because no contact of the fuel pin and the jacket in any of the elements was observed during postirradiation eddy-current tests for sodium bond and level.

Eighty-three of the 70%-enriched elements from C2175S were utilized in the fabrication of another subassembly, C2193S, along with eight 52%-enriched cold-line elements. Subassembly C2193S was then irradiated in EBR-II to a calculated maximum burnup of approximately 1.5 a/o during Run 34A. Postirradiation examination of these high-burnup elements will begin soon.

(4) Controlled-flow Experiment. Subassembly C2185S, the first subassembly of the controlled-flow subassemblies to reach target burnup, was irradiated to a calculated maximum burnup of 1.08 a/o (0.95 a/o average) in grid position 2C1 of the reactor core. Table I.D.39 summarizes the fuel swelling observed during postirradiation examinations. Average fuel-pin swelling for the Mark-IA elements in the subassembly was 7.0%; the range was from 3.0 to 8.8%. Average fuel-pin swelling for the Mark-IB elements was 7.3%; the range was from 5.7 to 8.8%. These swelling values are consistent with those observed for 70%-enriched fuel (shown in Fig. I.D.23) following comparable burnup. Calculated irradiation temperatures for the fuel elements in both types of subassemblies are comparable. As with the 70%-enriched fuel, the higher irradiation-swelling rates shown by the elements from the controlled-flow subassembly probably reflect the effects of higher irradiation temperatures when compared to reference 52%-enriched fuel of normal driver subassemblies.

TABLE I.D.39. Fabrication and Irradiation Data for
Controlled-flow Surveillance Driver-fuel Subassembly C2185S
(Burnup: 1.08 a/o max; 0.95 a/o avg)

Injection-casting Batch No.	Silicon Content of Fuel (ppm)	Number of Elements	Element- burnup Range (a/o)	Total Volume Swelling of Fuel ($\Delta V/V$, %)	
				Average	Range
Mark IA					
095 II	290	25	1.02-1.08	6.58	3.01-8.24
096 II	308	21	1.02-1.08	7.53	5.65-8.75
Mark IB					
095 II	290	25	1.02-1.08	6.86	5.67-8.23
096 II	308	20	1.02-1.08	7.97	6.09-8.82

(5) Driver-fuel Extended-burnup Program. Fuel elements from Subassembly C2164 were examined following irradiation to a calculated maximum burnup of 1.49 a/o (1.22 a/o average) in grid position 5D4 of the reactor core. This is the second driver subassembly that

has been irradiated to the 1.5-a/o level. The other subassembly was C2027 (see Progress Report for January 1969, ANL-7548, pp. 68-69), which attained a maximum burnup of 1.49 a/o during Run 32.

The results of postirradiation fuel-swelling measurements for C2164 are summarized in Table I.D.40. Average fuel-pin swelling for the subassembly was 6.4%; swelling of individual pins ranged from 3.3% to 7.8%. These values are very similar to those observed earlier for high-burnup Subassembly C2027 (mentioned above) and those depicted in the curve (broken line) for low-swelling alloy in Fig. I.D.23. It is noteworthy that the silicon content of the two fuel batches represented in C2164 was rather high (835 ppm and 920 ppm). From these data it can be tentatively concluded that irradiation swelling of U-5 w/o Fs alloy with a silicon content greater than specification (i.e., greater than 520 ppm) is very satisfactory to at least 1.5 a/o burnup.

TABLE I.D.40. Fabrication and Irradiation Data for
Extended-burnup Surveillance Driver-fuel Subassembly C2164
(Burnup: 1.49 a/o max; 1.22 a/o avg)

Injection-casting Batch No.	Silicon Content of Fuel (ppm)	Number of Elements	Element- burnup Range (a/o)	Total Volume Swelling of Fuel ($\Delta V/V$, %)	
				Average	Range
4263	835	47	1.33-1.49	6.56	3.28-7.82
4264	920	44	1.34-1.46	6.18	4.56-7.75

Subassembly C2065, which contains fuel having a low silicon content (<200 ppm) in addition to fuel having a silicon content greater than 200 ppm, attained a maximum burnup of 1.50 a/o at the end of Run 33. Postirradiation examinations of this subassembly are in progress.

Subassembly B362, which contains only elements fabricated from low-swelling (>200 ppm silicon) fuel, attained a calculated maximum burnup of 1.72 a/o at the end of Run 34. Postirradiation examinations of the elements from this subassembly will begin soon.

As part of the driver-fuel extended-burnup program, an additional number of normal driver subassemblies are now undergoing irradiation to 1.5 a/o burnup in the EBR-II core. These subassemblies represent both higher-swelling (<200 ppm silicon) U-5 w/o Fs alloy as well as low-swelling (>200 ppm silicon) alloy.

(6) Identification of Suspect Leaking Element (R. V. Strain)

Subassembly C2008 had previously been identified as containing a leaking element. This subassembly was a "half-worth"

subassembly, i.e., half of the fuel-element positions were filled with stainless steel rods. The sodium levels in all of the fuel elements from this subassembly were checked by the pulsed-eddy-current technique. The eddy-current traces indicated that the sodium level in one element (E47) was not above the top of the fuel pin. Neutron radiographs at TREAT confirmed this but also showed that the fuel had not undergone any observable changes in physical configuration. Visual examination of the element by remote periscope with 10X magnification indicated a suspect area in the weld where the lower tip is joined to the jacket. Heating to 500°C followed by impact bonding for 500 impacts at 500°C did not force any sodium out of the suspect leak area.

(iv) Fuel Management and Handling (N. R. Grant and P. Fineman)

A summary of fuel-handling operations during the reporting period is included in Tables I.D.33 and I.D.34.

(v) Experiment Handling and Interim Examination (V. G. Eschen and N. R. Grant)

As described in the Progress Report for March 1969 (ANL-7561, p. 56), problems were encountered during dismantling of Subassembly XO18, which contained seven materials capsules. The subassembly was successfully dismantled at TAN, after which the capsules were visually examined. All but the centrally located capsule had bowed. This bowing at midlength ranged from 0.05 to 0.20 in. Diametral profiles showed increases in midlength diameter ranging from 0.004 to 0.015 in. No obvious damage was apparent on the surface of the capsules. Five of these capsules, along with two new capsules, were assembled into Subassembly XO18A in the FCF. The other two capsules from XO18 were returned to the experimenter.

Subassembly XO15 was received and dismantled. Two of the capsules contain Mark-IA fuel elements that had been irradiated to a peak burnup of 3.4 a/o. These capsules were neutron radiographed, found to be acceptable for further irradiation, and were reassembled into Subassembly XO66 for an additional 0.4 a/o burnup. The other 17 capsules from XO15 were held for neutron radiography and other testing.

Subassembly XO10 was received and dismantled. The capsules for General Electric Company were loaded directly into their transfer coffin and shipped. The balance of the capsules from this subassembly were for other experimenters and are being held for shipment.

The following experimental subassemblies were fabricated with new capsules and transferred to the reactor:

XO58 (F37) Ge group F9D mixed oxides
 XO59 (F37) PNL series 4 mixed oxides
 XO61 (B7) INC structural
 XO62 (F37) GE group F9B mixed oxides

PUBLICATIONS

A Wide-band Charge-sensitive Preamplifier for Proton-recoil Proportional Counting

J. M. Larson

ANL-7517 (February 1969)

Time-optimal Digital Control of Zero-power Nuclear Reactors

Thomas J. Marciniak

ANL-7510 (October 1968)

Solid Fission Product Behavior in Uranium-Plutonium Oxide Fuel Irradiated in a Fast Neutron Flux

D. R. O'Boyle, F. L. Brown, and J. E. Sanecki

J. Nucl. Mater. 29(1), 27-42 (January 1969)

Fuel-failure Detection in LMFBR Power Plants

K. G. A. Porges

ANL-7533 (February 1969)

II. OTHER FAST REACTORS--CIVILIAN-- OTHER FAST BREEDER REACTORS

A. Fuel Development

1. Fuel Jacket Alloy Studies

a. Physical Metallurgy of Vanadium-base Alloys (A. E. Dwight)

Not previously reported.

Continued interest in vanadium-base alloys for fast reactor cladding materials makes knowledge of the V-Cr-Ti ternary diagram desirable. Russian investigators*,** have shown the general features of the system, but they were primarily concerned with titanium-rich alloys; metallographic work was reported, but no X-ray diffraction data were included.

In order to determine the effects of titanium and chromium on the lattice parameters of vanadium, a series of vanadium-rich alloys has been prepared and examined by X-ray diffraction. Lattice parameters of the bcc vanadium-base solid solutions are given in Table II.A.1. A preliminary analysis of the data shows that titanium expands the lattice and chromium contracts it, in agreement with predictions based on the atomic size of the alloying elements.

TABLE II.A.1. Lattice Parameters of
Vanadium-base Alloys

Nominal Composition (w/o)			Lattice Parameter (Å)
V	Ti	Cr	
80	20	-	3.074
70	30	-	3.099
80	-	20	3.000
70	-	30	2.986
80	0.5	15	3.003
80	10	10	3.013
80	15	5	3.04
70	7.5	22.5	2.996
70	15	15	3.033
70	22.5	7.5	3.064

* Mikheev, V. S., and Chernova, T. S., "Diagram of State of the Ternary System Ti-Cr-V," Titanium and Its Alloys, Moscow (1962).

** Samsonova, N. N., and Budberg, P. B., "Effect of V and Mo on the Properties and Phase Transformations of the Intermetallic Compounds TiCr₂," Soviet Powder Metallurgy and Metal Ceramics, 634 (1966).

b. Irradiation Studies of Fuel-jacket Alloys (R. Carlander)

Last Reported: ANL-7561, pp. 58-60 (March 1969).

(i) Effects of Irradiation of Type 304 Stainless Steel. Further tensile testing of irradiated Type 304 stainless steel specimens from the guide thimbles of EBR-II experimental Subassembly XG05 and from the EBR-II safety rod was done. The test results are presented in Figs. II.A.1 and II.A.2 for a 550°C test temperature and a strain rate of 1%/min. Previous data from tensile tests of Type 304 stainless steel from EBR-II control rod 12 are also included in the figures (see Progress Report for July 1968, ANL-7478, Table I.E.6, p. 56). The results are for irradiation at $422 \pm 50^\circ\text{C}$.

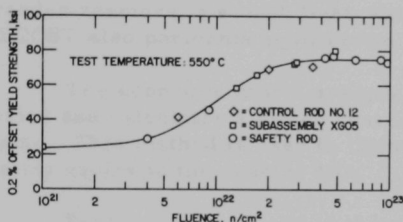


Fig. II.A.1. Effects of Irradiation at $422 \pm 50^\circ\text{C}$ of the Yield Strength of Type 304 Stainless Steel

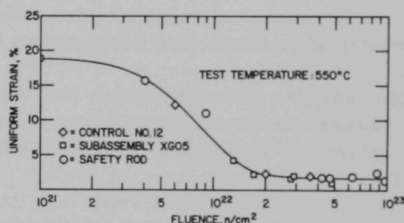


Fig. II.A.2. Effects of Irradiation at $422 \pm 50^\circ\text{C}$ on the Uniform Strain of Type 304 Stainless Steel

The strength of the stainless steel was not significantly affected by irradiation at fluences below $4 \times 10^{21} \text{ n/cm}^2$ (see Fig. II.A.1). At fluences of from 4×10^{21} to $\sim 3 \times 10^{22} \text{ n/cm}^2$, the yield strength increased rapidly with increasing neutron exposure. At fluences above $3 \times 10^{22} \text{ n/cm}^2$, the yield strength had a saturation value of $\sim 75,000 \text{ psi}$.

The irradiation-induced increases in matrix strength resulted in corresponding decreases in the uniform strain of the stainless steel (see Fig. II.A.2). The same relationship as was observed for fluence and strength (incubation period, rapid property change, and saturation) was observed for fluence and uniform strain. The saturation value of the uniform strain of the irradiated stainless steel was 1 to 2%.

Dislocation loops are the main strengtheners of the matrix of stainless steel irradiated in this temperature range ($371\text{--}474^\circ\text{C}$).^{*} The incubation period noted in this experiment is believed to correspond to the buildup of dislocation loops to a density sufficient to cause significant matrix strengthening. The rapid change in strength with increasing fluence then

^{*}Carlander, R., Harkness, S. D., and Yaggee, F. L., The Effect of Fast Neutron Irradiation on the Microstructure and Mechanical Properties of Type 304 Stainless Steel, to be published in J. Nucl. Mater.

corresponds to an increased density of the loop population. Saturation of the strength of the irradiated stainless steel at high fluences implies that the deformation mechanism changes, possibly to dislocation channeling, which has been suggested as a mechanism for the observed saturation in hardening of irradiated niobium.*

* Tucker, R. P., Wechsler, M. S., and Ohr, S. M., Transmission Electron Microscopy and the Dose Dependence of Radiation Hardening in Neutron-irradiated Niobium, presented at the Spring Meeting of The Metallurgical Society, Pittsburgh, Pennsylvania, May 12-15, 1969.

III. GENERAL RESEARCH AND DEVELOPMENT-- CIVILIAN--STUDIES AND EVALUATIONS

A. Fast Reactor Systems and Cost Analysis

1. Fuel-cycle Economic Analysis (K. A. Hub and T. D. Wolsko)

Not previously reported.

A fuel-cycle economics model and corresponding computer program were developed to analyze the economic fuel-cycle characteristics of nuclear reactors. The computer program, CYCOST, was specifically designed to investigate the startup and lifetime fuel-cycle economic characteristics of breeder reactors, although light-water reactors can also be analyzed. CYCOST also performs equilibrium and parametric fuel-cycle calculations.

The economic model assigns costs and credits to each reactor fueling period and calculates a power cost for each cycle based on these assessments. This method is used to illuminate the cost penalties of the early fueling cycles in the reactor life.

Separate subroutines in the program calculate fabrication costs, reprocessing costs, and U-235 value. Any of these economic parameters can be specified as input data, and internal subroutine operation can be bypassed. Fabrication costs are based on a large collection of cost data from a number of studies. This subroutine consists of sets of equations that are functions of pin diameter and fabrication-plant throughput rates. The reprocessing-rate subroutine is also a set of parametric equations in which the fissile concentration of discharged material is the determining parameter. Output from this subroutine is the time required for reprocessing the discharged fuel. The use charge per day for the reprocessing plant must be supplied by the program user. The U-235 cost subroutine calculations are based on a diffusion-plant model that optimizes the U-235 concentration in the tails; this optimization depends on the cost of natural uranium in the UF₆ form and on the separatory work charges.

Output edit consists of itemized values of fuel-cycle costs given in mills per kilowatt hour (inventory, recovery, plutonium credit, fabrication). In addition to the itemized fuel-cycle costs and the total for each fueling period, a levelized fuel-cycle cost is given for the operation of the plant to that date. The last value of levelized cost will reflect the average cost of power for the reactor life. All costs are present-valued to the beginning of each fueling period, and the levelized fuel-cycle costs are present-valued to the beginning of reactor life.

PUBLICATION

Elementary Neutronics Considerations in LMFBR Design

G. H. Golden

ANL-7532 (March 1969)

IV. GENERAL REACTOR TECHNOLOGY

A. Applied and Reactor Physics Development

1. Theoretical Reactor Physics

a. Cross Section Data Evaluation (D. Meneley)

Last Reported: ANL-7553, p. 76 (Feb 1969).

Since the ENDF/B Pu-241 has no resonance parameters, a version was prepared in the ENDF/B format including resolved and unresolved resonance parameters. This version of Pu-241 has been processed through CHECKER, DAMMET, ETØE, and MERMC2, so that it exists on an MC² library tape. Thus, MC² calculations can be made in which Pu-241 is shielded in the resonance region.

FORTTRAN program UR was originally written about a year ago and has since been modified several times. It calculates infinite dilution capture, and fission and scattering cross sections from unresolved resonance parameters by integration over the appropriate statistical distributions. Also, neutron and fission widths may be varied to fit input experimental capture and fission cross sections. The most recent modification consists of a new subroutine to perform the numerical integration involved in calculating the fluctuation integrals. This new subroutine is about 30 times as fast as the old one, and makes the speed of the program quite acceptable rather than too slow.

A routine based on the method used in UR has been added to program MAGIC, which plots data from the MC² library tape on the CDC-3600. Thus unresolved resonance cross sections can now be plotted.

b. Reactor Computations and Code Development (B. J. Toppel)

Last Reported: ANL-7561, pp. 61-63 (March 1969).

(i) Tests of PERT1D. The one-dimensional perturbation-theory module and its associated standard path, PERT1D, have been tested with respect to buckling changes for a parallelepiped reactor. This reactor has four regions with the same compositions as were used previously (see Progress Report for February 1969, ANL-7553, pp. 77-80). The outer dimensions of these regions were 9.2085, 54.0035, 94.3083, and 148.4063 cm, dimensions chosen such that a parallelopiped reactor with a bare height of 200 cm would have the same regional volumes as the cylindrical reactor that was previously considered.

A buckling search with PATHSH was used to find the critical transverse heights. It was found that with an extrapolation distance of 16 cm, the critical half-height of each of the two transverse directions was 101.96 cm. With use of these transverse heights a PATH1D (one-dimensional diffusion theory) problem was run to generate the real and the adjoint fluxes for use by PERT1D.

TABLE IV.A.1. Buckling Changes for Paralleloiped Reactor

Problem	Δh_1	Reg	ΔL_1	Reg	Δh_2	Reg	ΔL_2	Reg
1	+2	1-4						
2					-2	1-4		
3	+2	1-4			-2	1-4		
4			+2	1-4				
5							-2	1-4
6	+2	1-4	+2	1-4	-2	1-4	-2	1-4
7	+4	1						
8			+2	2				
9					-4	3		
10							-10	4
11	+4	1	+2	2	-4	3	-10	4
12	+2	1,3	-3	2,4	+4	1,4	-1	2,3

The perturbations are shown in Table IV.A.1, where Δh_i refers to a change in the half-height in the i th transverse direction, ΔL_i to a change in extrapolation distance, and Reg relates for which regions the perturbation applies.

The results of these calculations are given in Table IV.A.2. Previously diffusion-theory computations had been used to check of accuracy of those from PERT1D. However, because of difficulty in distinguishing discrepancies arising from the errors in perturbation theory from those arising from potential blunders in the programming of PERT1D, the DEL perturbation code in MACH1* is used to check the PERT1D computations. From Table IV.A.2 we see that the discrepancy between the results of PERT1D and of DEL-MACH1 is always less than 1%, which is satisfactory agreement.

TABLE IV.A.2. Comparison of PERT1D and DEL Computations for Paralleloiped Reactor

Problem	$\Delta k/k^2$	
	PERT1D	DEL-MACH1
1	0.0010696	0.0010611
2	-0.0011254	-0.0011165
3	-0.00005580	-0.00005540
4	0.0010696	0.0010611
5	-0.0011254	-0.0011165
6	-0.00022352	-0.00022111
7	0.00023717	0.00023618
8	0.00090738	0.00089950
9	-0.00008770	-0.00008752
10	-0.000000518	-0.000000522
11	0.0010563	0.0010476
12	-0.0019238	-0.0019073

Further comparisons were made for perturbations in the volume fraction of compositions for the cylindrical reactor considered previously. The results of these perturbations are summarized in Table IV.A.3. In the first four problems, the volume fraction of the composition normally assigned to a region was changed; in the last four problems the composition normally assigned to a region was augmented by a portion of another composition. The discrepancies between the results of PERT1D and MACH1-DEL range between 2.7 and 6%, too large to be acceptable. Study of the output from the two codes revealed discrepancies of this range of magnitudes in all terms contributing to $\Delta k/k$ (or $\Delta k/k^2$) and that the perturbations in the macroscopic cross sections were identical. It would seem that the

*Meneley, D. A., et al., ANL-7223 (1966).

discrepancy should arise because of noticeable differences in the flux distributions; however, when several real and adjoint fluxes were plotted, no significant differences between those from PERT1D and MACH1-DEL were detected. Investigation of the source of these discrepancies between the two perturbation theory codes is continuing.

TABLE IV.A.3. Comparison of PERT1D and MACH-DEL Computations for Composition Perturbations

Region	Composition	Change in Volume Fraction	$\Delta k/k$ by MACH-DEL	$\Delta k/k^2$ by PERT1D	Percent Difference
1	1	0.01	-8.0031×10^{-6}	-8.4839×10^{-6}	6.0
2	2	-0.001	-3.8165×10^{-4}	-4.0025×10^{-4}	4.9
3	3	0.01	5.0425×10^{-5}	5.2614×10^{-5}	4.3
4	4	1.0	-6.9550×10^{-7}	-7.1421×10^{-7}	2.7
4	6 ^a	0.0001	9.6307×10^{-6}	10.0054×10^{-6}	3.9
2	6 ^a	0.0001	3.1265×10^{-2}	3.2799×10^{-2}	4.9
3	2	0.001	2.5962×10^{-5}	2.7206×10^{-5}	4.8
1	5 ^b	0.0001	-9.1330×10^{-4}	-9.4908×10^{-4}	3.9

^aComposition 6 is ^{235}U with an atom density of $10^{24}/\text{cm}^3$.

^bComposition 5 is ^{10}B with an atom density of $10^{24}/\text{cm}^3$.

(ii) Spatial Synthesis in the ARC System. A modification of the functional used as a basis for the variational synthesis code in the ARC system has been formulated and has been incorporated into the code. The modification was needed in order to increase the range of boundary conditions that the code may treat properly. For its present version the code will accept zero flux, zero derivatives, or group-dependent logarithmic derivative boundary conditions at any one of the reactor boundaries in any desired combination. Testing of these capabilities is now underway.

(iii) MC² Capability in the ARC System. The further testing of the four modules comprising the MC² capability in the ARC system and the related MC² standard paths continues. A correction was made in subroutine ALRAGØ* to rectify an underflow error caused while converting the elastic transfer cross sections from a macroscopic to a microscopic quantity. Also, an error in AVER1* causing the lowest energy broad group to have wrong values for the average transport and anisotropic self-scattering cross sections was detected and corrected.

*Toppel, B. J., et al., ANL-7318 (1967).

Modifications made in the modules providing the MC² capability and the user input data module A.SXXPC* now permits one to add isotopes to a new or existing microscopic group cross sections data module XS.ISØ. The versatility of this modification allows one to include at a later time additional isotopes.

Another recent development being explored is the recompiling of all source programs to produce new object modules of all the subroutines and path drivers which provide the MC² capability. This has been done by using the FØRTRAN (H) ØPT = 2 (optimization) compiler which will become available for general use with the ØS/360 release 17 MVT** (Multiprogramming with a Variable number of Tasks). Problems involving a variety of input options are now being tested with this new compiler and compared with previous reliable runs. Currently, the various subroutines which represent the MC² capability have been compiled using the presently available FØRTRAN (H) ØPT = 0, 1, 2 and FØRTRAN (G) compilers. It has been necessary to invoke all these options for the various subroutines in order to get correctly compiled modules. The significance of successfully recompiling all the subroutines and path drivers of the associated modules of MC² with a single compiler and optimization will allow a reorganization of the subroutines and provide the user with a clearer representation of the structure for each module.

(iv) Cross-section Modification in ARC. An ARC system module which modifies isotopic group cross sections according to the algorithm

$$\tilde{\sigma} = A\sigma + B$$

is now available for production use. Any user of the ARC standard paths STP001, STP002, STP003, STP004, and STP005 may invoke the module by including a type 20 card, with the modified format described below, in the general neutronics input data set A.NIP.[†]

FØRMAT of Type 20 Card of A.NIP

20 Run-time Cross Section Modifiers (I2, 4X, A6, 3I6, 6X, 2E12.5, 2I6)

Cols. 7-12 Isotope Label

Cols. 13-18 Cross-section type being modified

- 1 σ_{tr} transport cross section
- 2 σ_c radiative capture (n,γ) cross section

*Stenberg, C. G., Modification of User Input to MC² in the ARC System, RP Internal Technical Memorandum (April 29, 1969).

**Operating System/360 - MVT, ANL Digital Computing Center Newsletter No. 12 (May 1969).

[†]Toppel, B. J., ANL-7332 (Nov 1967), p. 247.

- 3 $\sigma_{n,\alpha}(n,\alpha)$ cross section
- 4 $\sigma_{n,p}(n,p)$ cross section
- 5 σ_f fission cross section
- 6 $\nu\sigma_f$ number of fission neutrons per fission times fission cross section
- 7 $\sigma_{e\ell}^0(j \rightarrow j)$ isotropic elastic self-scattering consistent with anisotropic total cross section
- 70 $\sigma_{in}^{(\ell)}$ inelastic scatter cross section for all Legendre orders
- 71 $\sigma_{in}^{(0)}$ inelastic scatter cross section for isotropic scatter
- 72 $\sigma_{in}^{(1)}$ inelastic scatter cross section for linear anisotropic scatter
- 80 $\sigma_{e\ell}^{(\ell)}$ elastic scatter cross section for all Legendre orders
- 81 $\sigma_{e\ell}^{(0)}$ elastic scatter cross section for isotropic scatter
- 82 $\sigma_{e\ell}^{(1)}$ elastic scatter cross section for linear anisotropic scatter
- 90 $\sigma_{n,2n}^{(\ell)}(n,2n)$ cross section for all Legendre orders
- 91 $\sigma_{n,2n}^{(0)}(n,2n)$ cross section for isotropic scatter
- 92 $\sigma_{n,2n}^{(1)}(n,2n)$ cross section for linear anisotropic scatter

Cols. 19-24 Group Number IF1

Cols. 25-30 Group Number IF2 (IF2 \geq IF1)

Cols. 37-48 Cross Section Modifier Constant A

Cols. 49-60 Cross Section Modifier Constant B

Cols. 61-66 Group Number II1

Cols. 67-72 Group Number II2 (II2 \geq II1)

I. If the cross section type x in Cols. 13-18 is $x \leq 7$, then Cols. 61-72 are neglected and the type x cross sections for groups IF1 through IF2 are modified. If Cols. 19-24 are blank, the constants given in Cols. 37-60 will be applied to all energy groups. If Cols. 25-30 are blank, the constants will be applied to the group given in Cols. 19-24.

II. If the cross section type x in Cols. 13-18 is $x \geq 10$, then the scattering matrix is modified according to the same algorithm,

$$\tilde{\sigma}_x(g \rightarrow g') = B + A\sigma_x(g \rightarrow g').$$

In this case

Cols. 19-24 IF1 is the higher-energy final group number of the scattered particles for which constants apply

Cols. 25-30 IF2 is the lower-energy group number of the scattered particles for which constants apply

Cols. 61-66 I11 is the higher-energy initial group number of the incident particles for which constants apply

Cols. 67-72 I12 is the lower-energy initial group number of the incident particles for which constants apply

e.g., If IF1 = 3, IF2 = 5, I11 = 4, I12 = 5, then

$$\sigma_x(4 \rightarrow 3), \sigma_x(4 \rightarrow 4), \sigma_x(4 \rightarrow 5), \sigma_x(5 \rightarrow 3), \sigma_x(5 \rightarrow 4), \sigma_x(5 \rightarrow 5)$$

are modified.

If Cols. 61-66 are blank, the constants given in Cols. 37-60 will be applied to all groups of incident particles. If Cols. 67-72 are blank, the constants will be applied to the group given in Cols. 61-66. If Cols. 19-24 are blank, the constants will be applied for a single group down scatter for the groups as specified in Cols. 61-72,

$$\sigma_x(I11 \rightarrow I11+1), \sigma_x(I11+1 \rightarrow I11+2), \dots, \sigma_x(I12 \rightarrow I12+1).$$

If Cols. 25-30 are blank the constants will be applied to the group of scattered particles given in Cols. 19-24.

(v) Fuel-cycle Package

Last Reported: ANL-7548, pp. 82-83 (Jan 1969).

The preliminary search procedure described previously (see ANL-7548) does not reduce to an acceptable level the range of enrichment and burn-time adjustments which must be made by the more accurate but slower final search procedures. Because of this, an intermediate search procedure was developed to narrow the range of enrichment and burn-time adjustments. Thus, there are now three levels of search procedures in the fuel-cycle package. In the preliminary search procedure, one burn-step subinterval is utilized in obtaining the cyclic mode* with an enrichment and burn-step time specified as input. At this point the burn-step time that would

*Reactor Physics Division Annual Report, ANL-7310 (Jan 1968), pp. 493-501.

give the desired burnup is estimated. By use of this burn-step time and a second enrichment specified in the input, the cyclic mode is again obtained. A linear search of enrichment versus the multiplication constant is then initiated until an enrichment is obtained which gives the desired multiplication constant at the specified time in the cycle.

In the intermediate search procedure, the more general search procedures* are initiated with the exception that the iterations on the flux solution* at each time point in the cycle and the iterations on the cyclic mode are not done. Using these procedures the burn-time satisfying the desired burnup and the enrichment giving the desired multiplication constant at the specified time in the cycle are obtained.

The final search procedure with iterations on the flux solution at each time point and iterations on the cyclic mode is then initiated.

A basic change in the burnup search procedure was made. In the new procedure, the burnup is calculated after obtaining the cyclic mode. At this point a search of burnup versus burn time is now performed using the previously calculated power-normalized fluxes until the desired burnup is obtained. In the old burnup search procedure, the fluxes at each time point and the cyclic mode would have been obtained for each burn-time estimate.

The mesh point fluxes in FR.D2** at each time point in the cycle are now saved as separate data sets. These are used as initial flux guesses at each corresponding time point in the cycle during the enrichment and control searches. This reduces the number of outer iterations required by the diffusion-theory code DIF2D and saves on computer time.

The above procedures have reduced the required run time by a factor of 2 to 3 with no loss in accuracy.

Debugging of the fuel-cycle package has proceeded to the point that users may solve equilibrium fuel-cycle problems which do not require the specifications of an external cycle. The external cycle options will be tested in the near future.

* Ibid., see previous page.

** Toppel, B. J., ANL-7332 (Nov 1967).

2. Nuclear Data

a. Cross Section Measurements (C. E. Crouthamel and N. D. Dudey)

(i) Integral Cross Section Measurements

Last Reported: ANL-7561, pp. 63-65 (March 1969).

Preliminary flux levels in EBR-II have been determined from reaction-rate data (see ANL-7561) obtained in the EBR-II Dosimetry Test Experiment (Run 31F). The calculation method employed will be described in detail elsewhere. Briefly, the technique was to compute spectrum-averaged cross sections from published differential cross-section data and from a two-dimensional diffusion-theory calculation that was supplied by the EBR-II project of the neutron spectral distributions. The 22-group calculated spectra were smoothed by an analytical distribution, normalized to the calculated number of neutrons within each energy interval. The product integrals $\int \sigma(E)\phi(E)dE/\int \phi(E)dE$ were numerically integrated to provide a calculated spectrum-averaged cross section $\bar{\sigma}_c$ for each sample location. The flux values were then determined from the measured reaction rates and the computed spectrum-averaged cross sections. Table IV.A.4 summarizes the preliminary results of the analysis of our data from Run 31F.

TABLE IV.A.4. Preliminary EBR-II Flux Determinations from Run 31F

Reaction	Reaction Rate $\left(\frac{1}{\text{MW-D}}\right)$	$\bar{\sigma}_c$ (mb)	ϕ/MW^a $\left[\frac{n}{(\text{cm}^2)(\text{sec})(\text{MW})}\right]$	ϕ^b $\left[\frac{n}{(\text{cm}^2)(\text{sec})}\right]$
Row 2 (5.9 cm)	⁵⁴ Fe(n,p) 5.71 × 10 ⁻⁸	15.3	4.31 × 10 ¹³	2.29 × 10 ¹⁵
	⁵⁸ Ni(n,p) 8.43 × 10 ⁻⁸	23.0	4.22 × 10 ¹³	2.23 × 10 ¹⁵
	⁴⁶ Ti(n,p) 7.4 × 10 ⁻⁹	1.97	4.32 × 10 ¹³	2.30 × 10 ¹⁵
	¹⁹⁷ Au(n,γ) 8.09 × 10 ⁻⁷	222	4.22 × 10 ¹³	2.23 × 10 ¹⁵
	⁴⁵ Sc(n,γ) 5.02 × 10 ⁻⁹	13.9	4.18 × 10 ¹³	2.21 × 10 ¹⁵
Row 4 (15.6 cm)	⁵⁴ Fe(n,p) 5.50 × 10 ⁻⁸	16.5	3.47 × 10 ¹³	2.03 × 10 ¹⁵
	⁵⁸ Ni(n,p) 7.59 × 10 ⁻⁸	24.5	3.58 × 10 ¹³	2.10 × 10 ¹⁵
	⁴⁶ Ti(n,p) 6.9 × 10 ⁻⁹	2.13	3.75 × 10 ¹³	2.19 × 10 ¹⁵
	¹⁹⁷ Au(n,γ) 7.85 × 10 ⁻⁷	214	4.24 × 10 ¹³	2.48 × 10 ¹⁵
	⁴⁵ Sc(n,γ) 5.19 × 10 ⁻⁸	13.4	4.48 × 10 ¹³	2.62 × 10 ¹⁵
Row 6 (27.0 cm)	⁵⁴ Fe(n,p) 3.00 × 10 ⁻⁸	15.0	2.31 × 10 ¹³	1.90 × 10 ¹⁵
	⁵⁸ Ni(n,p) 4.52 × 10 ⁻⁸	22.3	2.33 × 10 ¹³	1.92 × 10 ¹⁵
	⁴⁶ Ti(n,p) 3.9 × 10 ⁻⁹	1.96	2.31 × 10 ¹³	1.90 × 10 ¹⁵
	¹⁹⁷ Au(n,γ) 6.07 × 10 ⁻⁷	232	3.02 × 10 ¹³	2.48 × 10 ¹⁵
	⁴⁵ Sc(n,γ) 4.41 × 10 ⁻⁸	14.5	3.50 × 10 ¹³	2.88 × 10 ¹⁵
Row 7 (31.2 cm)	⁵⁴ Fe(n,p) 1.10 × 10 ⁻⁸	8.59	1.48 × 10 ¹³	1.68 × 10 ¹⁵
	⁵⁸ Ni(n,p) 1.57 × 10 ⁻⁸	12.7	1.42 × 10 ¹³	1.61 × 10 ¹⁵
	⁴⁶ Ti(n,p) 1.4 × 10 ⁻⁹	1.13	1.43 × 10 ¹³	1.62 × 10 ¹⁵
	¹⁹⁷ Au(n,γ) 5.63 × 10 ⁻⁷	276	2.36 × 10 ¹³	2.68 × 10 ¹⁵
	⁴⁵ Sc(n,γ) 3.03 × 10 ⁻⁸	17.0	2.06 × 10 ¹³	2.34 × 10 ¹⁵

^aAt sample position.

^bCorrected to core center at a power level of 50 MW.

Column 4 lists the calculated spectrum-averaged cross sections at the respective sample locations (all of our samples were axially located ~5 cm below reactor midplane), column 5 lists the calculated flux per megawatt at the sample position, and column 6 lists the calculated total flux corrected (on the basis of the diffusion-theory calculation) to core center.

The average of five flux-monitor reactions from Row 2 indicate a core center flux value of $2.25 \times 10^{15} \text{ n}/(\text{cm}^2)(\text{sec})$ with an estimated uncertainty of ± 10 to 20%. This value is in substantial agreement with the value of $2.5 \times 10^{15} \text{ n}/(\text{cm}^2)(\text{sec})$ reported by the EBR-II Project. The flux values derived from our dosimetry measurements indicate a "softer" spectrum than that calculated by diffusion theory as the radial distance from the core center is increased; however, any quantitative interpretation must await further analysis.

A summary of preliminary results of all participants in the Dosimetry Test Experiment has been compiled by PNL/ANL.* The summary reports only the experimenters' data from Row 2; measurements are presented for both 50-MW (Run 31F) and 0.084-MW (Run 31E) reactor power levels. From these summarized results, their assigned standard deviations, and our spectrum-averaged cross sections, we have computed the flux per megawatt at both high and low power. These calculated values are given in Table IV.A.5. Column 2 lists the average values of the saturated activities

TABLE IV.A.5. Calculated Φ/MW for High- and Low-power Runs Derived from Average Saturated Activities of All Experimenters (Row 2 data only)

Reaction	A_0 (d/s/nucleus)	Φ , $\left[\frac{n}{(\text{cm}^2)(\text{sec})} \right]$	$\Phi/\text{MW},^a$ $\left[\frac{n}{(\text{cm}^2)(\text{sec})(\text{MW})} \right]$
High Power--50 MW			
$^{54}\text{Fe}(n,p)$	$3.74 \times 10^{-11} \pm 3.1\%$	2.44×10^{15}	$4.88 \times 10^{13} \pm 10.4\%$
$^{58}\text{Ni}(n,p)$	$5.21 \times 10^{-11} \pm 8.1\%$	2.26×10^{15}	$4.53 \times 10^{13} \pm 12.8\%$
$^{46}\text{Ti}(n,p)$	$4.89 \times 10^{-12} \pm 4.9\%$	2.48×10^{15}	$4.96 \times 10^{13} \pm 11.2\%$
$^{197}\text{Au}(n,\gamma)$	$4.97 \times 10^{-10} \pm 8\%^b$	2.24×10^{15}	$4.48 \times 10^{13} \pm 12.8\%$
$^{45}\text{Sc}(n,\gamma)$	$3.08 \times 10^{-11} \pm 8\%^b$	2.22×10^{15}	$4.42 \times 10^{13} \pm 12.8\%$
$^{235}\text{U}(n,f)$	$2.90 \times 10^{-9} \pm 5.0\%$	2.09×10^{15}	$4.19 \times 10^{13} \pm 11.2\%$
Average		$2.29 \pm 0.28 \times 10^{15}$	$4.57 \pm 0.56 \times 10^{13}$
Low Power--0.084 MW			
$^{54}\text{Fe}(n,p)$	$6.26 \times 10^{-14} \pm 1.7\%$	4.09×10^{12}	$4.86 \times 10^{13} \pm 10.2\%$
$^{58}\text{Ni}(n,p)$	$8.69 \times 10^{-14} \pm 3.5\%$	3.78×10^{12}	$4.50 \times 10^{13} \pm 10.6\%$
$^{46}\text{Ti}(n,p)$	$8.63 \times 10^{-15} \pm 10\%^b$	4.38×10^{12}	$5.22 \times 10^{13} \pm 14.1\%$
$^{197}\text{Au}(n,\gamma)$	$1.35 \times 10^{-12} \pm 25\%^b$	(6.08×10^{12})	(7.24×10^{13})
$^{45}\text{Sc}(n,\gamma)$	$6.72 \times 10^{-14} \pm 15\%^b$	4.84×10^{12}	$5.77 \times 10^{13} \pm 18.0\%$
$^{235}\text{U}(n,f)$	$5.28 \times 10^{-12} \pm 5.1\%$	3.81×10^{12}	$4.54 \times 10^{13} \pm 11.2\%$
Average (excluding Au)		$4.18 \pm 0.51 \times 10^{12}$	$4.97 \pm 0.62 \times 10^{13}$

^aAssigned errors assume a 10% uncertainty in $\bar{\sigma}_c$.

^bThese uncertainties have been estimated because only one measurement was reported at each power level, and the results of high- and low-power measurements were reported by different laboratories.

(d/s/nucleus) reported in BNWL-CC-2076, column 3 lists the total flux computed for Row 2 core-midplane, and column 4 lists the computed flux per megawatt. Because of the uncertainties in the computed values, it is difficult to make any definitive statement concerning the variation of flux or spectral shape between high and low power. Further evaluation of these Row 2 data, and data from Rows 4, 6, and 7 will continue.

b. Burnup Analysis and Fission Yields for Fast Reactors
(R. P. Larsen)

(i) Absolute Fast Fission Yield Determinations of Monitors for the Calculations of Relative Burnup in Fuels Containing Two Fissile Nuclides

Last Reported: ANL-7513, p. 95 (Oct 1968).

An irradiation is being carried out in EBR-II to provide materials for (1) determination of fast-fission yields of burnup monitors and study of nonfission nuclear transformations, and (2) calculations of relative burnup in fuels containing two fissile nuclides. The materials that are being irradiated are ^{233}U , ^{235}U , ^{239}Pu , ^{240}Pu , ^{241}Pu , ^{232}Th , and ^{237}Np . The irradiation, which began in December 1966, is estimated to be about 50% complete at the present time.

The subassembly in which these materials are being irradiated, XO-18, was removed from the reactor in March 1969 for reconstitution (see Progress Report for March 1969, ANL-7561, p. 37). The subassembly was returned to the reactor during April.

(ii) Development of Analytical Procedures for Fission Product Burnup Monitors

Last Reported: ANL-7548, pp. 83-85 (Jan 1969).

(a) X-ray Spectrometric Determination of Rare Earth Fission Products. Development of a method for determining rare earth fission products by X-ray spectrometry is continuing. In the procedure, an internal standard (a rare earth not produced in fission) is added to the sample; the rare earths are then separated from interferences, mounted on an aluminum plate, and assayed X-ray spectrometrically. Terbium is being used as the internal standard. The advantages of terbium as an internal standard and the precision attained by the use of line-intensity ratios (rare earth-to-terbium) have been discussed previously (see Progress Report for January 1968, ANL-7419, pp. 97-98).

Present efforts are being directed to the problem of interelemental interference in the X-ray spectrometric assay of the separated rare earths. Although adequate precision has been demonstrated in previous experiments (see ANL-7548), the accuracy of the method will depend upon our ability to make corrections for any interelemental interferences. These include the effects of one rare earth upon another and of cesium and barium (fission products that are not separated from the rare earths in the procedure) upon the individual rare earths. Possible interferences were assessed by X-ray spectrometric measurements of relatively large amounts (~1 mg) of the individual elements at appropriate wavelengths. Where significant interferences were observed (in a few cases, these were as large as 40%), intensity relationships were accurately established; these were used as coefficients in a set of simultaneous equations by which the necessary corrections are made.

Because of the many complex interrelationships that must be considered, a small computer program was devised to handle data reduction by converting the measured line intensities to micrograms of each rare earth. The ability of the computer program to make the appropriate corrections was tested in the following experiment. A series of plates containing microgram amounts of "fission product" rare earths and terbium internal standard were prepared by direct electroplating and were analyzed X-ray spectrometrically. Plates of individual rare earths served as "standards;" mixtures of the rare earths, with and without added cesium and barium, served as "unknowns." The amounts of the individual rare earths in the standards and unknowns were kept constant, as was the amount of terbium internal standard. The intensity ratios (rare earth-to-terbium) for the unknowns, as corrected by the computer program, showed a slight negative bias when compared with those of the standards. The bias was most pronounced (-5%) for lanthanum, the rare earth with the least energetic X ray, and was least pronounced (-1.1%) for neodymium, the rare earth with the most energetic X ray. The negative bias was found to result from mass absorption, which stems from the much larger amounts of solids on the "unknown" plates. To overcome this problem, it is planned to introduce an amount of yttrium that will be sufficient to "swamp out" the mass absorption effect.

c. Reactor Code Center (M. Butler)

Last Reported: ANL-7561, pp. 67-68 (March 1969).

During the past two-month period, twelve programs have been incorporated in the Code Center library.

Three of the five written for the IBM 360 computer were supplied by the South African Atomic Energy Board (AEB). They are No. 9, FIRE5, an extension of the FIRE2 one-dimensional multigroup diffusion program; No. 362, WELWING, a buckling calculation program; and No. 363, BLAST, a kinetics program for study of accident conditions. In addition, IBM has contributed a 360 version of the BAPL PDQ7 program, No. 275, and No. 368, the FLANGE2 program for processing ENDF/B thermal-neutron scattering data, has been received from the Savannah River Laboratory.

Two CDC-3600 programs prepared at ANL have been added: No. 366, CHEMLOC2, describing core heating and cladding-steam reaction following loss of coolant in a water-cooled power reactor, and No. 365, BOW2.

CDC-6600 programs incorporated during May were No. 359, PUN1, which evaluates unresolved resonance radiative capture integrals and related multigroup cross sections, written at BAPL; No. 364, SNEQ, a program to solve nonlinear algebraic equations, from KAPL; and a 6600 version of the 2DB two-dimensional diffusion-burnup program for fast reactor analysis, our No. 325, contributed by LASL. A revised UNIVAC 1108 version of the original 2DB program has been received from Battelle's Pacific Northwest Laboratory this month as well, along with the UNIVAC 1108 ISOGEN program No. 367, for calculating radioisotope generation and decay.

Supplement 2 to ANL-7411, the Center's Compilation of Program Abstracts, is presently being printed. It contains new abstracts 337 through 357, as well as some corrections and additions to previously issued abstracts, and should be available for distribution shortly.

B. Reactor Fuels and Materials Development

1. Fuels and Cladding

a. Behavior of Reactor Materials

(i) Fuel Element Behavior Modeling

(a) Bubble Migration Analysis (R. W. Weeks and S. R. Pati)

Not previously reported.

In conjunction with studies of fission-gas migration, an analysis of the elastic interaction energy between a bubble and a straight dislocation has been undertaken and completed.* An approximate solution for the interaction energy at large separation distances was derived from a result reported by Eshelby,** and a mathematically exact solution was derived for the limiting case when a bubble sits symmetrically on a screw dislocation. When the results are combined, a complete picture of the variation of interaction energy with distance is obtained. This information is now being used to obtain a better estimate of the critical size a bubble must attain before it is pulled free from a dislocation by a thermal-gradient driving force.

(b) Swelling Mechanisms and Models for Oxide Fuel (R. B. Poeppel)

Last Reported: ANL-7548, p. 88 (Jan 1969).

A preliminary program written for the ANL IBM 360/75/50 computer will be run as subroutine PLUTO in conjunction with a new code (LIFE) to predict the in-pile behavior of cylindrical oxide-fuel elements (see ANL-7548). The subroutine calculates the redistribution of plutonium in a mixed-oxide fuel under in-pile conditions. The flux of plutonium is given by†

$$\vec{J}^{\text{Pu}} = \rho_c^{\text{Pu}} U_D' \text{grad}(T - \rho D) \text{grad } c^{\text{Pu}},$$

where

\vec{J}^{Pu} is the flux of plutonium, g/cm²-sec, counted with respect to the center-of-mass velocity as reference velocity,

ρ is the density of the oxide fuel, g/cm³,

* Weeks, R. W., Pati, S. R., Ashby, M. F., and Barrand, P., The Elastic Interaction between a Straight Dislocation and a Bubble or a Particle, to be published in Acta Met.

** Eshelby, J. D., Proc. Roy. Soc. (London) **A241**, 376 (1957).

† DeGroot, S. R., and Mazur, P., Non-Equilibrium Thermodynamics, North Holland Publishing Co. Amsterdam (1962), p. 276.

c_{Pu} , c_{U} are concentrations of plutonium and uranium, respectively, w/o,

D is the diffusion coefficient of plutonium in the mixed oxide, cm^2/sec ,

T is the absolute temperature, $^{\circ}\text{K}$, and

D' is the thermal diffusion coefficient, $\text{cm}^2/\text{sec} \cdot ^{\circ}\text{K}$.

The equation for the time derivative of the concentration,

$$\rho \frac{dc_{\text{Pu}}}{dt} = -\text{div } \vec{J}^{\text{Pu}},$$

is also used.*

For purposes of computation, the diffusion coefficients are assumed to obey the following standard relationships:

$$D = D_0 \exp[Q/RT];$$

$$(D'/D)T = \alpha,$$

where D_0 , Q , and α are constants, taken as given values in the subroutine, D_0 has the same units as D , R is the gas constant, Q is given in units of cal/mole, R in units of cal/mol- $^{\circ}\text{K}$, and α , which is dimensionless, is the thermal diffusion factor.**

The fuel is divided into N concentric, cylindrical shells of equal mass. The plutonium flux between each shell is computed, and the result is used to compute the plutonium concentration in each shell after an interval of time. Data supplied from the main program must include:

Number of shells;

Radial position (cm), temperature ($^{\circ}\text{K}$), and temperature gradient ($^{\circ}\text{K}/\text{cm}$) at each shell boundary;

Density (g/cm^3) of fuel in each shell;

Time interval (sec) over which diffusion is to be computed;

Plutonium (w/o) concentration in each shell at the beginning of the time interval.

*DeGroot, S. R., and Mazur, P., Ibid., p. 13.

**Beissmenger, H., Bober, M., and Schumacher, G., Proc. IAEA Symp. on Plutonium as a Reactor Fuel, Vienna, 1967, p. 273.

PLUTO considers two effects only, namely, thermal diffusion in a temperature gradient and chemical diffusion in a concentration gradient. Among the phenomena that may be important but are not considered are oxygen redistribution, bubble migration, and melting and resolidification.

(ii) Swelling and Gas Release in Metal Fuels (D. R. O'Boyle)

(a) Interactions between Gas Bubbles and Moving Grain Boundaries (S. R. Pati)

Last Reported: ANL-7548, pp. 89-90 (Jan 1969).

Knowledge of interactions between gas bubbles and moving grain boundaries is important for a better understanding of gas-release mechanisms in metallic and ceramic fuel materials. To improve our understanding of these interactions, two Cu- ^{10}B alloys containing 0.083 and 0.333 a/o boron were irradiated in CP-5 for ten weeks to transmute ^{10}B to ^4He . This irradiation yielded 10^{-4} and 4×10^{-4} atomic fractions of helium in the Cu-0.083 a/o ^{10}B and the Cu-0.333 a/o ^{10}B alloys, respectively. Specimens from these alloys were annealed at 800-1020°C to obtain helium bubbles of different sizes.

In a preliminary experiment, the surfaces of two specimens (one of each alloy) were etched, and two grains were plastically deformed using 1- and 2-mm-dia Brinell balls, and loads from 10 to 60 kg. The specimens were recrystallized at temperatures from 600 to 900°C and polished for metallographic examination. Experimental difficulties encountered in the use of these polycrystalline Cu-B specimens (transmuted to obtain helium) to study sweeping of helium bubbles by moving grain boundaries are summarized below.

In specimens recrystallized at temperatures higher than 650°C, it was found that the recrystallization front that originated below the hardness indentation often extended to the original grain boundaries; this complicated the evaluation of sweeping. In addition, owing to large differences in the atomic weights of copper and boron and poor wetting of boron by copper, boron was not uniformly dispersed in copper even after the ingot had been remelted seven or eight times. Thus, there were regions in the alloys where boron, present in the form of elemental boron, obstructed the movement of the recrystallization front. Also, the concentration of helium obtainable by transmutation of ^{10}B is limited by the very low solubility of boron in copper, and the distribution of helium often was not uniform.

In order to circumvent these difficulties, helium was introduced into single crystals of copper by means of bombardment with 46-MeV alpha particles. To obtain a uniform concentration of helium in

copper to a depth of 0.009 in., a rotating aluminum wheel (varying in thickness from 0.006 to 0.032 in.) was positioned in front of the specimen during alpha irradiation. The specimen was water cooled to maintain the temperature below 250°C. It was possible to increase the helium concentration to 8×10^{-4} atom fraction by bombardment with a 10- μ A beam current for 10 hr. In a first trial with this approach, a single crystal of copper (1/4 by 1/4 by 1/4 in.) was bombarded with alpha particles to a dose of 7 μ A-hr and is being cooled for subsequent examination.

(b) Solid Fission-product Swelling (A. E. Dwight and D. R. O'Boyle)

Not previously reported.

Several investigators^{*,**} observed, in UO_2 - PuO_2 fuel irradiated in a fast neutron flux, white metallic inclusions that contained the fission products molybdenum, ruthenium, technetium, rhodium, and palladium. In one investigation, microprobe analysis performed on 42 different inclusions in the columnar-grain region^{*} yielded an approximate composition of 25 w/o Mo, 15 w/o Tc, and 50 w/o Ru, with smaller amounts of rhodium and palladium. The work of Bramman *et al.*,^{**} established that the inclusions contain an intermetallic compound with hexagonal crystal structure ($a_0 = 2.756 \text{ \AA}$; $c_0 = 4.426 \text{ \AA}$) and the following approximate composition: 35 w/o Mo, 20 w/o Tc, 35 w/o Ru, and 10 w/o Rh.

The crystal structure and unit-cell constants suggest that the compound is based upon a Ru-Tc^\dagger solid solution. However, the Mo-Rh binary system contains an epsilon phase^{††} (see Fig. IV.B.1) that closely resembles the hexagonal compound. In order to establish the general features of the Mo-Ru-Rh ternary system (the dominant ternary phase diagram for the fission-product inclusions), four ternary alloys were prepared to determine whether the Mo-Rh epsilon phase is continuous and isostructural with ruthenium. The alloys were homogenized at 1150°C, air-cooled, and examined by X-ray diffraction. The unit-cell constants (see Fig. IV.B.2) demonstrate that the Mo-Rh epsilon phase is isostructural with ruthenium and forms a complete solid solution with

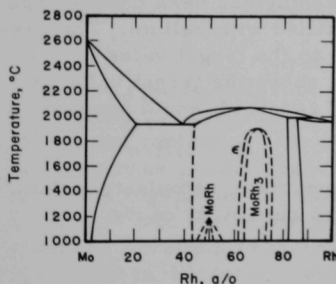


Fig. IV.B.1. Mo-Rh Equilibrium Diagram
(A. E. Dwight)

^{*}O'Boyle, D. R., Brown, F. L., and Sanecki, J. E., Solid Fission Product Behavior in Uranium-Plutonium Oxide Fuel Irradiated in a Fast Neutron Flux, J. Nucl. Mater. **29**(1), 27-42 (Jan 1969).

^{**}Bramman, J. I., Sharpe, R. M., Thom, D., and Yates, G., Metallic Fission-product Inclusions in Irradiated Oxide Fuels, J. Nucl. Mater. **25**, 201 (1968).

[†]Pearson, W. B., Handbook of Lattice Spacings and Structures of Metals, Pergamon Press (1967).

^{††}Dwight, A. E., "Alloy Chemistry of Th, U and Pu Compounds," Developments in the Alloy Chemistry of Alloy Phases, B. C. Giessen, ed., Plenum Press, to be published.

ruthenium. The hexagonal compound thus can be considered either a Mo-Rh epsilon phase or a Ru-Tc solid solution. Further work is underway to establish the crystal structure of a quinary alloy containing palladium.

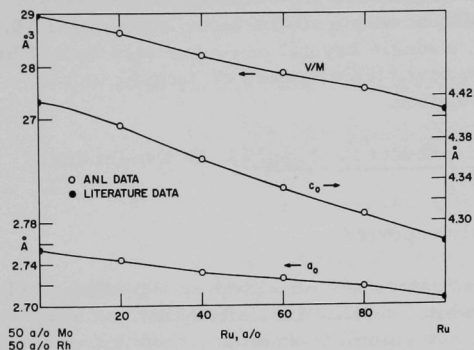


Fig. IV.B.2

Lattice Parameters and Atomic Volume in the Mo-Ru-Rh Ternary System. The literature data are from Pearson, W. B., Handbook of Lattice Spacings and Structures of Metals, Pergamon Press (1967)

b. Chemistry of Irradiated Fuel Materials (C. E. Crouthamel)

(i) Development of Analytical Facilities, Microstructure Sampling Techniques, and Analytical Procedures for the Analysis of Irradiated Fuels

Last Reported: ANL-7553, p. 81 (Feb 1969).

The Shielded Fuel Evaluation Facility is undergoing shake-down and acceptance tests. The in-cell metallographic equipment for cutting, polishing, vacuum coating, and cathodic etching has been checked and is operating satisfactorily. The cell has been filled with helium. The gas-purification system reduced the moisture level to the target value of 5 ppm, but oxygen levels are still considerably above the target value of 5 ppm. Some minor air leaks, which are being repaired, could account for the excessive oxygen levels.

The switching device for the pneumatic sample-transfer tube was tested. It is being modified to improve reliability of its performance.

(ii) Postirradiation Studies for Reactor Fuel

Last Reported: ANL-7553, p. 81 (Feb 1969).

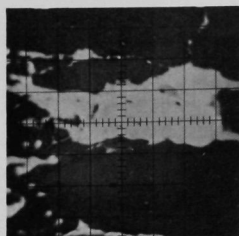
Electron microprobe studies of irradiated UO_2 - PuO_2 fuels are continuing. Preliminary results have been obtained from the electron microprobe analysis of SOV-3, a UO_2 -20 wt % PuO_2 fuel pin clad in Type 304 stainless steel, which had been irradiated in EBR-II to 3.7 at. % burnup.

Metallographic photographs of a midplane section of SOV-3 showed large particles of a "gray," nonmetallic phase distributed throughout the equiaxed and unstructured region of the pin and an appreciable number of metallic inclusions in the body of the fuel and near the cladding-fuel matrix interface. Further, there was indication of intergranular penetration of the cladding to a depth of $\sim 90 \mu\text{m}$. Recent effort has focused upon studies of the "gray" phase and upon the mechanism of the reaction at the cladding-fuel matrix interface.

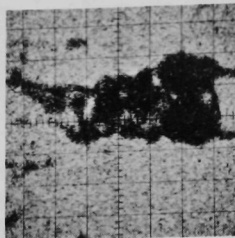
Electron microprobe examination of the "gray" phase found in the fuel matrix showed it to be principally alumina. X-ray scanning images of a typical alumina-containing particle are shown in Fig. IV.B.3. This particular particle was located at the cooler end of a long columnar grain. The tip of the columnar grain is outlined at the right in the specimen current image. Two longer columnar grains form the upper and lower boundaries of the particle. The presence of this phase is the result of an Al_2O_3 impurity introduced into the fuel during a ball-milling operation. Alumina that was in the columnar-grain region near the center of the fuel was not soluble in the solid $\text{UO}_2\text{-PuO}_2$ matrix and migrated outward to the cooler equiaxed-grain region. The particle under discussion collected around a metallic iron inclusion. The alumina acted as a getter for barium oxide, cesium oxide, and tellurium oxide (see Fig. IV.B.3). It has not yet been established whether this gray phase is a solid solution or a mixture of compounds such as $\text{BaO} \cdot 6\text{Al}_2\text{O}_3$ and $\text{Cs}_2\text{O} \cdot \text{Al}_2\text{O}_3$. In a cooler location at the top of the SOV-3 pin, the alumina particles did not contain barium, nor was any barium present in the surrounding fuel matrix. The alumina particles did contain cesium, but the cesium had not totally penetrated the particles, as evidenced by the small, dense core of high-purity alumina that was found in each particle.

Microprobe examination of the metal inclusions in the fuel indicated that constituents of the stainless steel cladding had been transported into the fuel matrix. In the midplane section of SOV-3, large metal inclusions containing iron were found near the boundary of the equiaxial and columnar grains, frequently as pure metal. However, in other temperature regions of this fuel, or in other fuels irradiated at different power densities, iron was often found alloyed with palladium or molybdenum. In contrast, chromium penetrated the fuel matrix only slightly and was found primarily in the outer regions of the fuel near the fuel-cladding interface. Nickel was found segregated in the cladding grain boundaries, but, in general, did not migrate into the fuel matrix.

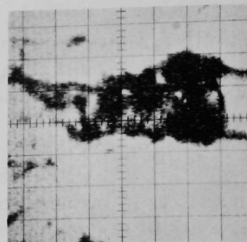
Electron probe examination of the fuel-cladding interface verified that intergranular attack of the cladding had occurred and showed that the mechanism of attack was interaction of the cladding with fission products in the fuel. A typical area of intergranular attack is shown in the X-ray scanning images in Fig. IV.B.4. In SOV-3, the average depth of



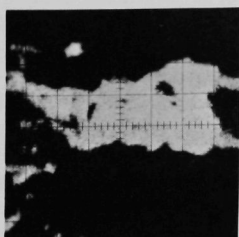
a) Specimen Current



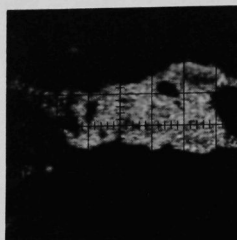
b) Plutonium



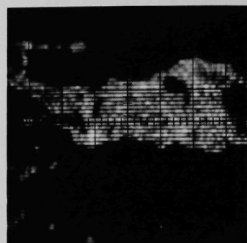
c) Uranium



d) Aluminum



e) Barium



f) Cesium

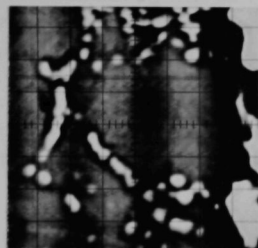


g) Iron



h) Tellurium

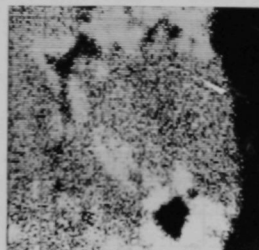
Fig. IV.B.3. Electron Microprobe Scanning Images of Aluminum Oxide Particle in Irradiated UO_2 -20 wt % PuO_2 Fuel (SOV-3). (All images represent areas 45 microns square.)



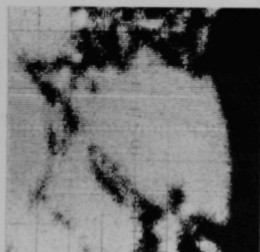
a) Specimen Current



b) Iron



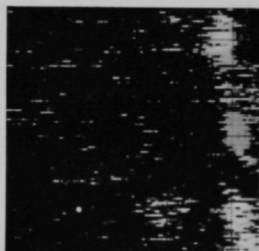
c) Nickel



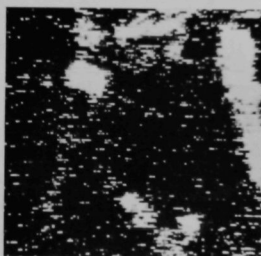
d) Chromium



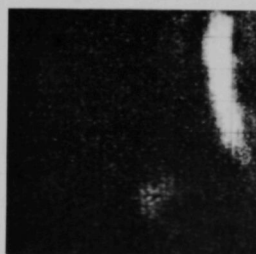
e) Cesium



f) Barium



g) Iodine



h) Tellurium

Fig. IV.B.4. Electron Microprobe Scanning Images of Fuel-Cladding Interface in UO_2 -20 wt % PuO_2 Fuel (SOV-3). (All images represent areas 45 microns square.)

cladding attack was $\sim 90 \mu\text{m}$, compared with a depth of attack of $40 \mu\text{m}$ for SOV-6 (see Progress Report for November 1967, ANL-7399, p. 121). The feature of most interest in SOV-3 can be seen in Fig. IV.B.4g, which shows, for the first time, the presence of iodine in the area of intergranular attack. The other X-ray scans in Fig. IV.B.4 show the distribution of iron, nickel, chromium, cesium, barium, and tellurium in the area of attack.

The presence of iodine in the areas of intergranular attack has led to the hypothesis that iodine is contributing significantly to the mechanism of metal transport from the cladding to the fuel matrix. It is suggested that the transport mechanism is similar to that of the van Arkel-de Boer* process, in which purification and vapor deposition of a metal is achieved by thermal decomposition of the metal iodide. In the fuel during irradiation, the transport mechanism would involve an iodine-cycling process in which fission-product iodine migrates to the cladding-fuel interface and reacts with the cladding, and the metal iodides formed vaporize and are transported to high-temperature zones in the fuel matrix, where iodide decomposition occurs. The process appears to be initiated only if the cladding temperature is high enough to produce (1) appreciable iodine attack on the steel and (2) vaporization of the metallic iodides formed.

The iodides of the three stainless steel components have stabilities at 1000°K^{**} that decrease in the following order: chromous iodide ($\Delta G_f^\circ = -26 \text{ kcal/mol}$), ferrous iodide ($\Delta G_f^\circ = -16 \text{ kcal/mol}$), and nickelous iodide ($\Delta G_f^\circ = -2 \text{ kcal/mol}$). The extent of reaction of fission-product iodine with the stainless steel components is probably most affected by the relative vapor pressures of their iodides at the cladding temperature; at 900°K ferrous iodide and nickelous iodide are three orders of magnitude more volatile than chromous iodide.

Although the free energy values indicate that chromous iodide is more stable than ferrous iodide, Samuel and Lockington† have reported that chromous iodide reacts with metallic iron in the presence of a copper catalyst to form ferrous iodide and metallic chromium. The driving force for this reaction must be the higher vapor pressure of ferrous iodide. The commercial process based on this reaction is usually carried out at temperatures between 900 and 1150°C . We believe that similar conditions exist in irradiated fuel, and it should not be surprising that one observes little or no transport of chromium from the cladding-fuel interface.

The iodine concentration available for metal transport during irradiation is greatly affected by competing reactions, i.e., reactions of iodine that do not contribute to metal transport and thereby limit the amount

* van Arkel, A. E., and de Boer, J. H., *Z. Anorg. Chem.* 148, 345 (1925).

** Wicks, C. E., and Block, F. E., Thermodynamic Properties of 65 Elements, Their Oxides, Halides, Carbides, and Nitrides, Bureau of Mines Bulletin 605 (1963).

† Samuel, R. L., and Lockington, N. A., British Patent 656734, August 29, 1951.

of iodine available. An example of such a reaction is the formation of cesium iodide. However, even if cesium iodide were formed, it might be unstable in a high radiation field, and its decomposition would release iodine for participation in a van Arkel-de Boer reaction. At present, the concentration of available iodine is not known, and further work is needed to elucidate the mechanism of metal transport.

Results obtained from laser sampling and gamma-spectrometric analysis of a cross section of SOV-6 ($\text{UO}_2\text{-PuO}_2$, 2.7 at. % burnup) have provided information that lends support to the metal-transport hypothesis discussed above. The data showed a marked difference in the ratio of ^{137}Cs to ^{134}Cs across the radius of the fuel pin. Cesium-137 was distributed throughout the fuel pin, whereas ^{134}Cs , which is formed from neutron capture by ^{133}Cs (stable), was detected only in samples taken within about 0.05 mm of the fuel-cladding interface. This sharp difference in distribution of the cesium isotopes could result from the differences in the half-lives of their iodine precursors, which are believed to migrate rapidly to the cladding. The half-life of ^{133}I is 21 hr, whereas that of ^{137}I is only 24 sec; therefore, considerably less migration of ^{137}I would be expected to occur.

The only long-lived iodine fission products expected to be present in the fuel at this time are ^{127}I (stable) and ^{129}I (1.6×10^7 yr), and these isotopes would not be detected by gamma spectrometry. However, iodine has been detected by spark-source mass spectrometry in a segment of the cladding of SOV-6. The concentration of iodine was about one-half that of the cesium. Further investigations of the behavior of cesium and iodine are planned.

c. Thermodynamics of Fuel Materials

- (i) Total Vapor Pressures and Carbon Potentials in the Ternary System U-C-Pu (P. E. Blackburn and M. Tetenbaum)

Last Reported: ANL-7548, pp. 91-92 (Jan 1969).

The study of the vaporization behavior of the uranium-carbon system is continuing. Measurements of the total pressure of uranium-bearing species and carbon activity are being made as functions of temperature and UC_x composition, using the transpiration method with hydrogen-methane mixtures as carrier gases. Emphasis has been placed initially on measuring carbon activities.

The results of the latest measurements of carbon activity as functions of UC_x composition at 2155, 2255, 2355, and 2455°K are shown

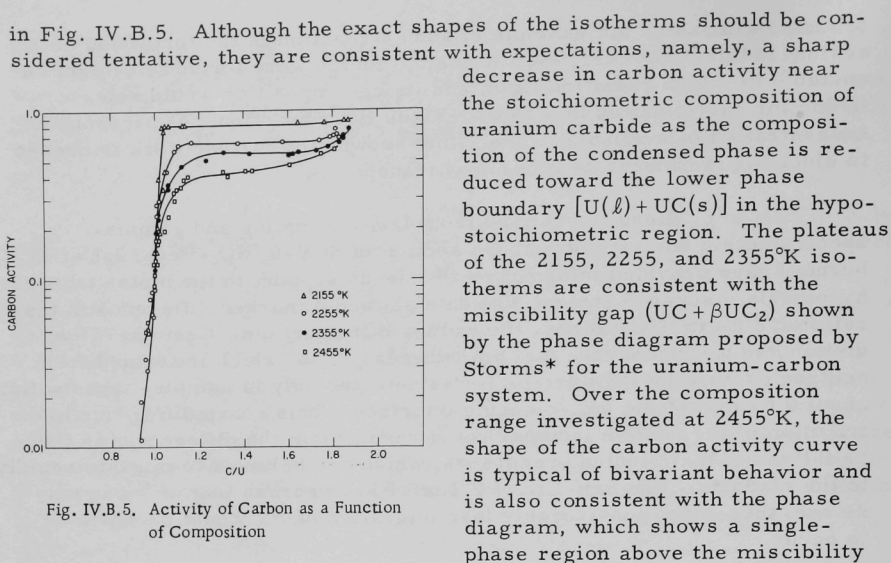


Fig. IV.B.5. Activity of Carbon as a Function of Composition

gap, with a critical temperature of $\sim 2100^\circ\text{C}$ at $\text{C/U} \approx 1.3$. Compositional values for the boundaries of the $\text{UC} + \beta\text{UC}_2$ diphasic region at 2155, 2255, and 2355 K derived from our measurements are given in Table IV.B.1. The low-carbon values are in good agreement with the compositions estimated from the phase diagram at these temperatures. The shallowness of the isotherms at the higher carbon compositions makes it difficult to estimate the terminal compositions of the $\text{UC} + \beta\text{UC}_2$ diphasic region from our data.

TABLE IV.B.1. Low- and High-carbon Compositions for Diphasic Region, $\text{UC} + \beta\text{UC}_2$

	Temperature (°K)	Composition (C/U)	
		This Work	Phase Diagram
Low Carbon	2155	1.05	1.13
	2255	1.15	1.14
	2355	1.25	1.20
High Carbon	2155	<1.65	1.61
	2255	<1.65	1.50
	2355	<1.60	1.35

*Storms, E. K., The Refractory Carbides, Academic Press, New York (1967), Chap. XI, pp. 205-213.

Calculated values for the free energies and heats for formation are given in Table IV.B.2. The free energy of formation values were calculated from our carbon-activity measurements shown in Fig. IV.B.5, the adjusted vapor-pressure values of Storms, and 126.5 kcal/mol as the heat of vaporization of uranium. Heat of formation values (at 298°K) were estimated from the calculated free energy of formation values and the known free energy functions (fef) for U, UC_{1.00}, "UC₂," and graphite. The Δfef values for UC_x compositions were interpolated on the assumption that a linear relationship exists for the Δfef values between UC_{1.00} and UC_{1.93}.

TABLE IV.B.2. Free Energies and Heats of Formation for UC_x
(All values in kcal/mol)

C/U	2155°K		2255°K		2355°K		2455°K	
	$-\Delta G_f^\circ$	$-\Delta H_{f(298)}^\circ$	$-\Delta G_f^\circ$	$-\Delta H_{f(298)}^\circ$	$-\Delta G_f^\circ$	$-\Delta H_{f(298)}^\circ$	$-\Delta G_f^\circ$	$-\Delta H_{f(298)}^\circ$
0.98	-	-	23.6	21.8	23.4	21.5	24.4	24.0
1.00	25.1	23.0	24.8	22.9	24.7	22.7	24.5	23.9
1.05	21.4	19.1	22.5	20.3	23.1	20.9	23.6	22.7
1.10	24.4	21.8	24.6	22.2	25.4	22.9	25.8	24.5
1.15	-	-	25.2	22.5	25.8	23.0	26.8	25.1
1.20	-	-	-	-	25.8	22.7	26.7	24.7
1.30	-	-	-	-	-	-	27.3	24.6
1.40	-	-	-	-	26.3	22.1	27.8	24.3
1.50	-	-	26.3	21.8	27.0	22.2	28.3	24.1
1.60	-	-	26.8	21.8	27.9	22.6	29.0	24.9
1.65	24.9	24.7	-	-	-	-	-	-
1.70	29.9	24.4	27.0	21.4	28.4	22.6	29.0	23.3
1.80	30.6	24.6	27.9	21.8	28.4	22.0	28.8	22.4
1.85	30.8	24.6	-	-	29.3	22.6	-	-

The heats of formation of UC_{1.00} and UC_{1.85} found by averaging values in Table IV.B.2 are $\Delta H_{f(298)}^\circ = -23.1 \pm 1.0$ and $\Delta H_{f(298)}^\circ = -23.6 \pm 1.0$ kcal/mol, respectively. The value chosen by the Vienna Panel for UC_{1.00} is $\Delta H_{f(298)}^\circ = -21.7 \pm 1.0$ kcal/mol; for UC_{1.91}, the value of $\Delta H_{f(298)}^\circ = -23 \pm 2$ kcal/mol was adopted.*

The free energy of formation values given in Table IV.B.2 are in reasonable agreement with the values derived from the mass-spectrometric measurements of Storms at 2100 and 2300°K. For UC_{1.00}, Storms obtains ΔG_f° values of -25.2 and -25.4 kcal/mol at 2100 and 2300°K, respectively; for UC_{1.80}, he obtains ΔG_f° values of -27.0 and -28.0 kcal/mol at 2100 and 2300°K, respectively.

Future work will emphasize measurements of the total pressure of uranium-bearing species over UC_x compositions.

*Vienna Panel, Technical Series No. 14, The Uranium-Carbon and Plutonium-Carbon Systems, IAEA, Vienna (1963).

d. Metal Fuels(a) Fuel-element Performance (H. V. Rhude)

Last Reported: ANL-7513, pp. 106-107 (Oct 1968).

Six capsules that contained experimental metallic fuel elements irradiated in EBR-II have been opened, and examination of the fuel elements has begun. The compositions and burnups of the elements are listed in Table IV.B.3.

TABLE IV.B.3. Compositions and Burnups of Metallic Fuel Elements

Fuel Element	Subassembly	Fuel Composition (w/o)	Cladding	Total MWd	Calculated Max Burnup (a/o)
ND24	XG05	U-15 Pu-10 Zr	V-20 w/o Ti	12,640	6.9
ND23	XG06	U-15 Pu-10 Zr	V-20 w/o Ti	9,317	5.2
BA01	XO28	U-15 Pu-10 Zr	304L SS	1,730	1.0
BC02	XO28	U-15 Pu-10 Zr	316 SS	1,730	1.0
NC17	XG05	U-15 Pu-10 Ti	V-20 w/o Ti	12,640	6.9
NC23	XG06	U-15 Pu-10 Ti	V-20 w/o Ti	9,317	5.5

Except in Element BC02, which ruptured in the capsule, no fission gas was detected in the capsules. Since this ruptured element could not be removed from the capsule by normal procedures, removal from the capsule by other means will be attempted so that the fuel element can be examined for the cause of failure. The other five fuel elements have been removed from their capsules, and photography, gamma scanning, and dimensional analyses have been completed. The changes in diameter are given in Table IV.B.4. The largest increases of diameter occurred near the midlength of the fuel columns, which is the region of highest neutron flux. However, the maximum increases of diameter for the five elements are not directly correlated with the maximum fluences. The measurements of diameter, which were made with a micrometer, will be checked with a profilometer.

TABLE IV.B.4. Increases in Diameter of Metallic Fuel Elements as the Result of Irradiation

Fuel Element	Maximum Fluence (n/cm ²)	Diameter before Irradiation (in.)	Diameter Increase (in.)		
			Top	Maximum ^a	Bottom
ND24	4.6×10^{22}	0.2086	0.0000	0.0006	0.0002
ND23	3.4×10^{22}	0.2086	0.0019	0.0021	0.0019
BA01	6.3×10^{21}	0.1955	0.0003	0.0009	-0.0001
NC17	4.6×10^{22}	0.2043	0.0006	0.0012	0.0011
NC23	3.4×10^{22}	0.2086	0.0015	0.0022	0.0014

^aNear the midlength of the fuel column.

2. Coolants, Moderators, and Control Materials--Fundamentals of Corrosion in Liquid Metals

a. Corrosion Mechanisms (D. L. Smith)

Last Reported: ANL-7553, pp. 82-83 (Feb 1969).

Vanadium-base alloys are being considered for use as fuel cladding in sodium-cooled fast breeder reactors. The major limitation for this application is the questionable corrosion behavior of the vanadium alloys exposed to liquid sodium. The presence of oxygen in the sodium is the primary cause of unacceptable corrosion behavior of the alloys. A quantitative determination of the detrimental effect of oxygen has been severely limited because of the inability to measure the oxygen content of the test sodium with the required degree of accuracy. Various laboratories have obtained significantly different corrosion behavior for vanadium alloys under reportedly similar test conditions. In some instances inconsistent results were obtained from different loops at the same laboratory. The conflicting data are believed to be the result of erroneous oxygen concentrations reported for sodium. The ability to control the oxygen concentration of sodium in laboratory size loops appears to be far superior to the ability to measure the concentration by the standard chemical techniques used at most laboratories. In some cases, therefore, the oxygen concentration in the sodium has been lower than the reported value. Therefore, it was proposed to measure the oxygen content of the sodium in the test loops of the various laboratories by the vanadium equilibration technique (see Progress Report for September 1967, ANL-7382, pp. 100-101). This method was developed at Argonne in conjunction with corrosion-mechanism studies of Group VB metals exposed to sodium. It involves the equilibration of oxygen between sodium and vanadium and the subsequent measurement of the oxygen concentration in the vanadium. The oxygen content of the vanadium is then related to the oxygen content of the sodium by the equilibrium distribution coefficient, which has been determined previously.

Vanadium wires were sent to investigators working on vanadium-alloy-corrosion programs at Argonne, Brookhaven, Karlsruhe, Los Alamos, Mine Safety Appliances Research, Saclay, and Westinghouse. An exposure time of 48 hr at the maximum loop temperature was suggested. This period was more than sufficient for exposure temperatures between 600 and 700°C. The wires were then returned to Argonne for oxygen analysis.

The oxygen analyses of the sodium determined from the vanadium wires are shown in Table IV.B.5 along with pertinent loop data supplied by the individual laboratories. When possible, this analysis was compared with the oxygen concentration of sodium reported by the investigator and the oxygen concentration obtained from solubility data* at the cold-trap temperature.

*Kassner, T. F., and Smith, D. L., Calculations on the Kinetics of Oxygen Solution in Tantalum and Niobium in a Liquid-sodium Environment, ANL-7335 (Sept 1967).

TABLE IV.B.5. Oxygen Analyses of Sodium from Test Loops Used for Vanadium-alloy-corrosion Experiments
(Determined by vanadium equilibration technique)

Sample No.	Loop Material	Flow Characteristics	Method of Oxygen Control	Trapping Temp (°C)	Oxygen ^a Solubility (ppm)	Investigator's Analysis for Oxygen in Sodium		Vanadium Equilibration Analysis		
						Technique	(ppm)	Exp Temp (°C)	Exp Time (hr)	O _{Na} (ppm)
MSA-1	-	2 gpm	Cold trap	121	0.68	UNC meter Plugging meter Hg amalgamation	2.4	650	48	1.6
BNL-1	321 SS	Forced circulation	Oxygen addition from reservoir as indicated by UNC meter	-	-	UNC meter Hg amalgamation	2.1-3.5	650	48	0.25
BNL-2	316 SS	Thermal convection ~0.1 ft/sec	Diffusion cold trap	-	-	-	1.5	650	48	1.7
ANL-1	304 SS	Forced circulation 4 l/hr	Full-flow cold trap	120	0.65	Vacuum distillation	0.5-1.5	650	43	0.60
ANL-2	Ni	Forced circulation 0.3 l/min	Full-flow cold trap	114	0.50	Vacuum distillation	0.6-2.0	600	70	0.39
ANL-3	Ni	Forced circulation 0.3 l/min	Full-flow Zr hot trap	600	-	Vacuum distillation	0.5-1.5	600	120	0.010
ANL-4	304 SS	Forced circulation 4 l/hr	Full-flow cold trap	120	0.65	Vacuum distillation	0.5-1.5	650	160	0.95
ANL-5	316 SS	Forced circulation 6 m/sec	4% flow cold trap	110	0.42	Vacuum distillation	0.5-1.5	650	160	0.13
ANL-6	347 SS	Forced circulation 8 l/min	7% flow cold trap	105	0.34	Vacuum distillation	-	650	42	0.34
WEC-1	316 SS	Forced circulation 0.64 gpm	Intermittent cold trap	-140	1.4	Hg amalgamation	~15	700	48	0.038
WEC-2	316 SS	Forced circulation 1.8 gpm	Intermittent cold trap	-140	1.4	Hg amalgamation	~15	700	48	0.024
LAL-1	321 SS	Forced circulation 0.1 gpm	Full-flow Zr hot trap	-	-	Vacuum distillation	3-9	650	48	0.0020
LAL-2	321 SS	Forced circulation 0.1 gpm	Full-flow Zr hot trap	-	-	Vacuum distillation	3-9	650	48	0.0056
KWG	18/8 Cr-NiTi SS	Forced circulation 50 cm/sec	Cold trap	-	-	Plugging meter	-	600	48	-

^aKassner, T. F., and Smith, D. L., ANL-7335 (1967); ANL-7527, pp. 101-104 (December 1968).

For several cold-trapped systems, reasonable agreement in oxygen concentrations was observed by the investigator and by the vanadium equilibration technique; however, in some cold-trapped systems, the vanadium equilibration technique gave values significantly lower than those reported by the investigator. The discrepancies may be explained by non-equilibrium conditions in the cold trap, depletion of the oxygen supply in the cold trap, or oxygen concentrations below the limit of detection by the more standard techniques used. It is also important to note that large differences in oxygen concentrations were obtained between hot-trapped and cold-trapped sodium. In one case (ANL-2 and -3), data were obtained for hot-trapped and cold-trapped sodium from the same loop. Although results are reported here, this technique has also been applied to sodium that contained the soluble getters calcium and magnesium. Values of the order of 0.01 ppm for the active oxygen in sodium were obtained.

The results of this survey analysis for oxygen in sodium are particularly pertinent to the program of vanadium-alloy corrosion. Although the equilibration technique is still in the development stage and has not been widely used, this technique appears to provide a suitable method for the determination of oxygen in sodium at the low oxygen concentrations of interest. The results obtained here indicate that the oxygen content of test loop sodium can be much lower than 1 ppm and that oxygen must be

supplied to the sodium used for corrosion tests of vanadium alloy, if constant oxygen concentrations are to be maintained. This method of analysis is being applied to EBR-II primary sodium to determine the oxygen concentration maintained in an actual reactor system.

3. Radiation Damage on Structural Materials--In-Reactor Creep Studies

a. In-pipe Creep (J. A. Tesk and W. F. Burke)

Last Reported: ANL-7553, pp. 85-86 (Feb 1969).

While CP-5 is undergoing repair, modifications of the cooling system for the circulating gas are being incorporated to meet the requirements of in-reactor creep tests. A new shield plug with larger gas-circulation tubes has been constructed (1/2-in.-ID tubes instead of the previous 1/8-in.-ID tubes). Laboratory and in-reactor tests have shown that the larger cooling capacity is needed to lower the in-reactor test temperatures to 350°C or less.

Tube-creep experiments in EBR-II have been planned. End plugs, caps, and pressurizing tubes are being fabricated for quality assurance testing.

b. Void Formation and Growth (S. D. Harkness)

Last Reported: ANL-7561, pp. 71-72 (March 1969).

(i) Temperature and Fluence Dependence of Void Formation.

For purposes of reactor design, it is important to know the dependence of void volume on irradiation temperature in austenitic stainless steel. A fundamental understanding of the phenomenon further demands knowledge of how the average void size and the void number density vary with temperature.

In an effort to gain this knowledge, five samples of Type 304 stainless steel were selected from various locations in EBR-II where all had been exposed to a fluence of $5 \pm 0.5 \times 10^{22}$ n/cm² at temperatures ranging from 410 to 607°C. Where possible, X-ray small-angle scattering (SAS), transmission electron microscopy (TEM), and immersion-density measurements were performed for each sample. Average void sizes were determined from the TEM and SAS studies (see the following section), the void volumes were deduced from the observed density changes, and the void number density was obtained by calculation from the above two results. No immersion-density data were available for the calculation of the void number densities for the samples irradiated at the two higher temperatures

because the small size of these samples prevented density measurement. Each sample consisted of a cladding-capsule pair sectioned from an experimental capsule that contained mixed-carbide fuel. By examination of the cladding and surrounding capsule material sectioned at the same axial position, it was possible to study the effect of temperature at constant fluence.

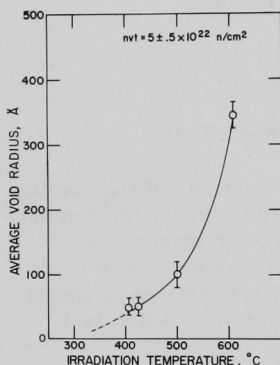


Fig. IV.B.6

The Effect of Irradiation Temperature on the Average Void Size in Type 304 Stainless Steel

Figure IV.B.6 shows the effect of irradiation temperature on the average void size. As can be noted, the void size increases rapidly with irradiation temperature.

Figure IV.B.7 depicts the observed change in void number density with irradiation temperature at constant fluence. This type of temperature dependence strongly suggests a nucleation-controlled process.

Figure IV.B.8 shows the variation of overall void volume with irradiation temperature at two fluence levels: 5×10^{22} and 3×10^{22} n/cm². At the higher fluence, a sharp temperature dependence is noted, with the maximum void volume occurring at ~500°C. The void volume at the location where the previously mentioned experimental fuel-irradiation capsule was irradiated at 500°C

agrees very closely with the observed diametral change of the capsule tube. The void volume for the cladding section irradiated at 607°C did not agree with the observed diametral change of the cladding. This indicates that creep had occurred during irradiation. The much increased dislocation density observed in the sample that had been irradiated at 607°C is consistent with this conclusion.

The absence of temperature dependence at the lower (3×10^{22} n/cm²) fluence was an interesting and surprising result. However, a nucleation and growth model for void formation, in which the voids act as the primary recombination sites, predicts such behavior.

The dependence of void formation on fluence is also of great design importance. Figure IV.B.9 shows the effect of fluence on void volume at three temperatures for samples of Type 304 stainless steel irradiated in EBR-II that have been studied at ANL and PNL.

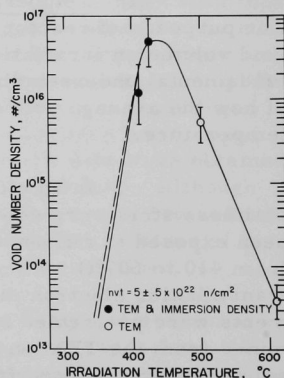


Fig. IV.B.7

The Effect of Irradiation Temperature on the Void Number Density in Type 304 Stainless Steel

Values were taken from swelling profiles of axial reactor components as determined by dimensional change and immersion-density measurement. The void volume is proportional to the neutron fluence raised to a power between 2 and 2.3. This result agrees well with a model formulated from nucleation and growth theory.

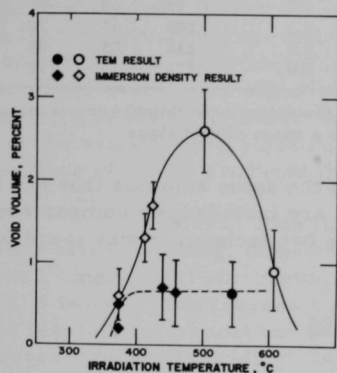


Fig. IV.B.8

The Effect of Irradiation Temperature on Void Volume in Type 304 Stainless Steel. Symbols \circ and \diamond -- $nvt = 5 \pm 0.5 \times 10^{22} \text{ n/cm}^2$; \circ and \diamond -- $nvt = 3 \pm 0.5 \times 10^{22} \text{ n/cm}^2$.

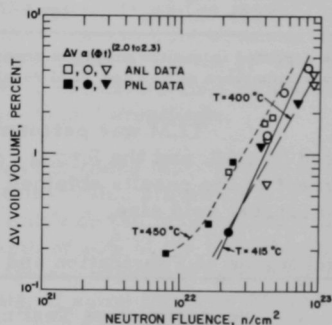


Fig. IV.B.9

The Effect of Neutron Fluence at Constant Irradiation Temperature on Void Volume in Type 304 Stainless Steel

(ii) Small-angle-scattering Studies of Void Formation. Small-angle scattering (SAS) has proved a valuable auxiliary tool to transmission electron microscopy (TEM) in the determination of void sizes. SAS measurements have been made with four samples with a Kratky collimating system that employs Mo $K\alpha$ radiation in conjunction with a balanced Zr-Y filter. The Guinier (R_G) and Porod (R^*) size parameters determined from the SAS curve are equivalent to moment ratios for size distribution of spherical particles;[†] that is,

$$R_G = |\langle R^7 \rangle / \langle R^5 \rangle|^{1/2}$$

and

$$R^* = \langle R^3 \rangle / \langle R^2 \rangle.$$

These moment ratios may be used to derive average size in terms of an assumed form of size distribution. A quite general distribution is the log-normal. This distribution was used to obtain the average void sizes, $\langle R \rangle$, for the four samples (see Table IV.B.6).

[†]Harkness, S. D., Gould, R. W., and Hren, J. J., Phil. Mag. 19, 115 (1969).

TABLE IV.B.6. A Comparison of Results for X-ray Small-angle Scattering and Transmission Electron Microscopy

Sample	Irradiation Temp (°C)	Estimated Fluence (n/cm ² x 10 ⁻²²)	R _G (Å)	R* (Å)	<R> (Å)	R _{TEM} (Å)
Control-rod Thimble ^a	450	4.1	74	69	68	60
Control-rod Thimble ^a	463	3.1	148	83	72	83
Subassembly XG05-Capsule	500	5.0	130	95	90	95
Subassembly XG05-Cladding	607	5.0	173	159	150	355

^aResults reported in earlier progress reports for the control-rod thimble are repeated here to allow comparison of SAS and TEM results over a range of void sizes.

TEM was performed on the same samples that had been analyzed by SAS, and the RTEM results are included for comparison. Good agreement of the results obtained by the two techniques was found for all but the largest void size.

4. Techniques of Fabrication and Testing

a. Nondestructive Testing

(i) Development of Nondestructive Testing Techniques (C. J. Renken)

Last Reported: ANL-7527, pp. 106-110 (Dec 1968).

(a) Development of Electromagnetic Testing Techniques.

Development work has continued on high-speed pulsed-electromagnetic inspection systems for the detection of defects in tubing. Multiaperture transducers, which induce a time-varying current in a specimen and detect the field established by the specimen current, have been designed and constructed for tubing of several sizes. One of the transducers is a six-aperture transducer for tubing of the current FFTF reference size. A trial was performed with 25 m of tubing (of the general size and type expected to be used in FFTF) provided by Battelle Northwest Laboratories. The tubing was deliberately selected from various lots of Types 304 and 316 stainless steel.

On the demodulated but unfiltered output of the instrument, various tubes provided signals with noise levels ranging from insignificant to fairly severe compared with the signal produced by a longitudinal electromachined notch on the inner surface of a standard tube. (The notch had a measured depth of 10% of the tube wall thickness, a length of 1 mm, and a width of 0.075 mm.) However, one of the advantages of a multiaperture test system that uses time sampling is the possibility of noise reduction, since such a system provides an abundance of information compared with conventional systems for testing electromagnetic tubing. With the

FFTF tubing, most of the noise originated from slight geometrical variations (all within specification) in the wall thickness and diameter of the tubing. From these variations, a roughly periodic 4.5-Hz signal that varied in amplitude from tube to tube was produced at the test system output. The 4.5-Hz signal was almost entirely eliminated by bucking the signals from opposite apertures. A residual 9-Hz signal that persisted despite the cross-bucking operation was eliminated by a 9-Hz slot filter. These modifications had little effect on the signal from the standard defect because of the width of its effective power spectrum, and because the standard defect appeared only under one aperture at a given time. The sampling points of the system were adjusted so that identical notches on the inner and outer surface of a tube produced the same signal amplitude.

Based upon the results of these tests and upon tests with other sizes of tubing, inspection of thin-walled stainless steel tubing to detect a longitudinal electromachined notch on the inner surface having a length of two wall thicknesses and a depth of 10% of the wall thickness appears feasible for almost any lot of stainless steel tubing having wall thicknesses typical of cladding. Inspection of some lots to a 5%-two wall thickness standard is probably practical. The present test system inspects at the rate of 4 m/min, but there are no technical reasons to prevent inspection at twice this speed.

The electronic system used is capable of simultaneous inspection of tubing for defects and measurement of wall thickness. This was demonstrated in tests with tubing of 7.36-mm diameter and 0.508-mm wall thickness. Wall thickness can be simultaneously measured at as many as six angular positions around the tube circumference, although it appears that for most applications a three-point measurement will be adequate. Neither a large enough variety nor a large enough quantity of tubing has been measured to evaluate fully the accuracy of the technique, but the non-destructive and direct measurements made thus far agree within 0.005 mm. If wall thickness is not measured simultaneously with inspection for defects, continuous measurement of wall thickness at a rate of 15 m/min should be practical.

Progress on the synthesis of transducer-broadbanding filters (see ANL-7527) that more nearly approach the ideal can be reported. The filters in use provide the proper amplitude versus frequency characteristics, but produce a phase shift as a function of frequency that is far from suitable. It appears that a six-pole Gaussian filter can be physically realized that will more closely approximate the filter theoretically required by our transducers. Construction of this type of filter has been deferred, however, until a new transducer design has been fully tested. The aperture diameter in the new transducer has been reduced from 1.77 to 1.25 mm. If this change results in an improvement in resolution, new broadbanding filters will be designed to match the new transducers.

Analytical work on the problem of the point defect in a conductor passing under a pulsed line source has continued. Computer programs that provide useful computed values of the various normalized field components have been developed for short values of normalized time and for very long values of normalized time, but thus far no program has been written that is capable of computing values for intermediate times.

5. Engineering Properties of Reactor Materials--High Temperature Mechanical Properties of Ceramic Fuels

a. High Temperature Mechanical Properties of Fuel Oxides (R. J. Beals)

(i) Stress Dependence on Strain Rate and Temperature

Last Reported: ANL-7553, pp. 88-92 (Feb 1969).

Investigation of the effects of temperature and strain rate upon the mechanical properties of stoichiometric uranium dioxide has continued.

Specimens were 97% of theoretical density with an average grain size of $5\ \mu$. All tests were carried out in a vacuum of 10^{-5} Torr. The measurements were made with at least five specimens at each test condition.

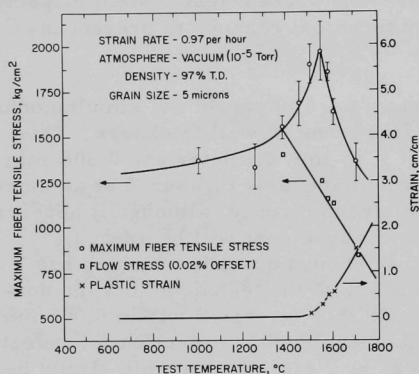


Fig. IV.B.10. The Effect of Temperature on the Maximum Fiber Tensile Stress, Flow Stress, and Plastic Strain of Stoichiometric Uranium Dioxide (Medium Strain)

approximately 1375°C , where the UTS was $1550 \pm 60\ \text{kg}/\text{cm}^2$. The UTS increased rapidly to $1970 \pm 160\ \text{kg}/\text{cm}^2$ as the temperature was increased to the critical temperature of 1550°C . At test temperatures above the critical temperature, the UTS decreased rapidly.

The relationship between strain rate and critical temperature for the three strain rates studied is shown in the following tabulation:

Strain Rate (1/hr)	Critical Temperature (°C)
0.097	1400
0.97	1550
9.7	1725

If it is assumed that (1) the critical temperature is associated with the onset of significant plastic strain resulting from a diffusion-controlled process that limits the maximum fracture stress, and (2) there is a constant stress, the strain-rate dependence on temperature is expressed as

$$\dot{\epsilon} \propto \exp(-Q/RT), \quad (1)$$

where $\dot{\epsilon}$ is the strain rate, Q is the activation energy, and T is the absolute temperature. By use of this equation the shift of the peak, as observed in Fig. IV.B.10 and Fig. IV.B.4 of ANL-7553, corresponds to an activation energy of approximately 93 kcal/mol. This compares favorably with the 94 kcal/mol reported on p. 92, ANL-7553, for the peak shifts between strain rates of 0.097/hr and 9.7/hr.

It was observed that until the temperature was increased to 1375°C, the uranium deformed in a brittle fashion and exhibited no plastic strain. Above this brittle-to-ductile transition temperature, plastic strain increased rapidly to a value of 0.015 cm/cm at 1700°C.

The flow stress for the stoichiometric UO_2 was measured at 0.02% offset. At a strain rate of 0.97/hr, the first indication of plastic strain occurred at 1375°C. Figure IV.B.10 shows that the extended flow-stress curve intersects the UTS curve at 1375°C and decreases linearly with increasing test temperature. By an interpretation of a linear least-squares regression, the relationship between flow stress and temperature at a strain rate of 0.97/hr is

$$\sigma_f = 4460 - 2.361t,$$

where σ_f is the flow stress in kg/cm^2 , and t is the test temperature in °C.

At strain rates of 0.097/hr and 9.7/hr, the modulus of elasticity (or Young's modulus) for stoichiometric uranium dioxide decreased linearly with increasing temperature at temperatures above 1000°C. The curves at these strain rates are shown in Fig. IV.B.11. The Young's modulus was slightly higher at the rapid strain rate than at the slower rate. By an interpretation of a linear least-squares regression, the relationship between Young's modulus and temperature for a strain rate of 9.7/hr is

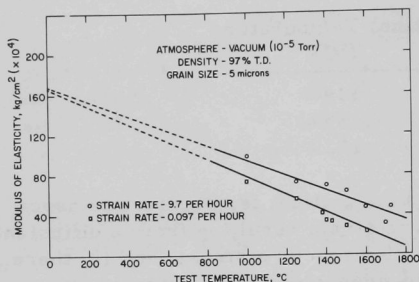


Fig. IV.B.11. The Effect of Temperature and Strain Rate on the Modulus of Elasticity of Stoichiometric Uranium Dioxide

atures, a Young's modulus of $1,660,000 \text{ kg/cm}^2$ (or $23.6 \times 10^6 \text{ psi}$) is recorded. This compares favorably with the values of $21 \times 10^6 \text{ psi}$ recorded by Lambertson and Handwerk* and $26.5 \times 10^6 \text{ psi}$ recorded by Lang.** Data for the Young's modulus for a strain rate of $0.97/\text{hr}$ are incomplete, but fall between the limiting values at elevated temperatures.

(ii) Compressive Creep. Specifications have been written and a purchase order has been placed for high-temperature compressive creep apparatus. The total load capacity of each creep machine is 1000 lb. Each machine is equipped with a precision extensometer to permit the measurement of strain under the various test conditions. Delivery is scheduled for late July 1969.

$$E = 1,689,500 - 741.7t,$$

and for a strain rate of $0.097/\text{hr}$ this relationship is

$$E = 1,671,500 - 924.4t,$$

where E is Young's modulus in kg/cm^2 and t is the test temperature in $^{\circ}\text{C}$.

Upon extrapolation of this curve to room temperature, with the assumption that the linear decrease holds over the extrapolated tempera-

*Lambertson, W. A., and Handwerk, J. H., The Fabrication and Physical Properties of Urania Bodies, ANL-5053 (Feb 1956).

**Lang, S. M., "Properties of UO_2 ," in J. Belle and B. Lustman, Fuel Elements Conference, Paris, TID-7546, March 1958, pp. 442-515.

C. Engineering Development

1. Instrumentation and Control

a. Boiling Detector (T. T. Anderson)

(i) Flux Noise Method

Not reported previously.

A program has been initiated to determine the feasibility of using neutronic noise as a method of detecting boiling in an LMFBR. The study aims to determine the absolute sensitivity of the various neutronic methods so that comparisons can be made easily with other means of detecting boiling and thus the best method for a particular LMFBR reactor system be selected.

A survey and review of previous work on the detection of boiling in water-cooled thermal reactors is nearly complete. It mainly concerns the measurement and determination of the power spectral density of the neutron-flux measurements. The survey indicates that there are problems in detecting boiling by neutronic means, let alone determining the characteristic power spectral density of the phenomenon. Conflicting results can be found; some results of power spectral density measurements indicate that boiling possesses a resonant effect at low frequency, others indicate that it is white noise.

The time for detecting boiling can be important from a control standpoint. However, because the power spectral density from a neutron detector of boiling might be weighted heavily in the low-frequency spectrum, such a device might take much longer to detect boiling than would a device that uses the high-frequency components from an acoustic detector. Therefore, alternative methods are being investigated to reduce the time for determining the presence of boiling in LMFBRs. It is hoped that the data-collection and evaluation times can be reduced to be comparable with the acoustic method.

2. Heat Transfer and Fluid Flow

a. Heat Transfer in Liquid Metal Cooled Reactor Channel (R. P. Stein and J. V. Tokar)

Last Reported: ANL-7548, p. 100 (Jan 1969).

(i) LMFBR High-flux Operation and Its Consequences. The liquid-metal helical induction pump was completed and tested with NaK. The

pump performed satisfactorily and will be adequate for the LMFBR burnout limitations tests.

A detailed piping flexibility analysis (see Progress Report for November 1968, ANL-7518, p. 97) is nearing completion. The vacuum pumping systems were received, checked for conformance to specifications, and accepted. The vacuum chamber is being fabricated. The loop superstructure is about 70% complete.

b. Electron Bombardment Heater Test Facility (R. D. Carlson)

Last Reported: ANL-7553, p. 97 (Feb 1969).

Work on the electron-bombardment-heated (EBH) 7-pin clusters was temporarily suspended to concentrate on cathode suspension and non-uniform electron-emission problems, which were causing considerable difficulty in the cluster development. A single pin, of 0.25-in. OD and 24 in. long, was chosen to investigate these problems. Several methods of cathode suspension were tried, and the 1%-thoriated tungsten was replaced with pure tungsten.

Uniform electron emission could not be obtained from the thoriated-tungsten cathode; uniform emission is very critical in this small-diameter pin geometry. The thoriated-tungsten cathode would spot, emit and cause pits to form on the anode wall, and eventually burn through.

The EBH pin now being tested has an 0.030-in.-dia, pure tungsten cathode operating at 2500-2600°K. The electron emission has been up to 18 Amp, the anode voltage has been as high as 3600 V, and the heat flux has been as high as 1.7×10^6 Btu/hr-ft² over the entire 24-in. length of the 0.25-in. tube.

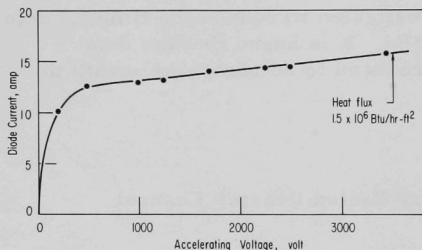


Fig. IV.C.1. Test of EBH Single-pin Anode Having 0.25-in. OD, 0.010-in. Wall, and 24-in. Length. The 0.030-in.-dia cathode of pure tungsten operated at 2530°K.

As of May 20, 1969, the pin has operated more than 16 hr at a heat flux of greater than 1.5×10^6 Btu/hr-ft². The outer wall of the anode reached a maximum of 95°F with a ΔT of approximately 133°F across the wall. A mass balance and power measurements substantiate that >60 kW of heat are being supplied to the coolant. Figure IV.C.1 shows an operating curve for this 0.25-in.-dia pin. Further experiments will determine: (1) the lifetime of the heater, (2) the maximum heat flux, (3) operability in sodium at >1000°F,

and (4) operability of 0.25-in.-pin bundles. Experiments with larger-pin bundles (of 0.375- and 0.312-in. diameter) also will continue with pure-tungsten cathodes.

3. Engineering Mechanics

a. Anisotropic Thermoelasticity Studies (R. A. Valentin)

Last Reported: ANL-7553, pp. 97-98 (Feb 1969).

(i) Isotropic Solutions for Comparison. The thermoelastic stress analysis of cylindrical fuel elements is usually based on the assumption of plane strain. These results give a good approximation to the exact solution near the midplane of the element, provided the ratio of length to radius of the cylinder is much greater than unity. To obtain more accurate information about the state of stress and deformation near the ends of the cylinder, the assumption of a plane deformation field must be removed.

The exact solution for the axially symmetric deformation of a solid circular cylinder of finite length with uniform internal heat generation and traction-free boundaries has been obtained with the aid of Youngdahl's* cylinder stress functions. Expressions for the stresses and displacements in the cylinder are obtained in the form of infinite series whose coefficients are the solutions of an infinite set of simultaneous linear algebraic equations. A computer program is being written to evaluate this solution.

Closely related is a study of the effect of interfacial shear on the nonplane deformation near the end of a fuel pin. Before considering the shear effect, it is desirable to determine both the pressure distribution between the cladding and the fuel and the deformation state for the simpler case of perfect interfacial slip. An analysis of this problem has been completed, and computer work is underway to evaluate the results. The solution method makes use of an approximate analysis of the type developed by Conway and Farnham** for shrink-fit problems combined with a modified version of a known elasticity solution for the effect of a band of pressure on a semi-infinite cylinder.[†]

*Youngdahl, C. K., On the Completeness of a Set of Stress Functions Appropriate to the Solution of Elasticity Problems in General Cylindrical Coordinates, Int. J. Eng. Sci. 7, 61-79 (1969).

**Conway, H. D., and Farnham, K. A., The Shrink Fit of a Flexible Sleeve on a Shaft, Int. J. Mech. Sci., Vol. 10 (1968), pp. 757-764.

†Tranter, C. J., and Craggs, J. W., Stresses Near the End of a Long Cylindrical Shaft Under Non-uniform Pressure Loading, Phil. Mag. 38, 214-225 (1947).

b. Structural Dynamics Studies--Parallel-flow-induced Vibrations
(M. W. Wambsganss, Jr.)

(i) Structural Dynamics Test Loops

Last Reported: ANL-7561, p. 78 (March 1969).

Construction of the small loop continues. The pump and accumulator have been installed; the piping is 50% complete. Design work began on a vibration fixture for a tube-stop impact experiment. Specifications are being prepared for construction details of the large loop.

(ii) Damping Analysis

Last Reported: ANL-7561, p. 79 (March 1969).

The influence of water flow velocity on the damping characteristics of a cylindrical tube in parallel flow is being studied experimentally. The tube, instrumented with a small accelerometer internally mounted at the midpoint, is supported in a test section that is vibrated on a shaker while water is pumped through the test section at flow velocities ranging from 7.5 to 50 ft/sec. The tests are performed by establishing a specific mean flow velocity of water, maintaining the acceleration imparted to the test section (tube supports) at a selected constant level while the frequency range from 40 to 55 Hz is swept, recording the time-history of the output acceleration on magnetic tape and plotting its frequency spectrum, and computing an effective damping factor (ratio of equivalent viscous damping coefficient to first-mode critical damping) by two different methods, from (a) the modal-magnification factor at resonance and (b) the bandwidth taken at the half-power point. To include the influence of input amplitude on damping, tests at a given flow velocity are performed at acceleration levels corresponding to peak input displacements (of approximately 2, 3, 4, 5, 6, and 8 mils) at resonance.

Qualitative agreement between the two methods of calculating damping is good. However, quantitative values computed by the modal-magnification method are approximately 2.5 times greater than the corresponding values obtained from the bandwidth method. For flow velocities greater than zero, the data are approximately linearly related. Data from each of the two computational methods were correlated with a straight line and the lines extrapolated to zero flow velocity. Then the results were normalized by their extrapolated zero-velocity values. The damping factor increases significantly with mean axial flow velocity; for example, at a typical coolant flow velocity of 30 ft/sec, effective damping is approximately 2.3 times greater than the value measured in static fluid. This dependence of damping on mean flow velocity can be very important because vibration amplitude at resonance depends directly on damping, as do certain forms of instability.

(iii) Parametric Vibration

Not reported previously.

The study of flow-induced vibration has been extended to include the investigation of parametric vibration, the influence of initial curvature, and the combined effects of parallel flow and crossflow.

To understand the fundamental dynamic mechanism of the vibration of a tube conveying fluid, free vibration is examined. Because the boundary-value problem associated with the system is not Hermitian in character, the analytical solution is not easy to obtain. However, if the flexural rigidity of the tube is neglected, the mathematical solution in closed form is feasible. The main characteristics of the dynamic behavior of the tube can be obtained from a simplified model.

It is well-known that natural frequencies depend on the axial transport velocity u of the fluid. The more interesting fact is that the system does not possess classical normal modes, because the various parts of the tube do not vibrate in the same phase, that is, the phase is not constant along the tube but propagates with a velocity V_p . The phase propagation velocity also depends on the transport velocity, as shown in Fig. IV.C.2, where β is the ratio of the "added" mass of fluid to the mass of the sum of fluid and tube. The history of the mode shapes of the first and second modes are given in Fig. IV.C.3. When $u/c = 0$, the tube vibrates in classical normal mode, but for $u/c \neq 0$, the phase propagates toward upstream. This phenomenon is due to the effect of Coriolis force, which is intrinsic to such a moving system in transverse vibration.

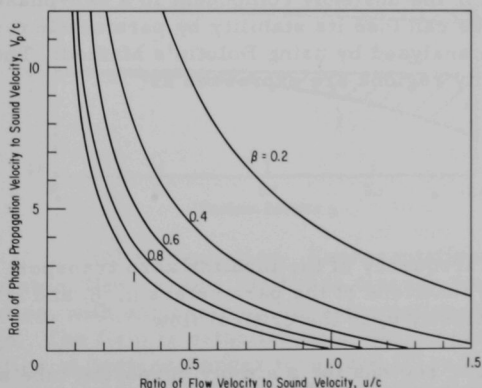


Fig. IV.C.2

How Phase-propagation Velocity
Decreases with Transport Veloc-
ity of Fluid

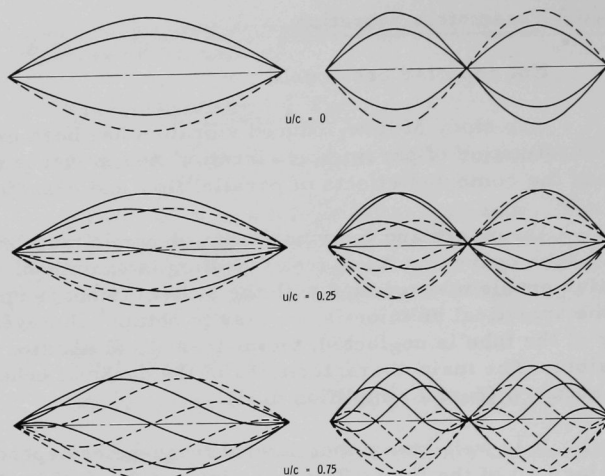


Fig. IV.C.3. History of Mode Shapes of Fundamental Mode (left) and Second Mode (right) for Three Values of the Ratio of Fluid Axial Transport Velocity to the Velocity of Sound

If the transport velocity varies with the time, we represent it in the form

$$u = u_0(1 + \mu \cos \omega t),$$

where u_0 and μ are constants. The fluctuation of flow velocity can result from the pumping operation or the unsteady component in a two-phase flow. Due to flow pulsation, the tube can lose its stability by parametric resonance. The stability boundaries are analyzed by using Bolotin's Method. The principal and secondary instability regions are expressed as

$$p_1 \leq \frac{\omega}{2\omega_1} \leq p_2;$$

$$q_1 \leq \frac{\omega}{\omega_1} \leq q_2,$$

where ω_1 is the fundamental frequency of the tube for zero transport velocity, and p_1 , p_2 , q_1 , and q_2 are functions of the parameters μ , β , and k , where k is the ratio of transport velocity u_0 to the critical flow

The instability regions for a simply supported tube are given in Fig. IV.C.4. From it and related figures we conclude that: (1) the second instability region is much narrower than the principal region, (2) the width of the instability region depends on the transport velocity component u_0 ; as k increases, the parametric resonance frequency decreases and the

width of the instability region increases, (3) the effect of Coriolis force, which is proportional to β , is to lower the instability regions, but it has little effect on the width of the instability region, and (4) the instabilities at constant flow velocity need not concern reactor designers because they occur at high transport velocities that are not likely to be used in reactor channels, but parametric resonance can occur at lower flow velocities.

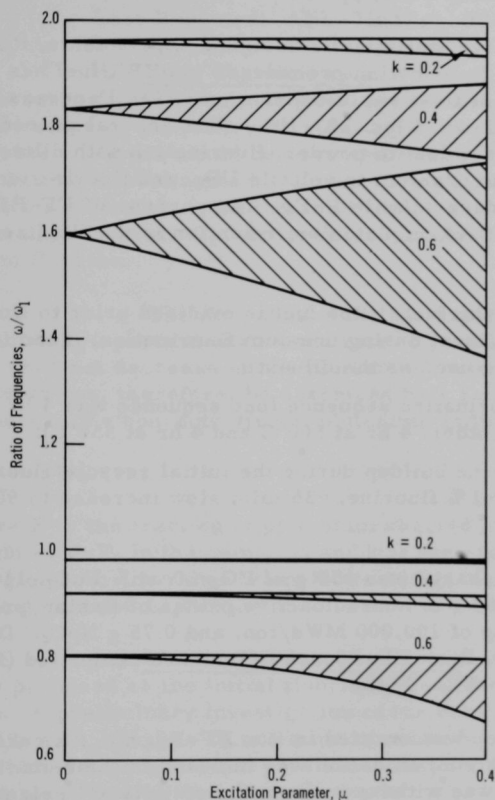


Fig. IV.C.4
Stability Diagram for $\beta = 0.2$

(iv) Consultation. Representatives of Foster-Wheeler Corp., Livingston, New Jersey, visited to discuss the ANL program in flow-induced vibration, with emphasis on instrumentation, data processing, and flow-loop design. The firm is establishing a test program (1) to study the flow-induced vibration of heat-exchanger tubes and (2) to evaluate given designs as to their potential for detrimental flow-induced vibration.

D. Chemistry and Chemical Separations

1. Aqueous and Volatility Processes--Fluoride Volatility Process

a. Fluorination Chemistry and Procedures (M. J. Steindler)

Last Reported: ANL-7548, pp. 105-107 (Jan 1969).

A second set of five statistically designed experiments, Runs FF-B1 to FF-B6, to develop fluorination procedures for FBR fuel has been completed. (For discussion of first set of experiments, see Progress Report for November 1968, ANL-7518, pp. 103-105.) The general procedure includes oxidation to reduce the fuel to powder, fluorination with dilute fluorine to convert the bulk of the uranium to volatile UF_6 , and fluorination with concentrated fluorine to produce volatile PuF_6 . The purpose of FF-B1 to FF-B6 is to determine the effect on plutonium retention in the fluidized bed of the following variables:

1. oxidation of the fuel (if the fuel is oxidized prior to fluorination, oxygen is used as the diluent during uranium fluorination; if the fuel is not first oxidized, nitrogen is used as the diluent);
2. recycle-fluorination sequence (one sequence was 4 hr at 400°C and 4 hr at 550°C; the other, 4 hr at 500°C and 4 hr at 550°C);
3. rate of fluorine buildup during the initial recycle-fluorination period (fast increase to 90 vol % fluorine, ~35 min; slow increase to 90 vol %, 1 hr).

In each run, the charge was 650 g of UO_2 -20 wt % PuO_2 , 1100 g of -40 + 170 mesh alumina, 69 g of nonradioactive oxides of fission-product elements simulating a burnup of 100,000 MWd/ton, and 0.75 g NpO_2 . During the current reporting period, Runs FF-B3 to FF-B6 were completed (for Runs FF-B1 and FF-B2, see ANL-7548).

The oxidation step was omitted in Run FF-B3; since a cake developed in the reactor in this run, oxidation was included in the remainder of the runs, and Run FF-B3 was withdrawn from the statistical design. The lowest retention of plutonium in the bed was achieved with Runs FF-B5 and FF-B6, which were planned as replicate runs to determine the experimental error. They indicated that, with oxidized fuel, recycle-fluorination temperatures of 400 and 550°C, and a rapid fluorine increase, residual plutonium in the bed could be reduced to about 1% of the charge.

The fluorination of plutonium with 90 vol % F_2 was found to follow a diminishing-sphere reaction model during the initial period of recycle-fluorination. Reaction rates as a function of temperature gave an apparent

activation energy of 8.6 kcal/mol, which is in good agreement with literature values (8.7 to 15.5 kcal/mol) reported for the temperature range from 170 to 500°C.*

b. Purification Procedures and Fission Product Chemistry
(M. J. Steindler)

Last Reported: ANL-7561, pp. 80-83 (March 1969).

(i) PuF₆ Chemistry and Purification. The most recent flowsheet for processing FBR fuels induces the removal of PuF₆ from various process gas streams by reaction with solid LiF. Since recovery of the plutonium from the LiF beds would be essential to keep the process loss within acceptable limits, experiments have been carried out to determine the recovery rates for plutonium from the solid complexes LiPuF₅ and Li₄PuF₈ that are apparently formed. The experiments involved reacting the complexes with 1-atm fluorine.

The data obtained in the experiments are not consistent with diminishing-sphere models--the rate of reaction of a sample of either complex does not decrease as the plutonium content of the solid phase decreases. The data can, therefore, be described by a rate law that is of zero order with respect to the concentration of plutonium in the solid phase:

$$FW_0 = kt,$$

where F is the fraction of plutonium reacted after time t, W₀ is the initial weight of PuF₄ in the complex, and k is the rate constant. The activation energies over the range from 350 to 450°C were 12 kcal/mol for LiPuF₅ and 10 kcal/mol for Li₄PuF₈.

(ii) Fission Product Chemistry. An oxygen-fluorine mixture has been proposed as the initial fluorinating agent in the fluoride volatility process. A preliminary investigation of the behavior of selected fission products in a 10:1 oxygen-fluorine mixture has been carried out because the available data suggest the possibility that compounds other than binary fluorides may form in this process step.

Results obtained through thermobalance weight-loss data and X-ray diffraction analysis of reaction intermediates indicated that, when fission products or their oxides are exposed to O₂-F₂ mixtures at elevated temperatures, both O₂ and F₂ react. The oxides, except RuO₂, react markedly slower than the elements. In most cases, a complex reaction takes place with a weight gain followed by a weight loss--each fission-product

element reacting differently. Volatile oxides and oxyfluorides (e.g., RuO_4 , MoOF_4 , and IOF_5) volatilize with the binary fluorides; the formation of RuO_4 appears to be catalyzed by F_2 ; antimony ignites to Sb_2O_4 and a nonvolatile unidentified species, and appears in the form of a fog.

(iii) Neptunium Fluoride Chemistry. During experiments to compare the relative tendencies of NpF_6 , PuF_6 , and UF_6 to decompose by various energy stimuli, it was discovered that PuF_6 can be formed at room temperature by ultraviolet irradiation (3125 \AA) of the system solid PuF_4 -gaseous fluorine (300 mm Hg). Spectrophotometric measurements of the quantity of PuF_6 produced and actinometric measurements of the number of the number of light quanta incident on the system were used to estimate an apparent quantum yield of 4×10^{-3} molecule of PuF_6 per quantum, i.e., $7 \times 10^{-2} \text{ kW-hr}$ energy were required per gram of PuF_6 produced. The quantum yield could possibly be improved by optimizing the mechanics of exposing this heterogeneous system to light.

c. Energineering-scale Development for FBR Fuels (N. M. Levitz)

Last Reported: ANL-7561, pp. 83-84 (March 1969).

(i) Alpha Facility Maintenance. Useful information on the durability of gloves has been obtained during the course of the operation of the smaller glovebox of the Engineering-scale Alpha Facility.

This glovebox, three-module by four-module unit, houses off-gas scrubbers, AEC filters, and oxygen and fluorine gas manifolds, which supply the process equipment located in the larger glovebox. The small box has been exposed mainly to filtered ventilation air at near-ambient temperatures.

Deterioration of 41 of the 95 seamless, milled neoprene gloves has been observed, and the 41 gloves have been replaced. Most of the deterioration consisted of cracking at folds and creases after long periods of nonuse. Polymer-coated neoprene gloves installed in 39 of the 95 positions showed no deterioration except discoloration. Little damage to gloves due to abrasion or wear was evident, although fairly heavy mechanical work was performed in this box.

Polymer-coated gloves (with the coated side exposed to the box interior) should be considered for more general use, although they are somewhat stiffer and more tiring to use. It was concluded that gloves should be left fully extended when not in use, and frequent inspections are desirable.

d. Engineering Design, Analysis and Evaluation (N. M. Levitz)

Last Reported: ANL-7553, pp. 98-100 (Feb 1969).

Final editing, prior to publication, is under way on the conceptual design study for a large fluoride volatility plant for reprocessing LMFBR fuels.

2. Closed Cycle Processes--Compact Pyrochemical Processes

a. Supporting Chemical Studies (I. Johnson)

Last Reported: ANL-7553, pp. 100-101 (Feb 1969).

In the pyrochemical process currently under development, de-cladding of the spent fuel elements is achieved by dissolution of the stainless steel cladding in molten zinc (see Sect. d, below). It has been proposed by Payrissat and Wurm* that a molten Sb-17.3 at. % Cu may be an attractive alternative to zinc because of the considerably higher solubilities of stainless steel constituents in the Sb-Cu alloy. However, it was pointed out that agitation of the system is necessary in order to achieve a satisfactory dissolution rate.

Several laboratory-scale experiments were performed to investigate the Sb-Cu system as a decladding solvent. In one case, two samples of Type 304 stainless steel (5/16-in. rods) were held in contact with liquid Sb-17.3 at. % Cu alloy at 925°C for 7 days under static conditions. About 20% of the stainless steel dissolved. Metallographic examination indicated that the low rate of dissolution resulted from the formation of one or more adherent intermetallic phases on the surface of the stainless steel. A subsequent experiment was conducted in which one side of a 3/8-in.-thick sample of Type 304 stainless steel was exposed with moderate agitation to Sb-17.5 at. % Cu at 900°C. Within a period of 60 min the sample had dissolved completely. These results substantiate the statement concerning the importance of agitation if the Sb-Cu system is used as a decladding solvent.

Samples of tungsten and Mo-30 wt % W (possible containment materials for the decladding solvent) were also held in contact with Sb-17.3 at. % Cu alloy at 925°C for 7 days under static conditions. The tungsten showed no noticeable attack, but the Mo-30 wt % W alloy was attacked severely through the formation of a Sb-Mo intermetallic phase.

*Payrissat, M., and Wurm, J. G., Decladding of UO_2 - PuO_2 /Stainless Steel Fast Reactor Fuels by Liquid Metals, presented before the EAES Symposium, Mol, Belgium, Oct. 28-29, 1968.

b. Process Engineering Studies (R. D. Pierce)

Last Reported: ANL-7553, p. 101 (Feb 1969).

Tantalum and niobium as well as their alloys are being tested as candidate container materials for pyrochemical processes. These materials have shown a tendency to become hardened and embrittled during exposure to salt mixtures and vapors during containment tests. Hydrogen embrittlement is known to be the principal mechanism.

Tests were performed with coupons of Nb-Zr alloy to determine whether degassing of furnace components before exposure of the coupons would have any effect on hardening of the alloy. The tests were performed in a furnace that had previously been exposed to a salt environment. Coupons of Nb-Zr alloy were exposed to an argon atmosphere at 700°C, with and without prior degassing of the furnace components.

The results of these tests indicate that degassing the furnace components before the tests reduces the increase in hardness, but that residual contaminants may never be completely removed because they are given off slowly. Degassing of furnace components prior to materials tests has been adopted as a routine procedure, and methods of improving the purity of the salt mixtures are being investigated.

Tests were also performed to determine if Nb-Zr alloy samples that had been hardened by exposure to a furnace environment containing salt could be freed of hydrogen and reduced in hardness by heating under a vacuum. The samples were heated at 500°C for one hour at $\sim 10^{-2}$ Torr pressure and cooled under the same pressure. The treatment was ineffective in reducing the hardness.

Individual tests of molybdenum, TZM (Mo-0.5 wt % Ti-0.08 wt % Zr), Mo-30 wt % W, and tungsten were made by exposing these materials to a MgCl_2 -30 mol % NaCl -20 mol % KCl salt mixture for 24 hr at 700°C. The molten salt and vapor phase above the salt had little effect on these refractory materials. Little or no change in hardness was observed and most of the samples had no measurable weight change. These four materials perform much better than niobium or tantalum under the same conditions.

c. Experimental Flowsheet Investigations (R. D. Pierce)

Last Reported: ANL-7561, p. 85 (March 1969).

Work is continuing on the Plutonium Salt Transport Experiment. Shop work is under way on the fabrication of the three transfer lines for glovebox 3 (see Progress Report for September 1968, ANL-7500, p. 115).

Stainless steel and Mo-30 wt % W parts are being machined, and a bending jig is being modified for bending the Mo-30 wt % W tubing sections for the transfer lines.

Specifications have been prepared and bids are being solicited for a processing vessel for box 3; this vessel is designed to operate under full vacuum for extended periods with wall temperatures of 1000°C.

A 30-kW induction-heating work station has been installed under the helium recirculation duct at the end of glovebox 3, and coupling and heating tests are being performed on the five vessels in box 3 that will utilize induction heating. When all of the heating equipment is installed, it will be possible to heat three furnaces simultaneously by induction heating and a fourth by resistance heating.

Electrical work that has been completed in glovebox 3 includes wiring for transfer-line heaters, process-vessel pressure control, thermocouples, controls for agitators, monitors for sound and vibration, liquid-level detectors, and power and control wiring for tower hoists. Power wiring for the traveling hoists, lights, and general glovebox service outlets is being installed.

All of the vacuum and helium piping that has been installed to date has been checked for leaks with helium and found to be leak tight. This includes all piping for the helium-purification system, helium storage and supply, vacuum tank and supply for all process vessels in box 3, and vacuum and helium piping for lock 7.

All of the windows were installed in glovebox 4, and leak checking of the box was completed.

c. Decladding and Fuel Resynthesis (R. D. Pierce)

Last Reported: ANL-7548, p. 110 (Jan 1969).

Two experiments were performed to study the kinetics of the dissolution of Type 304 stainless steel in molten zinc to provide information for the decladding step of the current pyrochemical process. The results of the experiments indicate that although the maximum loading of stainless steel constituents in solution in molten zinc is about 8 wt % at 800°C, rapid disintegration of the stainless steel continues up to a loading of about 15 wt %, even though the zinc is saturated with chromium and iron. The disintegrated stainless steel constituents are suspended in the zinc, and would be separated from the precipitated fuel oxide when the zinc is transferred from the decladding vessel.

In other work, a series of six experiments have been performed to develop equipment and techniques for removing the zinc heel from the decladding step of the current pyrochemical process. The zinc heel is evaporated from the decladding vessel and the distillate is collected in a horizontal, graphite-lined condenser. The distillate enters the condenser from one end and flows horizontally, impinging and condensing on vertical baffles staggered along the length of the condenser. A constant purge of argon from the decladding vessel through the condenser is employed to reduce the amount of zinc that condenses on the heat shields and secondary container in the decladding vessel.

In the most recent experiment, 4 kg of zinc was charged to the decladding vessel and 100% of the charge was evaporated. Approximately 85% of the zinc was collected in the condenser, 8% on the heat shields, and 7% on the upper portion of the secondary container. These results demonstrate that this type of equipment can be used to remove the zinc heel in the decladding step of the process.

3. General Chemistry and Chemical Engineering

a. Sodium Chemistry

(i) Characterization of Carbon-bearing Species in Sodium (F. A. Cafasso)

Last Reported: ANL-7548, p. 111 (Jan 1969).

Studies to determine the stability of solid disodium acetylide (Na_2C_2) in the presence of liquid sodium have begun. The results of preliminary experiments indicate that the solid acetylide decomposes above 400°C ; the behavior below this temperature is now under study.

(ii) Identification of Mechanism(s) of Carbon Transport in Sodium Systems (F. A. Cafasso)

Last Reported: ANL-7548, p. 111 (Jan 1969).

A model for carbon transport in sodium-steel systems has been developed in this laboratory. The model involves the formation of disodium acetylide (Na_2C_2) by the reaction of liquid sodium with carbon at the appropriate activity in steel, and postulates that transport of carbon between steels occurs via dissolved acetylide. Effort is now being directed toward establishing how the concentration of acetylide in sodium varies with temperature and with carbon activity in steels.

(iii) Kinetics of Solution and Precipitation of Sodium Oxide
(F. A. Cafasso)

Last Reported: ANL-7548, p. 112 (Jan 1969).

Initial effort in this area is being placed on establishing the morphology of sodium oxide crystallites and the kinetics of their growth in sodium. A combination of ultrahigh-vacuum and microscopical techniques will be needed for this purpose. Specifications for an ultrahigh-vacuum chamber have been prepared, and an order for its purchase has been placed. Until this equipment is received, microscopic examination of sodium samples will be made with an inert-atmosphere stage enclosure which has been constructed.

(iv) Surface Phenomena in Liquid Sodium (F. A. Cafasso)

Last Reported: ANL-7548, p. 112 (Jan 1969).

(a) Surface Diffusivity Studies. The role of surface diffusion in enhancing the corrosion of structural materials in liquid sodium has not yet been elucidated. A study of this effect by the technique of grain-boundary grooving is under way.

Specimens of α -iron with polished surfaces were exposed to liquid sodium at 800°C for up to seven days. Interferometric measurements of the grain-boundary groove angle showed that the ratio of the iron grain-boundary tension to the iron-sodium interfacial tension was $\gamma_{SS}/\gamma_{SL} = 0.49 \pm 0.09$. The ratio of the ridge height to the groove depth was found to be $h/d = 0.153 \pm 0.018$. It can be shown* that h/d is 0.149 when the groove is formed by volume diffusion and 0.208 when formed by surface diffusion. Work at other laboratories on annealing of α -iron in vacuum has ruled out volume diffusion through the solid as the controlling mechanism. Thus, the mechanism of grain-boundary grooving in α -iron, as indicated by these experiments, is volume diffusion of iron atoms through the liquid sodium.

(v) Total Vapor Pressure and Oxygen Potentials in the Ternary System U-Pu-O (P. E. Blackburn)

Last Reported: ANL-7553, pp. 103-104 (Feb 1969).

Segments of the transpiration apparatus designed for measuring both oxygen potentials and total pressures over PuO_{2-x} have been

*Mullins, W. W., J. Appl. Phys. 28, 333 (1957); Trans. Met. Soc. AIME 218, 354 (1960); Allen, B. C., *ibid.*, 236, 915 (1966).

dynamically tested. All safety devices and interlocks were found functional, as was the entire furnace system. Calibration of the instrumentation has been carried out. All construction short of sealing the box also has been completed. The preliminary experiments with U_4O_9 - U_3O_8 will begin shortly. Samples of U_3O_8 have been prepared, and the fabrication of iridium crucibles for containing U_4O_9 - U_3O_8 samples has been completed.

(vi) Total Effusion of Pu-O and U-Pu-O (P. E. Blackburn and R. K. Edwards)

Last Reported: ANL-7553, p. 104 (Feb 1969)

The effusion apparatus, previously used to determine the congruently vaporizing composition of urania as a function of temperature, has been installed in a glovebox so that effusion studies of plutonium-bearing materials may be carried out. Modification of the apparatus to incorporate the quadrupole mass spectrometer and the vacuum microbalance has been completed. Internal components, such as the Knudsen cell mounting device, are being assembled within the apparatus for testing. The effusion experiments will begin shortly. The equipment will also be used to measure the relative ionization cross sections for U-O and Pu-O molecules essential for the partial vapor pressure studies of U-Pu-O (see Progress Report for March 1969, ANL-7561, p. 89).

PUBLICATIONS

A Thermodynamic Study of the Urania-Uranium System

R. J. Ackermann, E. G. Rauh, and M. S. Chandrasekharaiah
J. Phys. Chem. 73, 762-769 (April 1969)

Neutron Radiography Using Non-Reactor Sources

J. P. Barton

Neutron Radiography Newsletter 8, 7-13 (April 1968)

Preparation and Properties of ThP and ThP-UP Solid Solutions

Y. Baskin

J. Am. Ceram. Soc. 52(1), 54-55 (January 1969) Note

Recent Progress in Neutron Imaging

Harold Berger

Brit. J. Non-Destructive Testing 10(3), 26-33 (June 1968)

A Fast Imaging Alignment Method for Neutron Radiographic Inspection of Radioactive Samples

Harold Berger

Czechoslovak Conf. on Nondestructive Control of Materials, Gottwaldov, September 17-20, 1968. Dom Techniky CSVTS, Bratislava, 1968, pp. 3-7

A Survey of Ultrasonic Image Detection Methods

Harold Berger

Acoustical Holography, Proc. First Intern. Symp., Douglas Advanced Research Laboratories, Huntington Beach, California, December 14-15, 1967, A. F. Metherell, H. M. A. El-Sum, and L. Larmore, eds. Plenum Press, New York, 1969, pp. 27-48

A Demountable Induction-Heater Power-Lead Coupling for Use in Ultrahigh Vacuum

P. M. Danielson

Rev. Sci. Instr. 40, 736-737 (May 1969) Note

Ultrahigh Vacuum Equipment for Materials Studies above 2000°C

P. M. Danielson and J. S. Hetherington*

Intern. Trans. Vacuum Metallurgy Conf., New York, June 1967, Ed. E. L. Foster. Am. Vac. Soc., New York, 1968, pp. 305-319

Dynamic Analysis of Liquid-metal-cooled Fast Power Reactors

J. A. DeShong, Jr.

ANL-7529 (January 1969)

Design and Application of Corrosion-resistant Heated Transfer Tubes for Liquid Metals and Salts

D. E. Grosvenor, I. O. Winsch, W. E. Miller, G. J. Bernstein, and R. D. Pierce

ANL-7522 (December 1968)

A High-temperature, Fluidized-bed Process for Converting Uranium Dioxide to Uranium Monocarbide

John T. Holmes, John R. Pavlik, Paul A. Nelson, and Johan E. A. Graae

ANL-7482 (November 1968)

The Enthalpies of Formation of Plutonium Dioxide and Plutonium Mononitride

G. K. Johnson, E. H. Van Deventer, O. L. Kruger, and W. M. Hubbard

J. Chem. Thermodynam. 1969(1), 89-98 (1969)

Uranium Purification by the Process of Salt Transport

J. B. Knighton, I. Johnson, and R. K. Steunenberg

ANL-7524 (March 1969)

Nuclear Magnetic Resonance and Relaxation of ^{31}P in the Paramagnetic State of the UP-US Solid Solutions

Moshe Kuznietz, G. A. Matzkanin, and Y. Baskin

Bull. Am. Phys. Soc. 14(3), 333 (March 1969) Abstract

* Varian Associates, Palo Alto, Calif.

Mass-spectrometric Effusion Study of Uranium Monophosphide

J. W. Reishus, G. E. Gunderson, P. M. Danielson, and R. K. Edwards
ANL-7514 (November 1968)

Transient Thermal Stresses Associated with Sudden Initiation of Internal Heat Generation in a Segment of a Circular Cylinder

R. A. Valentin and D. F. Schoeberle

Nucl. Eng. Design 9(1), 63-80 (January 1969)

Parallel-Flow-Induced Vibration of a Cylindrical Rod

M. W. Wambsganss, Jr. and B. L. Boers

Mech. Eng. 91(4), 64 (April 1969) Abstract

The CaCl_2 -Rich Region of the CaCl_2 - CaF_2 - CaO System

D. A. Wenz, I. Johnson, and R. D. Wolson

J. Chem. Eng. Data 14(2), 250-252 (April 1969)

V. NUCLEAR SAFETY

A. Reactor Kinetics

1. Accident Analysis and Safety Evaluation

a. Accident Mechanics (G. J. Fischer)

Last Reported: ANL-7548, pp. 115-116 (Jan 1969).

(i) Models for Calculating Sodium Expulsion from Reactor Coolant Channels. Work is in progress on developing a compressible flow model for theoretical studies of the behavior of sodium coolant during boiling and expulsion in LMFBR coolant channels.

As described previously (see Progress Report for September 1968, ANL-7500, p. 123), the two-phase part of the model is a characteristic solution to the coupled energy-momentum and continuity equations. The following tests or changes have been made in the computer program.

The program was rewritten to increase the computational speed and now takes 10 ms to calculate the pressure void fraction and mass flow rate (MFR) at one point in the time-space plane on a CDC-3600 computer. It was found that under certain conditions of pressure void fraction and MFR the equations changed from hyperbolic to elliptical, and the characteristic solution was not applicable. This change in the type of differential equations was dependent on how the terms of the energy and momentum equation were expanded and regrouped. The effect of slip, the sonic velocity, and other parameters on the type of differential equations was investigated.

The two-phase program calculates the pressure, MFR, and void fraction. A hand calculation of the energy, momentum, and mass balance showed that the mass and either the momentum or energy was conserved, depending on how the momentum and energy equations were expanded. This error is presently being investigated.

The program to calculate the pure liquid temperature, pressure, and velocity and the program to follow the interface between the pure liquid and the two-phase region has been written. Fuel-rod heat transfer has also been added.

2. Reactor Control and Stability

a. Reactor Stability Design Criteria for Spatially Dependent Systems (C. Hsu and L. Habegger)

Last Reported: ANL-7561, p. 93 (March 1969).

(i) Nonlinear Model. The study of space-time dynamics in nuclear power systems requires knowledge of initial steady-state space-dependent fluxes and thermohydraulic variables. Standard procedures for steady-state flux calculations (e.g., MACH-1*) are inadequate because of nonlinearities introduced by power and temperature dependency of the nuclear cross sections in power reactors.

An iterative procedure referred to as quasi-linearization has been investigated as a possible procedure for obtaining solutions to the nonlinear one-dimensional steady-state reactor equations. This numerical procedure has been reported effective in the solution of certain other nonlinear multipoint boundary-value problems.** Initial applications to the nonlinear diffusion equation

$$\frac{\partial}{\partial x} D(x) \frac{\partial}{\partial x} \phi(x) + \alpha \Sigma(x) \phi(x) + B(x) \phi^2(x) = 0;$$

$$\phi(0) = \phi(\ell) = 0; \int_0^\ell \phi(x) dx = P$$

indicate excellent convergence characteristics. The procedure simultaneously determines $\phi(x)$ and the parameter α for a given total power P , or vice versa, such that the system is critical.

Application to multigroup equations with thermohydraulic feedbacks and equations with various types of nonlinearities will be investigated to determine the value of the procedure in solving practical reactor-system problems.

*Meneley, D. A., Kvitek, L. C., and O'Shea, D. M., MACH-I, A One-dimensional Diffusion Theory Package, ANL-7223 (June 1966).

**Kalaba, R., On Nonlinear Differential Equations, the Maximum Operation, and Monotone Convergence, J. Math. Mech., 8, 519-574 (July 1959).

3. Coolant Dynamics

a. Critical Flow (H. K. Fauske and M. A. Grolmes)

(i) Sodium Tests

Last Reported: ANL-7548, pp. 117-118 (Jan 1969).

The experimental program measuring critical flow, pressure drop, void fraction, and nonequilibrium in sodium liquid-vapor mixtures was completed successfully. Thus the sodium flashing facility is being modified for testing various "plugging meters" for use in the Transient Test Facility that also is under construction.

Analyses pertaining to pressure drop and nonequilibrium of liquid sodium-vapor mixtures are continuing.

(ii) Sonic Velocity and Pressure-wave Propagation

Last Reported: ANL-7548, p. 118 (Jan 1969).

The preparation of a topical report on the recent studies of pressure-wave propagation in one- and two-component two-phase mixtures is being completed.

(iii) Voiding Models

Last Reported: ANL-7561, pp. 93-95 (March 1969).

Results of the transient voiding of single channels are being analyzed to determine: (1) characteristic flow regimes, (2) rates of expulsion or channel voiding, and (3) basic mechanisms governing various expulsion modes. Further analytical consideration is being given to determining all appropriate criteria for the simulation of sodium expulsion or voiding in studies with nonmetallic fluids. Finally, additional static depressurization tests have been initiated with multiple-pin channels (annulus and 7-pin). These tests, in addition to determining rates and modes of voiding, will determine radial and axial void growth and the applicability of single-channel analysis to multiple-pin geometries.

b. Coolant Dynamics (R. M. Singer and R. E. Holtz)

Last Reported: ANL-7561, pp. 95-96 (March 1969).

(i) Sodium Superheat Experiments. The superheat test vessel was removed from the Juggernaut reactor and was placed in the Juggernaut storage pit until the radiation level of the test vessel decreases to a tolerable level.

(ii) Coolant-expulsion Experiments. A quantity of data were collected; reduction and analysis are underway. Preliminary examination of these data indicate that the general ideas concerning expulsion are most likely correct, e.g., the expulsion velocity increases with increased superheat, the axial temperature gradient markedly affects the maximum expulsion distance, and pressures generated at boiling inception are rather small. It also was observed that slug-type expulsion occurs only at large superheats; at small superheats ($\sim 10\text{--}20^\circ\text{C}$), the flow patterns appear to be of a more dispersed character.

During these tests, a weld in the test section failed; a new, more highly instrumented test section is being installed. Difficulties are continuing with the pressure measurements. The pressure transducers are repeatedly failing at the instant of sodium re-entry (sodium hammer); remedial action is being taken. It is not known whether the transducer failures were due to overpressurization (which would require pressure greater than 200-400 psi) or the rapid rate of rise of pressure transients in which the pressure increases from 0 to 200 psi in 20 μsec .

(iii) Transient Experiments. Assembly of the Transient Test Loop is continuing. The loop piping being welded into the system is instrumented with thermocouples and insulated. Also, a small-scale test setup for testing the oscillating plugging meter is being built. Installation of this type of plugging meter will permit continuous monitoring of the concentration of dissolved impurities in the test sodium.

4. Core Structural Safety (C. K. Youngdahl)

Last Reported: ANL-7561, pp. 96-97 (March 1969).

a. Dynamic Plasticity Analysis of Circular Shells. Available solutions to dynamic plasticity problems have been reformulated in terms of the proposed equivalence parameters (impulse and effective load) in order to test the generality of this correlation for various structural geometries.

Consider a simply supported circular-plate mode of a rigid perfectly plastic material obeying the Tresca yield condition and loaded by a uniform pressure $P(t)$.* Let $P(t)$ increase to a maximum P_M which exceeds the static yield load P_s and then decrease monotonically to zero. If $P_M \leq 2P_s$, a plastic hinge forms at the center of the plate at $t = t_y$ when $P = P_s$, and plastic deformation continues to some time t_f . If $P_M > 2P_s$, the center hinge begins to broaden into a plastic hinge band at $t = t_b$ when $P = 2P_s$. The band increases in radius until $P = P_M$ and then decreases

*Hopkins, H. G., and Prager, Wm., On the Dynamics of Plastic Circular Plates, *Z. Angew. Math. Phys.* 5, 317-330 (1954); Perzyna, P., Dynamic Load Carrying Capacity of a Circular Plate, *Arch. Mech. Stos.* 10, 635-647 (1958).

until at a time t_c it shrinks to a center hinge again. The hinge-band radius and the time history of the plastic deformation are found from complicated transcendental equations. However, the final plastic deformation u_f at the center of the plate can be expressed in terms of the proposed equivalence parameters by

$$u_f = \frac{I^2}{\gamma P_s} \left[1 - \frac{P_s}{P_e} \right], \quad P_s \leq P_M \leq 2P_s; \quad (1)$$

$$u_f = \frac{I^2}{\gamma P_s} \left[1 - \frac{P_s}{P_e} - \frac{1}{2} \left(\frac{I_b}{I} \right)^2 \left(\frac{1}{2} - \frac{P_s}{P_{eb}} \right) \right], \quad 2P_s < P_M, \quad (2)$$

where γ is the surface density of the plate,

$$I = \int_{t_y}^{t_f} P \, dt, \quad (3)$$

$$P_e = \frac{I}{2t_m} = I^2/2 \int_{t_y}^{t_f} tP \, dt, \quad (4)$$

$$I_b = \int_{t_b}^{t_c} P \, dt, \quad (5)$$

and

$$P_{eb} = \frac{I_b}{2t_{mb}} = I_b^2/2 \int_{t_b}^{t_c} tP \, dt. \quad (6)$$

The times t_f and t_c are found from

$$I = P_s(t_f - t_y) \quad (7)$$

and

$$I_b = 2P_s(t_c - t_b). \quad (8)$$

For loadings such that no hinge band occurs, Eq. (1) shows that the final plastic deformation of the shell depends only on the proposed equivalence parameters. If a hinge band is produced, other quantities are involved also. However, Fig. V.A.1 shows that the final deformation still very nearly depends only on the equivalence parameters, i.e., the curves of u_f/I^2 versus P_e are very close together. For comparison, the same results are plotted in Fig. V.A.2 as a function of peak load P_M .

Again the conjecture that the average value of the load over the duration of the deformation is approximately equal to the static yield load (see Progress Reports for February 1969, ANL-7553, pp. 106-108, and March 1969, ANL-7561, pp. 96-98) is found to be exactly true, as can be seen from Eq. (7).

A topical report on the equivalence of dynamic ring loads for the final plastic deformation of a circular cylindrical shell has been prepared.*

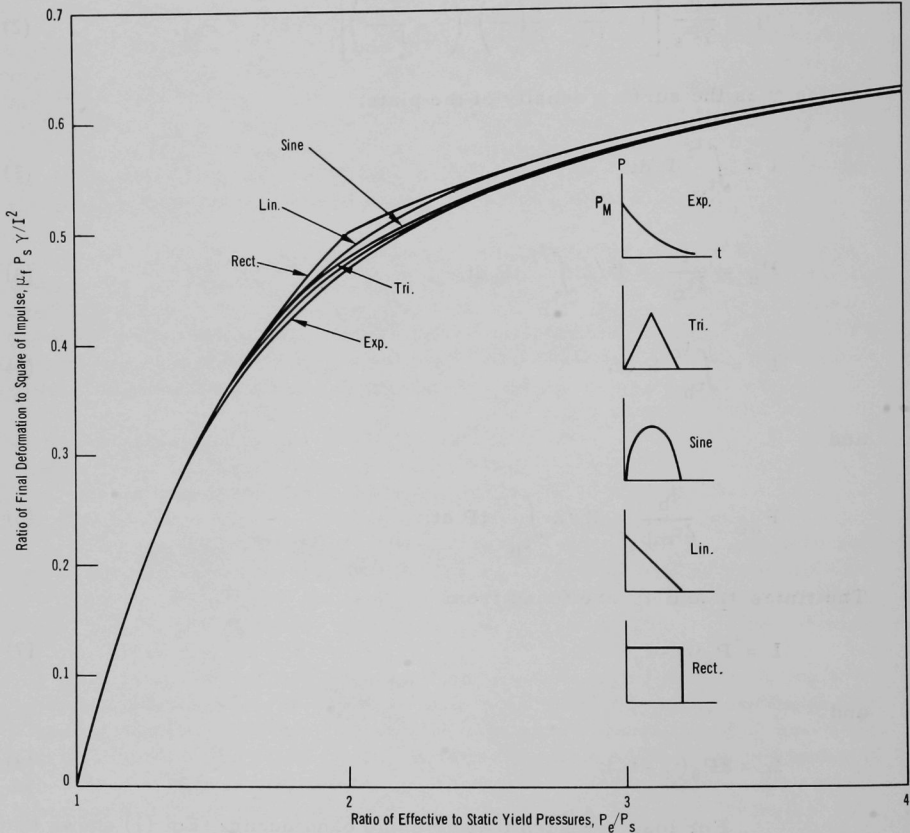


Fig. V.A.1. Ratio of the Final Deformation of a Circular Plate to the Square of the Impulse as a Function of the Effective Pressure for Pulses Whose Shapes Are Exponential, Triangular, Sine, Linear, and Rectangular

*Youngdahl, C. K., The Dynamic Plastic Response of a Tube to an Impulsive Ring Load of Arbitrary Pulse Shape, ANL-7562 (to be published).

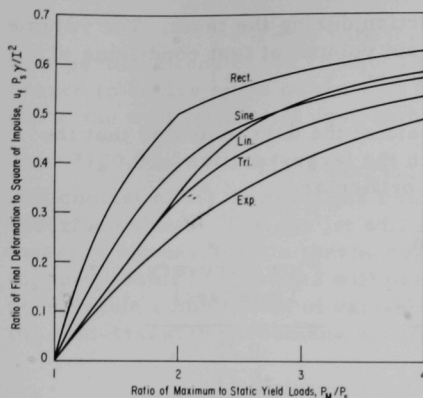


Fig. V.A.2

Ratio of the Final Deformation of a Circular Plate to the Square of the Impulse as a Function of the Maximum Pressure for Pulses Whose Shapes Are Exponential, Triangular, Sine, Linear, and Rectangular

5. Fuel Element Failure Propagation (J. F. Schumar)

a. Out-of-pile Studies (J. F. Marchaterre, R. E. Wilson, and B. M. Hoglund)

Last Reported: ANL-7513, p. 136 (Oct 1968).

(i) Propagation Phenomena. Propagation phenomena associated with an accidental release of fission gas from a fuel element can be divided into three regimes. The first is associated with a rapid gas release through a large break in the cladding, which would cause expulsion of the coolant from the subassembly but would be completed very quickly. The second is associated with a slower gas release that does not cause coolant expulsion, but gives rise to a high-velocity gas jet that might impinge on an adjacent fuel element and persist long enough to cause overheating. The third is an even slower gas release that might cause overheating due to local flow reduction brought about by the flow characteristics of the two-phase coolant-gas mixture.

(a) Gas-jet Tests with Single Channels in a Water Loop. The initial phase of the study of problems associated with a persistent gas jet has been completed. The flow channel was made of clear Lucite and was dimensionally identical to an electrically heated channel that will be used in the second phase of the experiment. High-speed motion pictures were taken so that physical observations could be correlated with the recorded data. These data were taken to obtain information on the coolant transient that would occur during the heated channel tests.

The rectangular channel was 0.050 by 0.578 by 22 in. Data were obtained for coolant velocities of 10, 20, and 30 ft/sec, orifice diameters of 0.0515, 0.025, and 0.016 in., and gas plenum pressures of 500, 750, and 1000 psi. An inlet pressure to the test section of 200 psi was

used to prevent boiling in the heated section during the tests. The volume of the gas plenum was sized to give a void volume at test conditions of 400 cm³ with a plenum pressure of 1000 psi.

Preliminary analysis of the data indicated that the channel was completely voided only with the largest orifice (of 0.0515-in. diameter). The data for the 0.0515-in. orifice are:

Coolant Velocity (ft/sec)	Gas Plenum Pressure (psi)	Flow Recovery Time (sec)
10	500	0.25
20	500	0.21
30	500	0.14
10	750	0.65
20	750	0.55
30	750	0.33
10	1000	0.89
20	1000	0.80
30	1000	0.54

The peak pressure pulses, measured 1 in. from the orifice, have a magnitude of about 100 psi for the tests with the 1000-psi plenum pressure.

The data from tests with the 0.025-in. orifice showed a small flow reversal with a rapid recovery. The motion pictures show what appear to be relatively large dry spots on the wall opposite the orifice. The high-velocity gas seems to hold a fairly stable interface with the liquid on this wall at a position about 1 in. upstream from the orifice. As the gas flow rate decays, this interface gradually moves downstream past the orifice.

Tests were run with the coolant bypass closed to compare the results with those for bypass-open experiments. The rate of flow through the bypass was ten times the rate of flow through the rectangular channel. With the bypass closed, the magnitude of the pressure pulses and the general shape of the pressure-time plots were generally similar to those obtained with the bypass open. The primary difference was that the bypass-closed traces had high-frequency (200-300 cps) pressure pulses of about 20 psi superimposed on the traces. The effect of these pressure pulses on the flow could be seen in the motion pictures. The main effect of opening the bypass seemed to be to filter out these high-frequency pressure pulses.

Tests with the 0.016-in. orifice showed only very minor flow perturbations of the coolant flow. These tests also produced what appeared to be dry spots on the wall and maintained an interface with the liquid at the wall (at a point upstream from the orifice).

Tests planned for the second phase of the experiment will consist of discharging gas into a heated test section under the conditions described above. The gas jet will impinge on a spot on the heated wall. To measure temperature, a thermocouple is attached to this spot. The resulting temperature transients will provide an insight into which is the most undesirable combination of variables, and will provide information about the heat-transfer phenomena occurring on the surface.

Existing electrically heated test sections are being modified. Three practice attempts, with an electron-beam welder, to braze a gas-injection tube to the copper test section without producing distortion have been completed successfully.

(b) Rapid-gas-release Tests with 19-fuel-element Bundle in Water Loop. Modifications to an existing water loop to accommodate rapid-gas-release tests in an unheated 19-element array essentially have been completed. The Plexiglas test section and all fittings have been received. Fabrication of the element bundle has started. The bundle will consist of $18\frac{1}{4}$ -in.-OD, wire-wrapped Plexiglas rods that surround a central stainless steel tube. The central tube has a predrilled orifice and an internal pressure-actuated valve that will allow repeated gas-release tests.

(c) Mechanical-damage Tests in Air and Stagnant Water. The major objective of the mechanical-damage tests is to gain an insight into the performance (particularly with respect to structural behavior) of a fuel-cladding tube that has been subjected to a sudden gas release. Also, the pressure-actuated valve in the simulated fuel element will be tested.

Development of the piston-type pressure-actuated valve for releasing gas has been essentially completed, and numerous tests have been performed successfully. The valve can instantly apply internal gas pressure to a hole in the tube wall in such a manner that (a) the internal pressurized cross section of the tube contains no restriction, and (b) the tube can be repressurized and the experiment repeated without disassembly of the tube.

Experiments simulating the sudden release of internally stored gas are underway to measure the time dependence of the force and impulse imposed on a single tube. The parameters being studied are the gas plenum pressure, plenum volume, hole size, and type of gas. The results are being compared with an analytical model. Measurements of the rod displacements as a function of unsupported length are also being made and will be compared with an analytical model.

(d) Construction of a Small Sodium Test Loop. To extend the results of the water tests to sodium, a small sodium test loop is being built. It is being constructed of 1-in.-dia Type 304 stainless steel pipe. All of the sodium-containing components of the loop are on hand except the test section, which is about 50% complete. The sodium-to-air heat exchanger has been installed, and the air ducts are 60% complete.

The initial test section, which will consist of a single heater in a small channel, will be used to shakedown the loop, verify the operating procedures, and set operating limits for the heater design. A single heater is being used, which can be replaced conveniently after burn-out. The next test section design will contain seven heaters in a hexagonal pattern.

6. Fuel Meltdown Studies with TREAT (C. E. Dickerman)

a. Meltdown Studies with Ceramic Fuel

Last Reported: ANL-7553, p. 108 (Feb 1969).

Nondestructive testing of the mixed oxide pins received from UKAEA has progressed as follows:

(i) Sixty-six Unirradiated Pins. Profilometry, dimensional checks, density and balance-point determination have been completed. The pins are undergoing radiography.

(ii) Seven Irradiated Pins. These 7 pins have been irradiated to ~5% burnup in the Dounreay Fast Reactor. Nondestructive testing, with the exception of neutron radiography, has been completed. Gas sampling and destructive material examinations remain to be done.

All pins show heavy longitudinal scratches in the cladding, and at least one is visibly bent. The scratches are believed to have occurred when the pins were removed from the irradiation holder at Dounreay, as described in TRG 3032D (revised).

Pin No. AO89, in addition to being bent, had three patches of whitish material resembling paste solder flux stuck to the cladding. A metal chip, similar to the "slivers of swarf" noted in the TRG report, was stuck in one of the pasty patches. Spectrochemical analyses indicated that the metal chip was an 18-8 stainless steel and the white material was probably a mixture of metal salts. No defect large enough to have furnished this chip was found in the cladding, however.

One of the pins will be selected for detailed destructive examination, at which time the visible cladding defects can be more fully explored.

b. Transient Coolant Behavior

(i) Radiation Effects on Superheat in Liquid Sodium

Not previously reported.

An analysis of the effects of radiation particles, such as fission fragments, alpha-particles, and protons, on the superheat attained by liquid sodium before vaporization has been undertaken. The methods employed are those used in the analysis of experiments conducted at Stanford University with water and fission fragments.* Results obtained from these calculations can be compared with those obtained earlier by Claxton** and will serve to indicate the importance of radiation particles in promoting bubble nucleation in liquid sodium.

Initial results have suggested that fission fragments are probably the only type of radiation that can induce bubble nucleation in sodium at reasonable superheats ($<200^{\circ}\text{C}$). These results also indicate that the required nucleation energy in sodium is strongly influenced by the rate at which a bubble must expand in the liquid to ensure that the critical bubble radius is attained before the available energy is dissipated by heat conduction. This means that the required nucleation energy is determined by the dynamics of growth from zero radius to the critical radius, and that the surface energy and heat of vaporization are less important. The opposite is true in the case of water.

Since the dynamics of formation of the bubble nucleus appear to govern the nucleation process, an improved method of calculation of the dynamics is being sought. Such an improved model will be used to estimate the importance of radiation-induced nucleation of bubbles in superheated sodium.

c. Analytical Support

(i) Analysis of Sodium Slug Impacts in TREAT Mark-II Loop

Not previously reported.

One of the most interesting features of the experiments to be conducted in TREAT Mark-II loops is expected to be the pressure pulses

*Deitrich, L. W., A Study of Fission-fragment-induced Nucleation of Bubbles in Superheated Water, Thesis, Stanford University, Dept. of Mechanical Engineering, AEC Report Su-326P13-4, in press. See also Deitrich, L. W., and Connolly, T. J., Fission-fragment-induced Nucleation of Bubbles in Superheated Water, Trans. ANS, June 1969, in press.

**Claxton, K. T., The Influence of Radiation on the Inception of Boiling in Liquid Sodium, Proc. of the Int'l Conf. on the Safety of Fast Reactors, Aix-en-Provence, 1967, CEA, Paris.

resulting from fuel meltdown. Pulses may arise from impacts of moving sodium ("sodium hammer") as well as from possible rapid sodium vaporization. To aid in understanding the impact pressure pulses, analysis of the impact of sodium slugs against a plane obstruction perpendicular to the direction of flow has been undertaken.

Initial calculations have been based on a "water-hammer" model using equations suggested by Streeter and Wylie.* This model retains the convective terms and fluid friction in the hydrodynamic equations. Compressibility of the liquid sodium and elasticity of the container walls are considered in calculations of the velocity of pressure waves. However, gross density changes in the liquid are not considered, nor are large deformations of the container.

Although this model appears to be adequate for scoping calculations, it has deficiencies when used for calculating pressures resulting from the conditions being considered for the more extreme TREAT experiments. It appears that a modification of the calculational procedure will be necessary to take account of the large density changes predicted by the scoping model. The revised procedure will require recasting the problem, either to a Lagrangian formulation, or to a Eulerian formulation with a moving boundary.

7. Materials Behavior and Energy Transfer (R. O. Ivins)

Last Reported: ANL-7561, pp. 99-103 (March 1969).

a. Pressure Generation due to Violent Meltdown (R. O. Ivins)

(i) Calculational Studies. Previous calculations of the pressures developed due to the rapid addition of heat to a localized volume of coolant included the cases of both spherical and linear acoustic constraint; graphs of the results were presented for the case of water coolant.

The parametric calculations have been extended to include sodium coolant; results for the case of spherical constraint are shown in Figs. V.A.3 and V.A.4. Because of the scarcity of thermodynamic data for sodium at high temperatures and in the region of the critical temperature, many of the properties used in the calculations were estimated using the results of Golden** and Dillon,[†] together with theories of corresponding states.

*Streeter, V. L., and Wylie, E. B., Hydraulic Transients, McGraw-Hill Book Co., Inc., New York (1967).

**Golden, G. H., and Tokar, J. V., Thermophysical Properties of Sodium, ANL-7323 (Aug 1967).

[†]Dillon, I. G., Nelson, P. A., and Swanson, B. S., Critical Temperatures and Densities of Alkali Metals, ANL-7025 (Aug 1965).

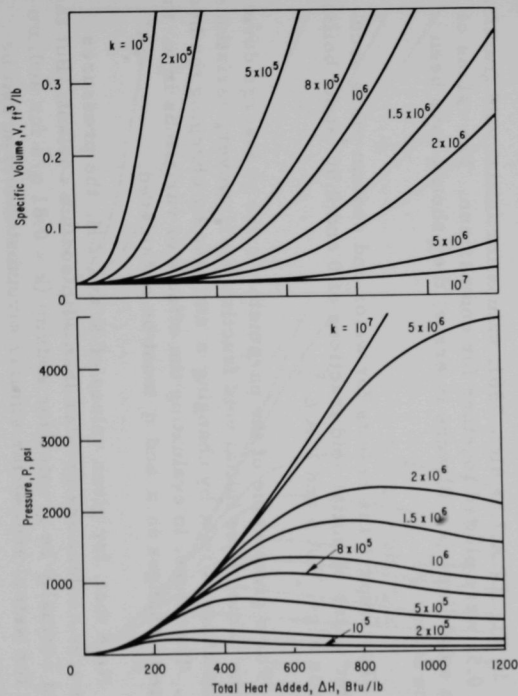


Fig. V.A.3. Pressure Developed by Adding Heat to Sodium under Spherical Acoustic Constraint (with initial vapor volume of 0% and k of 0.81 q/a)

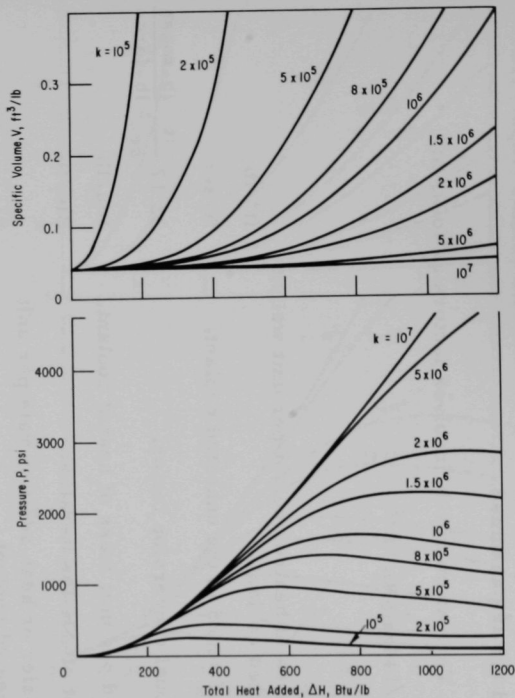


Fig. V.A.4. Pressure Developed by Adding Heat to Sodium under Spherical Acoustic Constraint (with initial vapor volume of 50% and k of 0.81 q/a)

In Figs. V.A.3 and V.A.4, the pressure P and specific volume V are plotted against the total heat ΔH added (above the boiling point) for various values of the parameter k . Initial void volume (vapor) fractions x of 0 and 0.5 are assumed.

The parameter k involves factors as follows:

$$k = \rho c q / 144 g a (\delta H),$$

where

a = surface area of heated coolant per unit weight of the heated coolant,	ft^2/lb
c = velocity of sound in the unheated coolant,	ft/sec
g = gravitational conversion factor,	$32.17 \frac{\text{ft}}{\text{sec}^2} \frac{\text{lb-mass}}{\text{lb-force}}$
ΔH = heat added per unit mass of heated coolant,	Btu/lb
δH = increment of ΔH for iteration,	Btu/lb
q = heat-transfer or heat-addition rate per unit mass of heated coolant,	$\text{Btu}/\text{sec-lb}$
ρ = density of unheated coolant,	lb/ft^3

In Fig. IV.A.7 of ANL-7561, values for initial void fraction x of both 0 and 0.55 were plotted together for comparison. The values of k shown for the solid lines ($x = 0$) were in error; they should have been multiplied by the factor $\sqrt{2}$.

To compare the results for water and sodium more accurately, graphs for water of initial void fractions of 0 and 0.50 (at its boiling point) are given in Figs. V.A.5 and V.A.6.

For a given value of the parameter k the pressures developed vary with the value of the initial void fraction x . However, variations in x could induce changes in k by changing a and also by changing the heat-transfer rate q . Therefore, in evaluating the effects of variations in x , the changes in k due to changes in a and q must be considered.

Note that, for given values of k and ΔH , the pressures developed with water coolant are greater than with sodium coolant. But the value of k would normally be greater for sodium ($k = 0.81 q/a$ for sodium versus $0.65 q/a$ for water) and, under similar circumstances, q can be greater for sodium.

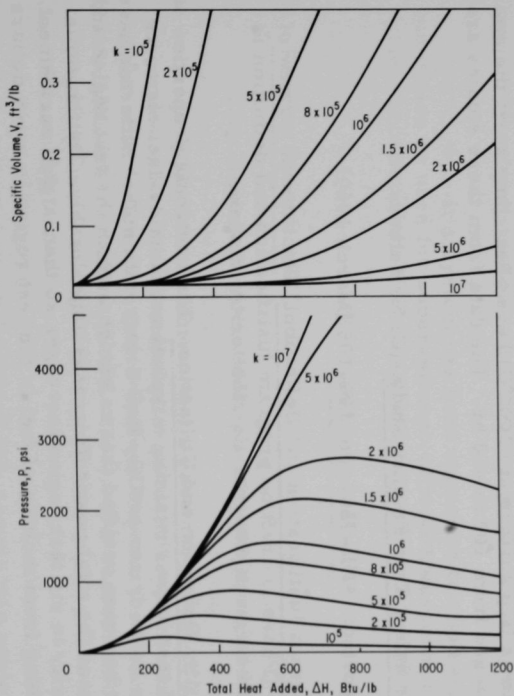


Fig. V.A.5. Pressure Developed by Adding Heat to Water under Spherical Acoustic Constraint (with initial steam-vapor volume of 0% and $k = 0.65 \text{ q/a}$)

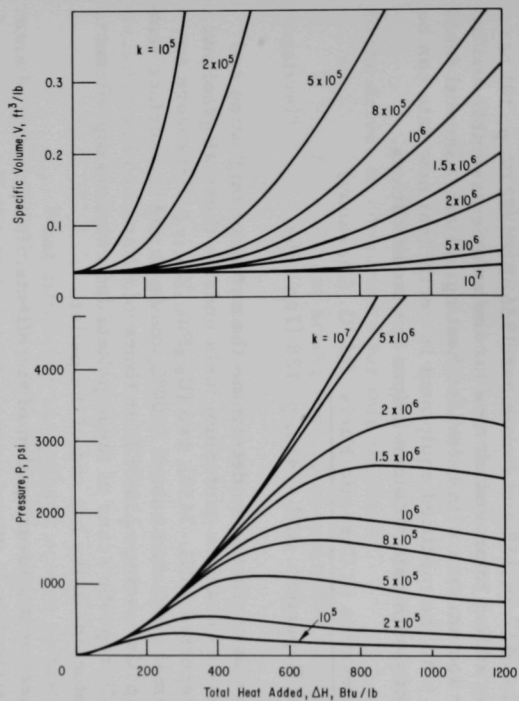


Fig. V.A.6. Pressure Developed by Adding Heat to Water under Spherical Acoustic Constraint (with initial steam-vapor volume of 50% and $k = 0.65 \text{ q/a}$)

(ii) Transient Heat Transfer Studies in Liquid Sodium. To allow heat-transfer data to be obtained at sodium temperatures up to 850°C, the experimental heat-transfer apparatus (see Progress Reports for February 1968, ANL-7427, p. 138 and November 1966, ANL-7279, p. 18) has been modified by adding improved clamps for the sphere assembly and by installing a new sodium tank with a revised heating system. Several tests are being made with the modified equipment to verify that new data can be correlated directly with data obtained before the modifications.

b. Segregation in Ceramic Fuels (M. G. Chasanov)

Last Reported: ANL-7458, p. 128 (Jan 1969).

Work is continuing to determine the extent of migration and segregation in mixed uranium-plutonium fuels under a thermal gradient. As previously reported (ANL-7458), two ($U_{0.8}Pu_{0.2}$) $O_{1.97}$ pellets were annealed in a thermal gradient of about 1000°C/cm (with the top surface temperature of the pellets being ~2350°C) for times of 97 and 125 hr, respectively. Microprobe scans of these pellets indicated no significant migration of plutonium to the hot end of the pellet.

Experimental investigation of the effects of thermal gradients on plutonium distribution in mixed-carbide fuel pellets is also underway. These pellets contain 4.61 wt % carbon, 81.0 wt % uranium, and 14.4 wt % plutonium. Four experiments in which pellets were heated in approximately 700°C/cm gradients (top surface at ~2000°C) have been completed; the annealing times ranged from 100 to 460 hr. The data from these studies are being analyzed.

8. Fast Reactor Safety Test Facility Study (C. N. Kelber)

Last Reported: ANL-7561, pp. 104-105 (March 1969).

a. Program Justification and Definition. The internal review of the preliminary (Phase 1) draft on program justification and definition is complete and will be given external distribution for review.

b. Facility Definition and Utilization. The neutronic properties of various sizes of test loops containing a typical set of oxide-fuel elements and driven by an oxide driver or UO_2 -BeO driver with nickel reflector have been studied. It has been verified that as enrichment in the test region and driver is increased the total power decreases considerably. By the same token the reactivity in the test region increases so that, at full enrichment, the reactivity swing from melting of fuel in the test region is many dollars of reactivity.

The neutronics effort in this task seeks to answer the following list of questions:

1. What is the best estimate of positive reactivity feedback and feedback rate from the test zone to the entire test reactor? (Not what the feedback would be in a large LMFBR.)
2. What prompt negative coefficient of reactivity is required in the driver to compensate for this feedback?
3. Can fast acting rods compensate for feedback (positive and negative)?

The answers to these questions should determine test-zone composition:

4. For a given nominal driver fuel composition and power density ratio, what is the variation of total power as test fuel is varied from nominal to full enrichment?
5. What difference in feedback occurs as test-zone enrichment varies? This includes feedback from sodium void and feedback from fuel collapse in the test zone.

Test conditions may eventually include super-prompt-critical transients as well as flow and small overpower transients. Hence we ask:

6. If a system has been optimized for flow transient studies can it also be used for super-prompt-critical transients, or can the same system accommodate a more satisfactory core?

B. TREAT Operations

1. Reactor Operations (J. F. Boland)

Last Reported: ANL-7561, pp. 105-106 (March 1969).

An EBR-II fuel element with a previous burnup of 2.5% was subjected to a series of five transients similar to those used previously for testing an element with 1.2% burnup (see Progress Reports for February and March 1969, ANL-7553, p. 117, and ANL-7561). The experimental capsules containing both the 1.2 and 2.5% burnup pins were shipped to the TAN hot cells for disassembly.

One zirconium-clad pelleted UO_2 sample was subjected to transient irradiation in a transparent capsule. This test was run to obtain additional

information on the mode of fuel failure and the extent of metal-water reaction obtained near the fuel-failure threshold (see Progress Report for August 1968, ANL-7487, p. 110).

Neutron radiographs were made of 17 groups of capsules from EBR-II.

Inspection of TREAT fuel elements that are handled frequently has recently been initiated (see ANL-7561). Inspection of ten special thermocouple assemblies revealed that five had distorted cladding, two appeared to have only a partial vacuum, and three appeared normal. Since the special thermocouple leads pass through the cladding, it is postulated that a very slow leak in some of these seals has allowed air to leak into the evacuated can, and heating of this air during transients has pressurized the assemblies sufficiently to cause permanent distortion of the cladding. Distorted cladding has not been observed on any standard fuel elements or standard thermocouple elements with brazed seals. All special thermocouple assemblies have been placed in storage. Since the thermocouples in these assemblies proved to be unreliable during initial operation in 1959, these elements have not been used for temperature measurements, but have been used as normal fuel elements; their removal from service will not affect reactor operations or experimental programs.

2. Development of Automatic Power Level Control System (J. F. Boland)

Last Reported: ANL-7561, p. 106 (March 1969).

Bid proposals for the stored-program digital-controller equipment to program the hydraulic control-rod-drive system were received during the first week of May, but additional information was required from some vendors before their proposals could be adequately evaluated. Evaluation of proposals was nearly complete at the end of this reporting period, and a purchase order for the equipment should be placed early in June.

MTS Systems Corp. completed the design of the control-rod actuator assembly and submitted an assembly drawing for our review. The design was found to be compatible with available space and was approved.

C. Chemical Reaction--Chemical and Associated Energy Problems (Thermal)

1. Analysis of Excursion Accidents (J. J. Barghusen)

Last Reported: ANL-7553, p. 118 (Feb 1969).

In the continuing in-pile study of the characteristics of fuel failure during a nuclear transient, six additional photographic experiments were

performed in the TREAT reactor. Three experiments were with Zircaloy-clad fuel rods containing vibrationally compacted UO_2 (5% enriched) particles identical to the rods previously tested in TREAT (experiments CEN-243T to -245T in Progress Report for August 1968, ANL-7487, pp. 110-112). In addition, to define fuel failure at reactor periods less than 120 msec, three experiments were performed with 0.375-in.-dia Zircaloy-clad fuel rods containing 10%-enriched UO_2 pellets. Previous experiments with this fuel type were made at reactor periods of 121 msec (see ANL-7487, pp. 110-112).

Table V.C.1 summarizes the results of the six experiments. Two separate failures, similar to those observed in experiment CEN-244T, occurred in Run CEN-246T. The failure at the bottom of the rod occurred at 218 cal/g UO_2 . Figure V.C.1 shows the condition of the fuel rod after the transient. The fracture at the top of the rod was not observed on the high-speed photographic film.

In Runs CEN-247T and -248T, cladding failure occurred at the bottom of the fuel rod at 256 and 238 cal/g UO_2 , respectively. In both cases, cladding failure probably resulted from the localized high internal pressure and intimate contact of the cladding with hot fuel. The final specimens from both runs showed complete dispersal of the oxide fuel and extensive cladding degradation by metal-water reaction, which occurred after the initial cladding rupture.

The fuel rods in Runs CEN-249T and -250T did not fail. The fission-energy input for Run CEN-251T was 354 cal/g UO_2 . Failure was

TABLE V.C.1. Results from TREAT Meltdown Experiments with Zircaloy-clad UO_2 Fuel Rods Submerged in Water

	CEN Run Number					
	246T	247T	248T	249T	250T	251T
<u>Characteristics of Fuel Rod</u>						
Fuel Type	Powder	Powder	Powder	Pellet	Pellet	Pellet
^{235}U enrichment, %	5	5	5	10	10	10
Rod diameter, in.	0.50	0.50	0.50	0.375	0.375	0.375
Fuel weight, g	169	169	169	87	87	87
Cladding weight, g	41	41	41	28	28	28
<u>Reactor Characteristics</u>						
Integrated power, MW-sec	379	507	499	214	217	320
Peak power, MW	1496	2790	2006	430	448	1111
Reactor period, msec	64	48	54	118	117	74
<u>Results</u>						
Total fission-energy input, cal/g UO_2	250	334	328	236	240	354
Fission-energy input at first indication of failure, cal/g UO_2	218	256	238	-	-	257
Zircaloy- H_2O reaction, g Zr	3.4	9.7	11.0	0.6	0.5	9.2
Final appearance of fuel rod	Two large holes; rod broken	Rod severely damaged; dispersal of fuel	Rod severely damaged; dispersal of fuel	Rod intact	Rod intact	Specimen completely destroyed

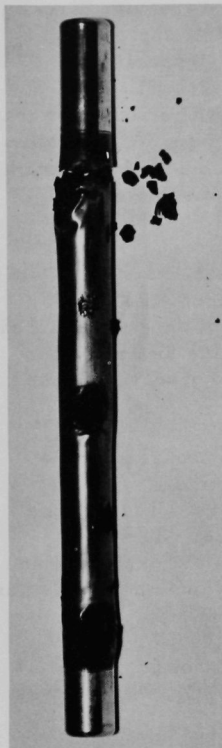


Fig. V.C.1

Vibrationally Compacted UO_2 Fuel Specimen from Run CEN-246T, Showing Two Failure Holes and Circumferential Fracture

observed on the photographic film at a fission-energy input equivalent to 257 cal/g UO_2 . This value, obtained at a reactor period of 74 msec, is nearly identical to the failure threshold value of 263 cal/g UO_2 established in Run CEN-242T performed at a reactor period of 122 msec. Similarly, this value is essentially the same as those observed at reactor periods 80 msec for 5%-enriched pellet fuel specimens.

To establish the magnitude of axial flux peaking in the 10%-enriched pelleted UO_2 fuel specimens, the specimen for the calibration test was sectioned and each pellet was analyzed separately by counting techniques. The peaking at the top and bottom of the specimen was found to be about 9 and 4%, respectively.

2. Pressure Generation due to Particle-Water Energy Transfer (R. O. Ivins)

a. Steam-explosion Experiments

Last Reported: ANL-7553, pp. 118-120 (Feb 1969).

Small-scale experiments of water injection into molten materials continue. Violent explosions were observed with silver chloride at 600°C, and with sodium chloride at 900 and 1000°C. A mild explosion was observed with yellow brass (63% Cu and 37% Zn) at 1100°C.

One of the most violent explosions occurred when 1 ml of water (at room temperature) was injected into a 65-g (45-ml) sample of molten sodium chloride at 1000°C. The sodium chloride was melted in a 1-in.-ID, $3\frac{1}{2}$ -in.-deep stainless steel crucible heated inductively. The thrust from the explosion was measured by the technique described in ANL-7553. The thrust consisted of four separate pulses. The initial pulse, which probably represented the major explosion, was a thrust of 205 lb. The three subsequent pulses, of much smaller magnitude, suggest that the major explosion was followed by several minor delayed effects. Examination of the first pulse shows the duration of the major explosion was approximately 0.6 to 0.9 msec. During the explosion about 70% of the molten mass was blown out of the crucible.

Water-injection experiments performed with molten aluminum (at 800 and 1000°C) and with silver (at 1100 and 1200°C) did not produce

explosions. Although some molten mass was splashed out of the crucible, the thrusts measured in these experiments did not exceed 5 lb. Several additional experiments of this type will be made because the molten material-water interaction appears to be extremely sensitive to the method and condition of contact.

D. Engineered Safety Features

1. Safety Features Technology--Containment

a. Hydrodynamics Response to High-energy Excursion (Y. W. Chang)

Last Reported: ANL-7553, pp. 120-123 (Feb 1969).

(i) Programming and Checking Axisymmetric Computer Code.

The computation of the sample problem was terminated by the computer at

$t = 811.28 \mu\text{sec}$ because the force

acting on the rotating plug exceeded the strength of the plug-holddown

device. To determine the maximum pressure and force that can be produced in the excursion, the compu-

tation was resumed by assuming

that the plug could be rigidly secured to the platform. Figure V.D.1 shows the variation of pressure at a typical

mesh zone underneath the plug

from $t = 811.28$ to $t = 1350 \mu\text{sec}$;

note that the pressure is of an oscillating nature and has several peaks.

The maximum peak pressure is about 33.3 kbar at $892 \mu\text{sec}$. Once the pres-

sure reaches a peak, the direction of the fluid is reversed. When the

returning fluid collides with the on-

coming fluid, the direction of the fluid

changes again. The total force acting

on the rotating plug is shown in

Fig. V.D.2. The maximum magni-

tude of the force is $\sim 6.44 \times 10^{14}$ dynes.

In this case, the plug-holddown

device should be designed to resist

the impulse resulting from such a

force.

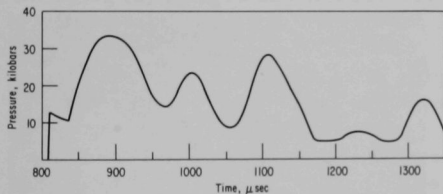


Fig. V.D.1. Variation of Pressure at a Typical Mesh Zone underneath the Plug

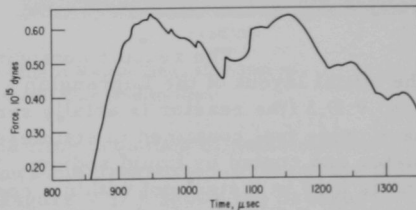


Fig. V.D.2. Total Force Acting on the Rotating Plug as a Function of Time

The computer code on the treatment of the "thin steel vessel" is almost complete.

b. Inelastic Response to High-energy Excursion (G. Cinelli, Jr.)

Last Reported: ANL-7527, p. 140 (Dec 1968).

(i) Analysis of Shock-wave Propagation. The analysis of shock-wave propagation is being extended to include sliding surfaces so that the code can be run for longer times. The sliding-surface routine will eliminate severe zone distortion at the interface between the sodium and the steel pressure vessel. Attainment of this routine is necessary to run the excursion code for longer times than is now possible.

(ii) Programming Finite-difference Equations in Fortran. The preliminary version of the two-dimensional computer code for the numerical calculation of the inelastic response of primary containment to a high-energy excursion has been completed. Outstanding features of the code are that it (1) contains equations of state of the reactor materials (the present version of the code contains the equation of state of the core, breeding blankets, plenum, sodium, steel pressure vessel, and argon), (2) gives the energy partition at all times, (3) gives the motion of the medium at all times, (4) determines whether or not, and when, the reactor vessel breaks, (5) gives the pressure loading on the plug and determines when the plug jumps, and (6) provides input to the definition of the plug-jump problem.

The code output, on printed sheets, gives displacements, velocities, pressures, internal energies, densities, and strains at every time step for all spatial points. The output of displacements and pressures can be given pictorially, showing the movements, deformations, and magnitude of pressure of all spatial points at any instant of time. This code will give the reactor designer information with which to adjust the geometry of the layout and strength of structural components to achieve a balanced design or a design that will dissipate the excursion energy with the least hazard to overall containment.

The reactor configuration selected for testing the code and the initial layout of the Lagrangian grids is shown for time zero in Fig. V.D.3 (the reactor is axially symmetrical). The core is assumed to have oxide fuel contained in stainless steel supported in stainless steel grid plates and cooled by liquid sodium. The sodium is covered by argon gas and is held in a steel pot within a concrete primary containment that has a rotatable shield plug in the platform at the top of the primary cavity.

For the excursion model, it is assumed at the start of the power excursion that the core is molten and the sodium has already vaporized and expelled from the core region. However, the blankets are assumed to be intact. The energy is released so rapidly in the excursion that the molten oxide fuels are assumed to be vaporized and superheated to high

temperature and pressure. Therefore, at the end of the power excursion, the core consists of only high-pressure oxide vapor.

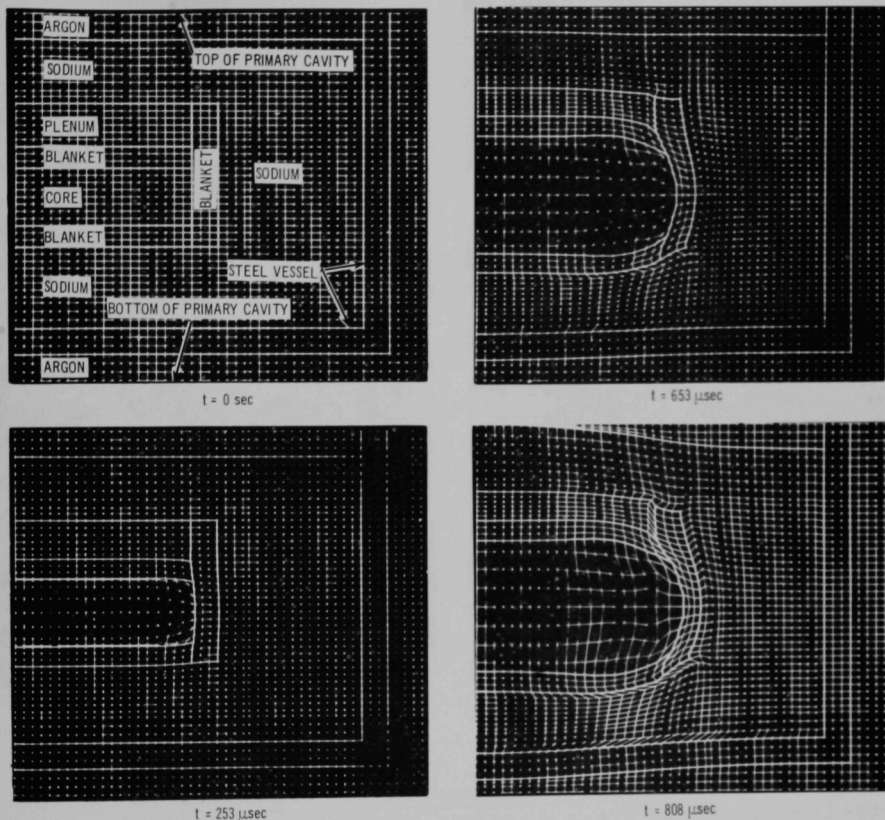


Fig. V.D.3. Deformation of Lagrangian Grids at Various Times after Start of a Power Excursion in a "Pancake" Core Configuration

Figure V.D.3 shows the time sequence of deformations of the Lagrangian grid. Figure V.D.4 shows the pressure profiles along the vertical centerline at various times. Figure V.D.5 shows the pressure profiles along the horizontal axis of the core at various times. The computation was terminated at $t = 808 \mu\text{sec}$ because the force acting on the plug exceeded the strength of the plug-holddown device. The total computer time for this sample problem was ~ 1 hr.

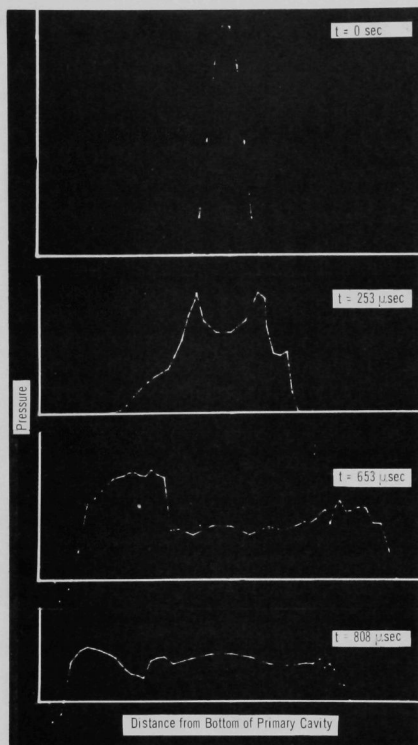


Fig. V.D.4. Pressure Profiles along Core Vertical Centerline at Various Times

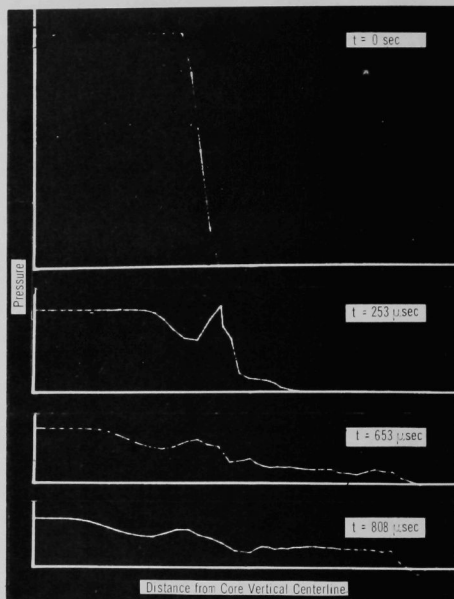


Fig. V.D.5. Pressure Profiles along Core Horizontal Axis at Various Times

(iii) Select Multiaxial Equations of State. A literature survey has been completed. From the survey, it was concluded that multiaxial equations of state exist that are applicable to the containment program. Therefore, experiments are needed.

PUBLICATIONS

The System Ta-Zn: Phase Studies

M. G. Chasanov, R. V. Schablaske, and I. Johnson
J. Electrochem. Soc. Japan 36, 192-196 (1968)

Critical Two-Phase Flow

H. K. Fauske

Chapter 6, Advanced Heat Transfer, B. T. Chao, Ed., University of Illinois Press, Urbana, Chicago, London, 1969

Approximate Solution of the Transient Free Convection Laminar Boundary Layer Equations

R. P. Heinisch

Z. Angew. Math. Phys. 20(1), 19-33 (1969)

Enthalpy of Solid Uranium Dioxide from 2500°K to Its Melting Point

L. Leibowitz, L. W. Mishler, and M. G. Chasanov

J. Nucl. Mater. 29, 356-358 (March 1969)

Optimal Digital Computer Control of Nuclear Reactors

Walter C. Lipinski

ANL-7530 (January 1969)

Strength-deformation Considerations of a Reactor Core Support Structure

A. H. Marchertas

Nucl. Eng. Design 9(1), 45-62 (January 1969)

Theoretical Study on Bubble Growth in Constant and Time-Dependent Pressure Fields

T. Theofanous, L. Biasi, H. S. Isbin,* and H. K. Fauske

Chem. Eng. Sci. 24, 855-897 (May 1969)

*University of Minnesota.

PUBLICATIONS--General

System and Component Design for Fast Reactors

L. J. Koch

Proc. Intern. Conf. on Constructive Uses of Atomic Energy,
Washington, D.C., Nov. 10-15, 1968. Am. Nucl. Soc., Hinsdale,
Ill., 1969, pp. 343-360

Nuclear Engineering

L. J. Koch

1969 Brittanica Yearbook of Science and the Future, Encyclopedia
Brittanica, Chicago, Ill., 1968, pp. 304-305

TRANTEMP: A Code for Calculating Transient Temperature Distributions
in Reactor Hydraulic Rabbit Facilities

Bryant N. Kristianson

ANL-7496 (November 1968)

Developments in the Elimination of Boron Loss from UO₂-Stainless Steel
Dispersion Fuel Plates for the Argonne Advanced Research Reactor
Mark I Core

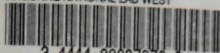
C. Victor Pearson

ANL-7477 (October 1968)

Chemical Engineering Division Research Highlights, May 1968-
December 1968

ANL-7550

ARGONNE NATIONAL LAB WEST



3 4444 00007979 8

+

